




# 京都大学化学研究所 国際共同利用・共同研究拠点

化学関連分野の深化・連携を基軸とする  
先端・学際グローバル研究拠点

令和4年度  
成果報告書

# 京都大学化学研究所 国際共同利用・共同研究拠点

化学関連分野の深化・連携を基軸とする  
先端・学際グローバル研究拠点



令和4年度  
成果報告書





まえがき

京都大学化学研究所は、平成22年度から「化学関連分野の深化・連携を基軸とする先端・学際研究拠点」（平成28年度から第二期）として国内外の共同利用・共同研究を推し進め、それを新たな糧としてより多様でグローバルな化学研究の展開と若手研究者の育成・輩出を図って参りました。特に本拠点では、化学関連コミュニティの研究者の皆様からの要請を踏まえながら、化学研究所の研究分野の広がりと深さに加えて、これまでの様々な連携実績を活かし、国内外の研究機関の相互協力を担保するハブ環境も提供しています。先端・学際的分野深耕にあたっては、関連コミュニティの研究者の皆様と化学研究所の教員が推進する分野選択型、課題提案型、施設・機器利用型、連携・融合促進型等の多彩な共同研究と、拠点として主催・共催する各種国際会議、シンポジウム、研究会等を通じて、多様性と先進性を担保し、さらに、国際的視点に基づいて次代の化学関連分野を担う若手研究者の育成にも注力しています。また、拠点運営では、所外、学外の関連分野有識者と化学研究所の教員を委員とする共同研究委員会および運営評議会を核として、共同研究課題の公募・採択などを戦略的に遂行しております。

このようなグローバルな拠点活動が評価され、化学研究所は、平成30年11月13日文部科学大臣から国際共同利用・共同研究拠点に認定され、「化学関連分野の深化・連携を基軸とする先端・学際グローバル研究拠点」として活動を強化しています。国際共同利用・共同研究拠点活動第二期初年度にあたる令和4年度には、化学研究所教員が丸となって、195件の応募の中から採択された136件の共同研究を遂行しました。そのうち、グローバルな化学研究の展開と人材育成のため、国際共同研究枠を採択数の46%に当たる63件（若手国際枠7件を含む）を遂行しました。しかし、令和2年度から続く世界的な新型コロナウイルス感染症拡大のため、国際・国内共同研究の実施にあたり対面交流が制限される状況が未だ続いております。これを補完する拠点活動支援として、本拠点ではリモート実験環境整備やハイブリッド会議システム導入など、研究・教育環境整備に引き続き取り組んで参りました。今後とも、国際的ハブ機能を活用し、国際共同利用・共同研究の一層の促進、国際学術ネットワークの充実、国際的・先進的視野をもつ若手研究者の育成に取り組むことで、化学を中心とする研究分野の深化と境界学術分野の新規開拓を一層推進して参ります。皆様にはさらなるご支援・ご協力のほどよろしくお願い申し上げます。

本報告書は、令和4年度の本拠点における研究成果をとりまとめたものです。本報告書をご一読頂き、今後の本拠点の目指すべき方向や活動の推進方法などに関する忌憚のないご意見・ご提案などをお聞かせ下されば幸甚に存じます。

化学研究所  
所長 青山 卓史



# 令和4年度 共同利用・共同研究報告書 目次

## 1. 共同研究成果報告

### 分野選択型共同研究

#### ビーム科学分野

2022-1	分岐構造を有するらせん状金ナノワイヤーの合成および光学特性評価	大阪産業技術研究所 中川 充	1
2022-2	Crystal Structure Analysis of GraE from Root-Nodule-Forming Bacterium	Kansai University Tadao Oikawa	2
2022-3	ナノ構造を持つ ISOL 用標的の開発	理化学研究所 大西 哲哉	3
2022-4	プリパルス付与による高変換TNSA イオン加速機構実証	光産業創成大学院大学 花山 良平	4
2022-5	Verification of radiochemical reactions with ultra-high dose rate electrons	National Institutes for Quantum Science and Technology Satoshi Kodaira	5

#### 元素科学分野

2022-6※	Design and Tailoring Advanced Functional Materials: Symmetry Operation and High Pressure Synthesis	National Taiwan University Wei-Tin Chen	6
2022-7※	Carboboration and Carbosilylation by Merging Iron and Visible-Light Photocatalysis	Visva-Bharati University Alakananda Hajra	7
2022-8※	Computational mechanistic study on the Co-catalyzed nitrogenase model reactions	University of Colombo W. M. C. Sameera	8
2022-9※	Development and device evaluation of new D- $\pi$ -A emitters based on rigidified triarylborone acceptors	Julius-Maximilians-Universität Würzburg Todd B. Marder	9
2022-10※	High pressure synthesis of novel hexagonal perovskite oxides containing unusually high-valence Fe ions and investigation of their magnetic properties	Chinese Academy of Sciences Zhenhong Tan	10
2022-11※	Preparation and Characterization of Novel Magnetic Quadruple Perovskites by High Pressure	CNRS Midori Estefani Amano Patino	11
2022-12※	High-pressure synthesis and ionic conducting study of novel Na-antiperovskites containing hydride and cluster anions as solid electrolytes in batteries	Chinese Academy of Science Koedtruad Anucha	12
2022-13※	Small molecule activation using anionic crypto-FLPs	University of Bonn Rainer Streubel	13
2022-14※	Development of Unsymmetrical $\pi$ -Electron Systems of Heavier Main Group Elements and Elucidation of Their Property	Tohoku University Takeaki Iwamoto	14
2022-15※	Development of 1,4-Addition Reactions via Iron Catalysis	Indian Institute of Engineering Science and Technology, Shibpur Laksmikanta Adak	15
2022-16※	Peptide Bolaamphiphile Anchored Nickel-based Metallohydrogel as Electrocatalyst for Hydrogen Production	Indian Institute of Technology Indore Apurba K. Das	16

※ 国際共同利用・共同研究



2022-17	Synthesis of Fe-containing Phosphorus Ligands and Their Application in the Preparation of Metal-Cluster Molecules	Tokushima University Masamichi Ogasawara	17
2022-18	自己集合性含ホウ素化合物の合成、集合過程解明ならびに機能開拓	鈴鹿医療科学大学 若林 成知	18
2022-19	MR-TADF 発光材料を用いた高効率塗布型有機EL 素子の開発	関西学院大学 小田 晋	19
2022-20	Synthesis and its catalysis of dinuclear complexes utilizing a pincer-type N,N,P ligand	Yokohama National University Yoshitaka Yamaguchi	20
2022-21	Synthesis of Alkyl Ethers Using Two Different Alcohols Catalyzed by Organosilane Compound	Sanyo-Onoda City University Toru Hashimoto	21
2022-22	Development of heteroacenes with excellent photophysical and electrochemical properties	Okayama University Koichi Mitsudo	22
2022-23	Creation of Effective Oxidation Scavenger for Efficient Perovskite-based Solar Cells	University of Tsukuba Takahiro Sasamori	23
バイオ情報学分野			
2022-24※	Developing machine learning approaches for prediction of protein stability changes upon missense mutations	Monash University Jiangning Song	24
2022-25※	Integrating omics data and module-based network with deep learning to develop cancer type predictive models	National Yang Ming Chiao Tung University Jinn-Moon Yang	25
2022-26※	Evolution of giant viruses and relationships with the origin of Life	CEA/Genoscope Morgan Gaïa	26
2022-27※	Revealing marine microbial-viral interactions through community interactome analyses	CNRS Samuel Chaffron	27
2022-28※	A Study on Statistical Machine Learning for Efficient Graph Structured Data Analysis	Nagoya Institute of Technology Masayuki Karasuyama	28
2022-29	オミクスデータと流束均衡解析に基づく高温適応進化の機序解明	東邦大学 岸本 利彦	29
2022-30	Control and Analysis of Complex Networks via Probabilistic Minimum Dominating Sets	Toho University Jose Nacher	30
2022-31	Development of a comprehensive detection method for coronaviruses originated in wildlife	Osaka University Tokiko Watanabe	31
2022-32	Microbial ecology in the dark sea	Kyoto University Takashi Yoshida	32
2022-33	効果的な分子ネットワーク解析方法の発展と医学・農学への応用	帯広畜産大学 茅野 光範	33

物質合成分野

2022-34※	Investigations into Catalytic and Biochemical Behaviors of Nitrogenase Fe protein using <sup>57</sup> Fe labeling	University of California, Irvine	Markus W. Ribbe	34
2022-35※	Precise synthesis and controlling higher order structure of tadpole-like Janus cellulose nanocrystal	Nanyang Technological University	Atsushi Goto	35
2022-36※	Exploration of perovskite solar cell composition: correlating device performance and fundamental property	Osaka University	Akinori Saeki	36
2022-37※	Precise synthesis and viscoelastic properties of ring polymers with high purity and high molecular weight	Nagoya University	Atsushi Takano	37
2022-38※	Exploration of Cycloaddition Properties of Guanidine Functionalized Isatins	Rudjer Boskovic Institute	Davor Margetic	38
2022-39※	Synthesis of Novel Nanotube Molecules with Different Hole Directions by Introducing a Double Heptalene Structure	Inner Mongolia University	Chaolumen	39
2022-40	金属酵素化学モデルの創製と材料・医化学への応用	山口東京理科大学	太田 雄大	40
2022-41	Dinitrogen Fixation based on nickel→Z-type (σ-Electron Acceptor) Ligand Interaction	Osaka Metropolitan University	Hajime Kameo	41
2022-42	キラルシリカの構造と分子認識との相関解明	大阪工業大学	平井 智康	42
2022-43	フロー合成法を用いた官能性ビニルテルリド合成法	北海道大学	永木 愛一郎	43
2022-44	環状ヘキサ-2,7-アントリレンエチニレン誘導体と環状パラフェニレンとのホスト-ゲスト化学に基づく複合化	静岡大学	小林 健二	44
2022-45	超分岐構造高分子の滑剤作用の解明と最適化	東北大学	高橋 裕	45
2022-46	Synthesis of Highly Strained Macrocyclic π-Conjugated Molecules via a Multinuclear Au(I)-Pt(II) complex	Tokyo University of Science	Yoshitaka Tsuchido	46
2022-47	有機電子材料を指向したアザアズレン3量体の合成と応用	久留米工業高等専門学校	黒飛 敬	47
2022-48	Development of Organometallic n-Type Materials with High Electrical Conductivity	Osaka Institute of Technology	Michihisa Murata	48
2022-49	未踏超不安定構造の単離および物性解明による新概念材料設計指針の創出	東北大学	上野 裕	49

現象解析分野

2022-50※	Non-linear viscoelasticity of unentangled polymers	Università degli Studi di Napoli “Federico II”	Giovanni Ianniruberto	50
2022-51※	Nonlinear Extensional Rheology of Entangled Poly(n-alkyl methacrylate) Melts with Fixed Number of Entanglements and Kuhn Segments per Chain	Chinese Academy of Sciences	Shilong Wu	51

※ 国際共同利用・共同研究

2022-52※	Trace metal elemental and isotopic composition in the North Pacific Ocean: sources and internal cycling (3)	Academia Sinica	Tung-Yuan Ho	52
2022-53※	Resolving the structure-dynamics-property relationship in polymer nanocomposites under uniaxial stretching-II	Stony Brook University	Tadanori Koga	53
2022-54※	High Frequency Response of Polymeric Liquids: Rheology and Dielectric Relaxation	Yamagata University	Sathish K. Sukumaran	54
2022-55※	Control of Mechanical Properties in Polymer Blend Materials by Hydrogen Bonding Interaction	Osaka University	Osamu Urakawa	55
2022-56	Analyzing Structural Fluctuation in Thermally Activated Delayed Fluorescence Materials with Ultralow-Frequency Raman Spectroscopy	Osaka University	Hikaru Sotome	56
2022-57	Effect of microplastics on distribution of trace heavy metals in sea water	Kindai University	Yuzuru Nakaguchi	57
2022-58	Exploration of liquid membrane transportation of metal ions with a polymer membrane containing ionic liquid by use of electric field response of ions	Kyoto University of Education	Hiroshi Mukai	58
2022-59	硫黄ポリマー材料におけるナノ構造不均一評価	関西学院大学	藤原 明比古	59
2022-60	Conformation analysis on polymer in food-grade oil	Okayama University of Science	Noboru Osaka	60
2022-61	プラズモニック合金ナノ粒子を設計するための理論的指針の構築	北海道大学	飯田 健二	61
2022-62	新規ハイブリッド型部分フッ素化リン脂質二分子膜の構造・物性の解析	群馬大学	園山 正史	62
2022-63	Identification of active gibberellins in the basal land plant <i>Marchantia polymorpha</i>	Kyoto University	Takayuki Kohchi	63
量子情報・スピントロニクス分野				
2022-64※	Characteristics of quantum magnon in magnetic insulators	Korea Advanced Institute of Science and Technology	Kab-Jin Kim	64
2022-65※	Observation of orbital Hall effect in transition metal dichalcogenides	University of Ulsan	Sanghoon Kim	65
2022-66※	Investigation on high efficient spin-orbit torque effect in multilayers with combine anisotropy and DMI	Far Eastern Federal University	Alexey Ognev	66
2022-67※	Research on the efficiency enhancement of the NV centers creation in nanodiamond	ETH Zürich	Takuya F. Segawa	67
2022-68※	Research toward stable NV centers at shallow region and spin dynamics in diamond	Helmholtz-Zentrum Dresden-Rossendorf	Gopalakrishnan Balasubramanian	68
2022-69	Demonstration of topological phase control in chalcogenide superlattices	AIST	Misako Morota	69
2022-70	人工反強磁性体のマグノンを用いた量子情報演算素子の基盤技術開発	東京大学	石橋 未央	70

2022-71	ダイヤモンド量子情報素子のための表面状態研究	金沢大学 徳田 規夫	71
2022-72	量子センサの高感度化に向けたリンダープダイヤモンド合成と量子科学技術研究	産業技術総合研究所 牧野 俊晴	72
課題提案型共同研究			
2022-73※	Self-Assembling Adjuvant-Built-In Vaccines for Cancer Immune Therapy	Tsinghua University Yan-Mei Li	73
2022-74※	Evaluation of CaCO <sub>3</sub> dissolution rates in deep-sea sediments by a novel tracer method	Xiamen University Pinghe Cai	74
2022-75※	Advanced Oxygen – mediated Flow Chemistry	Cardiff University Thomas Wirth	75
2022-76※	Novel strategy for intracellular delivery of nanomedicines	Institute for Advanced Chemistry of Catalonia Sílvia PUJALS	76
2022-77※	Structural and functional analysis of curvature-inducing peptides and application	Karlsruhe Institute of Technology Anne S. Ulrich	77
2022-78※	In-depth analysis of efficiency roll-off in highly efficient TADF-based organic electroluminescence devices	The University of Queensland Ebinazar B. Namdas	78
2022-79※	Intracellular delivery of biofunctional proteins using artificial protein nanocages	Jagiellonian University Yusuke Azuma	79
2022-80	Real-Time Visualization of Cellular Phase-Separating Proteins	Osaka University Kazuya Kikuchi	80
2022-81	合成小分子化合物による細胞の遠隔操作	東京理科大学 西川 元也	81
2022-82	有機合成・単分子測定・計算化学の協同による2次元ドナー・アクセプター分子系の構築	理化学研究所 木村 謙介	82
2022-83	両親媒性希土類錯体を利用した薄膜発光体の作製	大阪公立大学 三枝 栄子	83
2022-84	フッ素系樹脂の摩擦界面における分子挙動の解明	公立小松大学 粕谷 素洋	84
2022-85	エクソソームの細胞内への送達設計	大阪公立大学 中瀬 生彦	85
2022-86	細胞外小胞の標的細胞への移行メカニズムの解明	三重大学 江口 暁子	86
2022-87※	Role of PIP5K Genes in Pollen Tube Development	Peking University QU, Li-Jia	87
2022-88※	Construction of heterologous protein secretion system at low temperatures by using cold-adapted microorganisms	Southwest University Xianzhu Dai	88
2022-89※	Structural and functional analysis of the surface polysaccharides of outer membrane vesicles released by bacteria	University of Naples Federico II Maria Michela Corsaro	89
2022-90※	Molecular mechanisms for the inactivation of a growth hormone in rice	Chinese Academy of Sciences Zuhua He	90

※ 国際共同利用・共同研究



2022-91※	Analysis of novel transporters for strigolactones or their biosynthetic intermediates	University of California San Diego	Yunde Zhao	91
2022-92※	Phase separation in mixture of nematic liquid crystal and solvent	Japan Women's University	Ryoko Shimada	92
2022-93※	Chromatin, epigenetic and proteolytic regulation of RNA processing in plant morphogenesis	National Center of Biotechnology	RUBIO, Vicente	93
2022-94※	Site-Selective Protein Acetylation and Phosphorylation by Small Molecules	Fudan University	Lu Zhou	94
2022-95※	Developments of highly efficient and high color purity organic electroluminescent devices based on thermally activated delayed fluorescent materials exhibiting ultrafast reverse intersystem crossing process	Tsinghua University	Lian Duan	95
2022-96※	Fabrication of nanotopographical polymer surfaces for bactericidal properties-IV	Stony Brook University	Maya Endoh	96
2022-97※	Verification and Development of Dynamic Stiction Theory	Yokohama National University	Ken Nakano	97
2022-98※	Synthesis of Polyether Nanocomposite Solid Polymer Electrolytes for Lithium Ion Batteries	Michigan State University	Robert C. Ferrier, Jr.	98
2022-99※	Development and characterization of metal oxide nanocrystalline films for solar water splitting	RMIT University	Yasuhiro Tachibana	99
2022-100※	Interdisciplinary Approach to Nanostructured Materials for Applications	Université de Strasbourg	Jean-Pierre Bucher	100
2022-101※	Search for four-wave-mixing in the vacuum - Unveiling dark components in the Universe -	Hiroshima University	Kensuke Homma	101
2022-102※	Tin-perovskite thin film crystallization on new hole-transporting materials	Helmholtz-Zentrum Berlin	Antonio Abate	102
2022-103	Biochemical characterization of aldehyde dehydrogenases involved in the biosynthesis of plant volatile benzenoids	Yamaguchi University	Takao Koeduka	103
2022-104	Regulatory Role of Phytohormone Cytokinin on Leaf Epidermal Cell Differentiation	Nara Institute of Science and Technology	Shiori Aki	104
2022-105	Electronic and spintronic properties of multilayer system including $\text{NiCo}_2\text{O}_4$ and $\text{Fe}_3\text{O}_4$	Hokkaido University	Taro Nagahama	105
2022-106	アルツハイマー病治療に向けたアミロイド光酸素化触媒の構造最適化	東京大学	金井 求	106
2022-107	動的効果を考慮した熱活性化型遅延蛍光速度論の確立	早稲田大学	浦谷 浩輝	107
2022-108	Analysis of the physiological functions of extracellular vesicles produced by intestinal bacteria and their application	Kindai University	Atsushi Kurata	108

2022-109	Analysis of membrane lipid-dependent fermentation stress response in acetic acid bacteria	Ritsumeikan University	Yosuke Toyotake	109
2022-110	擬秩序ガラスの熱伝導	弘前大学	増野 敦信	110
2022-111	電気化学的プロトン脱挿入を利用した金属酸化物の新奇物性探索	物質・材料研究機構	土屋 敬志	111
2022-112	高圧合成による新規フッ化物イオン伝導体の探索	高エネルギー加速器研究機構	齊藤 高志	112
2022-113	界面活性剤を利用した溶媒含浸樹脂による金属分離	大阪公立大学工業高等専門学校	倉橋 健介	113
2022-114	全反射近赤外分光法による高分子ブラシ層内の水の構造解析	富山大学	源明 誠	114
2022-115	3D プリンタを用いたモノリスの3次元構造制御	共立女子大学	村瀬 浩貴	115
2022-116	単電子トランジスタにおける巨大磁気抵抗効果の検討	東京工業大学	真島 豊	116
2022-117	担持金属表面に金属酸化物クラスターを修飾した二元機能触媒の創製	東京都立大学	山添 誠司	117
2022-118	電子顕微鏡内での単一三次元量子ドット超格子の電子輸送特性と構造相転移挙動の同時観測	名古屋工業大学	浅香 透	118
2022-119	再生可能資源・木質バイオマスの先端化学材料への効率的変換法の開発	奈良県立医科大学	秦野 修	119
2022-120	Functional analysis of non-canonical strigolactones as plant hormones and root-derived signals	Meiji University	Yoshiya Seto	120
2022-121	Preparation of multi-stimuli-responsive polymer via controlled radical polymerization	University of Hyogo	Shinichi Yusa	121
2022-122	積層CNT ターゲットへの高強度レーザー照射による高圧ガス生成に関する実験研究	京都大学	松井 隆太郎	122
2022-123	高強度レーザーと構造性媒質の相互作用による高エネルギー密度プラズマの生成・保持に関する実験研究	京都大学	岸本 泰明	123
連携・融合促進型共同研究				
2022-124※	Determine the three-dimensional structure of $^{13}\text{C}$ labeled $\alpha$ -synuclein(61-95) in the Langmuir-Blodgett film and supported phospholipid bilayer by MAIRS2	Middle Tennessee State University	Chengshan Wang	124
2022-125※	The 16th International Workshop for East Asian Young Rheologists	Osaka University	Tadashi Inoue	126
施設・機器利用型共同研究				
2022-126※	Tackling the Electronic Instability of Charge-Density Waves by Electron Energy-Loss Spectroscopy	National Taiwan University	Ming-Wen Chu	128

※ 国際共同利用・共同研究

2022-127※	Micro- and Nano-structural Characterization by Advanced Transmission Electron Microscopy of Novel Functional Materials	Chiang Mai University Torranin CHAIRUANGSRI	129
2022-128※	High-pressure synthesis of transition metal oxides with novel physical properties	University of Edinburgh Kunlang Ji	130
2022-129※	Synthesis and Characterization of Novel Group 16 Element Compounds	Rikkyo University Mao Minoura	131
2022-130※	Analyzing chemical properties and origins of dissolved organic matter in lakes and soils by FT-ICR-MS	Kobe University Morimaru Kida	132
2022-131	Preparation of high-efficiency spin-injection materials using optimization of magnetism and crystal structure	Nagoya Institute of Technology Masaaki Tanaka	133
2022-132	Development of a highly efficient CsPbBr <sub>3</sub> scintillator	Kyushu University Hikaru Saito	134
2022-133	核融合プラズマ対向材料中の水素・ヘリウム挙動の高精度測定	島根大学 宮本 光貴	135
2022-134	Synthesis and Structural Characterization of Lewis Base Adducts of Tetraenes	Kindai University Tsukasa Matsuo	136
2022-135	Synthesis and structures of cationic aromatics bearing chalconenopyrylium units	Fukuoka University Noriyoshi Nagahora	137
2022-136	Theoretical design of low-dimensional silicon material embedded in a flat two-dimensional sheet and exploration for operating principles	Tohoku University Masae Takahashi	138

## 2. 国際学会、シンポジウム・研究報告会

### 国際会議

- ・ 24th International Colloquium on Magnetic Films and Surfaces (ICMFS2022) 139

### シンポジウム・研究会

- ・ 分子材料化学セミナー 141
- ・ 第 6 回 MAIRS ワークショップ 143

## 3. 成果発表論文

145

(令和 5 年 3 月までに刊行された論文で、平成 22—令和 3 年度の成果報告書に掲載されていないもの)

紙数の都合により、\*を付けた論文のみについて、別刷りを本報告書に記載する。

- 1)\* Nitrogen reduction by the Fe sites of synthetic  $[\text{Mo}_3\text{S}_4\text{Fe}]$  cubes, *Nature*, 607, 86–90 (2022).
- 2)\* Field-free superconducting diode effect in noncentrosymmetric superconductor/ferromagnet multilayers, *Nat. Nanotechnol.*, 17, 823–828 (2022).
- 3) Synthesis of perfluoroalkylene-vinylene-arylene copolymers via the Mizoroki-Heck copolymerization of 1,4-divinylperfluorobutane and 1,6-divinylperfluorohexane with dihalogenated arylene monomers, *J. Fluor. Chem.*, 261–262, 110033 (2022).
- 4) Boron complexes of  $\pi$ -extended nitroxide ligands exhibiting three-state redox processes and near-infrared-II (NIR-II) absorption properties, *Dalton Trans.*, 51, 13675–13680 (2022).
- 5) Synthesis and characterization of a polystyrene-type polymer bearing a cyclic perfluoroalkylene group, *Polymer*, 265, 125588 (2023).
- 6) Utilization of sym-tetrazines as guanidine delivery cycloaddition reagents. An experimental and computational study, *J. Mol. Struct.*, 1272, 134207 (2023).
- 7) Consecutive Utilization of Mechanochemical and Microwave Methods for the Synthesis of Boc-2-amino-quinazolin-4(3H)-ones and DFT Study of Mechanism  $6\pi$ -Diazaelectrocyclization Process, *ChemistrySelect*, 7, e202200633 (2022).
- 8) Formation and Stability of  $\text{Cs}_2\text{SnBr}_6$  Perovskite Nanocrystals from  $\text{CsSn}_2\text{Br}_5$  Nanocubes, *J. Photopolym. Sci. Technol.*, 35, 199–204 (2022).
- 9) Hot hole transfer at the plasmonic semiconductor/semiconductor interface, *Nanoscale*, 15, 657–666 (2023).
- 10) Determine both the conformation and orientation of a specific residue in  $\alpha$ -synuclein(61–95) even in monolayer by  $^{13}\text{C}$  isotopic label and p-polarized multiple-angle incidence resolution spectrometry (pMAIRS), *Anal. Sci.*, 935–940 (2022).
- 11) Optimized carrier extraction at interfaces for 23.6% efficient tin–lead perovskite solar cells, *Energy Environ. Sci.*, 15, 2096–2107 (2022).
- 12) Molecular Engineering of Enamine-Based Hole-Transporting Materials for High-Performing Perovskite Solar Cells: Influence of the Central Heteroatom, *Sol. RRL*, 6, 2200590 (2022).
- 13) Synergistic Surface Modification of Tin–Lead Perovskite Solar Cells, *Adv. Mater.*, 35, 2208320 (2023).
- 14) A Universal Surface Treatment for p-i-n Perovskite Solar Cells, *ACS Appl. Mater. Interfaces*, 14, 56290–56297 (2022).



- 15) Composition–Property Mapping in Bromide-Containing Tin Perovskite Using High-Purity Starting Materials, *ACS Appl. Energy Mater.*, 5, 14789–14798 (2022).
- 16) Topotactic Oxygen Release and Incorporation in  $\text{AFeO}_3$  with  $\text{Fe}^{4+}$ ,  $\text{AFeO}_{2.5}$  with  $\text{Fe}^{3+}$ , and  $\text{AFeO}_2$  with  $\text{Fe}^{2+}$  (A = Ca and Sr): Dedicated to the Occasion of the 100th Birthday of Prof. John B. Goodenough, *ECS J. Solid State Sci. Technol.*, 11, 043004 (2022).
- 17) High-Pressure Synthesized Perovskite  $\text{CdMnO}_3$  with C-Type Antiferromagnetic Spin Configuration, *Inorg. Chem.*, 61, 21011–21015 (2022).
- 18) Orientation-dependent electrochemical reduction and proton evolution in the oxygen-deficient perovskite  $\text{SrFeO}_{2.5+y}$ , *Appl. Phys. Express*, 16, 015506 (2023).
- 19) Film growth mechanism of mist-chemical-vapor-deposited magnetite, *Jpn. J. Appl. Phys.*, 61, 065505 (2022).
- 20) Charge Transfer between Fe and Ti Induced by Ln Substitution and Temperature in the B-Site-Disordered Perovskites  $\text{Ln}_2(\text{FeTi})\text{O}_6$  (Ln = La, Pr, and Nd), *Bull. Chem. Soc. Jpn.*, 95, 1011-1015 (2022).
- 21)  $\text{LiNbO}_3$ -Type Polar Antiferromagnet  $\text{InVO}_3$  Synthesized under High-Pressure Conditions, *Angew. Chem. Int. Ed.*, 61, e202203669 (2022).
- 22) Orthogonal antiferromagnetism to canted ferromagnetism in  $\text{CaCo}_3\text{Ti}_4\text{O}_{12}$  quadruple perovskite driven by underlying kagome lattices, *Communications Materials*, 3, 51 (2022).
- 23) A New Cation-Ordered Structure Type with Multiple Thermal Redistributions in  $\text{Co}_2\text{InSbO}_6$ , *Angew. Chem. Int. Ed.*, 61, e202203062 (2022).
- 24) Incorporation of an Asymmetric Mo-Fe-S Cluster as an Artificial Cofactor into Nitrogenase, *Chembiochem*, 23, e202200384 (2022).
- 25) Transition metal catalyzed cross-coupling and nitrogen reduction reactions: Lessons from computational studies, *Adv. Organomet. Chem.*, 78, 35–78 (2022).
- 26) Activation of unsaturated small molecules by bio-relevant multinuclear metal-sulfur clusters, *Coord Chem Rev*, 475, 214838 (2023).
- 27) Diastereo- and Enantioselective Metathesis Dimerization/Kinetic Resolution of Racemic Planar-Chiral Vinylferrocenes, *Org. Lett.*, 24, 7355–7360 (2022).
- 28) *n*-type diamond synthesized with *tert*-butylphosphine for long spin coherence times of perfectly aligned NV centers, *J. Appl. Phys.*, 132, 174504 (2022).
- 29) Low-Frequency Quantum Sensing, *Phys. Rev. Appl.*, 18, 034058 (2022).
- 30) Electroluminescence of negatively charged single NV centers in diamond, *Appl. Phys. Lett.*, 122, 072101 (2023).
- 31) Magnetic-field-induced polarity oscillation of superconducting diode effect, *Appl. Phys. Express*, 15, 113001 (2022).
- 32) Temperature dependence of domain wall creep motion in ferrimagnetic Tb/CoFeB/MgO microwires, *J. Magn. Magn. Mater.*, 553, 169251 (2022).
- 33) Polarization-Selective Excitation of Antiferromagnetic Resonance in Perpendicularly Magnetized Synthetic Antiferromagnets, *Phys. Rev. Appl.*, 18, 014032 (2022).
- 34) Bismuth composition, thickness, and annealing temperature dependence of the spin Seebeck voltage in Bi-YIG films prepared using sol–gel solution and spin-coating method, *J. Magn. Magn. Mater.*, 556, 169416 (2022).

- 35) Generation of spin-polarized electronic currents using perpendicularly magnetized cobalt ferrite spin-filtering barriers grown on spinel-type-conductive layers, *Appl. Phys. Lett.*, 122, 042401 (2023).
- 36) Comprehensive understanding of multiple resonance thermally activated delayed fluorescence through quantum chemistry calculations, *Commun. Chem.*, 5, 53 (2022).
- 37) Near-infrared-red-orange thermally activated delayed fluorescence emitters using a strong tetracoordinated difluoroboronated acceptor, *Jpn. J. Appl. Phys.*, 61, 081001 (2022).
- 38) Promoting Reverse Intersystem Crossing in Thermally Activated Delayed Fluorescence via the Heavy-Atom Effect, *J. Phys. Chem. A*, 127, 439–449 (2023).
- 39) Thioxanthone-containing blue thermally activated delayed fluorescent emitter, *Appl. Phys. Express*, 16, 011006 (2023).
- 40) Imidazole Acceptor for Both Vacuum-Processable and Solution-Processable Efficient Blue Thermally Activated Delayed Fluorescence, *ACS OMEGA*, 7, 16740–16745 (2022).
- 41) A multifunctional hole-transporter for high-performance TADF OLEDs and clarification of factors governing the transport property by multiscale simulation, *J. Mater. Chem. C*, 10, 8694–8701 (2022).
- 42) Dynamic nuclear polarization - nuclear magnetic resonance for analyzing surface functional groups on carbonaceous materials, *Carbon*, 206, 84–93 (2023).
- 43) Search for sub-eV axion-like particles in a stimulated resonant photon-photon collider with two laser beams based on a novel method to discriminate pressure-independent components, *J. High Energy Phys.*, 176 (2022).
- 44) Rice husk-derived nano-SiO<sub>2</sub> assembled on reduced graphene oxide distributed on conductive flexible polyaniline frameworks towards high-performance lithium-ion batteries, *RSC Adv.*, 12, 14621–14630 (2022).
- 45) Low-Cost Production of Fe<sub>3</sub>O<sub>4</sub>/C Nanocomposite Anodes Derived from Banana Stem Waste Recycling for Sustainable Lithium-Ion Batteries, *Crystals*, 13, 280 (2023).
- 46) Structure-Based Design of Dual Bactericidal and Bacteria-Releasing Nanosurfaces, *ACS Appl. Mater. Interfaces*, 15, 3420–3432 (2023).
- 47) Rheo-Dielectric Behavior of Unentangled Poly(butylene oxide) under Steady Shear: Preliminary Evaluation of Non-Equilibrium Parameters at the Onset of Nonlinearity, *Nihon Reoroji Gakkaishi*, 50, 371–385 (2022).
- 48) Distribution and stoichiometry of Al, Mn, Fe, Co, Ni, Cu, Zn, Cd, and Pb in the Seas of Japan and Okhotsk, *Mar Chem*, 241, 104108 (2022).
- 49) A carlactonoic acid methyltransferase that contributes to the inhibition of shoot branching in *Arabidopsis*, *Proc. Natl. Acad. Sci. USA*, 119, e2111565119 (2022).
- 50) Controlled lipid  $\beta$ -oxidation and carnitine biosynthesis by a vitamin D metabolite, *Cell Chem. Biol.*, 29, 660–669 (2022).
- 51) Self-assembling small-molecule adjuvants as antigen nano-carriers, *J. Hazard. Mater.*, 58, 12228–12231 (2022).
- 52) Magnetic Control of Cells by Chemical Fabrication of Melanin, *J. Am. Chem. Soc.*, 144, 16720–16725 (2022).
- 53) Polysaccharide corona: The acetyl-rich envelope wraps the extracellular membrane vesicles and the cells of *Shewanella vesiculosa* providing adhesiveness, *Carbohydr. Polym.*, 297, 120036 (2022).

- 54) Tight association between microbial eukaryote and giant virus communities in the Arctic Ocean, *Limnol. Oceanogr.*, 67, 1343-1356 (2022).
- 55) "Mamonoviridae", a proposed new family of the phylum Nucleocytoviricota, *Arch. Virol.*, 168, 80 (2023).
- 56) MSNet-4mC: learning effective multi-scale representations for identifying DNA N<sub>4</sub>-methylcytosine sites, *Bioinformatics*, 38, 5160-5167 (2022).
- 57) Densest subgraph-based methods for protein-protein interaction hot spot prediction, *BMC Bioinform.*, 23, 451 (2022).
- 58) iFeatureOmega: an integrative platform for engineering, visualization and analysis of features from molecular sequences, structural and ligand data sets, *Nucleic Acids Res.*, 50, W434–W447 (2022).
- 59) Demonstration of efficient relativistic electron acceleration by surface plasmonics with sequential target processing using high repetition lasers, *Phys. Rev. B*, 5, 013062 (2023).
- 60) Stearilated Macropinocytosis-Inducing Peptides Facilitating the Cellular Uptake of Small Extracellular Vesicles, *Bioconjug. Chem.*, 33, 869–880 (2022).
- 61) Control over Ligand-Exchange Positions of Thiolate-Protected Gold Nanoclusters Using Steric Repulsion of Protecting Ligands, *J. Am. Chem. Soc.*, 144, 12310–12320 (2022).
- 62) One-Pot Preparation of (NH)-Phenanthridinones and Amide-Functionalized [7]Helicene-like Molecules from Biaryl Dicarboxylic Acids, *J. Org. Chem.*, 87, 5510–5521 (2022).
- 63) Small molecule-based detection of non-canonical RNA G-quadruplex structures that modulate protein translation, *Nucleic Acids Res.*, 50, 8143–8153 (2022).
- 64) Chiral Open-[60]Fullerene Ligands with Giant Dissymmetry Factors, *J. Am. Chem. Soc.*, 144, 18829–18833 (2022).
- 65) Multivariate Analysis of Mixed Ternary and Quaternary A-Site Organic Cations in Tin Iodide Perovskite Solar Cells, *ACS Materials Lett.*, 4, 1124–1131 (2022).
- 66) Phosphorus ylides of cage-opened sulphide [60]fullerene derivatives, *Dalton Trans.*, 51, 17804-17808 (2022).
- 67) Aniline-Mediated Imination and Reduction of a Cage-Opened C<sub>60</sub> Derivative, *Asian J. Org. Chem.*, 11, e202200357 (2022).
- 68) Reaction of an Overcrowded 1,2-Diaryl-1,2-dibromodisilene with 1-Vinylcyclohepta-1,3,5-triene: Isolation of a 2-Vinylsilacyclopropane Derivative and Its Thermal Conversion to a Silacyclopent-3-ene Derivative, *Heterocycles*, 104, 389 - 396 (2022).
- 69) Selective Addition of Aniline to a Cage-opened Diketo Anhydride Derivative of C<sub>60</sub>, *Chem. Lett.*, 51, 949-952 (2022).
- 70) Discovery of a phase-separating small molecule that selectively sequesters tubulin in cells, *Chem. Sci.*, 13, 5760-5766 (2022).
- 71) A noncanonical endocytic pathway is involved in the internalization of 3  $\mu$ m polystyrene beads into HeLa cells, *Biomater. Sci.*, 10, 7093-7102 (2022).
- 72) Synthesis and structure–activity relationship of 16,17-modified gibberellin derivatives, *Phytochem Lett*, 49, 162-166 (2022).
- 73) Characterization of resonance structures in aromatic rings of benzene and its heavier-element analogues, *Phys. Chem. Chem. Phys.*, 24, 22557-22561 (2022).
- 74) C<sub>2</sub>-insertion into a fullerene orifice, *Chem. Commun.*, 59, 1645-1648 (2023).

- 75) Electric field effect on spectroscopic g-factor and magnetic anisotropy in a Pt/Co/MgO ultrathin film, *Jpn. J. Appl. Phys.*, 61, 103001 (2022).
- 76) Near-Infrared-Absorbing Chiral Open [60]Fullerenes, *Angew. Chem. Int. Ed.*, 62, e202215380 (2023).
- 77) Perovskite/Perovskite Tandem Solar Cells in the Substrate Configuration with Potential for Bifacial Operation, *ACS Materials Lett.*, 4, 2638–2644 (2022).
- 78) Pulse-width dependence of spin–orbit torque switching in Mn<sub>3</sub>Sn/Pt thin films, *Appl. Phys. Lett.*, 122, 122405 (2023).

#### 4. 参考資料

4-1.令和 4 年度公募要領	159
4-2.令和 4 年度採択課題一覧	163





## 1. 共同研究成果報告



## 分岐構造を有するらせん状金ナノワイヤーの合成および光学特性評価

中川 充 大阪産業技術研究所

【目的】局在表面プラズモン共鳴に由来した特異な光学活性を示すナノ材料は、不斉合成やメタマテリアルなどへの応用が期待されることから、盛んに研究されている。しかし、キラルな貴金属ナノ構造の複雑な制御やそれらの光学特性を調節する技術については改良の余地が多く残されている。本研究では、これまでに合成法を確立したらせん状金ナノワイヤー (Au NWs) について、分岐構造を修飾することでその特異な光学特性を制御、増強させることを試みた。

【方法】先行研究で合成に成功している直径 3 nm で分岐のない右巻きらせん状 Au NWs に化学的処理を施すことで分岐構造を形成させた。修飾はシード粒子となる Au NWs の水分散液に、金前駆体として塩化金酸、保護剤として長鎖アミン誘導体、還元剤として L-アスコルビン酸を添加し、23 °C で 7 日間攪拌することにより行った。

【結果と考察】得られた Au NWs のナノ構造を透過型電子顕微鏡 (TEM) により観察したところ、分岐構造の形成を確認した。シードとして用いた Au NWs は多結晶であり、「幹」となる部分の表面には結晶粒界などの格子欠陥を多く有している。今回試みた分岐修飾処理では、これらの格子欠陥を起点とした分枝の生成および異方成長が起こっていると推測される。そこで、分枝状 Au NWs の枝および幹の部分について、高分解能 TEM 観察による結晶構造の評価を行った。幹の部分についてはシードとして用いた Au NWs と同様に多くの結晶粒界や Au の面心立方格子に由来する様々な周期の格子縞が観察された。一方、枝の部分は幹の部分と比べて非常に大きな結晶ドメインにより形成されていることが分かった (Fig. 1)。また、これらの結晶ドメインの多くから Au(111) に由来する格子縞が観察されたことから、枝の部分は主に Au(111) 方向への異方成長によって形成されたと考えられる。

続いて、得られた分枝状 Au NWs について光学特性の評価を行った。分枝状 Au NWs はシードとして用いたらせん状 Au NWs と同様、近赤外領域に強い吸収帯を有し、円二色性を示すことが分かった。興味深いことに、吸光度に対する円二色性 ( $g$ -factor, Fig. 2) が、分岐構造の形成後大幅に増大した。円二色性の増強が Au NWs のどのような構造変化に起因するか現在調査中である。

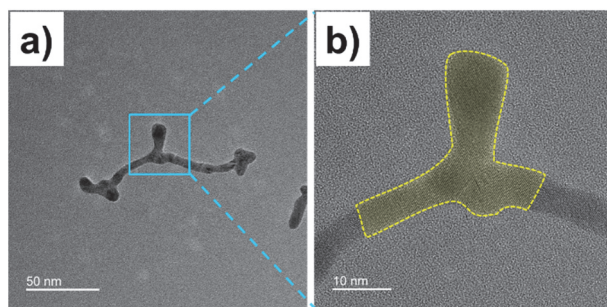


Fig. 1. TEM images of branched Au NWs. Yellow area shows crystalline domain.

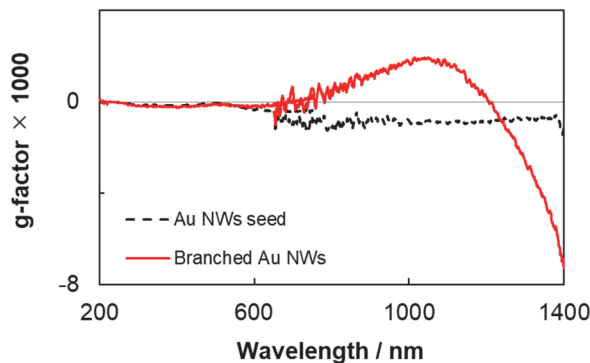


Fig. 2. Dis-symmetry factor ( $g$ -factor) of Au NWs.

## Crystal Structure Analysis of GraE from Root-Nodule-Forming Bacterium

Tadao Oikawa    Kansai University

*Rhizobium* is a genus of tubercle-forming bacteria. It grows in symbiosis with the root of a plant to fix nitrogen from the air. During a screening experiment, *Rhizobium* sp. strain MTP-10005 was isolated from natural river water. Enzymological and genetic studies showed that the translational products of the gene cluster *graRDAFCBEK* in the bacterium (GraR, GraD, GraA, GraF, GraC, GraB, GraE, and GraK, respectively) were probably involved in the degradation pathway of  $\gamma$ -resorcyate. To reveal the structure and function of all these proteins, I have collaborated with Dr. Tomomi Fujii and Prof. Emeritus Dr. Yasuo Hata, Institute for Chemical Research, Kyoto University, and have performed already X-ray structural studies of GraA, GraC, and GraD. In this study, we focused on GraE, whose function and role in the degradation pathway of  $\gamma$ -resorcyate are currently unknown. The protein consists of 112 amino acid residues. The X-ray crystal structure of GraE is expected to reveal its function and role *in vivo*.

N-terminal His-tagged GraE was overexpressed in *Escherichia coli* BL21 (DE3), purified, and used for crystallization. Thin plate-shaped crystals were obtained using a crystallization solution consisting of 1.17 M NaH<sub>2</sub>PO<sub>4</sub> · K<sub>2</sub>HPO<sub>4</sub>, pH 8.4. Diffraction experiments were performed on beamline BL-17A, Photon Factory, KEK, Japan. The crystal was mounted with a cryoloop and cooled with a cold stream of nitrogen. Diffraction data were collected up to 2.2 Å resolution. The crystal belonged to space group *P*2<sub>1</sub>2<sub>1</sub>2, with unit-cell parameters of *a* = 89.84 Å, *b* = 165.31 Å, and *c* = 45.20 Å. The structure was determined using the molecular replacement method with the structural model determined in the *P*2<sub>1</sub> crystal. The solution model was subjected to iterative model-building and refinement. The structure was refined to an *R*-factor and *R*<sub>free</sub> of 20.5 and 27.6%, respectively.

In the present crystal, three homodimer GraE molecules exist in an asymmetric unit. The subunit structure consists of three  $\alpha$ -helices and five  $\beta$ -strands, and it roughly resembles a bacterial-type ferredoxin fold. The dimer interface is formed by packing the four-stranded  $\beta$ -sheets from the two subunits against each other. The putative active site is located in a cleft made of an  $\alpha$ -helix  $\alpha$ 1 and two  $\beta$ -strands  $\beta$ 2 and  $\beta$ 3 from one subunit and C-terminal loop from the other subunit. In a dimer molecule, the phosphate ion in the putative active site binds to the side chains of arginine, histidine, and tyrosine residues. The arginine and histidine residues are conserved among related proteins and may be involved in substrate binding or catalysis. Additionally, the side chains of glutamic acid and aspartic acid residues presented on the molecular surface of an adjacent molecule, form hydrophilic interactions with the entrance of the active site of another dimer molecule.

## ナノ構造を持つ ISOL 用標的の開発

大西哲哉 理化学研究所

〔目的〕 不安定核生成法の一つである ISOL 法では、標的に高速の粒子を照射し、標的内で生成した不安定核を、標的を高温(～2000℃)にすることで取り出している。そのため、高温でも蒸気圧が低くかつ融点も高い、炭化物が標的として用いられることが多い。しかし、これまでの研究によって、炭化物標的の寿命が約一週間程度であることが分かっている。これは、高温環境下では炭化物の焼結が進むため、標的内部の隙間が小さくなり、不安定核が出てこなくなるためである。解決策として、近年カーボンナノチューブを用いた炭化物標的が提案されるが、ナノ構造を持つが故に燃焼しやすく、取り扱いには専用の設備が必要である。本研究の目的は、カーボンナノチューブやグラフェン等のナノ構造をもつ新たな炭化物を用いて、取り扱いやすい ISOL 用標的を開発することである。

〔実験手法〕 対象とする元素の化合物(酸化物など)を炭素材料と混合し、高压をかけ、厚さ 1 mm、直径 20 mm 程度の円板標的を作成する。作成した標的は真空チェンバー内で高温に加熱し、炭化物へと変換する。作成した炭化物標的は、電子顕微鏡を用いて、そのナノ構造を調べる。その後、電子ビームもしくは陽子ビームを照射し、不安定核生成量の変化から標的寿命や生成効率などを調べる。

本年度は研究協力者の阿部康志氏と共に、炭化ウラン標的を使って不安定核生成を行い、標的寿命などを調べ、不安定核-電子散乱実験のために不安定核ビームの供給を行った。

〔結果〕 昨年度整備した作業環境にて、炭化ウラン標的をリモートハンドリング用標的槽にセットアップ後、イオン源にセットした。放射線汚染を防ぎつつ、なるべく短時間でセットを行うべく、作業手順などを検討し、実施した。その結果わずか 5 秒程度でセットし、真空引きを行うことができた。また取り出し時も、作業環境や手順を検討し、放射線レベルが下がるまで期間をあけた後に、短時間で照射済み標的を保管容器に戻すことができた。

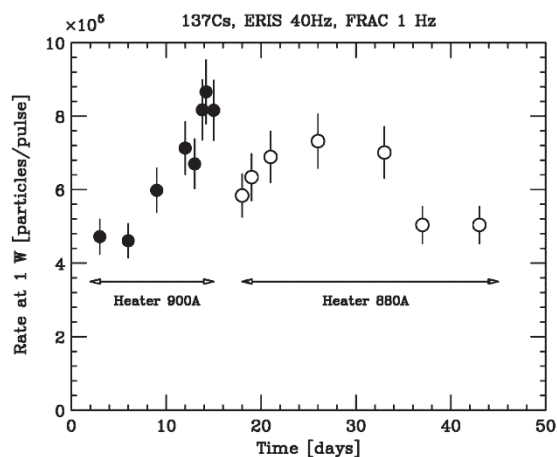


図 1: 不安定核ビーム強度の長期的時間変化。  
300 us 幅のパルスで測定。

電子ビームによる照射は約一ヶ月ほど続き、その間不安定核生成量をモニタすることで、標的寿命の測定を行った。結果を図 1 に示す。図からも分かる様に供給ビーム量はかなりゆるやかに下がっており、長時間の寿命を持つことが推測される。今回の測定では、約 77 日程度と予想される。

〔考察〕 今回得られた標的寿命は、従来よりもかなり長い。今後、他標的を用いた継続的な測定を行い、その理由(対象元素、標的の個性等)を調べるとともに、歩留まりが上がる作成方法を確立していきたい。

〔成果報告〕

特になし

## プリパルス付与による高変換 TNSA イオン加速機構実証

花山良平 光産業創成大学院大学

我々は Target Sheath Normal Acceleration(TNSA)イオン加速機構で得られる MeV 以上の高エネルギーイオンを利用し、高輝度（点光源）、短パルス（数 10 ナノ秒以下）で比較コンパクト（規模に比較して高フラックス）なレーザー駆動中性子源の実現を目指している。これを高時間分解中性子検出器と組み合わせることにより、共鳴散乱イメージングなど、レーザー加速中性子源の特徴を生かした研究展開が期待できる。

これまでの研究で、高強度フェムト秒レーザーパルスに先行して、適切なタイミングでプリパルスをターゲットに照射することにより、加速イオンのエネルギーと粒子数を増大させる手法の実証を京都大学化学研究所のレーザー施設を用いて行ない、加速プロトン数と最大エネルギーの増大を確認した。本課題では、プリパルスが初期ターゲット条件及び TNSA 機構に及ぼす影響を物理的に解明し、これを制御する手法の構築を目指した。

まず、昨年度の実験でプロトンエネルギー解析に用いたプラスチック飛跡検出器 CR39 のエッチピットの顕微鏡観察を行った。図 1 の 5 本のトレースの内、4 本目の 1MeV 付近では中央部が暗くなっている部分が存在した（図 2）。これを拡大して観察したところ（図 3）、無数のピットで埋め尽くされ、全体的にエッチングが進んだために暗くなったと考えられることが分かった。

次に、昨年度見出したレーザーシャインスルーがターゲットの初期状態に及ぼす影響について検討を行った。TNSA レーザーイオン加速の計算と実験結果の乖離を説明するためにレーザーシャインスルー数値モデルを構築して解析を行った。その結果、プリパルス照射によりプラスチックターゲットのレーザー照射側（前面）がブレイクダウンする際、ターゲットの反対側（裏面）の自由電子密度もほぼ臨界密度に到達することがわかった。このことはプリパルスのシャインスルーによりターゲット裏面の状態が変化し、TNSA によるイオン加速が阻害される可能性を示唆している[1]。

この結果を元に、レーザー照射点近傍のターゲットやプラズマの挙動を実験により詳細に観測することとした。ターゲット形状の計測やプラズマ観察用の干渉計などの準備を進めている。

- 1) 砂原淳, “高強度レーザーシース加速における“シャインスルー”, ” フォトニクスニュース, 8, 2, 72-77 (2022).

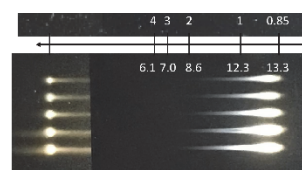


図 1 プロトンエネルギー解析用 CR39

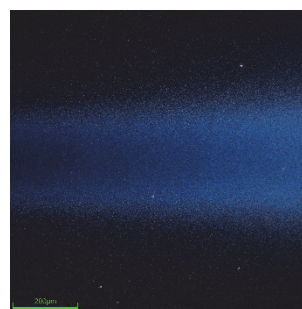


図 2, 顕微拡大 300 倍  
(4 本目, 1MeV 付近)

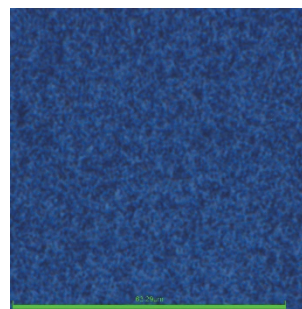


図 3, 顕微拡大 4000 倍  
(4 本目, 1MeV 付近)



## Verification of radiochemical reactions with ultra-high dose rate electrons

Satoshi Kodaira National Institutes for Quantum Science and Technology

The radiotherapy for cancer that is performed at an ultra-high dose rate ( $>40$  Gy/s) has attracted great interest because the tumor cell-killing effect is maintained while the damage to surrounding normal tissues is minimized. This sparing effect is related to the yields of water radiolysis products, which contributes to the indirect action toward DNA strand breaks. In this study, we verify the radiation chemical yields of products in water by irradiation of ultra-high dose rate electrons.

20 MeV electron beam irradiation was performed in ambient air condition at electron linac, KEL of ICR. The mean dose rates were 0.08 and 0.3 Gy/s, which correspond to the pulsed dose rates of 2.7 and 10 kGy/s, respectively. Aqueous solutions containing 2.5 mM sodium nitrate ( $\text{NaNO}_3$ ) were prepared to measure yields of hydrogen peroxide. Ultra-pure water was also irradiated to compare yields with/without sodium nitrate. After the irradiation, we analyzed the yields of hydrogen peroxide produced using an electro-chemical detector (ED743) connected to HPLC system (Shimadzu, Japan).

Figure shows yields of hydrogen peroxide produced in a 2.5 mM sodium nitrate solution (solid symbols) and ultra-pure water (open symbols) at low and high dose rates as a function of the absorbed dose. In  $\text{NaOH}_3$  solution, the slope at high dose rate is steeper than that at low dose rate. This result implies that reactions between OH radicals more efficiently occur in high dose rate region, resulting in high yields of hydrogen peroxide. The G values of hydrogen peroxide in  $\text{NaOH}_3$  solution were 0.99 sp/100 eV and 0.78 sp/100 eV at high and low dose rates, respectively. The value at low dose rate was in agreement with the previous study of gamma rays (0.7 sp/100 eV) at similar low dose rate of 5.6 Gy/min ( $\sim 0.09$  Gy/s). A similar trend that the slope of hydrogen peroxide generated becomes steep with increase of the dose rate was observed in ultra-pure water. The G values of hydrogen peroxide in ultra-pure water were 0.63 sp/100 eV and 0.36 sp/100 eV at high and low dose rates, respectively, which were much lower than that in  $\text{NaOH}_3$  solutions at the same dose rate in each. The sodium nitrate works as a scavenger of hydrated electrons, which disassemble hydrogen peroxide, thereby the hydrogen peroxide produced was maintained by suppressing roles of hydrated electrons. To explain the roles played by hydrated electrons in a wide scavenging time scale, we will address the hydrogen peroxide measurements by varying the concentration of sodium nitrate.

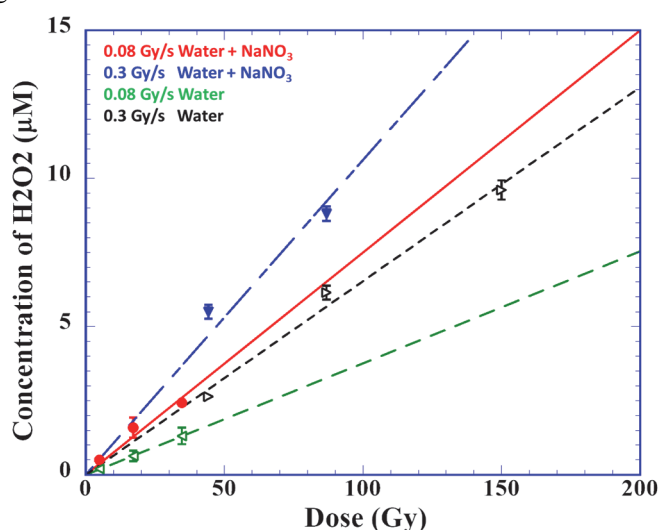


Figure. Dose dependencies of yields of hydrogen peroxide produced in a 2.5 mM sodium nitrate solution (open symbols) and ultra-pure water (closed symbols) at two dose rates of 0.08 Gy/s (low) and 0.3 Gy/s (high).



## Design and Tailoring Advanced Functional Materials: Symmetry Operation and High Pressure Synthesis

Wei-Tin Chen National Taiwan University

**[Introduction]** The exploration of fascinating functionalities and phenomena of novel materials is essential in modern condensed matter sciences which is motivated much by the succession needs of novel technology applications. With various advanced sample preparation approaches, high pressure synthesis techniques are one of most important methods in preparation of such novel functional materials. It is aimed to design and realize metastable oxide materials with exotic phase transitions contributed from the lattice/charge/orbital/spin degree of freedom. The joint collaborative research has been carried out with Advanced Solid State Chemistry Laboratory (Prof. Shimakawa) utilizing extreme pressure and temperature synthesis conditions, and high resolution synchrotron x-ray diffraction (SXR) at Taiwan Photon Source (TPS) for structure analysis.

**[Results and discussion]** The joint research remains difficult with the situation of pandemic in year 2022. Nevertheless, the idea exchange and online discussion were carried out, and high pressure experiment and diffraction data collection were conducted at ICR and TPS, respectively. For instance, an unreported  $A^{2+}Mn^{4+}O_3$  perovskite member  $CdMnO_3$  were realized with high pressure synthesis condition. The SXR experiment reveals that the compound crystallized in distorted perovskite structure, and magnetic susceptibility shows an antiferromagnetic behavior, in which First-principles calculation indicates a C-type magnetic structure. [1] The followed up investigation of previously reported on  $PrFe_{0.5}Cr_{0.5}O_3$  system [2] are continued. A series of praseodymium-containing perovskites were synthesized, and the evolution of crystal and magnetic structures were carefully examined. From neutron diffraction results, it is shown that with increasing Mn doping into  $PrCrO_3$  parent compound, the magnetic structure changes drastically from G-type dominant to A-type dominant. The further detailed analysis is ongoing and the manuscript is in preparation. [3]

### [Results and discussion]

1. Y. Xu *et al.*, *Inorg. Chem.*, **61**, 21011 (2022)
2. C.-W. Wang *et al.*, *JMMM*, **538**, 168273 (2021)
3. Y.-H. Tung *et al.*, manuscript in preparation

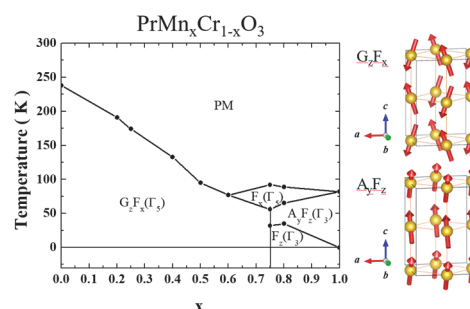


Fig. 1 Compositional magnetic phase diagram of  $PrMn_xCr_{1-x}O_3$  perovskite series.

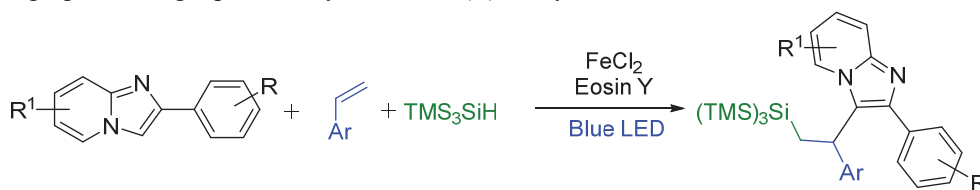
## Carboboration and Carbosilylation by Merging Iron and Visible-Light Photocatalysis

Alakananda Hajra Visva-Bharati University

**ICR partner researcher's name: Prof. Masaharu NAKAMURA**

Objective: Development of carboboration and carbosilylation reactions using earth-abundant non-toxic Fe-catalysis under visible light photo-catalysis at room temperature

Visible-light photocatalysis has become an impressive tool in organic synthesis. In this realm, the merger of transition metal catalysis and visible light photoredox catalysis offers an exciting opportunity to perform the organic transformations in mild conditions. Organosilicon compounds are one of the vital synthetic building blocks in the field of organic chemistry and they have widespread applications in material science, polymer science and agrochemistry. Notably, the silicon analogues of biologically active molecules and organosilicon compounds exhibit exceptional physicochemical properties, allowing them to be extensively used in medicinal chemistry. Presently we are studying a three-component carbosilylation of alkenes with imidazoheterocycles and silanes by merging visible light photocatalysis and iron(II) catalysis.



Presently we are focusing on the precise role of FeCl<sub>3</sub> and visible light, and late stage modification of the compound.

A review has been published. This work was also supported by the International Collaborative Research Program of Institute for Chemical Research, Kyoto University (grant # 2022-7).

**Title: Recent Advances in Carbosilylation of Alkenes and Alkynes**

Authors: Prajna Paramita Pal, Sumit Ghosh, and Dr. Alakananda Hajra\*

*Org. Biomol. Chem.*, 2023, Accepted Manuscript

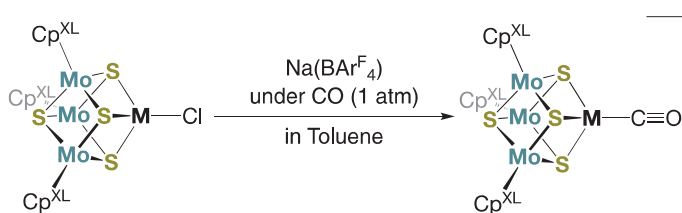
<https://doi.org/10.1039/D3OB00230F>

## Computational mechanistic study on the Co-catalyzed nitrogenase model reactions

W. M. C. Sameera University of Colombo

Transition metal clusters can be used as catalysts to perform chemically or biologically relevant reactions.<sup>1,2</sup> Relationships between the electronic structure and reactivity can be established by employing density functional theory (DFT). We have developed  $[\text{Mo}_3\text{S}_4\text{M}]$ -type clusters ( $\text{M} = \text{Fe}, \text{Co}, \text{Ni}$ ), consisting of bulky cyclopentadienyl ligands ( $\text{Cp}^{\text{XL}}$ ,  $\text{C}_5\text{Me}_4\text{SiEt}_3$ ). CO can be coordinated to  $[\text{Mo}_3\text{S}_4\text{M}]$  cubes. According to experimental data,  $[\text{Cp}^{\text{XL}}_3\text{Mo}_3\text{S}_4\text{M}(\text{CO})]^+$  ( $\text{M} = \text{Co}, \text{Ni}$ ) is stable, while  $[\text{Cp}^{\text{XL}}_3\text{Mo}_3\text{S}_4\text{Fe}(\text{CO})]^+$  complex revealed unexpected instability. DFT calculations analyzed their M-CO interactions.

An energy decomposition analysis (EDA), together with the natural orbitals for chemical valence (NOCV), was performed to rationalize the M-CO interactions. The interaction energy between M and CO follows the order of Fe-CO (-101.1 kcal/mol) > Co-CO (-81.5 kcal/mol) > Ni-CO (-77.3 kcal/mol). In all three cases, orbital



interactions become dominant compared to electrostatic, dispersion, and solvent interactions.

According to EDA-NOCV,  $\pi$  back-donation from Co to  $\pi^*(\text{CO})$  is stronger than  $\sigma$  CO to  $\text{M}(\text{d})$   $\sigma$  donation for all three systems. These findings give quantitative insights to develop bio-mimetic catalysts for the direct conversion of CO into hydrocarbons.

### Joint Publications of this fiscal year

- (1) Y. Ohki, K. Munakata, R. Hara, M. Kachi, K. Uchida, M. Tada, R. E. Cramer, W. M. C. Sameera, T. Takayama, Y. Sakai, S. Kuriyama, Y. Nishibayashi, K. Tanifuji, *Nature*, **607**, 86-90 (2022).
- (2) W. M. C. Sameera, Y. Takeda, Y. Ohki, *Adv. Organomet. Chem.*, **78**, 35-78 (2022).
- (3) K. Tanifuji, Y. Sakai, Y. Matsuoka, M. Tada, W. M. C. Sameera, Y. Ohki, *Bull. Chem. Soc. Jpn.*, **95**, 1190-1195 (2022).

## Development and device evaluation of new D- $\pi$ -A emitters based on rigidified triarylborone acceptors

T. B. Marder Julius-Maximilians-Universität Würzburg

Thermally activated delayed fluorescence (TADF) emitters are a promising avenue for the development of organic light-emitting diodes (OLEDs) for flat displays and solid-state lighting applications, as they show improved efficiency. Planar 3-coordinate boron can be used as an acceptor moiety due to the vacant  $p_z$  orbital. Triarylboranes have been employed for a number of applications such as linear and nonlinear optics, sensors, and OLEDs. One of the most successful examples of the use of triarylboron acceptors is their application to TADF emitters. We have recently reported methodologies to enhance the accepting properties as well as the stability of boron by the introduction of *ortho*-trifluoromethylaryl moieties. We computationally designed a series of D- $\pi$ -A TADF emitters with fluorinated triarylboron acceptors. We synthesized sufficient quantities of 3 blue to red emitters with relatively short delayed fluorescence lifetimes, implying efficient reverse intersystem crossing (RISC) from the triplet to singlet excited states (A. K. Narsaria *et al.*, *Adv. Funct. Mater.* **2020**, *30*, 2002064). These studies demonstrate the effectiveness of our design strategy for triarylboron-based TADF emitters based on accurate theoretical descriptions of the local and charge-transfer states. The Kaji group has been constructing OLED devices by both wet and vacuum processes from these compounds and examining their properties. A PLQY of 70% and an EQE of 10% have already been achieved for one of the compounds. They are continuing to attempt to improve device performance for the other compounds. In addition, the Kaji group has carried out computational work to design a new family of boron-based TADF chromophores employing a rigidified triarylboron core. Based on those calculations, my group has begun to synthesize a series of these new chromophores. We have already been successful in preparing the desired rigidified diboron-containing core and, using Ir-catalyzed borylation, have borylated it selectively at the 2 sites required for subsequent cross-coupling with a specific series of donor moieties. As the chromophore synthesis and purification is completed, we will send each compound to the Kaji group for incorporation into OLED devices.

This past year, due to COVID-19 related difficulties, and the inability to travel to Kyoto, our group and the Kaji group have independently advanced the project: our group carrying out the chemical synthesis of the chromophores and the Kaji group carrying out the photophysical measurements, device fabrication and

testing (Figure 1). Very promising results have been obtained from new OLED devices prepared from our original compounds. We will continue to prepare the new series of chromophores and the Kaji group will evaluate their device performance in the coming year. We anticipate that a breakthrough in OLED performance can be achieved by continuing our collaborative work, and this is highly desired in both the academic and industrial communities.

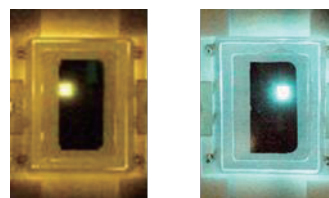


Figure 1. Fabricated OLEDs by the Kaji group using our designed materials.

# High pressure synthesis of novel hexagonal perovskite oxides containing unusually high valence Fe ions and investigation of their magnetic properties

Zhenhong Tan Chinese Academy of Sciences

【*Experimental Project*】 Perovskite oxides  $ABO_3$  have been widely explored and their intriguing physical properties have been also investigated since the last century. While the unusually high-valence Fe ions are of interest due to their specific physical properties such as charge disproportionation and intersite charge transfer. It is hence challenging and promising to combine unusually high-valence Fe ions with hexagonal perovskite oxides.

【*Objectives*】 Prepare the hexagonal perovskite oxides  $BaFe_{1-x}Ge_xO_3$ , and  $BaFe_{1-x}Ga_xO_3$  ( $x = 0.1 - 0.9$ ) by using high-pressure and high-temperature technique.

【*Experimental Methods*】 The precursors  $BaFeO_{2.6}$ , and  $BaGeO_3$  were first calcinated at 1323 K in oxygen atmosphere, by respectively mixing stoichiometric  $BaCO_3$  and  $Fe_2O_3$  for  $BaFeO_{2.6}$ , and  $BaCO_3$  and  $GeO_2$  for  $BaGeO_3$ . Then the target compounds were synthesized by mixing  $BaFeO_{2.6}$  and  $BaGeO_3$  according to the substitution index  $x$ , and treated at high pressure (3 GPa) and high temperature (1273 K).

【*Outcomes and Analysis*】 As shown in Figure 1, a new phase for the Ge-substituted compound at  $x = 0.3$  was obtained. Although it contains some impurities, a nearly novel single-phase compound was successfully synthesized using high pressure technique. A 21R-type hexagonal crystal structure with space group  $R\bar{3}m$  can reproduce this newly-obtained compound. The Rietveld refinement results were shown in Figure 2, and the lattice constants for BFGO ( $x = 0.3$ ) were refined to be  $a = 5.7084(1)$  and  $c = 50.1991(1)$  Å.

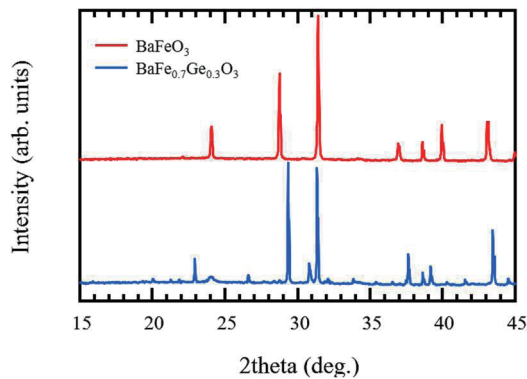


Figure 1. The XRD patterns of  $BaFeO_3$  and BFGO ( $x = 0.3$ )

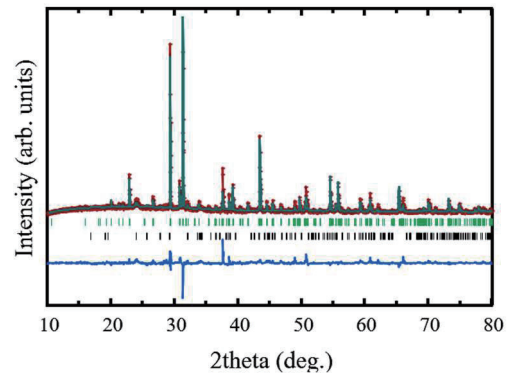


Figure 2. The XRD pattern and Rietveld refinement results for BFGO ( $x = 0.3$ ).  $R_{wp} = 9.76\%$ ,  $R_p = 7.3\%$ .

## Preparation and Characterization of Novel Magnetic Quadruple Perovskites by High Pressure

Midori E. AMANO PATIÑO CNRS

**Objectives.** We set out to investigate the formation of *A*-site ordered quadruple perovskite materials with formula  $\text{Ca}A'_3\text{Ti}_4\text{O}_{12}$  ( $A' = \text{Mn}^{2+}, \text{Fe}^{2+}, \text{Co}^{2+}, \text{Ni}^{2+}, \text{Cu}^{2+}$ ) and to characterize and compare the physical properties throughout the series. The transition metal cations in these materials take square-planar coordination geometry at the *A'* sites (Fig. 1). In addition to this coordination being rare, when only the *A'* sites are magnetic, their orthogonal arrangement in the quadruple perovskite structure leads to complex magnetic interactions and exotic magnetic orders that are not yet well understood.

**Methods.** Stabilizing quadruple perovskite structures is often challenging, and their preparation requires high pressure and temperature. In this collaboration, the high-pressure apparatuses at the Advanced Solid State Chemistry Laboratory led by Prof. Yuichi Shimakawa made it possible to investigate the preparation of the target  $\text{Ca}A'_3\text{Ti}_4\text{O}_{12}$  series. Following our success in stabilizing the member with  $A' = \text{Fe}^{2+}$ , [1] we focused on preparing  $A' = \text{Mn}^{2+}, \text{Co}^{2+}$  and  $\text{Ni}^{2+}$ . Initial exploration of the phases was carried out using laboratory X-ray diffraction (D8 Advance, Bruker) and SQUID magnetometry (MPMS-XL and 3, Quantum Design). For the  $\text{Mn}^{2+}$  and  $\text{Ni}^{2+}$  compositions, further detailed exploration of formation was required (high-pressure synchrotron X-ray diffraction, BL04B1, SPring-8). Meanwhile, neutron powder diffraction (NPD) measurements were performed for our product  $A' = \text{Co}^{2+}$  (ECHIDNA, OPAL reactor, Sydney, Australia).

**Results and Discussion.** Data collected *in situ* during the formation of the  $A' = \text{Mn}^{2+}, \text{Ni}^{2+}$  materials (from  $\text{CaTiO}_3$  and  $A'\text{TiO}_3$ ) at BL04B1, using several pressure and temperature combinations, revealed that the stabilization of the target materials is challenged by competing phases which are thermodynamically favored (e.g.,  $\text{CaMnTi}_2\text{O}_6$  and  $\text{NiO}$ , respectively). Therefore, isolation can only be achieved within a very narrow window of *P*, *T* conditions. The discussion of these results is being prepared for publication.

For the  $A' = \text{Co}^{2+}$  material, NPD confirmed the successful stabilization of the target structure. Additionally, unusual features detected by SQUID magnetometry led us to explore NPD under applied magnetic fields. The results reveal that in the absence of an external magnetic field, the  $\text{Co}^{2+}$  spins adopt antiferromagnetic ordering at 9.3 K. This magnetic arrangement consists of three interpenetrating spin sublattices perpendicular to each other. When a magnetic field is applied, the antiferromagnetic structure transforms into a canted ferromagnetic arrangement. In comparing this magnetic behavior with the  $A' = \text{Fe}^{2+}$  member and other quadruple perovskite systems previously investigated at Prof. Shimakawa's Laboratory, we discovered that underlying Kagome lattices (formed by 2<sup>nd</sup> *A'* neighbours) in these systems are crucial in determining the adopted spin structures.[2]

**Outcomes.** This collaboration has been successful in yielding many important results. Our investigations on this quadruple perovskite series provides a relevant contribution in understanding the composition-structure-property relationships in this class of materials. We have gained valuable insights into the underlying factors that govern these relationships.

**Acknowledgements.** MAP thanks Prof. Shimakawa's Laboratory members, and the beam scientists at BL04B1 and ECHIDNA, for their help and fruitful scientific discussion. **References.** [1] Amano Patino, M. et al. *Phys. Rev. Research*, 3(4), 043208 (2021). [2] Amano Patino, M. et al. *Commun Mater*, 3(1), 51 (2022).

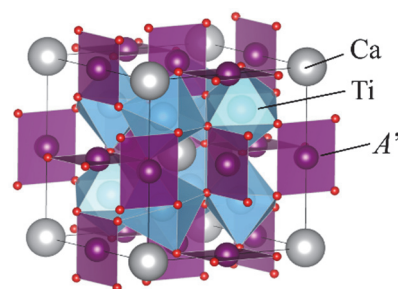


**Fig. 1** The quadruple perovskite structure adopted by  $\text{Ca}A'_3\text{Ti}_4\text{O}_{12}$  materials.



# High-pressure synthesis and ionic conducting study of novel Na-antiperovskites containing hydride and cluster anions as solid electrolytes in batteries

KOEDTRUAD Anucha CAS

## Research background and objectives

All-solid-state Na-ion batteries are considered next-generation energy storage devices. As the key component in the batteries, solid electrolytes with Na-ion conducting properties have been intensively investigated. Recently, hydride-based Na-antiperovskites,  $\text{Na}_3\text{HCh}$  ( $\text{Ch} = \text{S}, \text{Se}$  and  $\text{Te}$ ), have been revealed as potential electrolytes [*Nat. Commun.* **2021**, 12, 201]. Therefore, herein, we aim to explore new Na-antiperovskites containing hydride and cluster-anions (CA) with general formula  $(\text{Na})_n(\text{H})(\text{CA})$ . Initially,  $\text{Na}_3(\text{H})(\text{SO}_4)$  is focused.

## Materials Synthesis and Characterization

The materials were prepared via a high pressure high temperature technique using an ELEPHANT high pressure apparatus in the Advanced Solid State Chemistry laboratory in ICR. Starting materials, NaH and  $\text{Na}_2\text{SO}_4$  were mixed and grinded in a glovebox. The mixture was then loaded into a Pt or Au capsule (capsule size is about 10 mm diameter and 15 mm height). The capsule was then assembled before transferring from the glovebox to the high pressure apparatus. The applied pressure was between 60 - 250 ton and the temperature was 350 °C. The obtained materials were then characterized by a conventional XRD. Its phase was analyzed with rietveld refinement method.

## Results and discussion

Figure 1 shows XRD patterns of  $\text{Na}_3(\text{H})(\text{SO}_4)$  prepared under different pressures. At high pressure of 250, 200 and 100 ton, the patterns indicate mixed phases. With reducing pressure to 60 ton, the target antiperovskite phase becomes dominant with the minor NaH and  $\text{Na}_2\text{SO}_4$  phases remained.

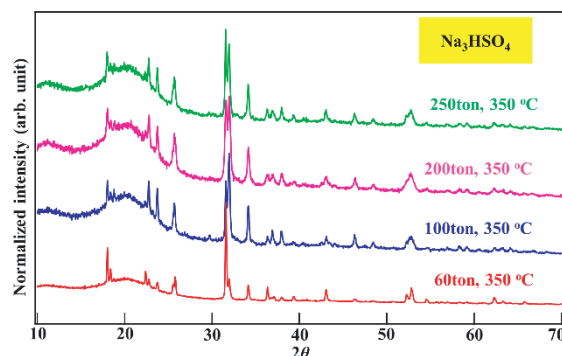


**Figure 1.** XRD patterns of the  $\text{Na}_3(\text{H})(\text{SO}_4)$  prepared at different pressures

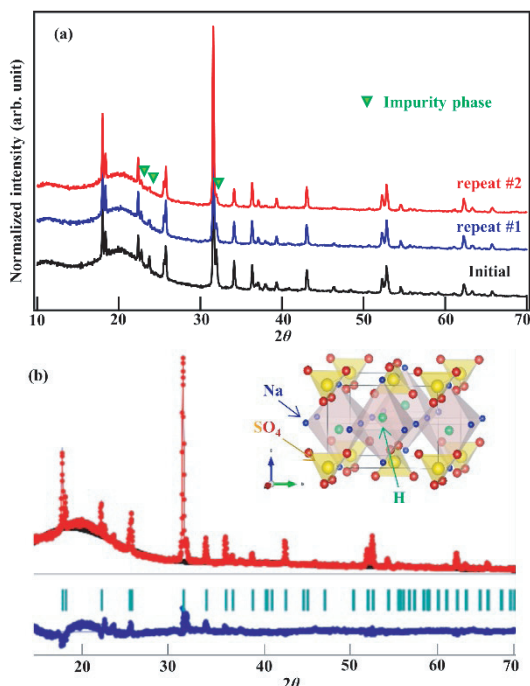


**Figure 2.** XRD patterns of the sample after grinding and repeating the synthesis for two times (a) and refinement result and refined structure of the sample (b).

With grinding the sample and repeating the synthesis at 60 ton and 350 °C for two times, yield of the antiperovskite phase is enhanced, accompanying with reduced impurity phases, as shown in Figure 2a. The best sample is then chosen for the rietveld refinement for analyzing structure (Figure 2b). The result indicates nearly phase-pure antiperovskite structure with a tetragonal unit cell, space group  $P4/nmm$ . The structure comprises of  $\text{HNa}_6$  octahedral networks and  $\text{SO}_4$  group in cavity of the network. However, the detailed structure needs further characterization with high resolution synchrotron XRD and/or neutron powder diffraction techniques. Conductivity of the compound will be next examined with AC impedance spectroscopy.



## Small molecule activation using anionic crypto-FLPs

Rainer Streubel University of Bonn

This collaborative research project was carried out with Prof. N. Tokitoh and Prof. Y. Mizuhata (ICR, University of Kyoto), and 1 PhD student from Bonn was hosted in Japan.

**Objectives:** The project targeted the synthesis of anionic FLPs, featuring an anionic phosphorus center as Lewis base and a tetravalent chloro(organo)silicon compounds as masked Lewis base.

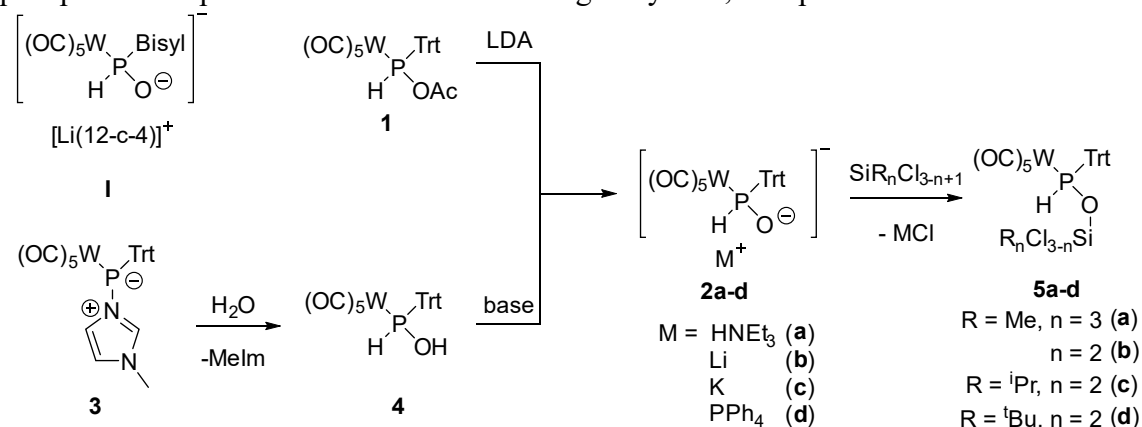
**Experimental methods:** Inert-gas synthesis techniques, analytical methods (NMR, IR, UV/vis, CV, X-ray).

### Experimental results:

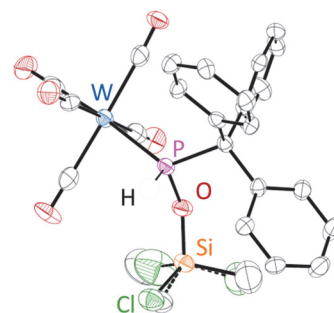
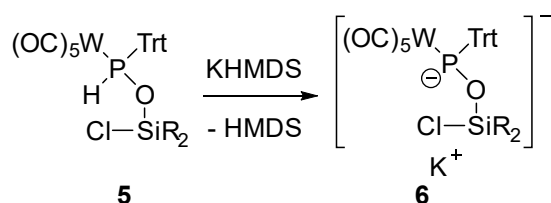
The project focused on a more reliable starting point using robust P-bound triphenylmethyl derivatives (Trityl, Trt).

**Discussion:** Firstly, we examined a route using HOAc to get **1**, then by reaction with LDA the desired precursor **2b**, but the product quality varied in an unpredictable manner. We then developed a new route relying on the imidazole-to-phosphorus adduct complex **3** which react with water to **4** and which was obtained in good yields, high purity and can be stored. Complex **4** was easily deprotonated with several bases, *e.g.* NEt<sub>3</sub>, <sup>n</sup>BuLi or KO<sup>t</sup>Bu; **2c** was used to access **2d**.

**2a** was treated with Me<sub>3</sub>SiCl, Me<sub>2</sub>SiCl<sub>2</sub>, <sup>i</sup>Pr<sub>2</sub>SiCl<sub>2</sub> and <sup>t</sup>Bu<sub>2</sub>SiCl<sub>2</sub>, and the resulting siloxy-phosphane complexes **5a-c** were obtained in good yields, except for **5d** as no reaction occurred.



Complexes **5b,c** react with KHMDS via deprotonation to give room temperature stable K/OR phosphinidenoid complexes **6b,c** being under current investigation.[1]



### Publications:

- [1] P. Brehm, D. Biskup, G. Schnakenburg, Y. Mizuhata, N. Tokitoh, R. Streubel, to be published.

## Development of Unsymmetrical $\pi$ -Electron Systems of Heavier Main Group Elements and Elucidation of Their Property

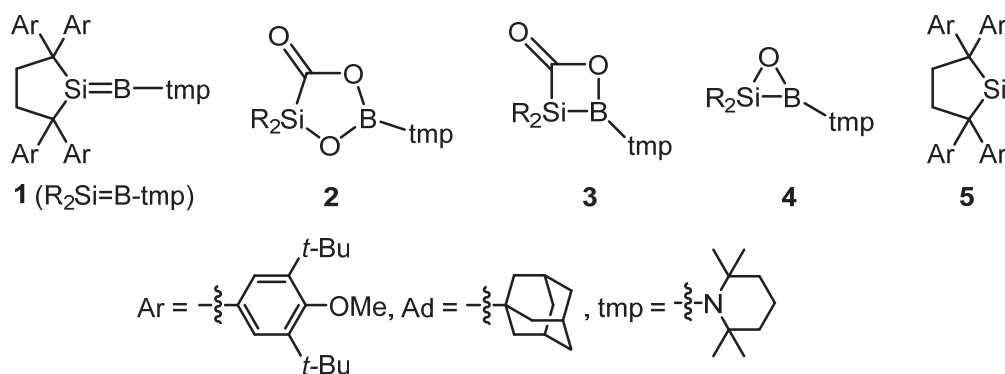
Takeaki Iwamoto Tohoku University

**Objectives:** We aimed at developing unsymmetrical  $\pi$ -electron systems containing a double bond between group-14 and group-13 elements, which remain scarce compared to other heavier  $\pi$ -electron systems but expected as prospects for advanced materials and reagents for small molecule activation.

**Experimental Methods:** Reactions of *B*-(2,2,6,6-tetramethylpiperidyl)dialkylborasilene **1** (Chart 1) with various reagents were examined.

**Outcomes:** Borasilene **1** reacted with CO<sub>2</sub> to provide **2** which is a product resulting from the activation of two CO<sub>2</sub> molecules. The detailed analysis of this reaction revealed that the initial product of this reaction is a formal (2+2) adduct of **1** and CO<sub>2</sub> (**3**). Then the elimination of CO from **3** provides borasilaepoxide **4**, which converts to **2** in the presence of CO<sub>2</sub>. Compound **4** was alternatively obtained by the reaction of **1** with N<sub>2</sub>O. To synthesize an aluminum analog of **1**, we examined the reaction of silylene **5** with AlI<sub>3</sub> and obtained the corresponding 1:1 adduct.

**Analysis:** All new products were fully characterized by a combination of NMR spectroscopy, elemental analysis, and MS spectrometry.



This project was done in collaboration with Professors Yoshiyuki Mizuhata (ICR Partner Researcher) and Shigeyoshi Inoue (International Collaborating Researcher, Technical University of München, Germany).

**Publications:** S. Abe, T. Iwamoto, “Synthesis, Structure, and Small Molecule Activation of Silicon-Boron Doubly-Bonded Compounds Having Alkyl Substituents on the Unsaturated Silicon Atom”, the 32<sup>nd</sup> Symposium on Physical Organic Chemistry, September 20-22, 2022.

## Development of 1,4-Addition Reactions via Iron Catalysis

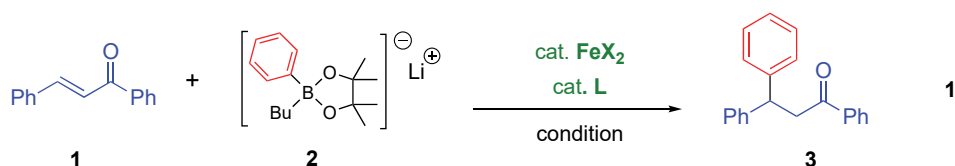
LAKSMIKANTA ADAK Indian Institute of Engineering Science and Technology, Shibpur

### Objectives

Iron is the highest ample transition metal in the Earth's crust, It is inexpensive, environmental and toxicology benign in nature. My interest is to explore the catalytic properties of ecologically and economically attractive iron catalysts. Institute for Chemical Research (ICR), Kyoto University is a well-furnished research institute. It has all the up-to-date research services to achieve each type of reactions. Our studies will certainties help the entire scientific people to realize the basic properties of iron-catalysis. Our goal is to acquire new reactions and new molecules to be helpful for expansion of new science and technology.

### Experimental Methods

The first goal of the present project is the development of iron-catalyzed 1,4-addition reactions of aryl-, alkenyl- and alkynylboron reagents to  $\alpha,\beta$ -unsaturated carbonyl compounds. Initially, we focused on the development of 1,4-addition reaction of phenylborate (**2**) (*J. Am. Chem. Soc.* **2010**, *132*, 10674) to enone (**1**) catalyzed by iron salt in combination of ligand to provide the product **3** (eq 1). The reaction may involve the B-Fe transmetalation as the key step.



To optimize and increase the yield of this reaction various reaction conditions including iron precursors, ligands/additives, reaction temperature, solvents have been studied. After optimization of reaction protocol (eq 1), we examined the scope of 1,4-addition reaction of various  $\alpha,\beta$ -unsaturated acyclic and cyclic ketones with diverse aryl/heteroaryl-, alkenyl- and alkynylboron reagents.

### Outcomes and Perspective

The development of iron-catalyzed 1,4-addition reactions of aryl, alkenyl and alkynylboron reagents to  $\alpha,\beta$ -unsaturated carbonyl and related compounds and mechanistic studies have been pursued. The most significant point is that the toxic and expensive rhodium or palladium catalysts can be replaced by modest iron catalyst. The iron catalyst will advance the known catalytic method as well as in innovation of novel synthetic methodologies for the synthesis of fine chemicals and drug molecules. Not only will the effect on the useful chemical synthesis, the new catalyst makes an academic interest. Thus, we believe that these studies will have very broad impacts in both academic and industrial standpoints of view.

### Publications

The corresponding manuscript is in preparation.

## Peptide Bolaamphiphile Anchored Nickel-based Metallohydrogel as Electrocatalyst for Hydrogen Production

Apurba K. Das Indian Institute of Technology Indore

Electrochemical water splitting is considered as a green method for the generation of sustainable and environmentally friendly energy conversion. The hydrogen evolution reaction is associated with two electrons transfer for the formation of the H-H bond and produced hydrogen energy with zero CO<sub>2</sub> emission. However, OER's intrinsically sluggish kinetics hinders water splitting's efficiency, which required 1.23 V thermodynamic overpotential due to the involvement of multiple proton-coupled electron transfer processes.

**Objectives:** The main aims of this project proposal are:

- (a) Design and develop peptide bolaamphiphile-anchored Ni-based electrocatalyst,
- (b) Experimental validation of electrocatalysts for electrocatalytic hydrogen generation,
- (c) To study the mechanistic insights for electrocatalytic hydrogen production.

**Experimental Methods:** Here, we have prepared a sonication induced boladipeptide (HO-YF-AA-FY-OH (PBFY); AA = Adipic acid, F = L-phenylalanine and Y = L-tyrosine) anchored self-assembled nickel-based coordinated polymeric nanohybrid hydrogel (Ni-PBFY). The metallo-hydrogel (Ni-PBFY-3) prepared by mixing of 3 mg NiCl<sub>2</sub>·6H<sub>2</sub>O metal salt along with 20 mM (15.33 mg) of boladipeptide (PBFY) in 1 mL final volume. The xerogel of Ni-PBFY has been used to fabricate the electrodes and utilized in OER (oxygen evolution reaction).

**Discussion:** Ni-PBFY-3 displays an ultralow Tafel slope of 74 mV dec<sup>-1</sup> and lower overpotential of 164 mV at the current density of 10 mA cm<sup>-2</sup> in 1M KOH electrolyte than other electrocatalysts under the same experimental conditions. Furthermore, the Ni-PBFY-3 is witnessed as a highly stable electrocatalyst during chronopotentiometry performance for 25 h. The biomolecule assisted electrocatalytic results open a new route to design efficient electrocatalysts for the significant implications in green energy conversion. The mechanism of OER shows that the easy availability of hydroxide ions in KOH promotes the formation of Ni-OOH species which facilitated the kinetics of the OER. However, the electrocatalyst does not show the HER in 1M KOH due to the additional energy required to generate the proton by breaking the water molecule. In an alkaline medium prior to adsorbed H\*, extra energy is required to break the strong covalent bond of H-O-H. Besides the water dissociation, the electrocatalyst has strong interaction with hydronium ions than the water molecule, which is another challenge in an alkaline medium to produce M-H bond. On the other hand, the catalysts perform good HER activity in an acidic medium due to the maximum number and large availability of H<sup>+</sup> facilitating the activity of electrocatalysts and making them more suitable for acidic HER performance.

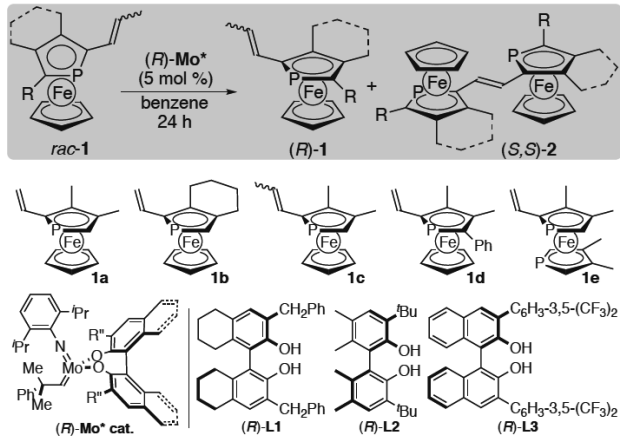
# Synthesis of Fe-containing Phosphorus Ligands and Their Application in the Preparation of Metal-Cluster Molecules

Masamichi Ogasawara Tokushima University

Olefin metathesis reaction has been proven to be a powerful tool in organic synthesis, and the enantioselective extension is a recent trend in the metathesis chemistry. The ring-closing metathesis reactions (RCM) were applied to the highly enantioselective synthesis of diverse planar-chiral transition metal complexes using the Schrock-Hoveyda chiral molybdenum-alkylidene precatalysts.<sup>[1]</sup> Here, an additional protocol for the asymmetric metathesis reaction is reported, which is asymmetric metathesis dimerization (AMD)/kinetic resolution (KR) of racemic planar-chiral vinylphosphaferrocenes.<sup>[2]</sup>

The phosphoferrocene substrates for this study (*rac*-**1a-e**) feature an  $\eta^5$ -(2-vinylphospholyl) ligand, which is an origin of the planar chirality in *rac*-**1**. Screening of the chiral precatalysts was examined using *rac*-**1a** as a prototypical substrate. A KR reaction using the chiral Mo/(*R*)-**L1** precatalyst at 60 °C, which facilitates the metathesis dimerization of (*S*)-**1a** preferentially and leaves most (*R*)-**1a** intact, attained 50% conversion in 24 h. The dimerized product consisted of the two diastereomers with a *chiral-2a/meso-2a* = 97/3 molar ratio. The enantiomeric purity of remaining (*R*)-**1a** was 74% ee and that of (*S,S*)-**2a** was 90% ee (Table 1, entry 1). The  $k_{rel}$  value for this reaction was estimated to be 130 based on a second-order equation. The catalytic activity of Mo/(*R*)-**L2** was much lower and only 13% conversion was attained under the otherwise identical conditions (entry 2). The Mo/(*R*)-**L3** precatalyst showed good enantioselectivity with the  $k_{rel}$  value of over 1000 but with poorer diastereoselectivity (entry 3). A reaction with Mo/(*R*)-**L1** at 20 °C showed the near-perfect diastereoselectivity with excellent enantioselectivity of  $k_{rel}$  = 880 (entry 4). The Mo/(*R*)-**L1** species was applied to the AMD/KR of other substrates *rac*-**1b-e**. While **1b** and **1d** were resolved as above with excellent diastereo-/enantioselectivities with  $k_{rel}$  = 950 and 870, respectively (entries 5 and 7), propenyl-substituted *rac*-**1c** was lowly reactive and needed higher temperature (60 °C) to attain the reasonable conversion, and the dimer was obtained in 98% ee (entry 6). The AMD/KR of diphosphaferrocene derivative *rac*-**1e** needed a higher temperature (40 °C) due to its lower reactivity. The excellent diastereo-/enantioselectivities were retained as above, and *rac*-**1e** was resolved with  $k_{rel}$  = 410 (entry 8). In the present AMD/KR, the dimerized products were obtained in >98% ee due to the VERY high  $k_{rel}$  values even with near 50% conversions.

**Table 1.** Mo-Catalyzed Asymmetric Metathesis Dimerization/Kinetic Resolution of Racemic Planar-Chiral **1**<sup>a</sup>



entry	( <i>R</i> )- <b>L</b> in ( <i>R</i> )- <b>Mo</b> *	substrate <b>1</b>	temp.	conv. <sup>b</sup>	chiral/meso in <b>2</b> <sup>b</sup>	%ee <b>1/2</b> <sup>c</sup>	$k_{rel}$ <sup>d</sup>
1	( <i>R</i> )- <b>L1</b>	<b>1a</b>	60 °C	50%	97/3	74/90	130
2	( <i>R</i> )- <b>L2</b>	<b>1a</b>	60 °C	13%	91/9	12/98	150
3	( <i>R</i> )- <b>L3</b>	<b>1a</b>	60 °C	60%	80/20	77/>99	1500
4	( <i>R</i> )- <b>L1</b>	<b>1a</b>	20 °C	40%	>98/<2	63/>99	880
5	( <i>R</i> )- <b>L1</b>	<b>1b</b>	20 °C	42%	>98/<2	65/>99	950
6	( <i>R</i> )- <b>L1</b>	<b>1c</b>	60 °C	53%	95/5	---/98	---
7	( <i>R</i> )- <b>L1</b>	<b>1d</b>	20 °C	44%	>98/<2	76/98	870
8	( <i>R</i> )- <b>L1</b>	<b>1e</b>	40 °C	35%	96/4	46/99	410

<sup>a</sup> The reaction was carried out in benzene in the presence of the molybdenum catalyst (*R*)-**Mo**\* (5 mol %). <sup>b</sup> Determined by the <sup>31</sup>P-NMR measurements of the crude reaction mixtures. <sup>c</sup> Determined by the chiral HPLC analyses. <sup>d</sup> Calculated based on a second-order equation. <sup>e</sup> Not determined.

## Publication from this joint project:

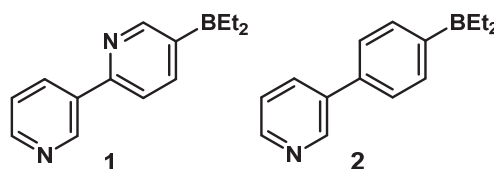
[1] Ogasawara, M. *Chem. Rec.* **2021**, *21*, 3509–3519.

[2] Nishimoto, K.; Taue, H.; Ohji, T.; Funakoshi, S.; Ohki, Y.; Ogasawara, M. *Org. Lett.* **2022**, *24*, 7355-7360.

## 自己集合性含ホウ素化合物の合成、集合過程解明ならびに機能開拓

若林成知 鈴鹿医療科学大学

【緒言】 我々はポリルピリジンにおける分子間ホウ素-窒素配位結合に着目し、幾つかの自己集合を達成し、超分子構築におけるユニット分子としての有用性を明らかにしてきた。昨年度の当共同研究において、フロー合成により得られた化合物 **1** は溶液中、室温で環状 3 量体と 4 量体の平衡混合物を形成し、その平衡は溶媒および濃度に依存して移動することを示した。本研究では化学研究所の大木靖弘教授と共同し、類似挙動を示す既報告の化合物 **2** との相違点を DFT 計算により明らかにし、さらに **1** のつくる多量体間の平衡移動に要する時間をフロー-NMR を用い検討した。



【結果と考察】 DFT 計算により得られた **1** の二面角 ( $25^\circ$ )、および CH/N 結合距離 ( $2.51 \text{ \AA}$ ) から、**2** のフェニレン部水素とピリジン環水素との立体反発は緩和され、かつ分子内での CH/N 水素結合により、両芳香環間の平面性は高いことが確認された。重ベンゼン中、3 量体の比率は同程度濃度での比較で、例えば 56% (**1**, 5.0 mM) vs 78% (**2**, 3.7 mM) であり、**1** のつくる 3 量体の比率は **2** のそれより低い。**1** の多量体間の平衡の熱力学的パラメータは  $\Delta H^\circ = -4.5 \text{ kcal mol}^{-1}$ 、 $\Delta S^\circ = -3.1 \text{ cal mol}^{-1} \text{ K}^{-1}$  であり、**2** のそれら ( $\Delta H^\circ = -8.8 \text{ kcal mol}^{-1}$ ,  $\Delta S^\circ = -23.7 \text{ cal mol}^{-1} \text{ K}^{-1}$ ) と比較し、小さなエントロピー変化が特徴的である。これらは、**1** は平面性が高いので、両芳香環が捻じれざるを得ない 3 量体形成は不利で、結果として 4 量体が優勢に存在することを示唆する。DFT 計算においても、**2** の二面角 ( $40^\circ$ ) はその 3 量体 ( $39^\circ$ )、4 量体 ( $38^\circ$ ) とほぼ同じであるが、**1** の二面角 ( $25^\circ$ )、および CH/N 結合距離 ( $2.51 \text{ \AA}$ ) は、その 3 量体 ( $30^\circ$ ,  $2.55 \text{ \AA}$ ) より 4 量体 ( $23^\circ$ ,  $2.50 \text{ \AA}$ ) において維持され、4 量体において平面性が保持されていることが再現された。二面角のわずかな相違は結晶構造においても反映されていた。

次に、多量体間の異常に早いと想定される平衡過程を Spinsolve 60 を用いフロー-NMR により追跡した (Figure 1)。**1** の重アセトン溶液に重ベンゼンを種々の比率で混ぜたところ、平衡移動は 1 分以内に起こっていることを示すことができた。

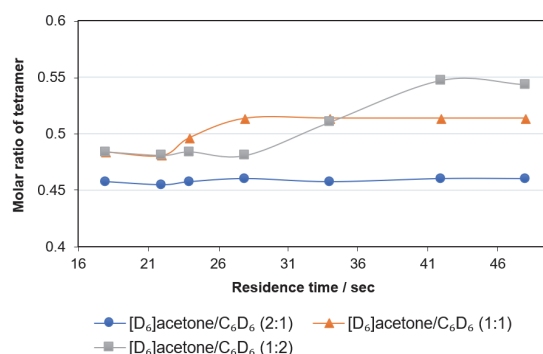


Figure 1. Residence time dependency of the molar ratio of **14** in various mixtures of [D<sub>6</sub>]acetone and C<sub>6</sub>D<sub>6</sub>.

【成果報告】 Wakabayashi S, Takumi M, Kamio S, Wakioka M, Ohki Y, Nagaki A. *Chem. Eur. J.* **2023**, 29, e202202882. [DOI: 10.1002/chem.202202882]



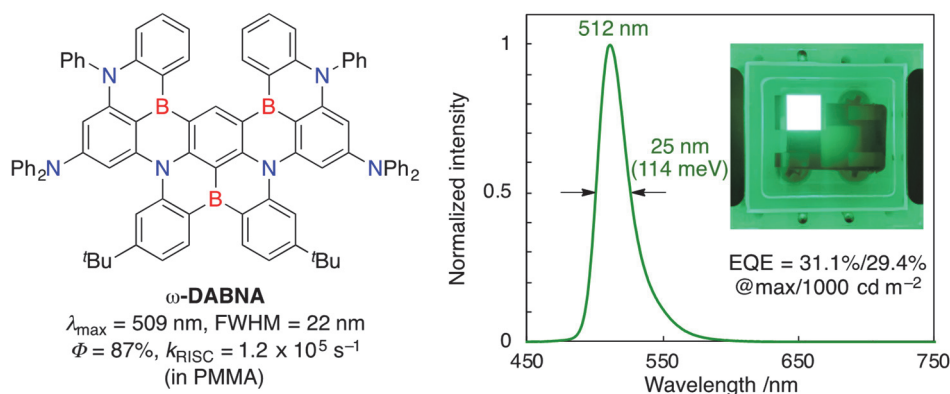
## MR-TADF 発光材料を用いた高効率塗布型有機 EL 素子の開発

小田 晋 関西学院大学

有機 EL 素子は、高いエネルギー効率や、高コントラスト比、薄型軽量などの優れた特性を有することから、液晶に代わるディスプレイ技術として社会実装が進んでいる。近年、貴金属を用いず、最大で 100% の内部量子効率を可能とする新たな発光材料として、熱活性化遅延蛍光 (TADF) 材料が注目されている。しかしながら、TADF 材料は既存の発光材料に比べ、幅広い発光スペクトルを示すため、色純度の向上が望まれている。これに対し応募者の所属する研究室では、ホウ素と窒素の多重共鳴 (Multiple Resonance: MR) 効果を利用することで、世界最高レベルの色純度を持つ青色 MR-TADF 材料 (**v-DABNA**) の開発に成功している。本研究では、MR-TADF 分子を発光材料として用いて高効率な塗布型有機 EL 素子を開発することを目的とする。

まず、塗布型有機 EL 素子に適した波長をもつ発光材料として、 $\pi$ 共役系を拡張した超高色純度緑色 MR-TADF 材料 ( **$\omega$ -DABNA**) の開発を行った。その結果、one-pot ホウ素化反応と one-shot ホウ素化反応を組み合わせることにより、高収率で **$\omega$ -DABNA**を得ることに成功した。合成した **$\omega$ -DABNA**の極大蛍光波長は 509 nm であり、有機 EL ディスプレイの緑色素子に要求される蛍光波長 (520–530 nm) と比較して近い値を示した。さらに、発光スペクトルの半値幅は 22 nm と幅狭であり、蛍光量子収率は 87% と比較的高い値を示した。また、逆項間速度定数 ( $k_{\text{RISC}}$ ) は  $1.2 \times 10^5 \text{ s}^{-1}$  と、従来の高色純度緑色 TADF 材料よりも高い値を示した。さらに、 **$\omega$ -DABNA**の有機 EL 素子を作製し、特性を評価したところ、発光極大波長は 512 nm、半値幅は 25 nm と有機 EL ディスプレイに適した狭帯域緑色発光を示した。また、最大外部量子収率は 31.1%、 $1000 \text{ cd m}^{-2}$ における外部量子収率は 29.4%であり、そのロールオフは 1.7%と従来の緑色 MR-TADF 材料と比較して小さい値となった。

今後、大きな  $k_{\text{RISC}}$ を示す TADF 分子と組み合わせることによって、有機 EL 素子の高性能化を目指す。具体的には、大きな  $k_{\text{RISC}}$ をもつ TADF 分子で生成したエネルギーを **$\omega$ -DABNA**に移動させる“Hyperfluorescence”機構を利用することで、高い色純度、発光効率および素子耐久性を併せ持つ高性能緑色有機 EL 素子の開発を行う予定である。

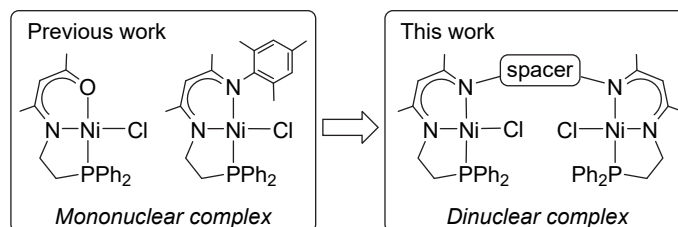




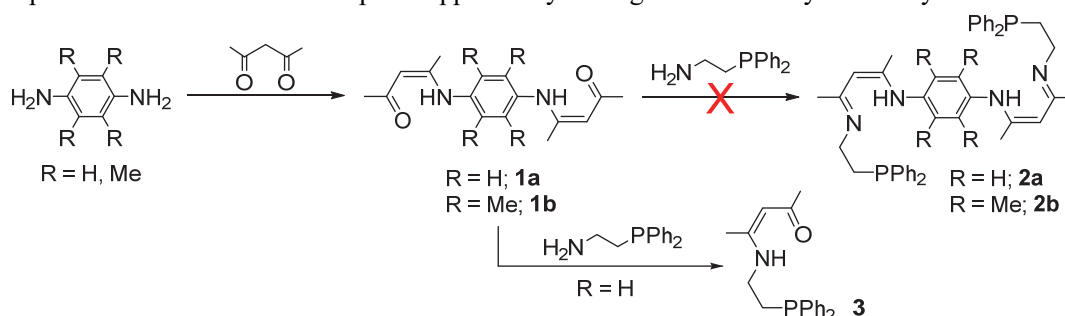
## Synthesis and its catalysis of dinuclear complexes utilizing a pincer-type *N,N,P* ligand

Yoshitaka Yamaguchi    Yokohama National University

Tridentate pincer-type complexes have generated a lot of interest because the pincer-type ligand stabilizes the metal complexes and its properties can be tuned to achieve the best reactivity of the complex. We have recently reported the synthesis of a series of pincer-type nickel(II) complexes utilizing a combination of  $\beta$ -aminoketonato or  $\beta$ -diketiminato frameworks with a third donor such as a phosphino or amino group. Our systematic study on these nickel(II) complexes revealed that the modification of the ligand framework has a significant influence on the catalytic performance in the cross-coupling reaction of aryl halides with arylmagnesium reagents (*Dalton Trans.* **2018**, 47, 8003.; *Eur. J. Inorg. Chem.* **2019**, 126.). We intended to develop a highly effective catalyst system for the activation of inert chemical bonds such as C-F and C-O bonds. The use of dinuclear complexes as catalysts has been considered as an efficient way to achieve this aim. Dinuclear catalysts have attracted considerable attention in recent years since a dinuclear complex containing two metals in close proximity would exhibit a bimetallic cooperative effect. Therefore, the bimetallic cooperativity can achieve to activate inert chemical bonds, which is difficult by mononuclear complexes. On the basis of the achievements of dinuclear catalysts reported so far and the studies of pincer nickel complexes by us, we designed dinuclear nickel complexes supported by a  $\beta$ -diketiminato-based pincer ligand.



1,4-Phenylenediamine was selected as a spacer for the construction of an *N,N,P*-type ligand precursor for a dinuclear complex. The condensation reaction of 1,4-phenylenediamine with 2 equivalents of acetylacetone in the presence of catalytic amount of  $\text{H}_2\text{SO}_4$  in toluene refluxing conditions afforded the phenylene-bridged bis( $\beta$ -diketimine) **1a** in 82% yield. Next, we examined the preparation of the ligand precursor **2a** by the reaction of **1a** with 2-(diphenylphosphino)ethylamine under various conditions, whereas the desired product **2a** was not obtained. In this reaction, amine exchange reaction occurred mainly to afford the *O,N,P*-type pro-ligand **3**. It was found that, for the preparation of an *N,N,P*-type pro-ligand, existence of the ortho substituents on the aromatic ring connected nitrogen atom is crucial preventing from the exchange reaction of amines. Thus, 2,3,5,6-tetramethyl-1,4-phenylenediamine was employed and the phenylene-bridged bis( $\beta$ -diketimine) **1b** was obtained. However, the reaction of **1b** with 2-(diphenylphosphino)ethylamine afforded complicated results and the desired ligand precursor **2b** was not obtained. The tetramethylphenylene unit as a spacer might be too sterically congested to construct the desired product **2b**. Finally, 4,4'-methylenebis(2,6-diethylaniline) was used as a spacer, and thus the formation of the desired ligand precursor was confirmed by NMR spectroscopy. The preparation of the dinuclear complex supported by this ligand is currently underway in our laboratory.



## Synthesis of Alkyl Ethers Using Two Different Alcohols Catalyzed by Organosilane Compound

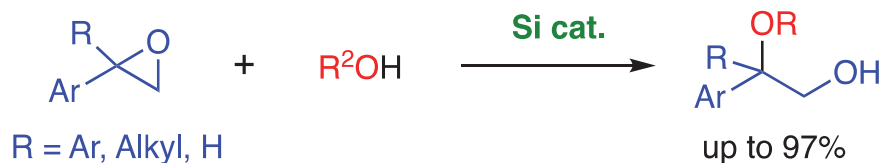
Toru Hashimoto Sanyo-Onoda City University

### Objective:

Alcohols and aryl alkenes derivatives are cheap and environmental benign substrates. Compared to fossil resources, these compounds are sustainable source and their direct use to access bulk and fine chemicals is of increasing interest. As environmental issues are growing concern, finding efficient, atom-economical and step-economical strategies for directly transformation using these compounds is a major challenge in organic chemistry. In this research project, we are challenging the development of a highly efficient and environmentally friendly synthetic process for alcohols and aryl epoxides by utilizing main group catalysts.

The ring-opening reactions of epoxides with alcohols provide access to synthetically important  $\beta$ -alkoxy alcohols. However, these reactions require either strongly acidic or basic conditions due to the usually poor nucleophilicity of alcohols; these harsh reaction conditions have spurred a search for new and milder methods. The use of Brønsted or Lewis acids is the most common method for the ring-opening of epoxides. Lewis-acidic metal salts have also been successfully applied in ring-opening reactions of epoxides with alcohols. Although these catalytic reactions generally lead to high product yields with good regioselectivity, the use of toxic and/or non-air-stable, expensive reagents restricts their widespread applicability.

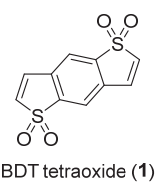
In this study, we have developed an organosilicon-catalyzed ring opening reaction of epoxide. The screening of reaction conditions for this ring opening reaction of epoxide were performed. Various organosilane catalysts were used for the optimization of reaction conditions. After screening of the reaction parameters, we found that the commercially available hydrosilane showed the catalytic activity for the ring opening reaction of epoxides with alcohols to afford the  $\beta$ -alkoxy alcohols in good yields.



## Development of heteroacenes with excellent photophysical and electrochemical properties

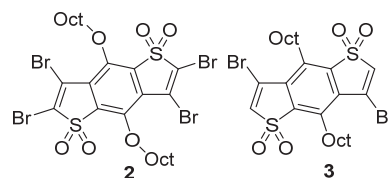
Koichi Mitsudo Okayama University

Thienoacenes, acene molecules bearing thiophene rings, have received considerable attention due to their excellent semiconductor properties and are used as active materials in organic field-effect transistors (OFETs) and organic photovoltaic cells (OPVs). Therefore, a variety of thienoacenes have been synthesized and their physical properties were investigated. It is well-known that the thiophene ring is an electron-rich donor aromatic ring. In contrast, thiophene dioxide, which is obtained by oxidation of the thiophene ring, loses its aromaticity and works as an electron-deficient acceptor molecule. In recent years, some  $\pi$ -extended molecules, having a thiophene dioxide skeleton, have been reported for their unique luminescent properties and have begun to attract attention. However, there have been few reports on the synthesis of thienoacene derivatives containing multiple thiophene-dioxides, even though they are expected to have interesting properties, and little is known about their physical properties. In this study, we focused on synthesis of thienoacenes which have benzo[1,2-*b*:4,5-*b'*]dithiophene 1,1,5,5-tetraoxide (BDT-tetraoxide, **1**) as a key skeleton.

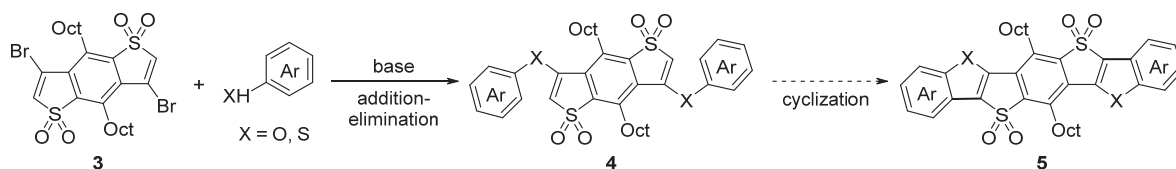


BDT tetraoxide (**1**)

Even though BDT is one of the most common skeletons in thienoacenes, few reports have been on synthesizing their oxides. In the previous period, we developed synthetic methods for the construction of BDT tetraoxide derivatives **2** and **3**. In



this period, we carried out the reaction of BDT tetraoxide **3** with several phenol and thiophenol derivatives to afford *O*- or *S*-linked BDT tetraoxides **4** via addition–elimination reaction. Thus-obtained **4** exhibited good fluorescent properties, and they are under investigation. We next examined Pd-catalyzed dehydrogenative double cyclization of **4** under several conditions, but the scission of C–X bonds proceeded predominantly and the desired thienoacenes **5** were not obtained. We screened several conditions and found that a cyclization reaction proceeded from the substrates without oxygen on the thiophene ring while the yield was still unsatisfactory. Further study revealed that the choice of oxidant was quite important for cyclization, and we successfully developed an efficient condition to construct C–C bonds on BDT derivatives. Now, we are applying this strategy to several BDT and BDT tetraoxide derivatives.

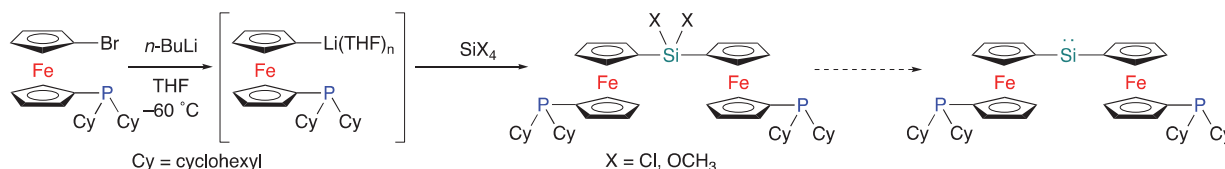


## Creation of Effective Oxidation Scavenger for Efficient Perovskite-based Solar Cells

Takahiro Sasamori University of Tsukuba

The goal of our collaborative research with Prof. Dr. Atsushi Wakamiya (ICR, Kyoto University) is development of an organic oxidation scavenger for the creation of efficient lead-free perovskite-based solar cells, and pioneering research achievements on the basis of the fusion of elemental science and functional physical chemistry. Challenges for lead-free efficient perovskite-based solar cells such as Sn(II)-based ones compared with their Pb counterparts predominantly include the facile oxidation of divalent Sn(II) into Sn(IV) which leads to the increased nonradiative charge recombination in the perovskite films. Thus, we have focused our research targets on the creation of low-coordinated main group element species as effective oxidation scavengers, which exhibit redox-active property and considerable solubility in organic solvents.

Silylenes ( $R_2Si:$ ) are attractive intrinsically extremely reactive species, which would exhibit possible ability of working as effecting oxidation scavengers. Isolable silylenes remain scarce, and in most hitherto reported examples, the silylene center is stabilized by electron-donating substituents (e.g., heteroatoms such as nitrogen), which results in electronic perturbation. We have been interested in the chemistry of redox-active silylenes with carbon-based substituents such as ferrocenyl groups. Furthermore, we have designed a ferrocene-based phosphonium ion with “reversible” intramolecular donor coordination,  $Fc^P_2Si:$  ( $Fc^P = 1'$ -dicyclohexylphosphino-1-ferrocenyl). The  $Fc^P$  group ascribes both stability and reactivity for the silylene center with its “switchable” donor coordination caused by the rotation of the cyclopentadienyl moiety. Accordingly, the possible precursor for the silylene such as  $Fc^P_2SiCl_2$  and  $Fc^P_2Si(OCH_3)_2$  were synthesized.<sup>1</sup> The attempted synthesis of the corresponding silylene is currently investigated. We are grateful to Prof. Wakamiya (ICR, Kyoto Univ.), Prof. Yoshida (Nagoya Univ.) and Prof. Tsuchiya (Kitasato Univ.) for their support on the research, and fruitful discussions.



1. Sasamori, T.; Ueno, H.; Morisako, S. *Inorganics* **2022**, *10*, 22.

## Developing machine learning approaches for prediction of protein stability changes upon missense mutations

Jiangning Song Monash University

**Objective.** It is important to predict the stability of a protein against mutations because even a single missense mutation of an amino acid can change a protein's structure and stability. Existing studies show that missense mutations can be harmful to health and disease-related by causing changes in the stability of a protein. Therefore, the accurate estimation of protein stability change ( $\Delta\Delta G$ ) measured as Gibb's free energy change is crucial for studying and understanding the relationship between protein missense mutation and function. Therefore, we will develop novel machine learning methods for this problem, by combining state-of-the-art machine learning techniques and various types of informative protein sequence and structural features. In this project, building upon these successful collaborative researches, we will continue and extend our development of next-generation bioinformatics methods for improved prediction of protein stability change. We may also study other related bioinformatics problems in the areas of sequence analysis and structural informatics.

**Results.** As a result of this project, we have developed a novel sequence-based method termed PROST for the protein stability change (Gibb's free energy change,  $\Delta\Delta G$ ) upon a single-point missense mutation [1,2]. In addition, we have also developed an open-source, Python-based software package iFeatureOmega [3], which is a powerful tool to generate, analyze and visualize 189 representations for biological sequences, structures and ligands.

### Publications

- [1] Iqbal, S., Ge, F., Li, F., Akutsu, T., ..., Song, J. PROST: AlphaFold2-aware Sequence-Based Predictor to Estimate Protein Stability Changes upon Missense Mutations, *J Chem Inf Model*. 2022 Sep 12;62(17):4270-4282 (2 citations).
- [2] Iqbal, S., Li, F., Akutsu, T., ..., Song, J. Assessing the performance of computational predictors for estimating protein stability changes upon missense mutations, *Briefings in Bioinformatics*, 2022, 22(6):bbab184 (15 citations).
- [3] Chen, Z., Liu, X., Zhao, P., Li, C., Wang, Y., Li, F., Akutsu, T., ..., Gao, X., Kurgan, L., Song, J. iFeatureOmega: an integrative platform for engineering, visualization and analysis of features from molecular sequences, structural and ligand data sets, *Nucleic Acids Res*. 2022 May 7;50(W1):W434-47. (7 citations).

## Integrating Omics Data and Module-based Network with Deep Learning to Develop Cancer Type Predictive Models

Jinn-Moon Yang National Yang Ming Chiao Tung University

**Objective.** Classification and prediction of cancer subtypes have been a major topic both in biomedicine and bioinformatics. To tackle this important issue, various machine learning methods have been developed to better utilize mRNA expression data and improve the classification accuracy. However, many of existing studies focus on specific cancer types, and thus it is needed to explore mechanisms across multiple cancer types. For understanding of such mechanisms, it is crucial to analyze the topology of biological networks and biochemical progress in cells. To this end, integrated analysis of omics data and biological networks is required. Although many such studies have recently been done, currently available approaches are not satisfactory. To address these issues, we will develop computational methods by integrating graph-based and machine learning methodologies. In this year, we focus on analysis of protein complexes because these play important roles in biological networks.

**Results.** We developed graph theory-based methods to predict hot spots from only a single residue interaction network constructed from three-dimensional protein complex data, where hot spots are sets of residues contributing most to the binding energy in protein interfaces. The methods are based on the concept of the densest subgraph and utilize linear programming and integer linear programming. By evaluating the results on 67 complexes from a publicly available database (SKEMPI database), our methods clearly outperform existing graph theory-based methods on recall and F-score. In particular, the Min-SDS method has an average recall of over 0.665 and an F2-score of over 0.364, while the recall and F2-score of the existing methods are less than 0.400 and 0.224, respectively.

### Publication

[1] R. Li, J-Y. Lee, J-M. Yang, T. Akutsu: Densest subgraph-based methods for protein-protein interaction hot spot prediction, BMC Bioinformatics, vol. 23, Paper ID. 451, 2023.

## Evolution of giant viruses and relationships with the origin of Life

Morgan Gaïa CEA/Genoscope

### Background:

The nucleocytoplasmic large DNA viruses (NCLDV) form a phylum of related families of large and giant DNA viruses, which collectively infect the entire diversity of eukaryotes. They are abundant, active and diverse in many environments, especially the oceans. Their immense diversity and broad host spectrum are likely the results of their ancestry; they were presumably already diversified before the emergence of the modern eukaryotes and infected their direct ancestors. Considering the large amount of gene transfers regularly occurring between cells and these viruses, including from the latter to the former, the NCLDV are suspected of having played a major role in the emergence and early evolution of modern eukaryotes. The evolutionary mechanisms and forces behind the gigantism of their genomes also remains to be investigated.

### Objectives:

- 1) Robust phylogeny of the NCLDV (evolutionary backbone);
- 2) Flow of gene transfers from and to the NCLDV (past interactions);
- 3) Inferred lifestyle from genomic functions (adaptation);
- 4) Characterization of the new classes' specificity (divergence).

### Results:

Objective 1 was achieved by identifying unstable branches from the phylogenomic tree of isolated viral genomes. Viruses identified to contribute to the instability of branches were removed from the dataset to build a robust phylogenomic tree. Objective 2 was performed by comparing “gene trees” for orthologous gene clusters to the above mentioned robust phylogenomic tree (“species tree”). We used the amalgamated likelihood estimation method to identify gene loss and gene gain events, the latter being further classified into gene transfers between viruses (T), gene duplications (D), and unknown originations (U). The result indicated that gene gain overwhelmed the gene loss events, and among different types of gene gains, gene transfers between viruses (T) were recognized, for the first time, as a quantitatively important evolutionary event. These results were obtained in a tight and intensive collaboration with a master student, Junyi Wu, in the partner laboratory at ICR. We also obtained specific results for Objective 3 and 4 (see: doi: <https://doi.org/10.1101/2021.12.27.474232>).



## Revealing marine microbial-viral interactions through community interactome analyses

Samuel Chaffron CNRS

### Background & Objectives:

As opposed to our conventional view on viruses as small particles, viruses of the phyla *Nucleocytoviricota* and *Mirusviricota* possess outsized virions even larger than small cells bacteria. These giant viruses can infect various eukaryotic hosts, from unicellular eukaryotes to large animals. The wide host spectrum of giant viruses makes them abundant, active, and ecologically important in the global ocean. However, known hosts of giant viruses are very poorly characterized due to isolation and technical limitations. Nevertheless, the diversity of giant viruses has been recently expanded through metagenome-assembled genomes (MAG) reconstructions. MAGs can provide genomic information to predict and support infection relationships, as for horizontal gene transfers evidence between hosts and viruses.

In this project, we aimed to improve our knowledge of inter-species interactions between viruses and eukaryotes and predict hosts of marine viruses using novel computational methods applied to a recently published Global Ocean Eukaryotic Viral (GOEV) database [1].

### Methods & Results:

First, using abundance profiles of the GOEV database and a marine eukaryotic environmental genomes database, we inferred a marine virus–plankton association network (referred to as an *interactome*) at a global scale (Fig.1). We analysed viral community composition and computed robust temperature optima for viruses and their predicted hosts. We then assessed a clear structuration of this interactome at the temperature-dependent polar/nonpolar boundary. The uniqueness of polar/nonpolar interactions likely causes the endemism of polar viral communities.



Fig. 1 Virus–plankton interactome

We then used a phylogeny-guided Taxon Interaction Mapper (TIM) method to predict hosts from interactome associations. Consistent with the findings above, our analyses suggested an unidentified virus–host relationship between polar diatoms and giant viruses. Taking advantage of genomic information, we further identified potential HGTs and viral insertions in diatom genomes to support our findings. Overall, our

graph-based computational approach has been instrumental to reveal novel marine host-virus interactions, which will have to be validated in vitro.

Publication: Lingjie M., Delmont T.O., Gaïa M., Pelletier E., Fernández-Guerra A., Chaffron S., Neches R.Y., Wu J., Kaneko H., Endo H., Ogata H. (2023) Genomic adaptation of giant viruses in polar oceans. *bioRxiv* 2023.02.09.527846; doi: <https://doi.org/10.1101/2023.02.09.527846>

## A Study on Statistical Machine Learning for Efficient Graph Structured Data Analysis

Masayuki Karasuyama Nagoya Institute of Technology

Data-driven approaches have attracted wide attention from a variety of scientific fields such as biology, chemistry and materials science. In particular, graph based representations are useful for capturing structured relations that are often difficult to be handled by using the standard numerical table based representation. For example, a chemical composition is typically represented as a graph in which a node indicates an atom and an edge indicates a bond. In this study, we focus on a knowledge extraction problem on the graph based data analysis.

Although there exist well-known machine learning algorithms that can incorporate graph information such as graph neural networks (GNNs) and graph kernels, it is still difficult to construct an interpretable learning model, because of the combinatorial nature of graph data. For example, identifying key substructures that increase the toxicity of compositions can be informative, but the number of possible substructures in the dataset can be intractable. We previously proposed an algorithm that can identify important substructures of a given graph prediction problem through distance metric learning of graphs [1]. In this framework, we used a sparse model in which only a small number of important features are used to construct the prediction. Since naïve computations can be computationally prohibitive, we combine a graph mining algorithm and the theory of the convex optimization so that important subgraphs can be identified without exhaustively searching possible candidates.

Our previous approach can identify important subgraphs, but it cannot deal with a graph having continuous attributes on its nodes or edges. For example, a graph node of a chemical composition can have numerical information derived from the three-dimensional position of each atom. To build an interpretable prediction model with those attributed graph inputs, we propose a novel sparse learning method that can identify important substructures as attributed subgraphs, called *attributed graphlets*. We show that an efficient pruning strategy can be derived for exploring subgraphs while estimating representative attribute vectors simultaneously. We confirmed this approach can actually identify a small number of important attributed graphlets while achieving similar prediction performance to other well-known approaches such as GNNs. We submitted the paper about this approach to an international conference [2] (currently under review).

[1] T. Yoshida, I. Takeuchi and M. Karasuyama, Distance Metric Learning for Graph Structured Data, *Machine Learning*, vol.110, no.7, 1765-1811, 2021.

[2] S. Tajima, R. Sugihara, R. Kitahara and M. Karasuyama, Under review.

## オミクスデータと流束均衡解析に基づく高温適応進化の機序解明

岸本利彦 東邦大学

(目的) 我々は、これまでに高温適応進化大腸菌の継代培養を 15 年以上継続して、48℃以上でも安定的に増殖する株を複数培養中である。高温適応進化大腸菌は、元の野生株とは異なる様々な表現型を示すが、その機序はほとんど未解明である。一方、継代培養を続けた株では、細胞増殖や各代謝反応の速度が安定するので、網羅的トランスクリプトーム解析で予測した反応速度分布を用いて、制約モデルによる流束均衡解析シミュレーションが有効である。本研究では、野生株や高温適応進化大腸菌の網羅的トランスクリプトームデータを用いて、流束均衡解析と GPR ネットワークに基づくシミュレーションを混合整数線形計画法で定式化して、高温適応進化による GPR ネットワークの変異を検出することを目的とした。

(実験方法) 解析対象となる大腸菌として、先祖株 と 2 系統の高温適応進化大腸菌の 45℃、46℃、47℃、48.1℃、48.3℃、及び系統 1 の 47.3℃、系統 2 の 47.4℃、47.9℃適応株を用いた。大腸菌の培養は、mM63 最小培地を用いて行い、対数増殖 (OD600<0.4) を維持するように実施した。RNA 抽出は、各株で 3 本の培養から RNAProtect bacteria reagent と RNAeasy (共に QIAGEN)を用いて行なった。RNAseq は、NEBNext rRNA Depletion Kit (Bacteria) (NEB)、NEBNext Ultra II RNA Library Prep Kit for Illumina (NEB)、NextSeq 500/550 High Output Kit v2.5 (Illumina)を用いてサンプル調整を行い、NextSeq 500 (Illumina)によりデータを取得した。RNAseq データの TPM データ化には、Kallisto を用いた。

(実験結果) 高温適応進化実験により、大腸菌は、2 系統とも 48.3℃適応まで達成された。このうち系統 2 の 48.3℃適応株は、その増殖至適温度が 45℃から 46℃の間に存在することが判明した。高温菌の増殖至適温度が 45℃以上であることから、実験室進化で中温菌である大腸菌を高温菌まで進化させることに成功した。実験室進化で種を超える進化の報告はないため、世界初の例となった可能性が高い。この大腸菌を含む、高温適応進化大腸菌株 12 株と進化の元株の計 13 株について、最小培地でそれぞれの株の適応最高温度で対数増殖期の RNA を採取した。このサンプルを慶應大学先端生命科学研究所河野先生に送付し、RNAseq 解析を行った。その結果、全てのサンプルで解析に利用可能なレベルのデータが取得された。これにより、GPR ネットワーク解析を実施する準備が整った。現在、共同研究者である田村先生にデータを送付し、3 月以降に解析予定である。

(考察) 本 RNAseq データを用いて GPR ネットワーク解析以外にも、高温適応進化により使用頻度が減少したネットワークの検出などにも応用可能である。本研究における高温適応進化は、通常大腸菌の 2 オーダー高い変異率で生じている。現存生命で維持されている遺伝子数は、ゲノムの変異率と一次の逆相関していることがわかっており、我々の高温適応進化で活用されている有効遺伝子数が減少していることが示されれば、実験的に遺伝子数と変異率の関係を証明できることになる。

(成果報告)

1) 岸本利彦、松尾萌、河野暢明、田村 武幸 大腸菌高温適応進化とその生き残り戦略

第 1 回総合微生物学研究会、ラフォーレ修善寺、2022

## Control and Analysis of Complex Networks via Probabilistic Minimum Dominating Sets

Jose Nacher Toho University

**Objective.** Various molecules interact with each other to carry out life activities in cells and organisms, and thus it is important to analyze networks formed by these interactions to understand life. To this end, we have been conducting studies on controllability of various biological networks such as protein interaction networks, metabolic networks, and ncRNA-protein networks. In recent years, we have been focusing on controllability studies using the minimum dominating set (MDS), which is a well-known concept in graph theory. We developed various extensions of the MDS-based control model. In particular, we developed methods to classify nodes into critical, intermittent, and redundant based on occurrence of nodes in MDS solutions. In this year, we further explore the MDS-based approach to analyze large-scale directed networks and to perform more detailed classification of nodes.

**Results.** We developed two graph theory-based methods for MDS-based analysis of biological networks. One is an efficient method for classifying nodes in large directed networks into three categories: critical, intermittent, and redundant, by utilizing novel pre-processing methods. The results of preliminary computational experiments on large-scale protein-protein interaction networks suggest that the identified critical proteins are associated to important biomedical functions [1]. The other one is introduction of a new controllability measure, and its associated efficient algorithm, that quantifies the importance of intermittent nodes in directed biological networks. The results of preliminary computational experiments demonstrate the biological importance of the intermittent nodes as well as their associations with specific human diseases [2].

### Presentations

[1] Y. Tokuhara, T. Akutsu, J. C. Nacher: An algorithm for identifying critical control nodes in probabilistic directed biological networks, IPSJ SIG Technical Report, vol. 2022-BIO-72, no. 7, 2022.

[2] W. Someya, T. Akutsu, J. C. Nacher: An algorithm for quantifying the importance of intermittent nodes in controlling biological networks, IPSJ SIG Technical Report, vol. 2022-BIO-72, no. 8, 2022.

## Development of a comprehensive detection method for coronaviruses originated in wildlife

Tokiko Watanabe Osaka University

Seven types of coronaviruses are currently known to infect humans, all of which originate from viruses that infect wild animals such as bats and rodents. In this study, we developed a system to comprehensively detect coronaviruses in environmental samples and applied this system to actual surveillance with the aim of strengthening surveillance for coronaviruses carried by animals such as bats. First, we established an RT-PCR method using degenerate primers designed by bioinformatics analysis to detect coronaviruses for divergent bat coronavirus surveillance. We designed 39 degenerate primer pairs for comprehensive detection of the RNA-dependent RNA polymerase gene sequences of coronavirus genes in the database. The RT-PCR conditions were optimized using these primer pairs, leading us to successfully detect RNAs of alpha-, beta-, gamma-, and deltacoronaviruses. Next, we performed the optimized RT-PCR using RNA extracted from organ samples from 26 bats captured in Sierra Leone, West Africa. An amplicon of 400–450 bp was detected in RNA extracted from the intestinal tract of one of these bats. This RNA sample was analyzed by RNA-seq and identified as a coronavirus sequence. Phylogenetic analysis revealed that this virus clustered with members of the genus *Alphacoronavirus* and the sequence of the ORF1ab genome shared less than 90% identity with the closest bat alphacoronavirus (Fig 1, magenta). We have thus established an RT-PCR method that can comprehensively detect coronaviruses, which will be useful for bat coronavirus surveillance and proactive measures against future outbreaks of coronavirus infection.

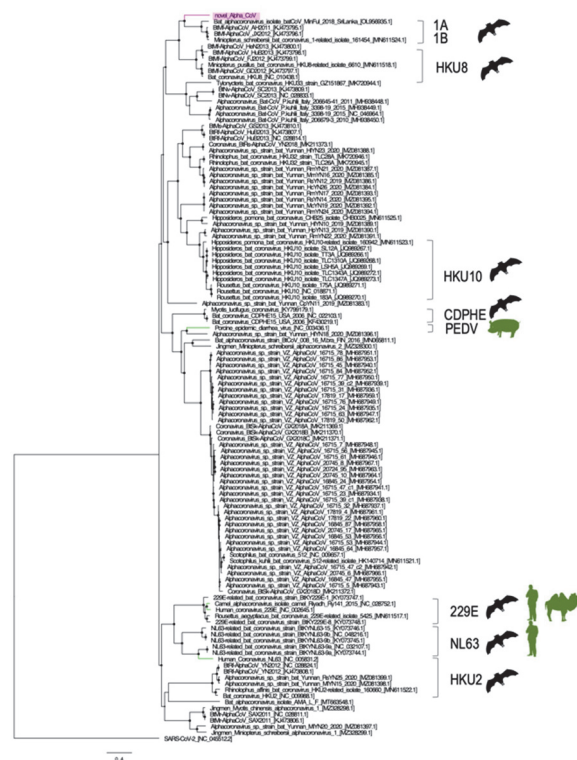


Fig 1. Phylogenetic tree of coronaviruses (ORF1ab gene)



## Microbial ecology in the dark sea

Takashi Yoshida    Kyoto University

Microorganisms account for two-thirds of the biomass in aquatic environments. In the marine ecosystem, viruses are the most numerous biological entities and can lyse one-third of the host cells daily. The interaction between viruses and microorganisms contribute to the variability and stability of the global environment, influencing overall biogeochemical cycling in the ocean. Much previous effort in marine microbiology focused on the photic zone, which is highly productive and relatively easy to perform observations. Aphotic zone (at depths below 200 m), accounting for 95% of the hydrosphere, is characterized as a harsher environment, with no light for photosynthesis, low oxygen concentration, high pressure and a high concentration of inorganic nutrients. However, the interaction between viruses and microorganisms in this zone is still under investigated due to the high difficulty in sampling this zone.

To analyze the community composition, potential hosts and metabolic capacity of viruses and microorganisms in deep sea, it is a prerequisite to obtain sufficient amount of DNA and RNA from samples. In this study, a long-term sampling is planned to conduct at Muroto Deep Seawater Research Institute in Kochi Prefecture. In this institute, deep seawater (320 m depth) and surface seawater (0.5 m depth) are pumped up from a spot within a 3 km distance from the coast. Four times of sampling in Muroto have been carried out from Dec 2021 to Dec 2022 to concept and develop an appropriate sampling system. In total, about 2,800 L deep seawater and 100 L surface seawater were filtered.

By building different type of filtration systems, including changing the filtration membrane pore-size, filtration pump type and RNA/DNA extraction methods, a high efficiency sampling protocol was built for obtaining sufficient DNA and RNA finally. In brief, seawater was prefiltered through 150  $\mu\text{m}$  mesh nylon mesh to remove large plankton, and then filter by 3  $\mu\text{m}$  pore-size membrane and 0.2  $\mu\text{m}$  sterivex, individually. Filtration time was strictly limited in 30 min to prevent RNA from degrading. Finally, nucleic acid yield increased. Especially for the 3-150  $\mu\text{m}$  size particles in deep sea, the RNA amount from one-liter deep sea water increased from under-detection limit to about 4.8 ng. High yields were also achieved by extracting DNA and RNA separately.

In future, metagenome and metatranscriptome sequencing will be performed to probe microorganism community compositions and viral gene expression level to better understand the ecology of virus-host system in the deep ocean.

## 効果的な分子ネットワーク解析方法の発展と医学・農学への応用

茅野光範 帯広畜産大学

本研究では、機械学習と統計学を融合させた統計的機械学習の観点から、効果的な分子ネットワーク解析法を提案し、それを用いて医学・農学における問題を解決する。分子レベルとして、ゲノム・遺伝子・代謝に焦点を当て、遺伝子ネットワークや代謝ネットワーク（代謝パスウェイ）の推定や、それらのネットワークへのゲノムの影響、実験条件（健常者と患者等）による違い等を検証するための解析方法を提案する。

我々は、これまで、図 1 に示した分子発現の相関構造の変化を捉える解析手法を提案し、これを改良した提案手法の数値実験による評価、公共の遺伝子発現データ (Gene Expression Omnibus ; GEO から入手した延べ約 100 万個の遺伝子群) に提案手法を適用し、生物学的に意義のある遺伝子群が検出出来ることを確認した。また、先行研究で報告されている、相関ネットワークが変化する遺伝子群の具体例を集めた。さらに、これまでの提案手法をさらに発展させ、グラフネットワーク理論、計算機統計学、アルゴリズムやマイニング理論を駆使した機械学習・統計学的な分子ネットワーク解析法の提案へ向けて検討を重ねている。

今年度は、これらの解析法の医学分野（特に加齢研究）および農学分野（特に農作物）における具体的な生命科学現象への応用を検討し、医学分野として、ヒトと動物の加齢および加齢関連疾患研究、また、農学分野として、農作物のオミックス解析研究を進めている。

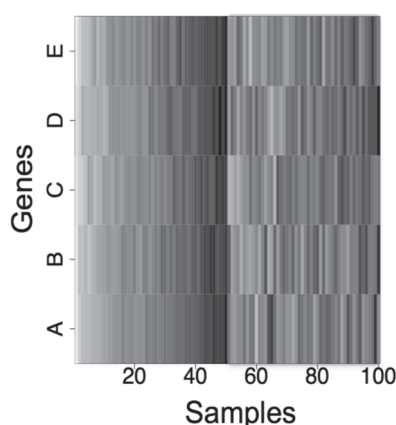


図 1. 2つの群間（サンプル 1～50 および 51～100）で相関構造が変化する 5つの遺伝子 A, B, C, D, E のヒートマップ表示（濃いほど発現量が高い）。遺伝子 A-E の中から任意の対をとると、サンプル 1 から 50 の群では相関を持つが、サンプル 51-100 の群では相関構造が崩れる [Kayano M., Shiga M. and Mamitsuka H., IEEE/ACM Trans. Comp. Biol. Bioinform., 11(1): 154-167, 2014 より転載]



## Investigations into Catalytic and Biochemical Behaviors of Nitrogenase Fe protein using $^{57}\text{Fe}$ labeling

Markus W. Ribbe University of California, Irvine

### [Objectives]

$\text{N}_2$ -reducing enzyme (nitrogenase) utilizes a sophisticated electron transfer system and a Mo-Fe-S-C cofactor ( $[(\text{cit})\text{MoFe}_7\text{S}_9\text{C}]$  or M-cluster) to reduce atmospheric  $\text{N}_2$  to bioaccessible  $\text{NH}_3$ . This work aims to repurpose the cofactor-free form of nitrogenase as a protein scaffold for the incorporation of a synthetic Mo-Fe-S cluster  $[\text{Cp}^*\text{MoFe}_5\text{S}_9(\text{SH})]^{3-}$  (**1**).

### [Methods]

The cofactor-free form of nitrogenase catalytic component was treated with cluster **1**. The resultant semi-artificial enzyme was analyzed by using ICP and EXAFS to gain insight into the structure of the incorporated cluster. Catalytic activity of the semi-artificial enzyme was also evaluated by  $\text{C}_2\text{H}_2$  and  $\text{CN}^-$  reduction assays.

### [Results and Discussion]

While full characterization of the incorporated cluster was unsuccessful, the enzyme displayed catalytic activity for the reduction of  $\text{C}_2\text{H}_2$  to  $\text{C}_2\text{H}_4$  (Fig 2) and  $\text{CN}^-$  to short-chain hydrocarbons. Thus, this work demonstrated the utility of the nitrogenase scaffold as a electron delivery platform to artificial cofactors.

### [Research Outcome]

Tanifuji, K.; Jasniowski, A. J.; Lee, C. C.; Solomon, J. B.; Nagasawa, T.; Ohki, Y.; Tatsumi, K.; Hedman, B.; Hodgson, K. O.; Hu, Y.; Ribbe, M. W. Incorporation of an Asymmetric Mo-Fe-S Cluster as an Artificial Cofactor into Nitrogenase. *ChemBioChem* **2022**, 23 (19), e202200384.

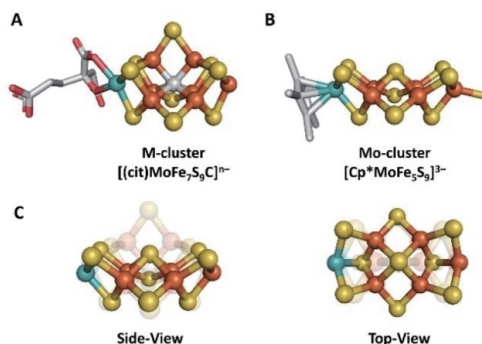


**Fig. 1** Molecular structures of (a) the natural Mo-Fe-S-C cofactor (M-cluster) of  $\text{N}_2$ -reducing enzyme (nitrogenase) and (b) the Mo-Fe-S cluster applied to a reconstitution with cofactor-free nitrogenase and (c) structural comparison of the two clusters. Extracted from the publication.

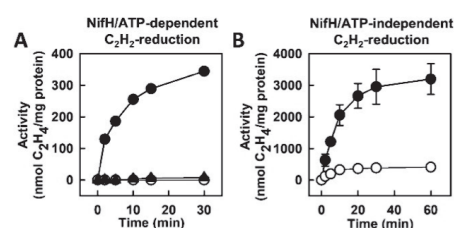


**Fig. 2** Reduction of  $\text{C}_2\text{H}_2$  to  $\text{C}_2\text{H}_4$  by NifDK reconstituted with Mo-Fe-S cluster in the presence of (A) enzymatic electron carrier and (B) non-enzymatic reductant. Legend: •, full assay conditions; ○ and ▲, controls in the absence of the electron carrier or reductant. Details are shown in the publication.

## Precise synthesis and controlling higher-order structure of tadpole-like Janus cellulose nanocrystal

Atsushi GOTO Nanyang Technological University

**Objectives** – Cellulose nanocrystal (CNC) is a rod-like nanoparticle with intriguing properties such as high strength and high stiffness. We focus on the CNC with different polymers (in chemical composition or degree of polymerization) grafted regioselectively on the reducing end-groups and the lateral hydroxyl groups of CNC (tadpole-like Janus CNC; Figure 1), which could form novel higher-order structures otherwise impossible. In this study, as a key step of the versatile synthetic route toward tadpole-like Janus CNC, we have tried to introduce an initiating group of atom transfer radical polymerization (ATRP) via click reaction.

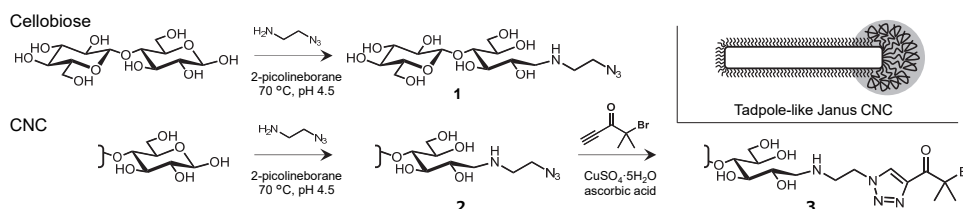


Figure 1. Schematic illustration of structures of Tadpole-like Janus CNC and CNC and tadpole-like Janus CNC and Scheme for Chemical modification of reducing end-groups of cellobiose and CNC.

**Results and Discussion** – To confirm the effectiveness of reductive amination reaction with azido ethylamine, reductive amination with cellobiose was carried out according to the reported procedure,<sup>1</sup> indicating that hemiacetal structure decreased by 97% by the bicinchoninic acid assay. Then, we applied the same reaction condition to CNC and achieved approximately 60% reduction of the hemiacetal structure of CNC. Thus, we concluded that sufficient reducing end-groups of CNC was successfully modified with 2-azidoethylamine. As for the succeeding click reaction toward CNC-**3**, the peak derived from the azido group disappeared in the IR spectrum of the obtained sample, indicating the successful synthesis of CNC with ATRP initiating groups. We are going to purify the cellobiose derivative **1** and analyze its structure and hence the detail of the reductive amination reaction with 2-azidoethylamine. We are going to carry out the ATRP using CNC-**3** to synthesize tadpole-like Janus CNC forming a novel higher-order structure.

[1] Delepierre, G., et al. *Biomacromolecules* **2021**, 22, 2702–2717

## Exploration of perovskite solar cell composition: correlating device performance and fundamental property

Akinori Saeki Osaka University

Connecting data science (machine learning) with experimental methods is critical for accelerating material science research. We report a multivariate analysis for exploring A-site organic cation mixing in tin iodide perovskite ( $\text{ASnI}_3$ ) solar cells (PSC), which are the most suitable Pb-free PSC candidates. To address the common drawbacks of Sn perovskites (facile oxidation of  $\text{Sn}^{2+}$  to  $\text{Sn}^{4+}$  and large degree of mixing), we proposed an efficient experimental screening method using 133 types of environmentally stable  $\text{A}_2\text{Sn(IV)I}_6$  zero-dimensional pseudo-perovskites to predict the power conversion efficiency (PCE) of  $\text{ASn(II)I}_3$ , in which A is a ternary or quaternary mixed organic cation (namely methylammonium, formamidinium (FA), dimethylammonium, guanidinium, ethylammonium, acetamidinium, trimethylammonium, imidazolium, or phenylethylammonium (PEA)). The high correlation coefficient of our model (0.953) and experimental validation (0.982) allowed us to identify a new  $(\text{FA}_{0.92}\text{IM}_{0.08})_{0.9}\text{PEA}_{0.1}\text{SnI}_3$  Sn-PSC with a PCE of 7.22%. Our results provide a basis for exploring A-site cation mixing in Sn-PSCs for improving their performance.

Two-dimensional pseudo (quasi) perovskites, such as Ruddlesden–Popper (RP) and Dion–Jacobson (DJ) perovskites, have garnered significant attention. Controlling the orientation of their layered crystallites is key to vertical charge transport in two-dimensional (2D) PSCs; however, their detailed electronic properties are yet to be fully understood. We investigated the effect of processing additives (ammonium salts:  $\text{NH}_4\text{Cl}$ ,  $\text{NH}_4\text{Br}$ ,  $\text{NH}_4\text{I}$ ,  $\text{NH}_4\text{SCN}$ , and  $\text{CH}_3\text{NH}_3\text{SCN}$  with/without alkali metal salts ( $\text{NaCl}$ ,  $\text{KCl}$ ,  $\text{RbCl}$ , and  $\text{CsCl}$ ) in water) on the crystallographic nature and anisotropic microwave photoconductivity of RP and DJ perovskites. Importantly, a strong correlation ( $r = 0.882$ ) was observed between the power conversion efficiencies (1–11%) of inverted PSCs and anisotropic (both out-of-plane and in-plane to the substrate) photoconductivities for the 34 compositions of additives analyzed herein. These results underscore the importance of anisotropic mobility in 2D PSCs and could serve as guidelines for their further development.

- [1] E. Nakanishi, R. Nishikubo, F. Ishiwari, T. Nakamura, A. Wakamiya, A. Saeki, *ACS Materials Lett.* **2022**, 4, 1124.  
 [2] R. Shimono, R. Nishikubo, F. Ishiwari, A. Saeki, *J. Phys. Chem. C* **2022**, 126, 17894.

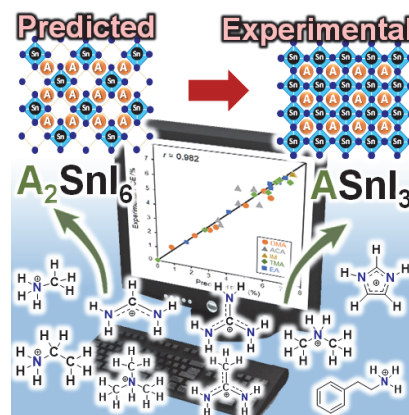


Fig. 1. Exploration of A-site cation of Sn-PSC.

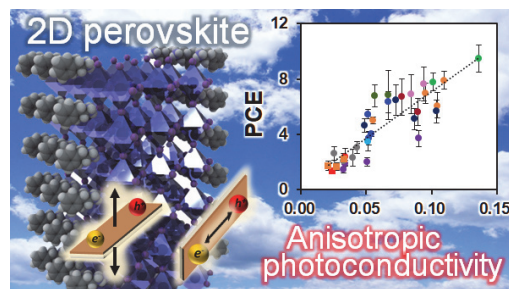


Fig. 2. Anisotropic photoconductivity of 2D-PSC.

## Precise synthesis and viscoelastic properties of ring polymers with high purity and high molecular weight

Atsushi Takano Nagoya University

**Introduction** A ring polymer has topologically interesting structure with no chain ends and it is considered as a model polymer to clarify the topological effect on physical properties such as viscoelastic properties. The dynamics of ring polymers were theoretically predicted by several models such as lattice-animal (LA) model<sup>1</sup> and fractal loopy globule (FLG) model<sup>2</sup>, when their molecular weights are high enough to penetrate each other and form a certain entanglement. But high molecular weight ring polymers have not been synthesized experimentally so far because of the synthetic difficulty. In this study, ring polybutadienes with relatively high molecular weight and high ring purity was prepared, and the melt rheology was measured and the dynamics of high molecular weight ring polymers was discussed.

**Experimental** A series of ring polybutadienes with the molecular weight ranging  $10\text{k} < M_w < 50\text{k}$  and with high ring purity ( $>99.5\%$ ) were carefully prepared by anionic polymerization and HPLC separation techniques<sup>3</sup>. Purity of Ring samples was checked by interaction chromatography (IC) analyses<sup>3</sup>.

**Results and Discussion** The dynamic viscoelastic measurements of the ring PBs and also linear counterparts were carried out. Figure 1 shows the angular frequency  $\omega$  dependence of the storage and loss moduli,  $G'(\omega)$  and  $G''(\omega)$  for high molecular weight sample, ring-50k, compared with the linear counterpart (linear-50k). The entanglement molecular weight ( $M_e$ ) of PBs was calculated from  $G_N^0$  as  $M_e = 2.1\text{k}$ . Linear-50k exhibits relatively long rubbery plateaus since the entanglement number is larger ( $M_w = 50\text{k} = 23M_e$ ), while ring-50k also revealed rubbery plateaus with lower storage/loss moduli than those for linears. Actually the longest relaxation times for the ring-50k and linear-50k are almost comparable, therefore it is confirmed that this high molecular weight ring PB start entanglement each other.

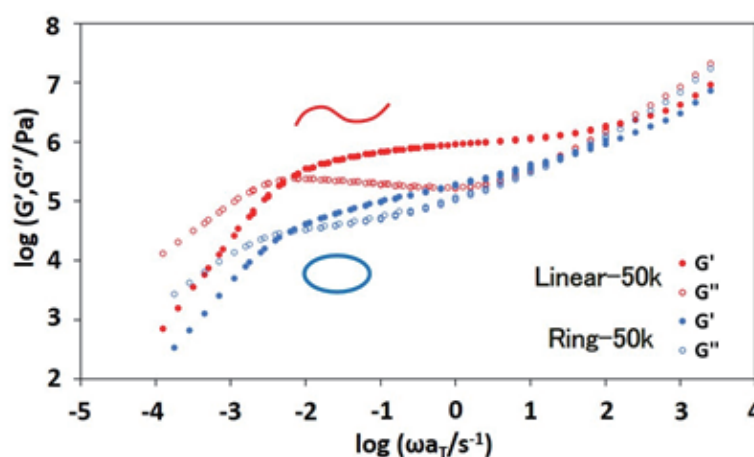


Figure 1: Master curves of  $G'$  and  $G''$  for ring/linear PBs ( $M_w = 50\text{k}$ ) at  $T_{\text{ref}} = -15^\circ\text{C}$ .

### References

1. M, Rubinstein.; *Phys. Rev. Lett.* **1986**, 24, 3023-3026
2. T, Ge.; S, Panyukov.; M, Rubinstein.; *Macromolecules*. **2016**, 49, 708-722
3. Y, Doi.; K, Matsubara.; Y, Ohta.; T, Nakano.; D, Kawaguchi.; Y, Takahashi.; A, Takano.; Y, Matsushita.; *Macromolecules*. **2015**, 48, 3140-3147

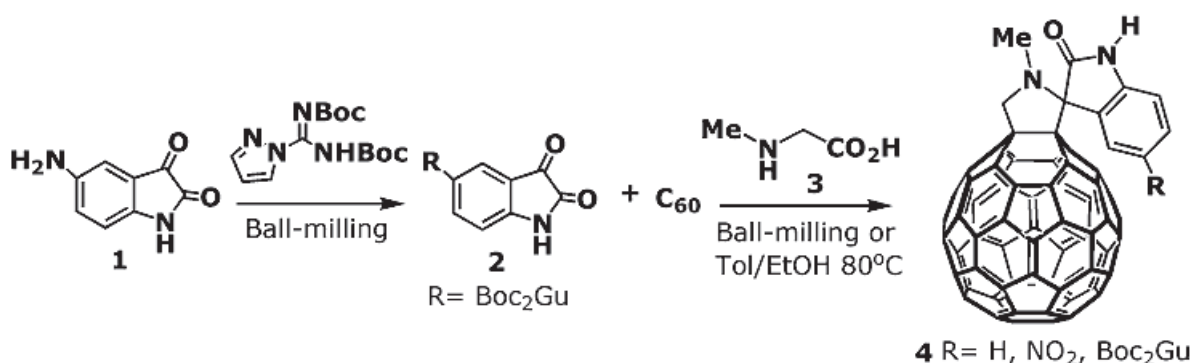
## Exploration of Cycloaddition Properties of Guanidine Functionalized Isatins

Davor Margetic   Rudjer Boskovic Institute

### Objectives

Synthesis of novel guanidinium isatin reagents and investigation of their reactivity for fullerene derivatization with partner ICR researcher Professor Murata Yasujiro.

**Experimental results.** Synthetic route to guanidino functionalized isatins was established. Synthetically most productive procedure (Scheme 1) is two-step reaction from 4-nitroisatine, which by reduction afforded amino 4-aminoisatindole **1**. The guanylation reaction of **1** carried out in ball mill mechanochemically using *N,N'*-bis-Boc-1-pyrazole-1-carboxamide provided guanidine **2**. Intermediate isatine azomethine ylides were prepared *in situ* from **2** by the addition of sarcosine **3** and several reactions were carried out to investigate their cycloaddition reactivity with dipolarophiles. With reactive *N*-methylmaleimide and norbornene cyclobutene diesters, the cycloadducts were obtained stereospecifically, whereas reaction with fullerene C<sub>60</sub> afforded pyrrolidine cycloadducts **4** as single product. Fullerene was readily reacted with isatine, nitro isatine and Boc-protected guanidine-isatine providing functional derivatives of **4**. All new products were spectroscopically fully determined (<sup>1</sup>H, <sup>13</sup>C NMR, and IR or MS).



Scheme 1

**Theoretical results.** Experimental results were corroborated with computational study. Density functional (DFT) calculations using HF/6-31G(d,p)//M062X/6-31G(d,p) SMD(EtOH) method were carried out to predict the influence of guanidine substituent on the reactivity of isatine derivatives. Relative 1,3-dipolar cycloaddition reactivity of isatins was estimated from ground state calculations of energies of highest-occupied molecular orbitals (HOMO) of azomethine ylides. No significant influence of substituents on the reactivity of isatin azomethine ylides was determined, which is in good accordance with experimental results.

Planned travel to visit ICR was organized in January and lecture at ICR was held on January 24, 2023. The results of the projects were also presented at the Tokyo Metropolitan University.

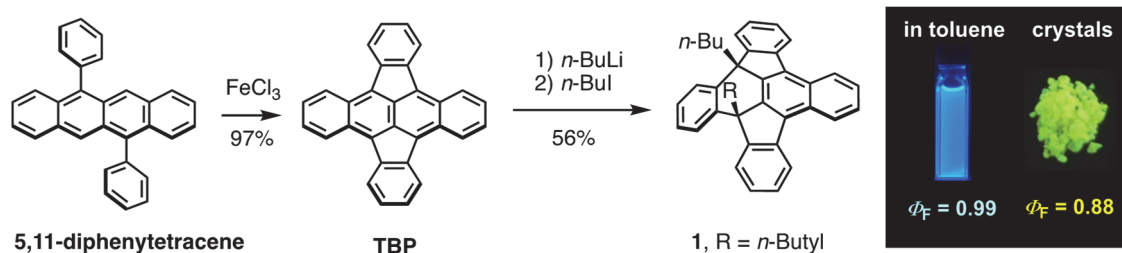


## Synthesis of Novel Nanotube Molecules with Different Hole Directions by Introducing a Double Heptalene Structure

Chaolumen Inner Mongolia University

Exploring efficient synthesis and novel properties of polycyclic aromatics with pentagons are significantly important for developing new optoelectronic materials. In 2015, we found that 5,11-diphenyltetracene can smoothly undergo an oxidative coupling under the Scholl cyclization conditions to give tetrabenzo-fused pyracylene (TBP), which can further react with *n*-BuLi and *n*-BuI to give a 1,4-adduct (**1**) with unique emissive properties in a solid state (Scheme 1).

**Scheme 1. Synthesis and Properties of TBP**



Chaolumen, M. Murata, Y. Sugano, A. Wakamiya, Y. Murata, *Angew. Chem. Int. Ed.* **2015**, 54, 9308-9312.

In this project, we focus on synthesis and properties of novel molecular nanocarbons containing non-hexagonal rings. The research outcomes are shown below.

Although 5,11-diphenyltetracene can proceed efficient cyclization under the Scholl conditions with an excellent yield, 5,11-dinaphthyltetracene (**2**) afforded an unexpected product **3** with a very low yield of 4%. The X-ray diffraction analysis disclosed that one naphthyl group migrated during the oxidative cyclization. Delightfully, a newly proposed precursor, i.e., 5,12-dinaphthyltetracene (**4**), can readily give **3** with an excellent yield of 90%. The synthesis of the related aromatic compounds with extended  $\pi$ -conjugation motifs is currently ongoing. We believe that this strategy opens a new window for us to explore various molecular nanocarbons containing non-hexagonal rings.

As mentioned in Scheme 1, although the 1,4-adduct of TBP exhibited intriguing emissive properties, the synthesis of TBP is expensive and further functionalization of **1** is rather difficult. During the course of this project, we found that indeno[1,2,3-*cd*]fluoranthene also can undergo the similar 1,4-addition to give dialkylindeno[1,2,3-*cd*]fluoranthene **5**. The X-ray crystallographic analysis revealed that **5** contains an isolated C=C bond, which is expected to be further functionalized toward the synthesis of new optoelectronic materials. Accumulating these findings, we are planning to construct novel nanocarbons such as tubular molecules containing non-hexagonal rings. In this research, all of X-ray crystallographic analysis were performed by Dr. Hashikawa at Institute for Chemical Research, Kyoto University.

# 金属酵素化学モデルの創製と材料・医化学への応用

太田雄大 山口東京理科大学

## 目的

小分子活性化を高効率に行う金属酵素化学モデルを開発し、構造化学的研究と触媒材料または薬剤としての応用に向けた基礎研究を行う。金属ポルフィリン二量体および酸化還元活性なヒドロキノン-N4 配位子からなる新規錯体を合成し、各種研究を行う。

## 実験方法

各種金属ポルフィリン二量体の合成を行い、酸素還元反応と二酸化炭素還元反応について調べた。酸素還元反応では分子触媒とカーボンナノチューブ (CNT) からなる複合体を電極触媒として調製し、回転リングディスク電極を用いて実験した。また分子触媒による二酸化炭素還元反応は、サイクリックボルタンメトリーで分析した。さらに、ヒドロキノン-N4 型の新規配位子からなる各種金属錯体を調製して、抗酸化活性について WST-1 法で評価した。

## 結果と考察

X 線結晶構造解析により各種金属錯体の分子構造を決定した。酸素還元反応の研究では、多核化したポルフィリン錯体において単量体と比べて過電圧の抑制と酸素の四電子還元選択性の向上が見られた。今後さらに CNT 上の修飾密度を上げることで高効率な酸素還元触媒になることが期待される。また、二酸化炭素還元反応において、過電圧および反応速度において単量体と比べて著しく反応性を高めた錯体の合成に成功した。今後、ファラデー効率の見積もりが必要になる。抗酸化活性の評価においては、鉄および銅錯体において高い活性 ( $IC_{50} \sim 2 \mu M$ ) であることを明らかにした。

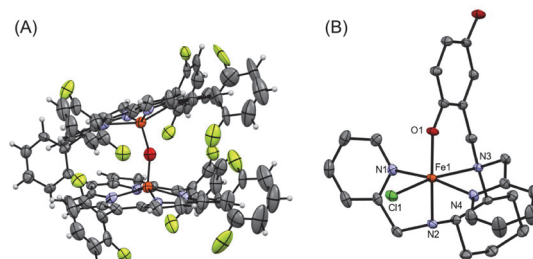


図 1 ポルフィリン二量体(A)とヒドロキノン-N4 錯体(B)

## 学会発表

1. 見鳥茉実, 脇岡正幸, 大木靖弘, Roger E. Cramer, 太田雄大, “亜鉛ポルフィリン二量体による低過電圧での二酸化炭素還元反応”, 日本化学会中国四国大会広島大会 (広島大学, 東広島市), 講演番号: 2B-04, 2022 年 11 月
2. 好川大智, 脇岡正幸, 檜垣達也, 大木靖弘, 太田雄大, “ヒドロキノン-N4 型配位子を含む鉄錯体の合成と反応性”, 日本化学会中国四国支部大会広島大会 (広島大学, 東広島市), 講演番号: 1PA-10, 2022 年 11 月
3. M. Mitori, M. Wakioka, Y. Ohki, R. E. Cramer, and T. Ohta, “Electrocatalytic CO<sub>2</sub> Reduction with a Cofacial Zinc Porphyrin Dimer”, 10th Asian Biological Inorganic Chemistry Conference (Kobe International Conference Center, Kobe), Program No. P-119, Nov 2022.
4. T. Yoshikawa, M. Wakioka, T. Higaki, Y. Ohki, R. E. Cramer, and T. Ohta, “Synthesis, Structure, and Reactivity of Iron(III) Complexes with Hydroquinone-N4 Ligands”, 10th Asian Biological Inorganic Chemistry Conference (Kobe International Conference Center, Kobe), Program No. P-42, Nov 2022.



# Dinitrogen Fixation Based on Nickel→Z-type ( $\sigma$ -Electron Acceptor) Ligand

Hajime Kameo Osaka Metropolitan University

## Purpose

Nickel has been considered unsuitable as a catalyst for the reduction of dinitrogen due to its low nitrogen affinity and low reduction potential. On the other hand, its characteristics

are potentially able to create energy-saving catalysts that work with only a small amount of overvoltage. I considered the possibility that the  $\sigma$ -electron-accepting (Z-type) ligand could enhance the electrophilicity of the Ni center via the Ni→Z bond, facilitating the uptake of dinitrogen (Figure 1). In addition, the flexible Ni→Z bond interaction was expected to induce the multi-electron transfer necessary for the reduction of dinitrogen. Previously, Group 13 element-based multidentate ligand  $1^Z$  (E = B, Al, Ga) was developed, and Ni(0) complexes bearing  $1^Z$  were found to afford rare nickel dinitrogen complex  $2^Z$ . The present study aims to achieve the transformation of dinitrogen using nickel complexes  $2^Z$  under mild reaction conditions as is done by enzymes.

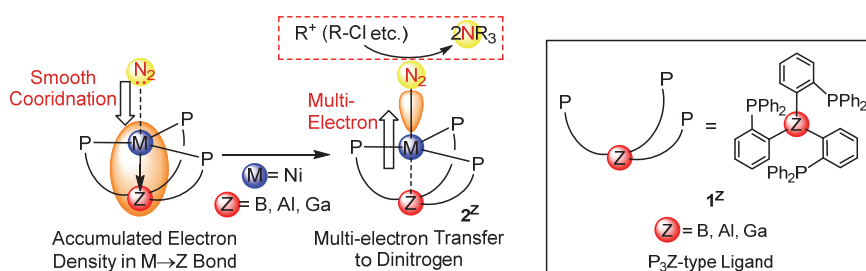


Figure 1  $N_2$  uptake and multi-electron transfer to  $N_2$  ligand.

## Experimental Methods and Results

Cyclic voltammetry measurements were performed on complexes  $2^Z$  for developing the reduction of dinitrogen on the Ni center. A reversible redox wave based on one-electron oxidation Ni(0/I) was observed in  $2^Z$  (Figure 2). Interestingly, the redox waves ( $E_{1/2}$ )

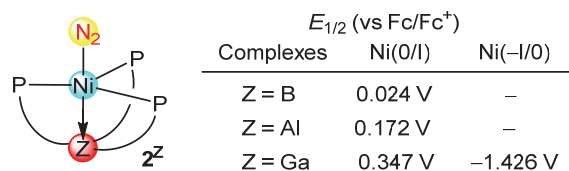


Figure 2 Cyclic Voltammetry of  $2^Z$  (in THF).

shifted to higher potentials in the order  $1^{Al}$  (24 mV) <  $1^{Ga}$  (172 mV) <  $1^B$  (347 mV), suggesting that the borane ligand enhanced the electrophilicity of the Ni center most efficiently. Importantly, a reversible redox wave based on one-electron reduction Ni(-I/0) was also observed in the Ga system ( $2^{Ga}$ : –1426 mV), despite of the Ni(0) states of  $2^{Ga}$ . Although some attempts to isolate the reduction products of  $2^{Ga}$  were unsuccessful at this

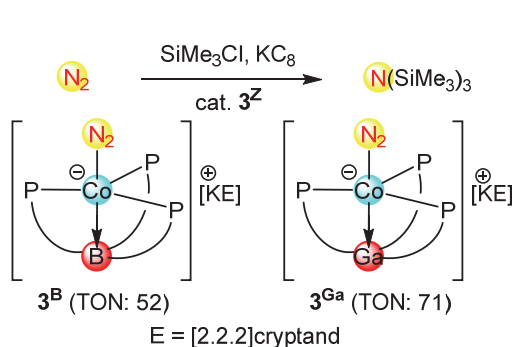


Figure 3 Catalytic silylation of  $N_2$ .

stage, it is worth noting the possibility of the reduction of the  $N_2$  ligand. Also, catalytic dinitrogen silylation was investigated using  $2^Z$  as catalysts, but the reproducibility could not be guaranteed. Hence, Co analogs  $3^Z$  (E = B, Ga) of  $2^Z$  were prepared and employed as catalysts (Figure 3). Here, good catalytic activities were observed (TON: 52 for  $3^B$ , 71 for  $3^{Ga}$ ). Manuscript is in preparation for reporting the results described here.

## キラルシリカの構造と分子認識との相関解明

平井智康 大阪工業大学

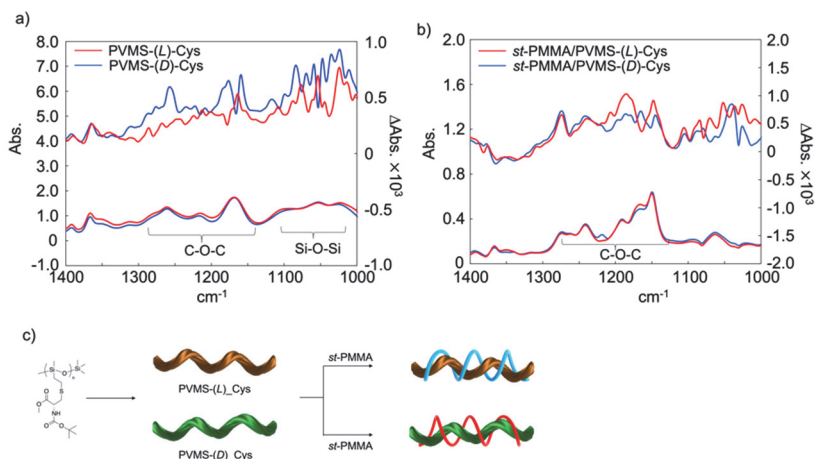
キラルシリカは他の有機物と比較して耐熱性、機械的強度に優れていることから、次世代キラル分離剤としての期待が集まっている。キラルシリカを効率よく調製する手法としてらせん状に配列させたミセルを鋳型としてエトキシシラン誘導体を用いるアプローチが幅広く展開されている。一方、報告者のグループでは、シロキサン含有高分子のらせん構造を制御することで、キラルシリカを調製するアプローチを提案してきた。本年度は線状シロキサンのらせん構造制御に取り組んだ。PDMS を始めとする線状シロキサンの分子鎖凝集構造に関する議論が X 線回折測定法に基づき行われ、数多くのモデルが提唱されている。しかしながら、線状シロキサンの主鎖を一方方向に巻き方向を制御したらせん構造はこれまでに成し遂げられていない。そこで報告者らはビニル基を側鎖に有する線状シロキサン(PVMS)を開環アニオン重合法に基づき調製し、さらに側鎖基として嵩高く、不斉中心を有するシステイン誘導体をエンーチオール反応に基づき導入することで PVMS-Cys を調製した。

Figure 1a は調製した PVMS-Cys 膜の円二色性分光光度計(VCD)測定結果である。1100~1000  $\text{cm}^{-1}$  の Si-O-Si の伸縮振動に帰属されるピーク上において分裂型のコットン効果が観測され、さらに *L* および *D* システインの間において鏡像関係が観測された。この結果より、PVMS 中の線状シロキサン成分は一方方向に巻き方向が制御されたらせん構造を形成していると結論付けた。PVMS-Cys の機能評価を行うために、シンジオタクチック PMMA(*st*-PMMA)と混合した。WAXD および DSC に基づく評価より、PVMS-Cys は *st*-PMMA が形成するらせん空孔内に取り込まれ包摂錯体を形成することを見出した。Figure 1b は包摂錯体の VCD 測定の結果である。*st*-PMMA のエステル基の伸縮振動に帰属される 1300-1150

$\text{cm}^{-1}$  のピーク上において分裂型のコットン効果が観測されており、さらにそのコットン効果は PVMS-Cys の *L* と *D* の間で鏡像関係を示した。この結果は、PVMS-Cys が *st*-PMMA のらせん構造の巻方向を誘起していることを示しているものである(Figure 1c)。

1. Hirai et al., *Chem. Lett.*, **2022**, 51, 781.

2. Hirai et al., *J. Polym. Sci.*, **2022**, 60, 766.

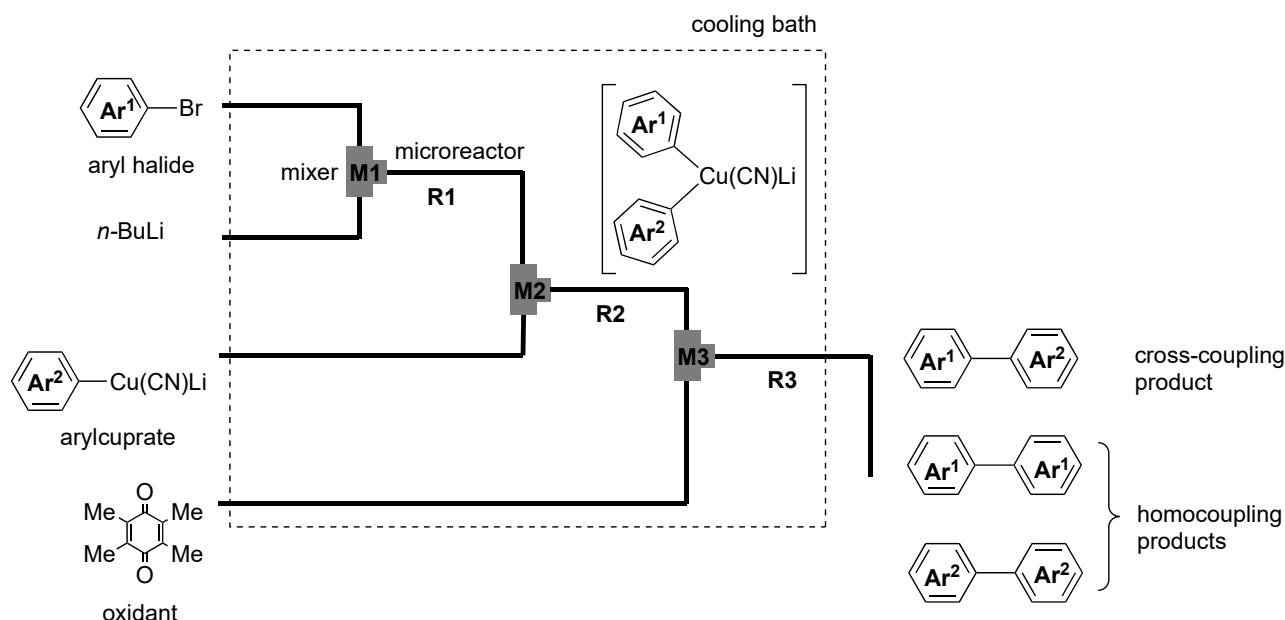


**Figure 1.** VCD spectra of a) PVMS-Cys and b) *st*-PMMA/PVMS-Cys inclusion complex. c) Schematic illustration for this work.

## フロー合成法を用いた官能性ビニルテルリド合成法

永木愛一郎 北海道大学

ビアリールの合成は極めて重要な分子骨格形成反応の一つであるが、様々なクロスカップリング反応がこれまで開発されてきたにも関わらず、立体障害の大きい基質に対しては依然として多くの課題を抱えている。そこで本研究では高反応性活性種を介する炭素-炭素結合形成反応を主軸とする合成化学を展開する共同研究者の協力を得て、熱的に不安定なジアリールクプラート中間体を鍵とする酸化的カップリングにより、立体障害の大きなビアリールを選択的に合成する手法の開発を目指して検討を行った。ただし中間体のクプラートは熱的に極めて不安定であり、通常のバッチ反応条件での制御は困難である。そこで申請者が得意とするフローマイクロリアクターを用いた反応の精密制御によって反応条件をコントロールすることが不可欠である。そこでまず、有機溶媒に可溶性銅塩溶液としてシアニ化銅錯塩を用い、低温で対応するハロゲン化アリールとブチルリチウムから高速混合にてアリールリチウムを発生させ、続いて別途バッチ容器にて発生させたアリールクプラートを反応させることでヘテロジアリールクプラートを発生させ、最後に **quinone** を用いたフロー中での速やかな酸化的カップリング反応により、目的とするヘテロビアリールの生成が確認された。ホモカップリング体の副生は流速などの混合条件の精査と、試薬の当量関係を制御することで抑制される可能性があるため、今後の研究においてさらなるフロー条件の検討で高選択性を得ることを目的として研究を行う予定である。



# 環状ヘキサ-2,7-アントリレンエチニレン誘導体と環状パラフェニレンとのホスト-ゲスト化学に基づく複合化

小林健二 静岡大学

我々は、環状ヘキサ-2,7-(4,5-ジアリール)アントリレンエチニレン誘導体 **1a** の合成に成功し、環状体 **1a** は $\pi$ -スタック自己会合せず、また、**1a** の環の内孔サイズに適合した環状 *p*-フェニレン 9 量体[9]CPP をサイズ特異的に包接することを見出している(図 1)。また、昨年度本申請課題において、**1a** の 6 つのアセチレン結合のうち対角位置の 2 箇所をブタジイン結合で置換した環状体 **2a**、および、**1a** に比べ側鎖の嵩高さが若干小さい環状体 **1b** を合成し(図 1)、単量体として振る舞う **2a** は環内孔サイズ特異的に[10]CPP を包接すること、**1b** は  $\text{CDCl}_3$  中で単量体と $\pi$ -スタック自己会合二量体  $(\mathbf{1b})_2$  の平衡混合物として存在し、**1b** と  $(\mathbf{1b})_2$  共に[9]CPP を包接して 4 つの平衡状態をとることを見出している。今回、**2a** および **1b** のさらなる会合特性を明らかにしたので報告する。

山子先生らは[10]CPP がフラーレン  $\text{C}_{60}$  を包接することを見出している( $\text{C}_{60}@[10]\text{CPP}$  の形成)。今回、 $\text{C}_{60}$  を包接した[10]CPP をさらに環状体 **2a** が包接する二重包接体  $\text{C}_{60}@[10]\text{CPP}@\mathbf{2a}$  の形成を見出した(図 2)。3 者が溶解する 10%  $\text{CDCl}_3$ -90%  $\text{CS}_2$  中 298 K で会合状態を  $^1\text{H}$  NMR にて解析した。 $\text{C}_{60}@[10]\text{CPP}$  の形成の会合定数は  $K_a = 107,000 \text{ M}^{-1}$  と算出された。[10]CPP@**2a** の形成は、 $\text{CDCl}_3$  中  $K_a = 3,170 \text{ M}^{-1}$  に対し、10%  $\text{CDCl}_3$ -90%  $\text{CS}_2$  中では  $K_a = 4,250 \text{ M}^{-1}$  に増加した。10%  $\text{CDCl}_3$ -90%  $\text{CS}_2$  中で  $\text{C}_{60}@[10]\text{CPP}$  の形成を 100% と仮定すると、**2a** と  $\text{C}_{60}@[10]\text{CPP}$  との包接会合定数は  $K_a = 5,590 \text{ M}^{-1}$  と算出され、[10]CPP@**2a** 形成の  $K_a$  より増加することがわかった。また、サイズが適合しないため  $\text{C}_{60}$  を包接できない **2a** は 10%  $\text{CDCl}_3$ -90%  $\text{CS}_2$  中室温にて徐々に  $\text{C}_{60}$  と Diels-Alder 反応するのに対し、二重包接体  $\text{C}_{60}@[10]\text{CPP}@\mathbf{2a}$  は殆ど Diels-Alder 反応を起こさないことがわかった。

環状体 **1b** は  $\text{CDCl}_3$  中で単量体と $\pi$ -スタック自己会合二量体  $(\mathbf{1b})_2$  の平衡混合物として存在する(図 3,  $K_a = 3,560 \text{ M}^{-1}$  in  $\text{CDCl}_3$  at 298 K)。単量体 **1b** と会合二量体  $(\mathbf{1b})_2$  の  $^1\text{H}$  NMR シグナルは平均化せず独立して観測される。今回、環状体 **1b** はシクロヘキサン- $d_{12}$  中で定量的に $\pi$ -スタック自己会合二量体  $(\mathbf{1b})_2$  を形成することを見出した。 $\text{CDCl}_3$ -*c*- $\text{C}_6\text{D}_{12}$  混合溶媒中 *c*- $\text{C}_6\text{D}_{12}$  の割合が増加するに連れて  $(\mathbf{1b})_2$  形成の  $K_a$  は増加し( $K_a = 8,360 \text{ M}^{-1}$  in 10% *c*- $\text{C}_6\text{D}_{12}$ ,  $K_a = 63,300 \text{ M}^{-1}$  in 30% *c*- $\text{C}_6\text{D}_{12}$ )、50% *c*- $\text{C}_6\text{D}_{12}$  中では  $(\mathbf{1b})_2$  の  $^1\text{H}$  NMR シグナルのみが観測された。また、318 K における  $(\mathbf{1b})_2$  の[9]CPP 包接は  $\text{CDCl}_3$  中  $K_a = 9,440 \text{ M}^{-1}$  に対し、70% *c*- $\text{C}_6\text{D}_{12}$  中では  $K_a = 13,200 \text{ M}^{-1}$  に増加することがわかった。

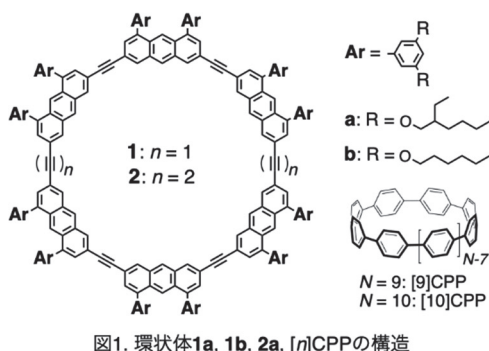


図1. 環状体**1a**, **1b**, **2a**, [n]CPPの構造

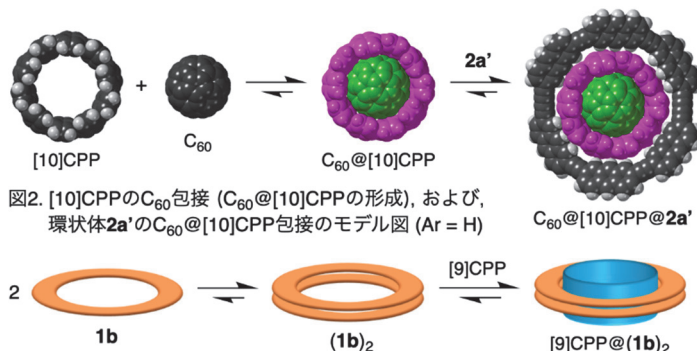


図2. [10]CPPの $\text{C}_{60}$ 包接 ( $\text{C}_{60}@[10]\text{CPP}$ の形成)、および、環状体**2a**の $\text{C}_{60}@[10]\text{CPP}$ 包接のモデル図 (Ar = H)

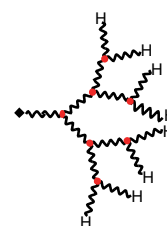


図3. 環状体**1b**の会合二量体  $(\mathbf{1b})_2$  の形成と、 $(\mathbf{1b})_2$  の[9]CPP包接の模式図

## 超分岐構造高分子の滑剤作用の解明と最適化

高橋裕 東北大学

【目的】一般的に潤滑油の特性を表すストライベック曲線は、その摩擦係数と粘度、速度、荷重の関係で示される。ストライベック曲線の流体潤滑において、低粘度油を用いることは摩擦を低減させることができる。しかしながら、低粘度油では境界潤滑において摩擦を増加させる。潤滑油の添加剤として超分岐構造高分子 (**Fig. 1**) を用いることは、摩擦増加の抑制が期待される。そこで本研究では、潤滑油の基油に対する添加剤としての超分岐構造高分子の摩擦特性を明らかにすることを目的とした。



**Fig. 1** 超分岐構造高分子の模式図

【方法】超分岐構造高分子は制御されたラジカル重合によって合成された (共同研究者の登阪准教授の担当)。潤滑基油として PAO401 を用いた。潤滑油の摩擦評価は、種々の回転速度 ( $V$ ) および荷重 ( $L$ ) の条件でボールオンディスク法による摩擦試験機によって行った。

【結果】合成した超分岐構造高分子の PAO401 に対する溶解性を紫外可視分光光度計を用いて評価した。超分岐構造高分子は、室温では溶解しなかったが、40 °C以上で完全に溶解した。

**Fig. 2** は、40 °Cにおける超分岐構造高分子を溶解させた潤滑油の摩擦試験の結果を示している。超分岐構造高分子の潤滑油の摩擦係数は、ストライベック曲線の流体潤滑 ( $300 < V/L < 3,000$ ) 領域において、基油である PAO401 とほとんど同じであった。流体潤滑における摩擦係数は溶液粘度に依存するため、超分岐構造高分子の潤滑油の溶液粘度は PAO401 とほぼ同じであることが分かった。この結果は、超微量粘度計による粘度測定結果とよく一致していた。一方で、境界潤滑 ( $0.003 < V/L < 0.03$ ) における摩擦係数は、超分岐構造高分子の添加により著しく減少した。このことから、本研究でのマクロスケールにおける摩擦試験は、超分岐構造高分子が高い潤滑性を有していることを示す。また、この結果はこれまでに検討してきたナノスケールにおける共振ずり測定の結果とよく一致していた。

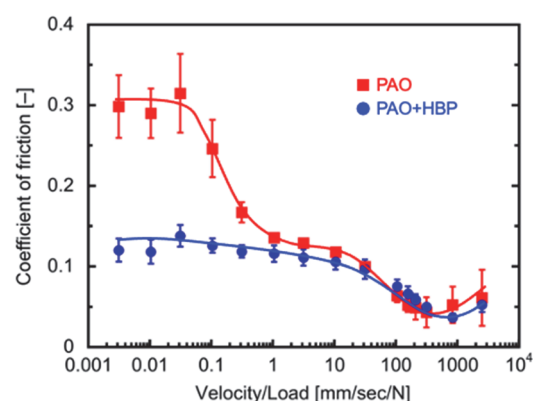


**Fig. 2** PAO401 と超分岐構造高分子 (HBP) の潤滑油のストライベック曲線。

【学会発表】 Y. Takahashi, M. Mizukami, Y. He, M. Tosaka, S. Yamago, K. Kurihara, 71st SPSJ Annual Meeting, 3J07.



# Synthesis of Highly Strained Macrocyclic $\pi$ -Conjugated Molecules via a Multinuclear Au(I)-Pt(II) complex

Yoshitaka Tsuchido Tokyo University of Science

$[n]$ Cycloparaphenylenes ( $[n]$ CPPs, where  $n$  is the number of phenylene groups), consisting of 1,4-linked phenylene unit, are macrocyclic organic molecules, which have attracted much attention due to their unique  $\pi$ -conjugated structures and physical properties. We have developed a new CPP synthesis method *via* a macrocyclic gold complex and have succeeded in synthesizing  $[n]$ CPPs containing phenylene groups with multiples of three ( $n = 6, 9, 12, 15$ ) within short reaction steps and in high yields. A notable feature of this method is that the formation of macrocyclic gold complexes, proceeds with extremely high efficiency. We found from our kinetic experiments with acyclic dinuclear gold biaryl complexes that the Au-C bonds are exchanged rapidly between the complexes, thus causing the macrocyclization to proceed efficiently. In this study, we developed a new CPP synthesis method utilizing the Au-C bonds, a new dynamic covalent bond that we discovered. Mixing two macrocyclic gold complexes with terphenylene or quarterphenylene linkers at 50 °C, followed by the reductive elimination upon addition of  $\text{PhI}(\text{Cl})_2$ , resulted in the selective formation of four  $[n]$ CPPs ( $n = 9, 10, 11$ , and 12) (Figure 1a). The presence of the gold complexes bearing two different phenylene linkers were experimentally confirmed by Fourier transform ion cyclotron resonance (FT-ICR) MALDI-TOF MS measurement of the crude products after mixing at 50 °C (Figure 1b). These results indicate that macrocyclic gold complexes are reorganized by intermolecular Au-C bond exchanges. This synthetic method is applicable not only to oligophenylene linkers but also to various arylene linkers containing such as fused aromatic rings, and various nanohoops have also been successfully synthesized.

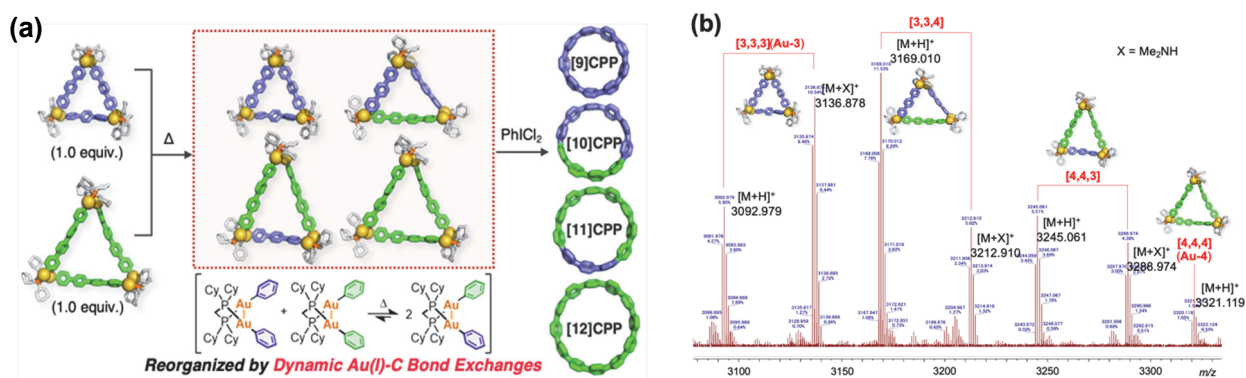


**Figure 1.** (a) Synthesis of  $[n]$ CPPs ( $n = 9, 10, 11$ , and 12) via reorganization of macrocyclic Au complexes. (b) FT-ICR MALDI-TOF MS spectrum of the reaction mixture of two different complexes after mixing at 50 °C.

## 【成果報告】

[1] Y. Yoshigoe, Y. Tanji, Y. Hata, K. Osakada, S. Saito, E. Kayahara, S. Yamago, Y. Tsuchido, H. Kawai, *JACS Au* **2022**, 2, 1857–1868.

[2] 丹治洋平, 畑優成, 吉越裕介, 斎藤慎一, 茅原栄一, 山子茂, 小坂田耕太郎, 土戸良高, 河合英敏, 第 32 回基礎有機化学討論会, 2021 年 9 月 22 日, 3A05.

[3] 平田沙弥, 森隆博, 茅原栄一, 土戸良高, 河合英敏, 山子茂, 第 32 回基礎有機化学討論会, 2021 年 9 月 22 日, 3A06.

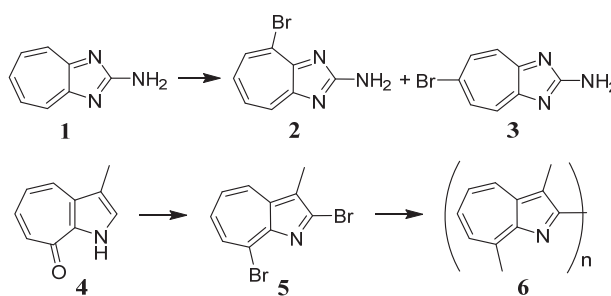
## 有機電子材料を指向したアザズレン 3 量体の合成と応用

黒飛敬 久留米工業高等専門学校

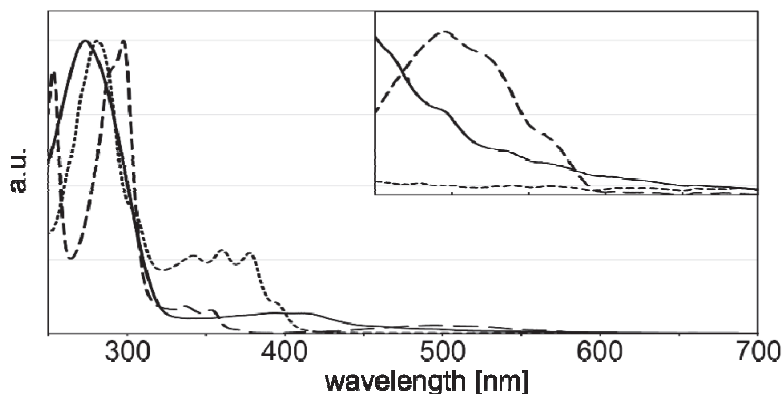
今日、 $\pi$  共役系分子がもつ様々な機能は有機電子材料や医薬品などに広く応用されており、新たな機能性分子を探索する意義は大きい。青色の天然色素であるアズレンはナフタレンの構造異性体であるが、その物性は極めて特異的である。例えば、アズレンは  $1.0\text{ D}$  の双極子モーメントを持ち、 $S_2$  発光を示し、アズレンの最長波長部の吸収末端は  $700\text{ nm}$  に及ぶ。そこで、我々は新たな  $\pi$  共役系創出の基本分子としてこのアズレンユニットを用いた機能性分子の設計を試みている。また、近年、我々はアズレン類（含窒素複素環を含む）のオリゴマー合成について幾つかの有効な知見を得ている。これら一連の合成法の研究は、アズレン類特有の反応性の活用方法を開拓することによって進められてきた。一方、国内でも直線形のターアズレンの有機電子デバイスへの応用などの報告があり、アズレンの電子材料への応用も徐々に注目されつつある。本研究では、有機電子材料への応用を目指し、アズレンの 5 員環部へ窒素原子を導入した 1-アザアズレンおよび 1,3-ジアザアズレン誘導体の直線型ならびに環状型のオリゴマーとして 3 量体合成を検討したので報告する。

実験方法は、まず直線型オリゴマーの原料として 1,3-ジアザアズレンの 2,6-ジハロゲン体の合成方法の検討および環状型オリゴマーの原料として 3-アルキル-1-アザアズレンの 2,8-ジハロゲン体の合成方法の検討をそれぞれ行なった。その後、いくつかのカップリング反応の条件を検討した。

1,3-ジアザアズレンのハロゲン化については種々の臭素化試薬によって 2-アミノ体 **1** に対する直接の臭素化を試みた。その結果、NBS を用いることでアミノ基の誘起効果による 4,6 位の位置選択的臭素化が進行し、6-ブロモ体 **3** が収率 23% で得られた。しかし、その溶解性



は非常に低く、次のステップであるアミノ基の官能基変換およびカップリング反応の進行が困難であった。一方、3-アルキル-1-アザアズレンの 2,8-ジハロゲン体の合成については、アルキル基について種々検討した結果、今回、メチル基を導入した誘導体で 2,8-ジブロモ体 **5** に成功した。これは環状オリゴマーの安定性と溶解性について検討した結果である。続く  $\text{Ni}(\text{cod})$  を用いたカップリング反応によるオリゴマー合成では酢酸亜鉛を共存させることでテンプレート効果を試みた結果、オリゴマー **6** が得られた。マスマスペクトル及び吸収スペクトルより環状 3 量体の他に多数のオリゴマーとの混合物であり、更なる精査を検討する予定である。

Figure 1. UV-Vis スペクトル (..... **4**, --- **5**, — **6**)



# Development of Organometallic n-Type Materials with High Electrical Conductivity

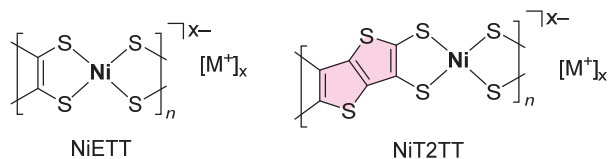
Michihisa Murata   Osaka Institute of Technology

## Introduction

n-Type semiconducting films are indispensable in organic (opto)electronic devices. The synthesis of solution-processable n-type organic materials has been attracting growing interest for quite some time, whereby a recent focus has been placed on their application in flexible thermoelectric generators, which can convert waste heat into electricity. However, n-type solution-processed films based on organic materials have exhibited serious issues associated with their instability toward atmospheric oxidation and their low electrical conductivity (generally  $< 10 \text{ S cm}^{-1}$ ). Recently, Guo and Facchetti have reported very high conductivity in an n-type semiconducting polymer ( $> 100 \text{ S cm}^{-1}$  under  $\text{N}_2$ ) by developing a transition-metal-catalyzed n-doping process.<sup>1</sup>

## Results and Discussion

In this study, we have designed a concise synthetic route to the n-type nickel coordination complex NiT2TT, which contains a thieno[3,2-*b*]thiophene unit in the ligand. An air-stable n-type composite



film of NiT2TT and PVDF fabricated using a solution process revealed excellent electrical conductivity ( $> 200 \text{ S cm}^{-1}$ ), which is, to the best of our knowledge, the highest value hitherto reported for solution-processed n-type films of organic or organometallic compounds and polymers.<sup>2,3</sup> A grazing-incidence wide-angle X-ray diffraction (GIWAXD) analysis of the NiT2TT/PVDF film revealed, for the first time, that the orientation of the nickel coordination complexes in such films can be controlled by the molecular design of the  $\pi$ -conjugated ligand. In these films, NiT2TT exhibits a  $\pi$ -stacked structure in predominantly the in-plane direction (edge-on), which stands in contrast to the standard NiETT, in which the  $\pi$ -stacking occurs mainly in the vertical direction (face-on) along the film. The edge-on orientation of NiT2TT should contribute to the enhanced conductivity and reasonable n-type thermoelectric properties in the in-plane direction.

## References:

- 1) H. Guo, C.-Y. Yang, X. Zhang, A. Motta, K. Feng, Y. Xia, Y. Shi, Z. Wu, K. Yang, J. Chen, Q. Liao, Y. Tang, H. Sun, H. Y. Woo, S. Fabiano, A. Facchetti, X. Guo, *Nature* **2021**, 599, 67–73.
- 2) K. Ueda, Y. Yamada, T. Terao, K. Manabe, T. Hirai, Y. Asaumi, S. Fujii, S. Kawano, M. Muraoka, M. Murata, *J. Mater. Chem. A* **2020**, 8, 12319–12322.
- 3) K. Ueda, R. Fukuzaki, T. Ito, N. Toyama, M. Muraoka, T. Terao, K. Manabe, T. Hirai, C.-J. Wu, S.-C. Chuang, S. Kawano, M. Murata, *J. Am. Chem. Soc.* **2022**, 144, 18744–18749.

## 未踏超不安定構造の単離および物性解明による 新概念材料設計指針の創出

上野裕 東北大学

【目的】分子が定常的に存在するには、それぞれの物質固有の安定性を揺るがす “刺激” がない環境に置かれている必要がある。極めて安定性の低い分子・構造体は、大気下室温どころか、それ以上に温和な条件でも容易に反応・分解し、そのため、物性や物性の起源となる構造情報などの基礎的な性質を解明することすら困難である。本研究では、有機合成、およびプラズマを用いたフラーレン内部への原子・分子挿入法を段階的に併用することで、超不活性空間として知られるフラーレン内部における未踏不安定化学種のその場構築によって構造・物性を定常化させ、未知の構造・物性相関を発見・理解・応用することを目的とした。

【実験手法】村田（ICR）らにより報告された有機合成による水分子挿入法、および代表者らが研究対象とするプラズマを用いたフラーレンへのイオン挿入法を段階的に駆使することで、『一分子の水で水和されたリチウムイオン』を内包した  $C_{60}(Li^+ \cdot H_2O@C_{60})$  の合成を試みた。得られた試料をイオン交換カラムクロマトグラフィーおよび電解質添加 HPLC により精製し、NMR および X 線構造解析による構造解析を実施した。

【結果・考察】各種 NMR スペクトルを **Figure 1** に示した。 $^7Li$  NMR スペクトルでは、 $-7.8$  ppm 付近にトリプレットシグナルが見られ、これは水分子の二つのプロトンとのカップリングによる分裂に帰属される。また、 $^1H$  NMR スペクトルでは、 $-2.1$  ppm 付近にシグナルが観測され、 $^7Li$  の核スピンの ( $3/2$ ) により 4 本に分裂している。これらのシグナルは、デカップリング測定によりシングレットシグナルとなったことから、 $Li^+$  と  $H_2O$  の相関によるものと結論された。NMR によって  $^7Li$  と  $^1H$  のカップリングが明確に観測された例は少なく、隔離空間に閉じ込められることで相関が観測された例として重要な成果となった。単結晶 X 線構造解析についても実施済みであり、目的化合物の完全構造同定を達成している。本研究により、有機合成による  $C_{60}$  内部への

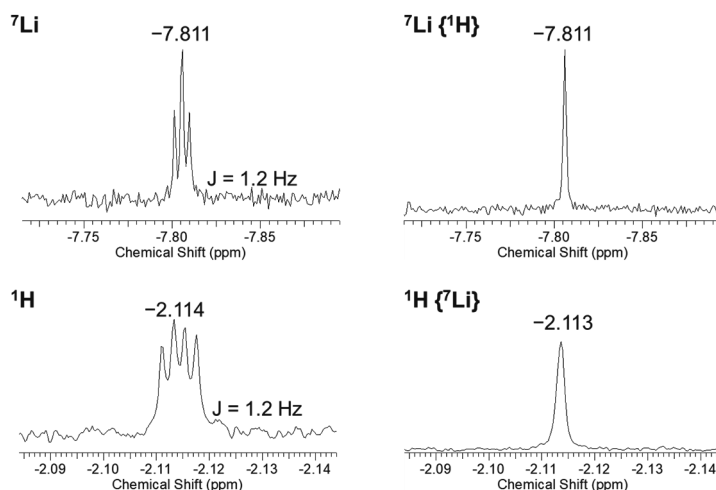


**Figure 1.**  $^7Li$ ,  $^1H$ ,  $^7Li\{^1H\}$  and  $^1H\{^7Li\}$  NMR spectra of the purified product in  $CD_2Cl_2$  at RT.  $LiCl/D_2O$  (0 ppm) was used as an external standard for  $^7Li$  NMR measurements.a

の小分子配置、およびこれに続くプラズマによるイオン挿入反応によって  $C_{60}$  内部における不安定化学種のその場構築が可能であることを実証した。今後、得られた化合物の物性評価や、当該手法を活用した新規分子の合成について継続的に実験を推進し、未踏不安定化学種の物性を活用した新しい材料科学を発展させていく。

## Non-linear viscoelasticity of unentangled polymers

Giovanni Ianniruberto   Università degli Studi di Napoli “Federico II”

While extensive studies reveal that the *linear* rheological properties of unentangled polymers can be well reproduced by the Rouse model, there are still lots of unsettled problems on *nonlinear* rheological properties. In the Rouse model, a polymer chain is modeled by consecutive beads connected by Hookean springs. To reproduce the unentangled polymer dynamics, this model considers three forces, i.e., the spring, frictional, and Brownian forces. We can naively expect that the Rouse model can be used to predict the nonlinear rheological properties. However, by construction, this model does not exhibit any nonlinear viscoelastic behavior such as viscosity thinning under shear flow. Thus, several nonlinear rheological models based on the Rouse model have been proposed. For example, if the Hookean spring considered in the original Rouse model is replaced with the finitely extensible nonlinear spring, the modified model predicts shear-rate dependent viscosities, which is in qualitative agreement with experimental observations. Nevertheless, there are still several discrepancies between existing theories and experimental results, especially under extensional flow.

In this research project, we planned to develop a molecular-based model for *nonlinear* rheological properties of unentangled polymers under both shear and extensional flow. For such a purpose, it might be required to consider nonlinear factors that characterize the above three forces in the Rouse model. The team members have been separately developing mesoscopic models and attained success to reproduce (some) rheological properties. For example, GI developed a Brownian dynamics (BD) simulation method for the nonlinear rheology of unentangled polymers and considered the change of monomeric friction accompanied by segmental orientation [1]. TS and his group members at the ICR have formulated the nonlinear effects associated with the above three forces [2].

Our group and the molecular rheology group at the ICR independently conducted the research activity while sharing information via several online meetings this year. We have discussed the BD simulation method with the effects of the finite extensibility, the friction reduction, and the Brownian force intensity variation. While it is possible to develop a simulation code at the BD level, the difficulty lies in how to validate the simulation results. Currently, the molecular rheology group is conducting combined rheological and dielectric measurements to provide the detailed dynamical properties of unentangled polymers. Moreover, TS has started molecular dynamics simulations to obtain microscopic structures under flow. In the future, we hope to unify these experimental and numerical results for a further understanding of the rheology of unentangled and even entangled polymers.

### References:

- [1] G. Ianniruberto and G. Marrucci, *Macromolecules*, **53**, 1338 (2020).
- [2] T. Sato, Y. Kwon, Y. Matsumiya, and H. Watanabe, *Phys. Fluids*, **33**, 063106 (2021).

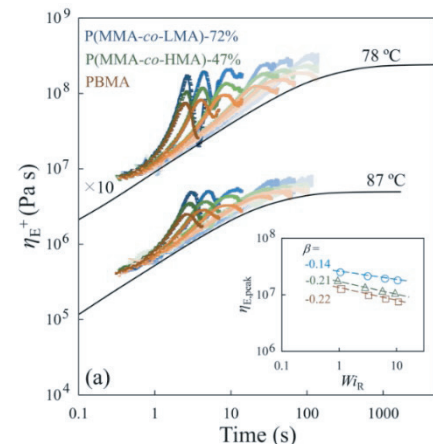
# Nonlinear Extensional Rheology of Entangled Poly(n-alkyl methacrylate) Melts with Fixed Number of Entanglements and Kuhn Segments per Chain

Shilong Wu Chinese Academy of Sciences

Understanding of the non-linear rheology of polymer melts is essential in optimizing their processing conditions, particularly in fiber spinning and membrane blowing processes where elongational flow is dominant. Although structure and dynamics of polymer melts have been extensively studied in the past half century, studies of their nonlinear rheological behavior, in particular the elongational behavior under fast flow, are still quite limited. Thus, we have collaborated with Profs. Watanabe, with a support from the *collaborative research program of ICR, Kyoto University* in 2022 (Grant No. 2022-51), to examine characteristic elongational features of polymer melts.

In this study, we investigated the effect(s) of side chain length distribution on the transient elongational hardening behavior of polymer melts. For either entangled or unentangled system, we successfully prepared three polymers, poly(butyl methacrylate), poly(methyl methacrylate-*co*-hexyl methacrylate), and poly(methyl methacrylate-*co*-lauryl methacrylate), abbreviated as PBMA, P(MMA-*co*-HMA), and P(MMA-*co*-LMA). These samples exhibited a similarity of their linear viscoelastic behavior.

For nonlinear extensional rheology, as shown in Figure right, the transient strain hardening is enhanced on an increase of the side chain length distribution. Those differences are most clearly noted in the top panel of Fig. 3, where  $\eta_E^+$  is directly compared for the three samples (Vader 1000). namely, in the order of PBMA < P(MMA-*co*-HMA) < P(MMA-*co*-LMA): The side chain would have behaved as a “solvent” to weaken the frictional reduction and enhance the hardening. For PBMA, the short monodisperse side chains as a whole always stay near the backbone, thus they should exhibit a stronger orientational correlation with the backbone thereby suppressing the strain hardening. In contrast, for P(MMA-*co*-HMA) and P(MMA-*co*-LMA), the outer part of the long side chains is located far away from the backbone and would have a rather isotropic conformation not correlated with the backbone. For this case, the outer part of the side chains should behave as the solvent to enhance the hardening, in particular for P(MMA-*co*-LMA) having the largest fraction of that part.



**Shilong Wu**, Hiroshi Watanabe, Quan Chen, Side-Chain Length Distribution Promotes Transient Elongational Hardening of Polymer Melts, *Physical Review Letters*, under review.

## Trace metal elemental and isotopic composition in the North Pacific Ocean: sources and internal cycling (3)

Tung-Yuan Ho Academia Sinica

### **Objectives:**

The major objective of this extended joint study is to investigate the sources and internal cycling of dissolved and particulate trace metals in the water column of the Northwestern and subarctic Pacific Ocean and to evaluate the impacts of lithogenic and anthropogenic aerosols on the cycling processes. Prof. Yoshiki Sohrin is my host at ICR, Kyoto University.

### **Methods:**

We have joined two Japanese GEOTRACES cruises, KH11-7 and KH15-3, with Prof. Yoshiki Sohrin's and other Japanese research groups in the subarctic North Pacific Ocean. We have collected seawater and particulate samples in the oceanic regions during the cruises. Both dissolved and suspended particulate samples were collected for trace metal elemental and isotopic composition analysis. Elemental and isotopic composition of trace metals have been determined by my Ph.D. students (W.-H. Liao and C.-C. Hsieh) by using HR-ICPMS and MC-ICPMS. The detailed information of the sampling and pretreatment are described in our previous two published papers.

### **Result and Discussions:**

The details of the results and discussions are under preparation. Chih-Chiang Hsieh, my current Ph.D. student, has finished the measurement of Fe isotopic composition in the samples and is writing the manuscript. We found that the quantitative contribution of lithogenic aerosols still play a dominant role for the deposition fluxes of dissolvable aerosol Fe in the studied region due to their high mass fraction and deposition rates (Hsieh et al. in prep).

### **Publications:**

In spite of the limitation of Covid-19 pandemics on in person visit, Prof. Sohrin's and my laboratory members have still kept close interaction in the research topics proposed. In 2022, we have published a paper in *Marine Chemistry*. Two other collaborative papers are under preparation. I am also deeply honored to receive the 2022 Oceanochemistry Award, partially attributed to my close collaboration with many renowned Japanese chemical oceanographers.

Takano, S., W.-H. Liao, **T.-Y. Ho**, and **Y. Sohrin** (2022) Isotopic evolution of dissolved Ni, Cu, and Zn along the Kuroshio through the East China Sea. *Marine Chemistry* doi.org/10.1016/j.marchem.2022.104135.

**Ho, T.-Y.** (2022) Multidisciplinary study of trace metal biogeochemistry in the ocean. *Transactions of The Research Institute of Oceanochemistry* 35:2, 85-98.

## Resolving the structure-dynamics-property relationship in polymer nanocomposites under uniaxial stretching-II

Tadanori Koga Stony Brook University

**Objective.** The addition of nanoparticles (NPs) to a polymer matrix is a simple route to improving the mechanical property and designing next-generation polymer nanocomposites (PNCs). The key role in this phenomenon is ascribed to polymer chains (physically) adsorbed on the NP surface (“bound polymer”) that act as *tight* polymer-mediated bridges between neighboring NPs at high NP loadings above the percolation threshold, leading to a network-like microstructure that reinforces the PNCs. However, a comprehensive understanding of the complex role of polymer bridges in reinforcement under deformation remains unsolved due to the lack of experimental tools capable of providing structural and dynamic information at the relevant length and time scales. Here we tackle the challenge to probe the collective motions of NPs associated with bridging network formation under oscillatory tensile deformation using speckle echo X-ray photon correlation spectroscopy (XPCS).

**Experimental.** The so-called *speckle echo* XPCS technique under oscillatory shear allows us to capture the irreversible nanoscopic rearrangements of NPs associated with the yielding of a material<sup>1</sup>. Calcium carbonate (the size of 30 nm, the filler loading ( $x$ ) = 20%, which is above the gel point ( $x_c \approx 16$  vol%)) filled cross-linked silicone elastomer was used. XPCS probes the dynamics over a wide range of timescales ( $10^{-3} < t < 10^3$  seconds that is commensurate with the time window for rheology). When the structure and corresponding dynamics of NPs change (“out-of-equilibrium”) on the time scale of experiments, a one-time correlation function,  $g_2$ , which describes the equilibrium dynamics of NPs, does not correctly describe such a phenomenon. Therefore, a two-time correlation function is necessary, which defines the intensity-intensity autocorrelation for any respective times  $t_1$  and  $t_2$  in the time series. The details have been described elsewhere.<sup>2</sup> The samples were subjected to oscillatory tensile deformation at room temperature.

**Results.** We captured speckle patterns and compared them at a given strain amplitude and oscillation frequency (Fig. 1a) from which  $g_2$  was determined in the directions parallel and perpendicular to the stretching direction.  $g_2$  displays periodic peaks corresponding to “echoes” in the speckle patterns (Fig. 1b). The change in strain between extrema leads to gradients in the particle displacements that significantly alter the speckle pattern even for modest strain values. Thus,  $g_2 \approx 1$  at  $t = (n + 1/2)T$  (Fig. 1b), where  $n$  is an integer (periods of oscillation), and  $T$  is a repeat time for the strain ( $\sim 15$  s for the test). On the other hand, at  $t = nT$ , the strain returns, and the speckle pattern is recovered, causing  $g_2$  to increase above one (Fig. 1b). If the deformation is linear and reversible, echoes follow the equilibrium static dynamics (indicated by the dotted line in Fig. 1b). Instead, if the deformation is not linear, echoes peaks are reduced (Fig. 1c). This attenuation provides a measure of the “nanoscopic” irreversibility of filler rearrangements. Hence, the results clearly indicate that deformation plays no role in the decorrelation at this strain amplitude, while the significant irreversible rearrangements of NPs occur in the parallel direction even when the macroscopic response is still in the linear response regime. The XPCS data will be correlated with the macroscopic mechanical properties which will be measured ex-situ by using a rheometer. These studies will shed light on a connection between nano-irreversibility and macroscopic nonlinear deformation, ultimately allowing us to establish the microscopic criteria for measuring the degree of internal material failure non-destructively.

### References

1. Rogers, M. C.; Chen, K.; Andrzejewski, L.; Narayanan, S.; Ramakrishnan, S.; Leheny, R. L.; Harden, J. L., Echoes in x-ray speckles track nanometer-scale plastic events in colloidal gels under shear, *Phys. Rev. E*, 90, 062310, 2014.
2. Yavitt, B. M.; Wiegart, L.; Salatto, D.; Huang, Z.; Endoh, M. K.; Poeller, S.; Petrash, S.; Koga, T., Structural dynamics in UV curable resins resolved by in situ 3D printing X-ray photon correlation spectroscopy, *ACS Appl. Polym. Mater.*, 2, 4096-4108, 2020.

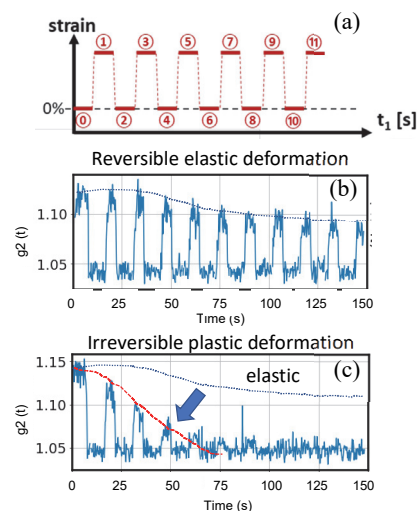


**Fig. 1.** (a) Schematic of a strain profile using the tensile stage. The strain is ramped back and forth between 0% and a given value and held constant at each extreme for about 5s during which an X-ray exposure was obtained. Representative echoes in the  $g_2$  functions for cross-linked calcium carbonate filled silicone measured at room temperature are shown: (b) in the vertical direction and (c) in the parallel direction during application of quasi-oscillatory strain with  $\gamma=0.5\%$  at  $q = 0.023 \text{ nm}^{-1}$ . The degree of the correlation of echoes reflects how similar the nanoscale structure is between two strain plateaus (e.g., strain plateaus (“0” and “2”) and (“0” and “4”) shown in (b) and “0” corresponding to the initial state of the sample).



## High Frequency Response of Polymeric Liquids: Rheology and Dielectric Relaxation

Sathish K. Sukumaran Yamagata University

Experiments performed under isothermal conditions are typically used to investigate the response of polymeric liquids to imposed fields. Needless to add, the interpretation of the experimental results relies on the assumption that the system temperature is not altered by the imposed field and remains uniform throughout the system. Therefore, the isothermal response functions are appropriate descriptor for any quantitative analysis of the system. However, if the experimental time scale is shorter than the thermal equilibration time scale, the assumptions of constant and uniform temperature are likely to become invalid. An experimentally relevant case is the response at high frequencies/short times where, adiabatic response functions might be more appropriate. To investigate this, the theoretical and experimental expertise of ICR (Sato), and the computational, theoretical and experimental expertise of international (Chen, Watanabe; Changchun) and domestic (Masubuchi; Nagoya) researchers were combined to form a collaboration between ICR and several international and domestic research partners.

The effect of imposing isothermal and adiabatic conditions on the linear dynamics and viscoelasticity of an unentangled polymer melt was investigated. The polymer chains were modelled as Lennard-Jones beads connected by finitely extensible nonlinear elastic springs and the motion of the beads were simulated using molecular dynamics (Kremer-Grest model). Isothermal conditions (NVT ensemble) were simulated by using a Langevin thermostat to control and maintain the temperature. In the adiabatic simulations, the system was decoupled from the thermostat thereby preventing energy exchange and thermal equilibration. Oscillatory shear deformation of sufficiently small amplitude (linear regime) was imposed at several frequencies and the storage modulus,  $G'$ , and the loss modulus,  $G''$ , were determined. Negligible difference was found between the isothermal and the adiabatic  $G'$  and  $G''$ . This implied that, at least in the linear regime investigated here, the imposed conditions had negligible effect on the relaxation times or equivalently, the dynamics of the polymer chains. Under adiabatic conditions however, the system temperature progressively increased with time and the temperature increase under high frequency oscillatory shear deformation was significantly larger than under low frequencies. Needless to add, the increase in temperature under adiabatic conditions cannot be sustained indefinitely without affecting both the state of the system and its response to the external field and therefore, clearly unphysical. We are currently investigating the response when the shear (oscillatory and step) is applied for longer times. Based on these results, we plan to investigate the more interesting but significantly more difficult nonlinear response regime in the future.



## Control of Mechanical Properties in Polymer Blend Materials by Hydrogen Bonding Interaction

Osamu Urakawa Osaka University

It has long been known that introducing specific attractive interactions, such as hydrogen bonding, into a compatible polymer blend can enhance its thermal and mechanical properties<sup>1</sup>. However, the quantitative relationship between the strength of the interaction and the rheological properties has not yet been established especially for the entangled systems. In this study we examined rheological behaviors for miscible polymer blends, poly(2-vinyl pyridine) / poly(4-vinyl phenol) (2VPy/VPh), in which intermolecular hydrogen bonds play an important role<sup>2</sup>. The molecular weight of the 2VPy (2VPy182) was  $M_w=1.82 \times 10^5$ , higher than the entanglement-molecular-weight  $M_e$ , while those of VPhs were  $M_w=1.9 \times 10^3$  (VPh2) and  $M_w=4.5 \times 10^3$  (VPh5), both lower than  $M_e$ . In the mixture of 2VPy/VPh, only the 2VPy chains entangle each other, and the low molecular weight VPh can be regarded as a diluent.

We found that the time-temperature superposition principle approximately holds, and composite curves of the complex moduli could be constructed. WLF equation with a single parameter set ( $c_1$  and  $c_2$ ) could represent their shift factors by setting the reference temperatures  $T_r^*$  to be  $T_g+64^\circ\text{C}$ , where  $T_g$  is the glass transition temperature of each blend. Figure 1 shows the composite curves of storage moduli  $G'$  at  $T_r^*$  for 2VPy182/VPh5 blends with several compositions. The rubbery plateau modulus  $G_N$  observed in the frequency between  $10^{-1} \text{ s}^{-1}$  and  $10^2 \text{ s}^{-1}$  decreased with decreasing the 2VPy concentration (the weight fraction  $w_{2VPy} \sim$  volume fraction  $\phi$  was varied from 1 to 0), according to the following relationship:  $G_N \sim w_{2VPy}^2$ . This means that the entanglement density decreases simply by the dilution effect, even though hydrogen bonds between VPh and 2VPy exist. Contrary, the zero shear viscosity  $\eta_0$  and the cross point relaxation time  $\tau_x$  (determined from the frequency at which  $G' = G''$ ) show weaker concentration dependence than polymer / diluent systems. As shown in Figure 2, the following relations were confirmed:  $\eta_0 \sim w_{2VPy}^{1.8}$  and  $\tau_x \sim w_{2VPy}^{0.53}$ . These exponents are smaller than the ordinary solution values<sup>3</sup>:  $\eta_0 \sim \phi^{3.6}$  and  $\tau \sim \phi^{1.3}$ , suggesting that the terminal flow of the 2VPy/VPh blends is affected by the hydrogen-bonded associates.

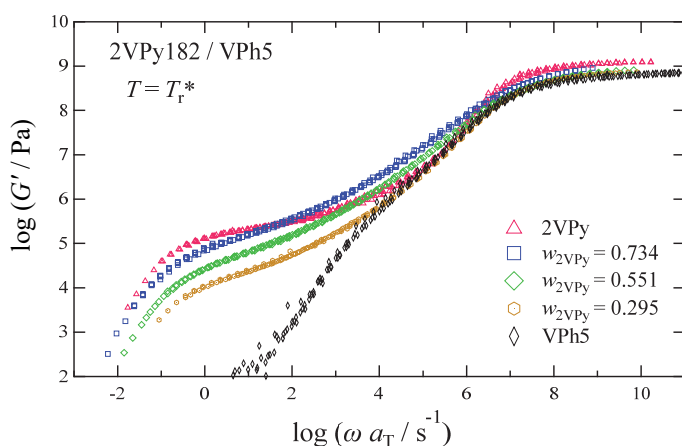


Figure 1 Composite curves of  $G'$  for 2VPy182 blends with several compositions.

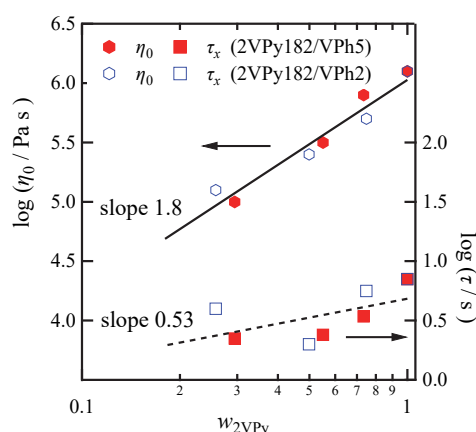


Figure 2 Dependence of  $\eta_0$  and  $\tau_x$  on the 2VPy concentration.

1 Z. Yang, and C.D. Han, *Macromolecules*. 49, 153 (2021).

2 O. Urakawa, et al., *Nihon Reoroji Gakkaishi (J Soc Rheo Jpn)*. 49, 155 (2021).

3 R.H. Colby et al., *Macromolecules*. 24, 3873 (1991).

# Analyzing Structural Fluctuation in Thermally Activated Delayed Fluorescence Materials with Ultralow-Frequency Raman Spectroscopy

Hikaru Sotome Osaka University

Thermally activated delayed fluorescent (TADF) materials are luminescent materials that can achieve an internal quantum efficiency of 100% by utilizing the triplet state produced by charge recombination. The key to this high emission quantum yield is the reverse intersystem crossing (RISC) from the triplet state ( $T_1$  state) to the fluorescent singlet state ( $S_1$  state). Recent studies suggest that not only the energy gap between the  $S_1$  and  $T_1$  states but also dynamic structural fluctuation contributes to the high RISC efficiency. Such dynamic structural changes correspond to low-frequency vibrational modes involving the overall molecular framework, but conventional vibration spectroscopy has difficulty in visualizing the above nuclear displacements due to the limited detection wavenumber region. In the present work, to elucidate the role of low-frequency vibrational modes in the RISC process we have analyzed such vibrational modes using Raman spectroscopy in the ultralow-frequency region down to  $5\text{ cm}^{-1}$ .

We first measured Raman spectra of powder MA-TA (Figure 1a), which is a blue emissive TADF molecule recently developed in Kaji group (Kyoto Univ., ICR), and compared with those obtained from quantum chemical calculation. Figure 1b shows experimental and calculated Raman spectra of MA-TA. Five low-frequency modes were observed at 18, 46, 66, 81 and  $122\text{ cm}^{-1}$ , and this spectral pattern was well reproduced by calculated one of a single MA-TA molecule. This result indicates that we can analyze the low-frequency modes involved in the overall molecular skeleton free from lattice phonon modes. To identify the vibrational modes assisting RISC, we calculated nuclear displacement vector in the conversion from the  $T_1$  state to the  $S_1$  state. The magnitudes are plotted as a function of normal mode frequencies, as shown in Figure 1c. Two modes at 13 and  $16\text{ cm}^{-1}$ , which correspond to the experimentally observed mode at  $18\text{ cm}^{-1}$ , show prominent amplitude. These vibrational modes are ascribable to relative rotation between MA and TA units. A series of the results show that this rotational motion promotes the efficient  $T_1$ - $S_1$  conversion and a key nuclear displacement in the RISC process.

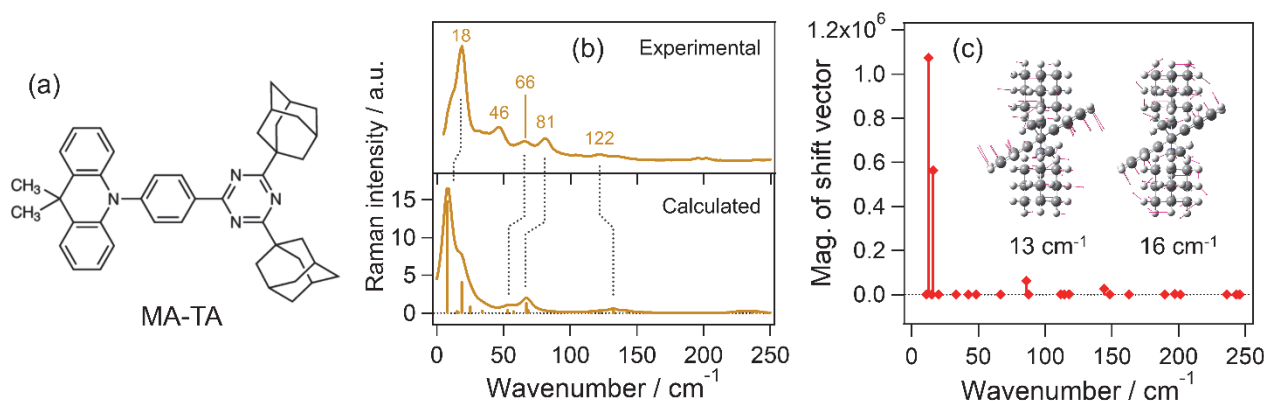


Figure 1. (a) Chemical structure of MA-TA. (b) Experimental and calculated (scaled by 1.2) Raman spectra. (c) Magnitude of nuclear displacement vectors in RISC. The vibrational modes at 13 and  $16\text{ cm}^{-1}$  are depicted.

## Effect of microplastics on the distribution of trace heavy metals in seawater

Yuzuru Nakaguchi Kindai University

**Purpose)** Trace metals were play an important role in marine biogeochemistry. These elements exist as the dissolved state (dMs) and labile particulate (lpMs) in seawater. The particulate matter in seawater includes metal oxides, hydroxides, sulfates, carbonate compounds, mineral particles, and biological particles. In recent years, microplastics produced by UV degradation and weathering have been added to particulate matter in seawater. However, the detail relationship between trace metals and microplastics remain unknown. In this research, In this study, we targeted Osaka Bay, Yodo River and Yamato River, which is greatly affected by human activities. In order to clarify the relationship between the trace metal speciation and microplastics, we determined trace metals and microplastics in seawater.

**Experimental)** Sea water samples were collected by Niskin sampler in September. 28 in 2022 and February 1 in 2023. River water samples were collected at the Yodo and Yamato River in June, August and October in 2022. All sea water samples were transferred to precleaned LDPE Nalgene bottles. Unfiltered samples were directly collected from Niskin bottles to determine the concentrations of total dissolvable trace metals (tdMs). Some portions of samples were filtered through PTFE membrane filters with pore size 0.22  $\mu\text{m}$  to determine the concentrations of dissolved trace metals (dMs). All the filtered and unfiltered samples for trace metals were acidified with 20% HCl (Tamapure AA-10) to achieve a final HCl concentration of 0.010 mol/kg (pH  $\sim$ 2.2). Nutrients were determined by autoanalyzer. Chlorophyll a was determined by high performance liquid chromatography. The trace metals were preconcentrated using a chelating resin which ethylenediaminetriacetic and iminodiacetic acids were immobilized. Trace metals are determined by a high-resolution ICP-MS (HR-ICP-MS) equipped with a magnetic sector mass spectrometer. The sample solutions for microplastics were filtered by PTFE membrane filters with pore size 5.0  $\mu\text{m}$ . After filtration, the samples with filters transferred to separatory funnel. A saturated NaI solution was added to the separating funnel, and the microplastics were separated by the difference of density. After separation, the organic matters remaining in the sample were decomposed by mixed acid ( $\text{HNO}_3 + \text{HClO}_4 + \text{HF}$ ). Microplastics were identified by Microscopic Raman photoluminescence system.

**Results and discussions)** The load of MP which supplied from the Yodo River to Osaka Bay was estimated. The weight of MP were measured by size as MPfine (particle size  $<100 \mu\text{m}$ ), MPcoarse (particle size from  $100 \mu\text{m}$  to  $4.75 \text{ mm}$ ). The average loads of MP were calculated to be 43.0 ton/year for MPfine and 13.2 ton/year for MPcoarse from the concentration of MP and the river discharge of the Yodo River.

**Achievement report)** Nakaguchi, Y., Sakamoto, A., Asatani, T., Minami, T., Shitashima, K., Sohrine, Y. Distribution and stoichiometry of Al, Mn, Fe, Co, Ni, Cu, Zn, Cd, and Pb in the Seas of Japan and Okhotsk. Mar. Chem. 241, 104108, doi.org/10.1016/j.marchem. 2022.104108 (2022)

## Exploration of liquid membrane transportation of metal ions with a polymer membrane containing ionic liquid by use of electric field response of ions

Hiroshi Mukai    Kyoto University of Education

**[Introduction]** Liquid-liquid extraction is one of the useful methods for metal recycling which is getting more important for sustainable use of metal resources. Hence, liquid membrane transportation of metal ions using a thin layer of a liquid membrane (LM) instead of an organic solvent is an alternative method of liquid-liquid extraction which use a large amount of harmful organic solvents and valuable carrier molecules. This LM method is expected to reduce these risks and costs. In our previous work, an almost quantitative transportation of copper (II) ions using polyvinyl chloride (PVC) membrane containing ionic liquid (IL) was achieved. However, the flow rate of metal ions was not sufficient for practical use. In order to improve the flow rate, the use of electric field response of the ions in IL was attempted. Weak alternating current by ionic conduction of IL was generated through a LM by two mesh electrodes located at both sides of the LM. This electric field response of IL ions in a LM was expected to stir the LM phase and to promote the diffusion of metal species transported. The influence of the electric field response to metal transportations was examined.

**[Experimental]** (1) Preparation of membranes: 1-Phenyl-3-methyl-4-benzoylpyrazol-5-one (PMBP) was dissolved in 1-butyl-3-dodecylimidazolium bis(trifluoromethanesulfonyl)imide ( $[C_{4}C_{12}im][Tf_2N]$ ) at the concentration of  $0.005 \text{ mol kg}^{-1}$ . This solution of 1.0 g and PVC of 0.1 g was dissolved in tetrahydrofuran of 5 g in the glass petri dish of 49 mm inner diameter and were dried. (2) LM transportation: The membrane (38.5 mm in diameter) was fixed at the center of a U-shaped reaction tube of PVC. The  $30 \text{ cm}^3$  of aqueous supplying phase ( $[Fe(NO_3)_3] = 2.0 \times 10^{-5} \text{ mol dm}^{-3}$ ,  $[CH_3COONa] = 0.01 \text{ mol dm}^{-3}$ ,  $[NaClO_4] = 0.1 \text{ mol dm}^{-3}$ , pH 5.0) and the  $30 \text{ cm}^3$  of aqueous receiving phase ( $[CH_3COONa] = 0.01 \text{ mol dm}^{-3}$ ,  $[NaClO_4] = 0.1 \text{ mol dm}^{-3}$ ,  $[HNO_3] = 0.1 \text{ M}$ , pH 1) were poured into each part of the reaction tube separated by the membrane, which was put between copper mesh electrodes (32 mm in diameter) with 0.5 V alternating voltage. After 24 hours, the pH values, the volumes and the Fe concentrations of the supplying and receiving aqueous phases were measured.

**[Results and discussion]** The fresh mesh electrodes made of copper wires were gradually dissolved in acidic aqueous media. To prevent the dissolution of copper, the electrodes were used once in the reaction tube under alternating voltage of 0.5 V before LM transportation of metals. Because of the influence of the dissolution of copper in the aqueous phases, LM transportation experiments were carried out for iron (III) ions. The transportation rates of Fe (III) ions after 24 hours under alternating voltage of 0 V and 0.5 V are 0.18 and 0, respectively, and the removal rates from the receiving phase are 0.81 and 0.56, respectively. Contrary of expectations, the both of the rates decreased under electric tension probably because of electrode reactions. The removal of iron (III) ions in the supplying phase by reduction to metal on the electrode and the depletion of protons on the surface of LM in the receiving phase by reduction to hydrogen are considered as reasons.

**[Outcome report]** 1. H. Mukai, S. Miyamoto, A. Nishimura, R. Konishi, Y. Sohrin, 71st JSAC annual meeting abstracts, PA3025 (2022).

## 硫黄ポリマー材料におけるナノ構造不均一評価

藤原明比古 関西学院大学

1. 緒言 : X 線小角散乱 (SAXS) -CT 法では、材料内部のナノスケールの構造分布を非破壊で観測することが可能である。本法は、各投影角で走査しながら SAXS 測定を行うことで、得られた散乱像のシグナルから CT 像を再構成する手法である。このシグナルは、ナノスケールの構造情報に起因しているため、対応する構造情報の分布が CT 像より明らかにできる。しかしながら、測定時間が 2-3 時間程度有するため、計測の短時間化が大きな課題である。これまで、共同研究者の竹中・小川らとともに、計測については投影角度を間引くことで測定を短時間し、得られた再構成画像をトータルバリエーション (TV) 正則化により画像回復を実現した。しかしながら、依然として測定には 1-2 時間程度を有している。硫黄ポリマー材料等への応用にはさらなる測定の短時間化が必要であるため、ビームを複数方向(マルチビーム)から入射する SAXSCT 法の開発研究を始めた。

2. 実験 : マルチビーム SAXSCT 法に向けて、従来の 1 ビームからマルチビーム化を実現する必要がある。まずは 2 ビーム化の方法に関する基礎的な検証を、大型放射光施設 SPring-8 の BL03XU において実施した。

3. 結果 : 2 ビーム化の検討を進め、同時に、2 ビームに対していかに効率よく試料全面をスキャンするかについても検討を行った。2 ビーム化には、大きく分けて波面分割 (例えば図 1 (案 1) : 結晶の Bragg 反射 (2 回反射) を利用)、振幅分割 (例えば図 1 (案 2) : 結晶の Bragg 反射 (1 回反射) を利用)、図 1 (案 3) : 結晶による多波同時 Bragg 反射 (2 回反射) + ダイレクトビーム利用) の 3 種類が考えられる。案 1

及び 2 については、試料後に散乱した X 線を検出するための真空パスや検出器などの設置に大幅な改良が必要であり、実現するには膨大なコストがかかってしまう。本計測を効率的に実施するため案 3 を候補として絞り、その結果、案として、結晶による多波同時 Bragg 反射 (2 回反射) + ダイレクトビーム利用) について検討した。1 ビーム目に対して最も条件が厳しい 90 度で入射可能な最適条件と、それを実現するための光学素子の設計を進めた。その結果、X 線のエネルギーを 7.51keV を選択し、図 1 に示すような三つの結晶系(第一結晶:Si(111)面、第二、三結晶:Si(311)面)で反射することで、90 度の入射が可能であることがわかった(図 2)。

□マルチビームSAXS法の検討案 (Top view)

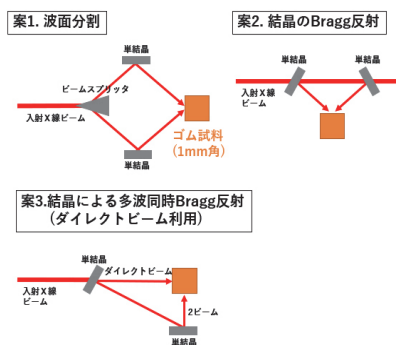


図 1 : 2 ビーム化に向けた光学系案。

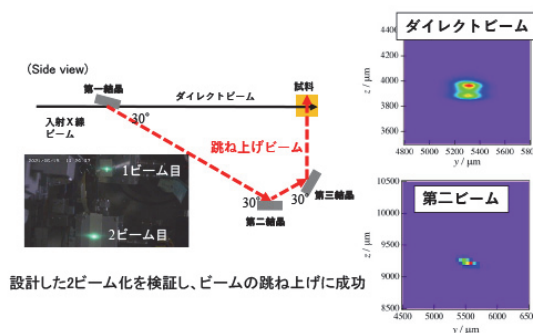


図 2 : 本研究で成功した 2 ビーム化の概要と各ビームプロファイル。



## Conformation analysis on polymer in food-grade oil

Noboru Osaka    Okayama University of Science

In recent years, in order to reduce the intake of unhealthy fats and oils such as trans-fatty acids and saturated fatty acids, the development of food-grade oleogels, which consist of unsaturated fatty acids such as oleic acid, has been rapidly progressing. In our previous work, we performed time-resolved SAXS/WAXS measurements on macromolecular oleogels to elucidate the gelation mechanism, but due to uncertainties in the analysis, the structure could not be identified. Therefore, in this subject, we aimed to understand the conformation of macromolecular chains in fats and oils in detail in dilute systems, and to investigate the concentration, temperature, and solvent dependence to gain a comprehensive understanding of the structural changes during gelation. Specifically, ethyl cellulose (EC) was used as an edible polymer, and not only triolein, a fat used in oleogel, but also methyl oleate and oleic acid as unsaturated fatty acids and ethanol and chloroform as ordinary organic solvents were used as solvents for comparison.

Ethylcellulose (EC, 45 cP) was supplied from NISSHIN & CO., LTD. Oleic acid (OA, 99%), methyl oleate (MO, 99%), triolein (TO, 99%), ethanol (99.5 %), and chloroform (99.8 %) were purchased from Sigma-Aldrich. They were mixed with stirring at the appropriate temperatures. SAXS measurements were carried out at BL40B2 of SPring-8. The camera length was 4.3 m and the wavelength of X-ray was 0.15 nm except for chloroform (0.7086 nm). The total exposure time for each sample was about 600 s.

Figure 1 shows the SAXS curves of dilute EC solutions in fat (TO) and fatty acids (OA and MO) at different temperatures. All the curves showed the upturn in low  $q$  region, suggesting the existence of the higher-order structures even at the low concentrations. In particular, the scattering intensities of the EC solutions using TO and MO as solvents increased with cooling, respectively. While the exponents were almost unchanged to be -4, the changes in the higher-order structures were detected, which would be related to the gelation at the higher EC concentration. The EC in OA showed the asymptotic behavior as  $q^{-1.3}$  in the low  $q$  region, which might suggest the rod-like assembly of EC. This result would be due to the better solubility of OA in EC.

Figure 2 shows the SAXS curves of dilute EC solutions using ethanol and chloroform as solvents at 25 °C. The EC in ethanol showed a similar curve to that of EC in OA. On the other hand, the EC in chloroform did not show a prominent upturn of the intensity in the low  $q$  region, which might suggest that the dissolution of EC without forming the higher-order structure. Our results indicated that the morphology of EC highly depended on the solvent.

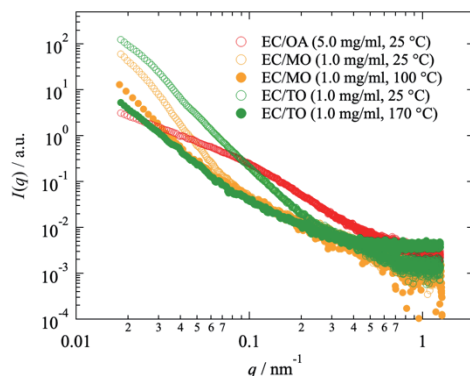


Figure 1. SAXS curves of EC in fat and fatty acids at various temperatures.

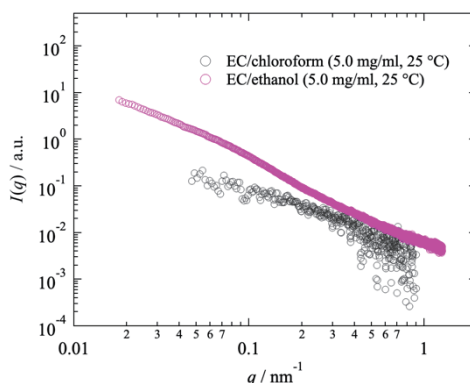


Figure 2. SAXS curves of EC in ordinary solvents at 25 °C.



## プラズモニック合金ナノ粒子を設計するための理論的指針の構築

飯田健二 北海道大学

**[目的]** 可視域に局在表面プラズモン共鳴(LSPR)吸収を示す材料としては、周期表 11 族の単金属(Cu, Ag, Au)のみが使われてきた。しかし近年、B2(塩化セシウム)型やC1型の合金ナノ粒子が可視域にLSPR吸収を示すことが京大化研寺西研究室にて見いだされた。我々は、合金ナノ粒子の設計に資する知見を得るべく理論計算研究を進めてきた。2022年度は、C1型構造を持つPtIn<sub>2</sub>に着目して、光励起の機構を解析した。

**[計算手法]** 高い並列化効率を有する第一原理計算プログラムSALMONを用いた大規模計算によって、直径数nmのナノ粒子の光励起電子ダイナミクスをシミュレーションした。結晶構造から直径約3nmのPt<sub>249</sub>In<sub>432</sub>合金ナノ粒子(図1)を切り出して計算した。また、光触媒や光電極の研究へと展開していくため、溶液中のナノ粒子や固液界面の光や電圧に対する応答を計算することが出来るようにプログラムを拡張した。<sup>1,2</sup>

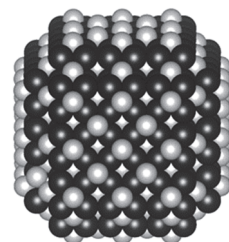


図 1. 対象とした Pt<sub>249</sub>In<sub>432</sub> ナノ粒子。

**[結果と考察]** 光励起の機構を明らかにするべく、2.8 eVで20 fsのパルス光を照射したときの電子占有数の変化を解析した。光照射中の10 fsの時に比べると、光照射後の20 fsでは占有数が全体的に大きく変化していた。これは光の照射にともない電子遷移が進んだことを示す。さらに遷移強度の軌道エネルギーに対する依存性を比較したところ、10 fsではフェルミレベル(0 eV)近傍の-1 ~ 1 eVで大きく変化していた一方で、20 fsでは-3 ~ -2 eVおよび2 ~ 3 eVで大きく変化していた。金ナノ粒子では、フェルミレベル近傍の自由電子のバンド内遷移がd電子のバンド間遷移を誘起することが知られている。Pt<sub>249</sub>In<sub>432</sub>に対する本計算結果は、-1 eVから1 eVにある電子が光応答して、その後に-3 ~ -2 eVの電子がバンド間遷移することを示す。PtIn<sub>2</sub>ナノ粒子の光励起について、LSPRに起因するキャリア生成の機構が発現していることが分かった。

### [論文(謝辞あり)]

[1] K. Iida, J. Phys. Chem. C, 126, 7492-7499 (2022).

[2] K. Iida, J. Phys. Chem. C, 126, 9466-9474 (2022).

### [学会発表(招待講演)]

[3] K. Iida, "Theoretical Study on Heterogeneous Interface under Light and Voltage Bias" IMS-ICAT Joint Symposium of Surface Science for Catalysis, Hokkaido University., Oct. 11, 2022.

[4] K. Iida "Theoretical and Computational Study on Nanostructures under Light and Voltage Bias" ICAT-FHI Symposium: New Dimension of Catalytic Surface Study, Hokkaido University., Sep. 16, 2022.

## 新規ハイブリッド型部分フッ素化リン脂質二分子膜の構造・物性の解析

園山正史 群馬大学

【目的】 私たちはこれまで、膜タンパク質研究に資する部分フッ素化リン脂質の設計指針を得るための物理化学的な研究により、リン脂質 Dimyristoylphosphatidylcholine (DMPC) の 2 本の疎水鎖の末端にパーフルオロアルキル基( $R_f$ ,  $C_nF_{2n+1}$ )を部分的に導入したアナログ分子群  $F_n$ -DMPC ( $n = 2, 4, 6, 8$ ) は、 $R_f$  鎖長依存的な際だった膜物性を示すこと等を明らかにして来た。本研究では、DMPC の一方の疎水鎖の末端を部分フッ素化した新規 Hybrid 脂質シリーズ  $F_n$ -Hybrid を新たに合成し、膜物性および分子構造を調べることで、膜タンパク質研究への応用の可能性を探ることを目的とした。

【方法】 これまでの方法に準じて合成した新規 Hybrid 脂質  $F_n$ -Hybrid ( $n = 4, 8$ ) を用いて、示差走査熱量測定 (DSC) により脂質膜の熱物性を調べた。また、水面上単分子膜の表面圧-面積 ( $\pi$ -A) 等温曲線を 25°C において測定した。さらに水面上単分子膜を金基板に転写し、赤外反射吸収 (RAS) スペクトルを測定した。

【結果と考察】  $F_n$ -Hybrid 懸濁液の DSC 測定を行ったところ、F4-Hybrid は 0.97 °C に主転移と考えられる吸熱ピークを示したが、F8-Hybrid では 0 °C 以上に明確なピークが観測されなかった。したがって F8-Hybrid の主転移温度は氷点下と考えられ、DMPC の 24.4 °C に比べて F8-DMPC の主転移温度が約 40 °C 上昇することと対照的であった。25 °C において測定した F4-Hybrid および F8-Hybrid の水面上単分子膜の  $\pi$ -A 曲線を DMPC とともに右図に示す。F4-Hybrid では F4-DMPC より低面積側で気体膜が現れた。これは、 $R_f$  基とアルキル基の異なる占有面積が原因と考えられる。F8-Hybrid は、DMPC よりも高面積側に

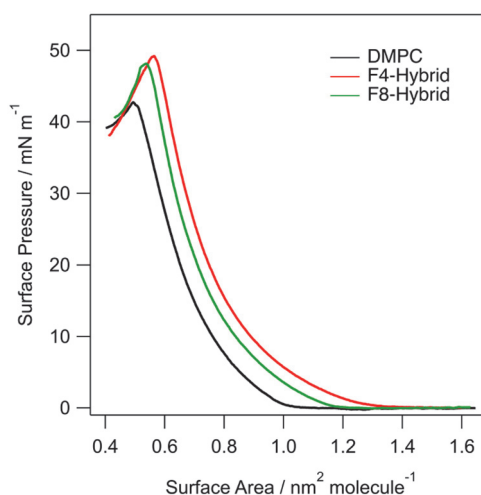


図.  $F_n$ -Hybrid ( $n = 4, 8$ ) および DMPC 水面上単分子膜の表面圧-面積等温曲線 (25 °C)

に先ず液体膨張膜を形成した。これも  $R_f$  基の占有面積がアルキル基よりも大きいことに由来すると考えられる。興味深いことに、2 本の疎水鎖に  $R_f$  基を導入した F8-DMPC に比べ、F8-Hybrid の液体膨張膜は高面積側に現れた。これは、両方の疎水鎖に  $R_f$  基が導入された F8-DMPC は、 $R_f$  基間の強い相互作用により分子が密に凝集した膜を形成するのに対し、一方の疎水鎖のみ  $R_f$  基を導入した F8-Hybrid では分子間相互作用が抑制されているためと考えられる。RAS スペクトルで観測された  $CF_2$  対称伸縮振動バンドも、分子パッキングに関する本考察を支持している。

## 【成果報告】

中川原ら、1 本の疎水鎖末端をフッ素化した新規 Hybrid 脂質シリーズの水面上単分子膜の特性評価、日本化学会第 103 春季年会 (2023 年 3 月 22 日 (予定))、他 2 件。

## Identification of active gibberellins in the basal land plant *Marchantia polymorpha*

Takayuki Kohchi    Kyoto University

Active gibberellins (GAs) are important plant hormones that regulate plant growth and development. A number of GA-related factors, including biosynthetic enzymes and receptors, have been identified, and the physiological functions of GAs have been elucidated mainly from *Arabidopsis* and rice plants. To systematically understand the origin of GAs and the molecular evolution of their signaling pathways, we focused on the liverwort, *Marchantia polymorpha*. Phylogenetic analysis has shown that *M. polymorpha* is located at the basal land plant lineage, and is an excellent model with basic genetic information and technologies. From our previous experiments, we found that GA signaling factors found in vascular plants are partially present in *M. polymorpha*. To identify the active GA, we developed a bioassay of *M. polymorpha*. Since GA biosynthetic mutants of *M. polymorpha* showed the delayed sexual organ formation, we prepared fractionated samples from extracts of according to the two-phase partitioning method, and conducted a bioassay using the timing of sexual organ formation as an indicator in collaboration with Dr. Shinjiro Yamaguchi (co-researcher) and Dr. Kiyoshi Mashiguchi (research collaborator) of the Institute for Chemical Research, Kyoto University. We found that the fraction in which low polar acidic substances accumulated showed the activities of restoring the delayed sexual organ formation of GA biosynthesis mutants. We further analyzed this fraction using HPLC and reverse-phase columns, and identified a specific subfraction that affected sexual organ formation. We are planning to determine the structure of the active GA by combining mass spectrometry and NMR. We are also searching for potential GA receptors by genetic approaches. Mutants of MpSABATH2, which possibly encodes an inactivating enzyme of GA, showed severe phenotypes such as dwarfism and growth inhibition. In order to obtain mutants that suppress these phenotypes, we conducted an EMS mediated mutant screen. As a result, we could obtain five independent mutants. NGS analysis revealed a candidate transcription factor (TF), which was considered to be the causal gene of all the mutants. Complementation test confirmed that this TF as the causal gene. We plan to investigate the possibility of the TF as a receptor in the future.

### Conference reports

Okabe *et al.* (2022), Exploration of gibberellin related compounds in liverworts *Marchantia polymorpha*. The 86th Annual Meeting of the Botanical Society of Japan

Shimokawa *et al.* (2022), Screen for mutants affecting methyltransferase function related to gibberellins in *Marchantia polymorpha*. The 86th Annual Meeting of the Botanical Society of Japan

Shimokawa *et al.* (2023), Exploration for a novel signaling factor of gibberellin in *Marchantia polymorpha*. The 64th Annual Meeting of the Japanese Society of Plant Physiologists

## Characteristics of quantum magnon in magnetic insulators

Kab-Jin Kim KAIST

### Objective:

The aim of the research is to study the characteristic properties of magnon in magnetic insulators.

### Experimental methods:

We measured magnon propagation in YIG (Yttrium iron garnet), which is a magnetic insulator, in the frequency/time domain using micro-patterned coplanar waveguide antennae and a 25 GHz vector network analyzer. We observed the effect of heavy-metal (HM) distributed Bragg reflector (DBR) on the magnon propagation. We also measured the magnon excitation mode in the vicinity of the microwave resonator, to investigate the magnon-photon coupling phenomena. For that, microwave transmission at the YIG sphere mounted at the center of a ring-shaped NbN-based superconducting microwave resonator is measured using a VNA and the real-time oscilloscope.

### Experimental results:

The magnon spectrum in YIG film shows a distinct magneto-static surface wave characteristic. By altering its period, we observed the impact of the magnonic DBR effect on magnonic transmission dispersion. Injection of current through the magnonic DBR, which applies spin-orbit torques in the YIG layer, suppressed magnon modes that did not match the period of the HM grating. During the magnon-photon coupling experiment, we observed a prominent anti-crossing between the magnon and microwave photon bands, and the Rabi-like oscillation between two coupled magnon modes in YIG spheres.

### Discussion:

The magnonic gating effect plays a crucial role in regulating magnon transport for future quantum magnonic technology. Using the DBR effect to selectively control magnon modes opens the possibility of single magnon qubit processing, such as a magnonic Hadamard gate. The magnon-photon coupling phenomenon and Rabi-like oscillation between two magnon modes offer potential applications in hybrid quantum magnonic devices, serving as a quantum interface for future quantum computers.

## Observation of orbital Hall effect in transition metal dichalcogenides

Sanghoon Kim University of Ulsan

Next-generation memories called as non-volatile RAMs (NVRAM) are demanded to overcome the speed of DRAM, and storage density of the NAND flash memory. Magnetoresistive random access memory (MRAM) is a representative next-generation non-volatile memory and has been successfully commercialized as an embedded type by Samsung Electronics and TSMC. The MRAM consists of nanometer-sized magnets, and stores information by using a phenomenon in which a resistance difference occurs depending on the direction of magnetization directions. In order to increase the energy efficiency of the MRAM, a high conversion rate from charge to spin current is required. Here, spin current can be defined as a flow of electrons' spin angular momentum. The memory using this phenomenon is called spin-orbit torque (SOT) MRAM because it simultaneously utilizes spin and orbital, which are the rotational motion and the orbital motion of electrons, respectively. The SOT-MRAM is considered as the next-generation technology of currently commercialized MRAM, so research is being focused around the world.

The key to improving the efficiency of spin-orbit torque (SOT) MRAM technology is to generate a sufficient amount of spin current. Recently proposed orbital-Hall-induced torque (OHT) can be a candidate to enhance the efficiency because the orbital current  $j_{\text{orbital}}$ , as a result of the orbital Hall effect (OHE), has been expected to be quite larger than the  $j_{\text{spin}}$  in some elements.

A research team led by Professor Sanghoon Kim from the Department of Physics at the University of Ulsan has conducted an international joint research program with Professor Teruo Ono group at Kyoto University. Using atomic-level thin film deposition technology, the team fabricated a W/Co/Pt asymmetric artificial superlattice and observed that the generated spin current was more than 300% higher than that of Pt, an element that has been studied as important in existing SOT-MRAM. We found that this result is attributed to the orbital structure of the superlattice. Our result can be a standard approach to observe the orbital Hall effect in transition metal dichalcogenides. Details can be found in our recent paper; Adv. Sci. (2023) 2206800.

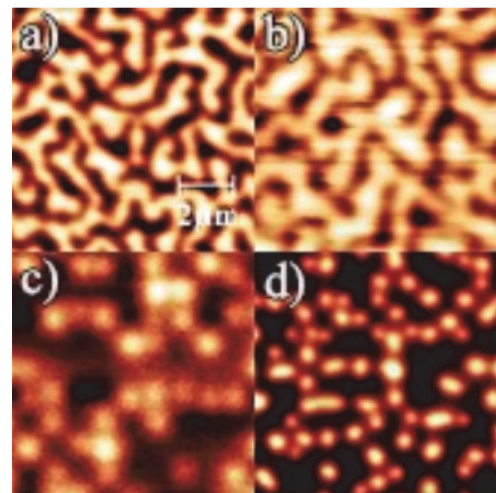
## Investigation on high efficient spin-orbit torque effect in multilayers with combine anisotropy and DMI

Alexey Ognev Far Eastern Federal University

Epitaxial [Pd/Co/CoO] $n$  superlattices were grown on the single crystal Si(111) substrates by the molecular beam epitaxy technique. The samples were grown in an ultrahigh vacuum chamber (Omicron Nanotechnologies) with pressure  $P \approx 10^{-10}$  Torr. Si(111) substrates were prepared by chemical cleaning before loading into the chamber. Each ferromagnetic layer (Co) was oxidized for 3 minutes in a dry oxygen atmosphere in the separated chamber which equipped with a gas flow system. The deposition of each following layer was controlled by recording the RHEED. The magnetic parameters of the samples were studied using a vibrating sample magnetometer (LakeShore VSM 7410). The study of the domain structure was carried out using a magneto-optical Kerr microscope (MOKE, Evico Magnetics) and a magnetic force microscope (MFM, Ntegra Aura) allowing the manipulation of the magnetic structure by high coercivity magnetic probes.

In epitaxial [Pd/Co/CoO] $n$  superlattices the perpendicular magnetic anisotropy is observed. The curvature of the loops at values of the applied magnetic field ( $H$ ) close to saturation indicates the manifestation of the dipole-dipole interaction between magnetic layers. The partial oxidation of the Co layer broke the structural inversion symmetry of the system promoting the existence of the interfacial Dzyaloshinskii-Moriya interaction. The competitive contributions of the i-DMI, PMA and interlayer dipole-dipole interaction create conditions favorable for the origin of chiral domains (labyrinth ordering of domain walls).

Magnetic force microscopy is used for formation the skyrmion lattices from the labyrinth structure of [Pd/Co/CoO/Pd] $n$  samples, where  $n = 7$  and  $n = 10$ . We demonstrated that of the two-pass scan by the MFM probe led to the complete formation of the skyrmion lattice as shown in the right figures. The size and density of skyrmions depended on the periodicity of the labyrinth domain structure and on the distance between two adjacent scanning lines. These results can be used to create a novel type of magnetic memory based on skyrmions, which will allow significantly improve the speed of reading/writing of information.





## Research on the efficiency enhancement of the NV centers creation in nanodiamond

Takuya F. Segawa ETH Zürich

For the life science application, the NV centers in nanodiamonds are significantly interested as a nanoscale probe for dynamics, magnetic field, electric field, temperature, and pH in a living cell. Yet, knowledge regarding the formation mechanism in very small particles is still limited. Half-field signals in electron paramagnetic resonance (EPR) spectroscopy are recorded as a reliable method to quantify NV<sup>-</sup> centers in nanodiamonds. Enhancing the efficiency of creating the NV centers in nanodiamonds is required for a higher sensitivity of the NV sensor. The investigation of the mechanism is very important for elucidation and improvement of it.

We measured the EPR spectrum of the NV center in nanodiamonds, which were produced by various methods. One of the main targets in the project is detonation nanodiamonds (DND), which our collaborators produced. In Figure 1, half-field EPR spectra ( $\nu = 9.87$  GHz) of electron irradiated DNDs with 2 MeV electrons (dark green) and 1 MeV electrons (light green) at a fluence of  $5 \times 10^{18}$  e<sup>-</sup>/cm<sup>2</sup> are shown and are reported in [1]. The spectra shown were background corrected. In addition, we measured TEM (Transmission Electron Microscopy) and DLS (Dynamic Light Scattering) to estimate the size of nanodiamonds. We discussed and analyzed the EPR spectra and enhancement of the efficiency of creation of the NV centers in nanodiamond. The obtained results and information are important for higher sensitivity and the life science application of the NV sensor.

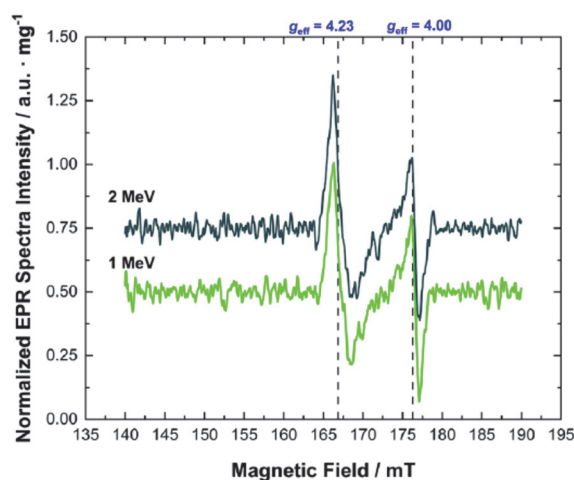


Figure 1. Half-field EPR spectra ( $\nu = 9.87$  GHz) of electron irradiated DNDs with 2 MeV electrons (dark green) and 1 MeV electrons (light green) at a fluence of  $5 \times 10^{18}$  e<sup>-</sup>/cm<sup>2</sup>. The spectra shown were background corrected. [1]

### Published papers

- [1] F. T.-K. So, A. I. Shames, D. Terada, T. Genjo, H. Morishita, I. Ohki, T. Ohshima, S. Onoda, H. Takahsima, S. Takeuchi, N. Mizuochi, R. Igarashi, M. Shirakawa, T. F. Segawa, *The Journal of Physical Chemistry C*, 126 (11), 5206-5217 (2022).
- [2] D. Terada, F. T. K. So, B. Hattemdorf, T. Yanagi, E. Ōsawa, N. Mizuochi, M. Shirakawa, R. Igarashi, T. F. Segawa, *Nanoscale Advances* 4, 2268 (2022).

## Research toward stable NV centers at shallow region and spin dynamics in diamond

Gopalakrishnan Balasubramanian   Helmholtz-Zentrum Dresden-Rossendorf

Recently, NV centers in diamond have been significantly interested as a candidate for a resource for quantum sensing with nanoscale spatial resolution and ultra-high sensitivity. It is because single spins can be coherently controlled, and the spin coherence times are significantly long even at room temperature (RT) in the NV center. By utilizing nanoscale shallow NV centers, applications for nanoscale imaging and nanoscale nuclear magnetic resonance were demonstrated.

Toward these issues, Kyoto University group synthesized Phosphorus doped n-type diamond [1]. To make stable NV centers at shallow regions, the n-type diamond plays important roles in the long spin-coherence time ( $T_2$ ), the stabilization of the charge state, and an improvement of the creation yield of NV centers formed by the ion-implantation technique [2]. The n-type diamond samples were synthesized by CVD using tert-butylphosphine, which is much less toxic than phosphine. Hall measurements confirmed n-type conduction in measured samples prepared under different growth conditions. The highest measured Hall mobility at room temperature was  $422 \text{ cm}^2/(\text{Vs})$ . The  $T_2$  was increased to  $1.62 \pm 0.10 \text{ ms}$  in the sample with the lowest nitrogen concentration. Optically detected magnetic resonance spectra indicated that all measured NV centers were aligned along the [111] direction. This study provides appropriate CVD conditions for growing phosphorus-doped n-type diamonds with perfectly aligned NV centers exhibiting long spin coherence times, paving the way to developing and applying diamond quantum sensing devices.

### Published paper

- [1] R. Kawase, H. Kawashima, H. Kato, N. Tokuda, S. Yamasaki, M. Ogura, T. Makino, N. Mizuochi, *Journal of Applied Physics*, 132, 174504 (2022).
- [2] A. Watanabe, T. Nishikawa, H. Kato, M. Fujie, M. Fujiwara, T. Makino, S. Yamasaki, E. D. Herbschleb, N. Mizuochi, *Carbon*, 178, 294-300 (2021).

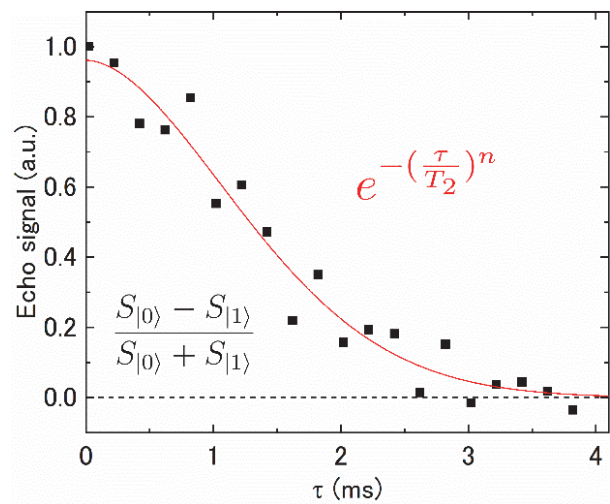


Fig. 1, Hahn-echo signal of the NV center in diamond (data with black dots, exponential-decay fit with red line,  $T_2 = 1.62 \pm 0.1 \text{ ms}$ ). The dashed black line at 0 corresponds to the states being populated equally. To remove common-mode noise, two results were subtracted and normalized [1].

## Demonstration of topological phase control in chalcogenide superlattice

Misako Morota AIST

**Purpose:** This study aims to create a variety of topological materials by simply changing the combination of thickness, number of layers, repeat counts of multilayers consisting of a few types of chalcogenide materials and to demonstrate new topological properties, and this is a continuing project from the previous year. Topological insulators are anticipated to exhibit highly efficient spin-charge current conversion due to surface states caused by strong spin-orbit coupling. In the previous year, we measured spin-torque ferromagnetic resonance (ST-FMR) using  $\text{Sb}_2\text{Te}_3$ /ferromagnetic metal bilayers, as a result, we succeeded in obtaining a frequency-dependent ST-FMR signal. However, the signal intensity is too weak for detailed measurements because of its the high resistivity around 1000 Ohm. In this year, we tried to measure ST-FMR superimposed with ferromagnetic resonance due to an induced magnetic field by adding a metallic layer to the  $\text{Sb}_2\text{Te}_3$ /ferromagnetic metal bilayer film.

**Experimental:** First, multilayer films of  $\text{Sb}_2\text{Te}_3$ /NiFe/Ru were deposited on thermally oxidized silicon substrates by RF sputtering without breaking the vacuum at AIST. Next, device processing and ST-FMR measurements were performed at Institute for Chemical Research, Kyoto University. The NiFe and Ru layer thicknesses were fixed for all samples at 5 nm and 10 nm, respectively, and the  $\text{Sb}_2\text{Te}_3$  layers were crystalline highly oriented crystalline film and prepared at three different thicknesses of 4, 5, and 10 nm.

### Results and Discussion:

Figure shows the ST-FMR voltage for the  $\text{Sb}_2\text{Te}_3$  5nm/NiFe 5nm/Ru 10nm sample at each frequency. These signals of the sample were about 5 times stronger than that of the previous sample with the same thickness of  $\text{Sb}_2\text{Te}_3$  and ferromagnetic bilayer. In addition, the asymmetry of these signals also evidences that ferromagnetic resonance is caused by the induced magnetic field of the current flowing across the Ru layer. In the future, this sample structure will be optimized for further detailed measurements by using ST-FMR.

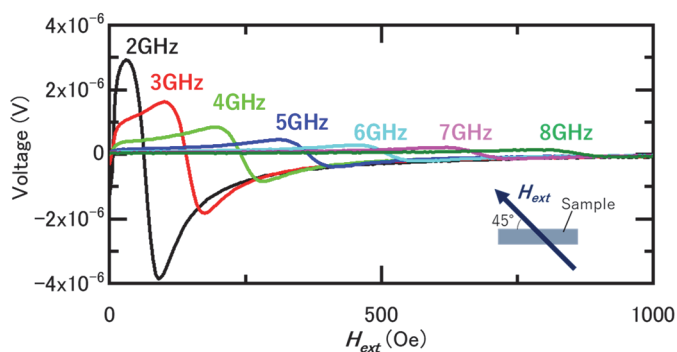
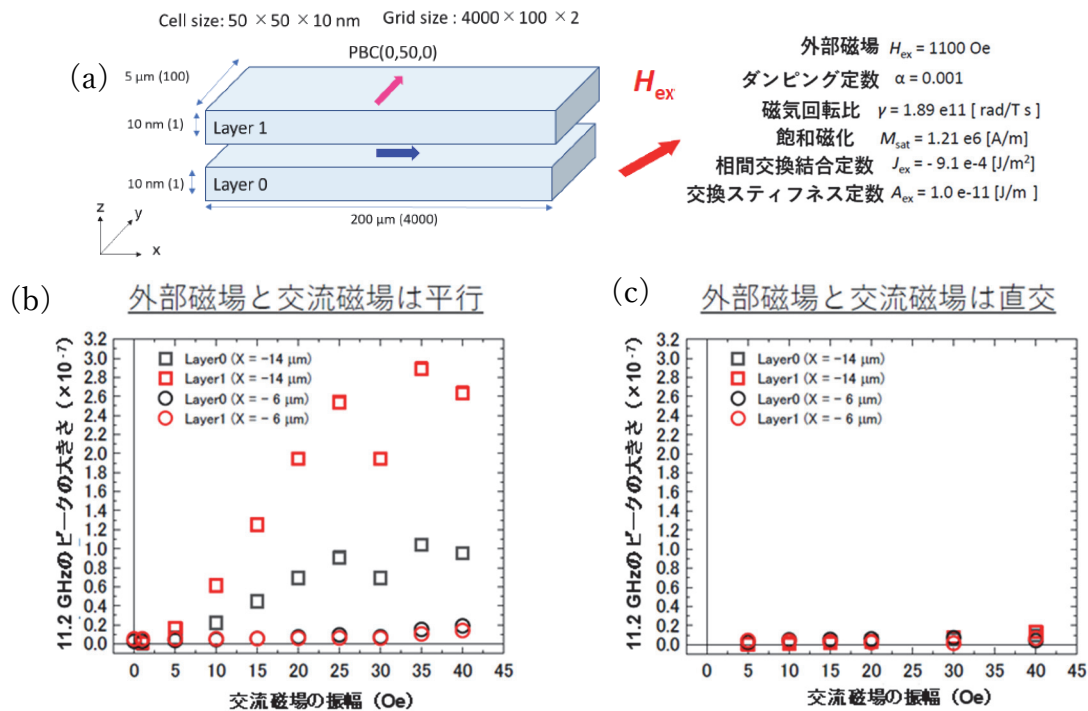


Figure. Signal of ST-FMR on a  $\text{Sb}_2\text{Te}_3$  5nm/NiFe 5nm/Ru 10nm sample measured under frequencies of 2-8 GHz. The inset is direction of the applied external field to the sample.

# 人工反強磁性体のマグノンを用いた量子情報演算素子の基盤技術開発

石橋未央 東京大学

本研究では、人工反強磁性面内磁化膜において観測された音響モードと光学モードのマグノン結合[1]を利用した新しい情報素子開発を目的として、マイクロマグネティックシミュレーション[2]を用いて、マグノン結合した人工反強磁性面内磁化膜に外部からギャップ周波数に対応した交流磁場を印加することで、マグノン結合状態の制御を試みた。図(a)に示すように、音響モードと光学モードが最も強く結合する、マグノンの伝播方向に対して 45 度だけ傾けた方向に面内磁場を印加した人工反強磁性面内磁化膜を再現する。理論計算から、この系は 10.2 GHz と 11.2 GHz の共鳴周波数を有している。低い方の共鳴周波数である 10.2 GHz のマグノンをアンテナによって励起する。アンテナの中心部から 10  $\mu\text{m}$  だけ離れた位置の幅 2  $\mu\text{m}$  の領域に、ギャップ周波数に対応した 1 GHz (11.2 GHz と 10.2 GHz の差分) の交流磁場を印加する。この 1GHz の交流磁場を印加した領域の通過前と通過後の位置での  $z$  方向の磁化の時間変化をフーリエ変換することで、伝播するマグノンの共鳴周波数が得られる。図 (b)、(c) は、1 GHz の交流磁場を 45 度の外部磁場に平行に印加した場合と、直交して印加した場合の 11.2 GHz の共鳴ピークの大きさの交流磁場の振幅依存性である。交流磁場を外部磁場と平行に印加した場合 (図 (b))、通過後、11.2 GHz の共鳴周波数のマグノンが通過前よりも多く伝播していることがわかる。本研究結果より、ギャップ周波数の交流磁場の印加によって伝播するマグノンのモード遷移を確認できたと考えられる。



図(a) シミュレーション設定。(b)、(c) シミュレーションによって得られた磁化の振動を解析した結果。

[1] Y. Shiota *et al.*, Phys. Rev. Lett. **125**, 017203 (2020). [2] A. Vansteenkiste *et al.*, AIP Advances **4**, 107133 (2014).

# ダイヤモンド量子情報素子のための表面状態研究

徳田規夫 金沢大学

【緒言・目的】ダイヤモンド中の NV 中心は、超高感度量子センサとして幅広い分野での応用が期待される。特に、表面からナノレベルの深さに存在する NV 中心は、高い空間分解能を実現することが期待されるが、表面付近ではスピンコヒーレンス時間 ( $T_2$ ) が短くなって感度が低下することや、電荷状態の不安定化が知られていた。近年、リンドーブダイヤモンドにイオン注入法により作製したナノレベルの深さに存在する NV 中心では、 $T_2$  の長時間化と電荷の安定性向上が報告されていた[1]。このことから、ダイヤモンドへのリンドーピングの重要性が高まっている。従来、化学気相成長(CVD)法によるダイヤモンドへのリンドーピングではホスフィンが用いられてきたが、ホスフィンは毒性及び爆発性が高く、合成作業に危険が伴い、無毒化のために高額な装置を導入しなくてはならないという問題点があった。本研究課題では、ホスフィンと比較して格段に爆発性・毒性が低いターシャリーブチルホスフィン(TBP)を用いてリンドーブダイヤモンドを合成した。

【実験と結果】リンドーブダイヤモンドは、原料ガスに水素で希釈した高純度  $^{12}\text{C}$  メタンを用いて、ARIOS 社製のマイクロ波プラズマ CVD 装置によって、Ib(111)基板上に合成した。二次イオン質量分析法により不純物濃度を測定した。ホール測定から、n 型伝導性を示すことを確認した。今回、ダイヤモンド試料中の不純物を、微量のリンが取り込まれつつ、窒素混入を抑制できたことを確認した。 $T_2$  の測定は、室温下で自作の共焦点顕微鏡を用いたハーン・エコー法を行い、NV 軸の方向は光検出磁気共鳴測定により確認した[2]。更に、最適化した条件での合成試料で、長い  $T_2$  を有する単一 NV 中心が生成していることを確認した (図 1)。これは  $T_2$  を短くする不純物を抑制できたことを示していると考えられる。更に、NV 軸の配向性についても、[111]方向への高い配向性を確認した。また、新たな量子センシング手法を考案し、実証した[3]。これらの成果は、今後の量子センシング応用研究にとって重要な結果である。

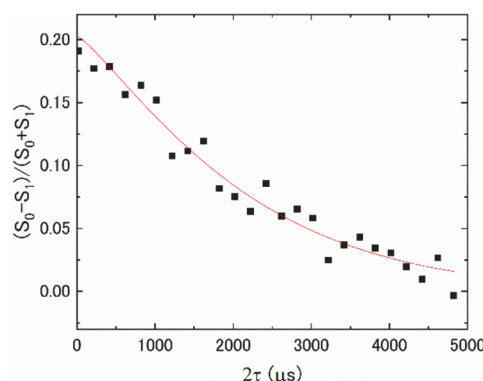


図 1 コヒーレンス時間 ( $T_2$ ) をハーン・エコー法によって室温で測定した結果。

【参考文献】[1] A. Watanabe, T. Nishikawa, H. Kato, M. Fujie, M. Fujiwara, T. Makino, S. Yamasaki, E. D. Herbschleb, N. Mizuochi, "Shallow NV centers augmented by exploiting n-type diamond", *Carbon*, 178, 294 (2021).

【成果報告】[2] R. Kawase, H. Kawashima, H. Kato, N. Tokuda, S. Yamasaki, M. Ogura, T. Makino, N. Mizuochi, "n-Type diamond synthesized with tert-butylphosphine for long spin coherence times of perfectly aligned NV centers", *Journal of Applied Physics*, 132, 174504 (2022).

[3] H. Tabuchi, Y. Matsuzaki, N. Furuya, Y. Nakano, H. Watanabe, N. Tokuda, N. Mizuochi, J. Ishi-Hayase, "Temperature Sensing with RF-Dressed States of Nitrogen-Vacancy Centers in Diamond", *Journal of Applied Physics*, 133, 024401 (2023).



## 量子センサの高感度化に向けたリンドーブダイヤモンド合成と 量子科学技術研究

牧野俊晴 産業技術総合研究所

【緒言・目的】ダイヤモンド中の NV 中心は、量子科学技術分野において精力的に研究され、特に固体中のスピンとしては群を抜く長いスピンコヒーレンス時間を持つことにより、高い量子センサ感度が実現し、磁場、電場、温度、圧力、pH などの高感度センサとして幅広い分野での応用が期待される。今後の社会への波及効果を考える際、スピンの電氣的制御・検出や、センサ手法開発が重要で、本研究課題ではそれらに取り組んだ。

【実験と結果】以前、我々は pin 構造を持つダイヤモンドダイオード素子を作製し、電氣的に単一光子を室温で発生させることに世界で初めて成功していた[1]。この時は、NV 中心の中性状態を単一光子源としていたが、センサなどへの応用には負電荷状態からの発光が望まれていた。今回、産総研グループが  $p^+-i(n^-)-n^+$  構造を有する作製したダイヤモンドダイオード素子を用いることにより、負電荷の NV 中心からのエレクトロルミネッセンスと考えられる発光を観測することができた(図1、[2])。今後の量子情報応用研究にとって重要な結果である。

また我々は、低周波数の交流磁場を高感度に、且つ高周波数分解で計測できる新たな量子センシング手法を考案し、実証した。この手法を用い、これまで NV 量子センサを用いて計測した NMR 信号の線幅としては世界最小線幅 (1.6 Hz) を実証した[3]。更に、高品質で優れたスピン特性を有するリンドーブ n 型ダイヤモンドの合成に成功した[4]。

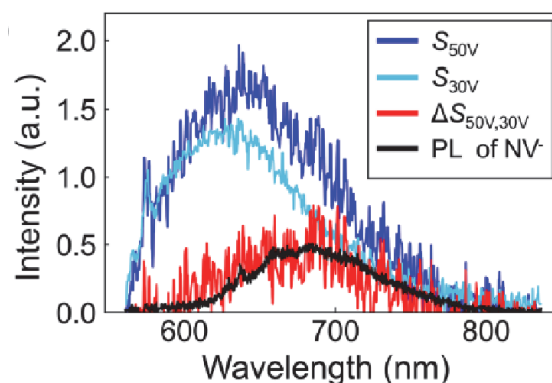


図1 観測された NV 中心のエレクトロルミネッセンス (EL) スペクトル. 青色、水色がそれぞれ 50 V, 30 V を印加したときに得られた EL スペクトル. 赤がそれぞれの差から得られたスペクトル. 黒が NV 中心の負電荷状態のフォトルミネッセンススペクトル.

【参考文献】 [1] N. Mizuochi, T. Makino, H. Kato, D. Takeuchi, M. Ogura, H. Okushi, M. Nothaft, P. Neumann, A. Gali, F. Jelezko, J. Wrachtrup, S. Yamasaki, "Electrically driven single photon source at room temperature in diamond", *Nature Photonics*, 6, 299 (2012).

【成果報告】 [2] M. Haruyama, H. Kato, M. Ogura, Y. Kato, D. Takeuchi, S. Yamasaki, T. Iwasaki, H. Morishita, M. Fujiwara, N. Mizuochi, T. Makino, "Electroluminescence of negatively charged single NV centers in diamond", *Applied Physics Letters*, 122, 072101 (2023).

[3] E. D. Herbschleb, Y. Ohki, K. Morita, Y. Yoshii, H. Kato, T. Makino, S. Yamasaki, N. Mizuochi, "Low-frequency quantum sensing", *Physical Review Applied*, 18, 034058 (2022). (Editor's suggestion)

[4] R. Kawase, H. Kawashima, H. Kato, N. Tokuda, S. Yamasaki, M. Ogura, T. Makino, N. Mizuochi, "n-Type diamond synthesized with tert-butylphosphine for long spin coherence times of perfectly aligned NV centers", *Journal of Applied Physics*, 132, 174504 (2022).



## Self-Assembling Adjuvant-Built-In Vaccines for Cancer Immune Therapy

Yan-mei Li Tsinghua University

The development of synthetic cancer vaccine adjuvants has been an area of active research. One promising class of small-molecule anti-cancer adjuvants are agonists of TLR7/8 that usually sense viral single-stranded RNA to elicit a Th1-type cellular innate immune response. In this collaborative research with ICR, we extended ICR's previous discovery of a self-assembling vaccine adjuvant named cholicamide, with the goal of identifying a potent cancer vaccine adjuvant with an improved safety profile. Our collaboration resulted in a cholicamide derivative (cholicamide  $\beta$ ) as a non-cytotoxic small-molecule cancer vaccine adjuvant that stimulates antigen-presenting cells to induce antigen-specific T-cell activation.

To prepare a series of cholicamide derivatives, the Uesugi group of ICR replaced deoxycholic acid with four other bile acids (cholic acid, lithocholic acid, chenocholic acid, and ursodeoxycholic acid) or changed the length of the diamine linker. To assess their ability to stimulate the immune response, we treated bone marrow-derived dendritic cells (BMDCs) with the cholicamide derivatives and measured the production of IL-6, a cytokine typical for activation of antigen-presenting cells. Two compounds exerted more potent activity than cholicamide at 100  $\mu$ M. When we examined their effects on the cell viability, compound **6** showed essentially no cytotoxicity up to 80  $\mu$ M. We named this molecule (**6**) as cholicamide  $\beta$ .

The non-cytotoxic characteristics of cholicamide  $\beta$  (**6**) prompted us to use it as a cancer vaccine adjuvant. Our lab in Beijing examined whether cholicamide  $\beta$  (**6**) combined with an OVA antigen inhibits tumor growth in a B16-OVA melanoma model. C57BL/6 mice were inoculated on day 0 with  $1.5 \times 10^5$  B16-OVA melanoma cells by subcutaneous injection. Cholicamide  $\beta$  (**6**) combined with the OVA antigen significantly reduced tumor proliferation with negligible body weight. Cholicamide  $\beta$  (**6**) may serve as a starting point of small-molecule cancer vaccine adjuvant.

### Publication

Self-assembling small-molecule adjuvants as antigen nano-carriers

Jin, S., Zhuo, S., Takemoto, Y., Li, Y., Uesugi, M.

*Chem. Comm.* 58, 12228–12231 (2022)

## Evaluation of $\text{CaCO}_3$ dissolution rates in deep-sea sediments by a novel tracer method

Cai Pinghe Xiamen University

**Objectives:** By working with **Prof. Yoshiki Sohrin at ICR**, this project aims to 1) quantify  $\text{CaCO}_3$  dissolution rates and 2) examine what controls  $\text{CaCO}_3$  dissolution rates in the Pacific Ocean floor.

**Experimental methods:** Sediment and porewater samples were collected along a transect in the North Pacific Ocean between mid-September and late October, 2021 (Figure 1).

Radium-226 ( $^{226}\text{Ra}$ ) and thorium-230 ( $^{230}\text{Th}$ ) in sediment and porewater were measured using a high sensitivity ICP-MS. Porewater profiles of dissolved inorganic carbon (DIC) was determined by Apollo Dissolved Inorganic Carbon Analyzer. Calcium ( $\text{Ca}^{2+}$ ) concentrations in porewater were determined using an ICP-OES.

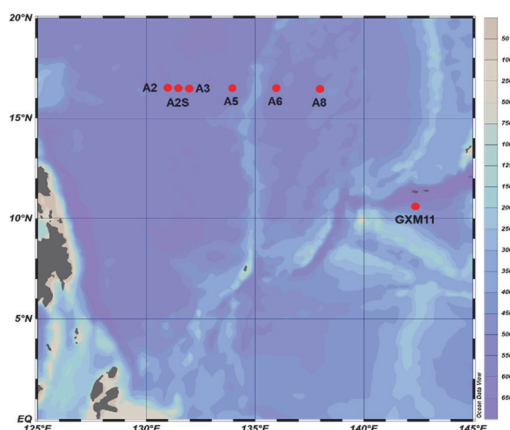
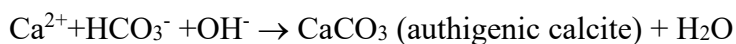


Figure 1. Sampling stations in the North Pacific Ocean

**Experimental results:** Despite continuous flushing of the upper layer of the ocean floor, all pore water profiles consistently manifest a marked depletion of  $\text{Ca}^{2+}$ . Strikingly, pore water profiles show a concomitant depletion of DIC relative to bottom seawater.

**Discussion:** The results suggest that in contrary to the dissolution theory, authigenic  $\text{CaCO}_3$  is forming in the upper sediment column of the Pacific Ocean floor lying below the compensation depth. The reaction can be expressed as:



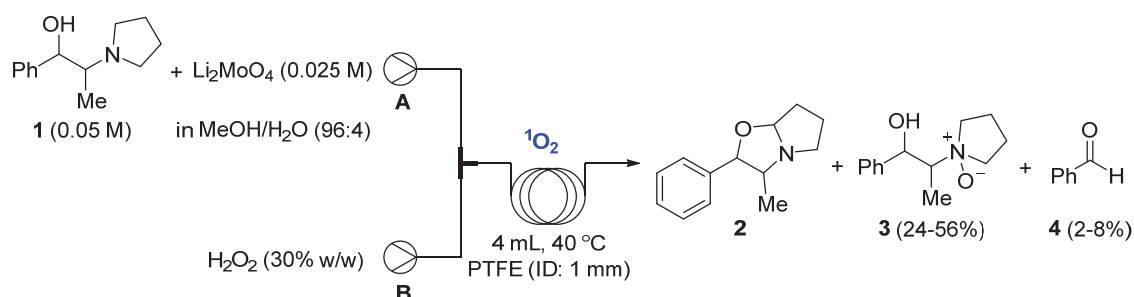
By use of the  $^{226}\text{Ra}/^{230}\text{Th}$  disequilibrium approach, we estimate a range of 12 to 120  $\text{mmol m}^{-2} \text{yr}^{-1}$  (average: 60  $\text{mmol m}^{-2} \text{yr}^{-1}$ ) for the rate of authigenic  $\text{CaCO}_3$  formation. However, it is still unclear what reactions can produce  $\text{OH}^-$  in sediment porewaters

**Outcome report :** Not yet available.

## Advanced Oxygen – mediated Flow Chemistry

Thomas Wirth Cardiff University

Molecular oxygen is the most appealing reagent to perform oxidation reactions. Yet, lower reactivity of molecular oxygen from its ground state (triplet oxygen,  $^3\text{O}_2$ ) generally requires high pressure and temperatures for oxidation reactions. In contrast, the excited singlet oxygen ( $^1\text{O}_2$ ) is highly reactive with different organic molecules even under very mild conditions. Recently, Nakamura, Isozaki (the ICR collaborating researchers on this project) and coworkers have synthesized gold nanoclusters (AuNCs) and utilized those AuNCs as efficient photocatalysts for oxidative cyclization of amino alcohols to generate oxazolidine cores (*ACS Catal.* **2021**, *11*, 13180-13187). Generation of singlet oxygen by the photoexcited AuNCs was proposed as the key intermediate in the mechanism. To investigate if the AuNPs only generate the singlet oxygen responsible for the subsequent reaction steps, treatment of **1** with singlet oxygen was initially performed in the absence of AuNPs. The generation of “dark singlet oxygen” was confirmed from the quantitative formation of ascaridole from  $\alpha$ -terpinene (*Chem. Eur. J.* **2019**, *25*, 12486-12490). In all cases, **3** was found as the major product with traces of **4** in some cases as indicated in the Scheme below.



We introduced the AuNPs under identical reaction conditions to investigate if the Au nanoclusters could provide the cyclized product with pre-generated singlet oxygen in the absence of light. However, even in the presence of AuNPs, no trace of the cyclized product **2** was observed, although the formation of **3** was slightly improved (38-62%). The formation of **4** was not observed in the presence of AuNPs. From many experiments we concluded that the light and photoexcited AuNPs are involved in more than one step in the formation of final cyclized product **2** rather than just generating singlet oxygen.

Our numerous efforts to cyclize **1** to **2** using “dark singlet oxygen” were not yet unsuccessful. We now propose employing alternative singlet oxygen sources (photochemical approaches, use of endo-peroxides) to effect the transformation, also investigating modified starting materials and include solvent modifications in the experiments.

## **Novel strategy for intracellular delivery of nanomedicines**

Silvia PUJALS   Institute for Advanced Chemistry of Catalonia

Nanomedicine arose 20 years ago with the promise of selectively delivering drugs to target sites, thus increasing their effectivity while minimizing undesired side effects. However, despite the great promise behind nanomedicine for drug delivery, very few products have been approved for patient use. This poor translation into clinic comes from different factors, some of them being a poor characterization of the nanomaterials or a simplistic model to evaluate them. Poor cellular uptake efficacy of these nanomedicines is also a big obstacle. Our research group has a speciality in preparation of nanoparticles being applied for nanomedicine. We also have strong background of nanomaterials characterization and intracellular behavior using various microscopic techniques (including electron microscopy and super resolution microscopy). On the other hand, Prof. Futaki at ICR, Kyoto University is an expert on intracellular delivery of nanomedicines. This joint research aims to establish novel approaches for stimulating cellular uptake of nanomedicines created by Pujals group (IQAC) with the know-hows of Futaki group at ICR, Kyoto University.

Our group has formulated few batches of Poly(D,L-lactide-co-glycolide) (PLGA) nanoparticles. They are around 200 nm and have DiI (excitation at 550 nm) or DiO (excitation at 484 nm) for visualization of their methods of cellular internalization. PLGA-based nanoparticles are biodegradable and widely employed in drug delivery systems in various medical applications. In addition to discussions via e-mail, Prof. Futaki visited Barcelona in the August of 2022 and made detailed planning of our studies. Methods in cellular uptake of these particles are now understudy in Futaki laboratory. Pujals is planning to visit ICR in the fiscal year of 2023 to extend the collaboration.

## **Structural and functional analysis of curvature-inducing peptides and application**

Anne S. Ulrich   Karlsruhe Institute of Technology

Epsin-1 is a representative protein which induces the positive curvature necessary for the formation of clathrin-coated pits during endocytosis. Modulating the structural dynamics of biomembranes by inducing bilayer curvature and lipid packing defects has been highlighted as a practical tool to modify membrane-dependent cellular processes. Collaborative research of Ulrich research group at KIT with Futaki research group at ICR, Kyoto University has already shown that the N-terminus 18-residue peptide of epsin-1 (EpN18) possess curvature inducing abilities of the parent protein.

The method of curvature induction by EpN18 is thought by way of shallow insertion of its hydrophobic face into the lipid bilayer. Possible steric hindrance among the lipids by the insertion of helix leads to increase in surface area of outer leaflet of the membranes, yielding curvature in the cell membranes. Through the functional refinement of EpN18, the ability of membrane structural alteration may be more enhance and utilized for artificially controlling cellular phenomena involving membrane structural alteration. We therefore aimed to elucidate the important structural factors of the helical segment for the curvature induction for the better understanding of curvature inducing mechanisms and future design of more effective means of curvature control.

The structural factors of amphiphilic helical peptides include hydrophobicity, helicity ( $\alpha$ -helix content), charges, amphiphilicity balance (hydrophobic surface area), and peptide length. We thus synthesized structurally simplified peptides and see the effects on the curvature inducibility through physicochemical and cell biological evaluations. As a result, we found a positive correlation between hydrophobicity/helicity and the abilities of curvature induction and lipid-packing loosening. The report on these results is now under consideration for publication.

## In-depth analysis of efficiency roll-off in highly efficient TADF-based organic electroluminescence devices

Ebinazar Namdas The University of Queensland

### Project Background:

This project is focus on the understanding of loss mechanism processes related to the efficiency roll-off in next generation of thermally activated delayed fluorescence (TADF) based OLEDs, in particular, i) the impact of exciton decay parameters of high reverse intersystem crossing (RISC) exhibiting TADF materials on OLED device performance through advance device characterisation and spectroscopic methods; and ii) strategies to improve device performance at high brightness regime.

### Project Progress:

The project started in Jan 2022. The planned international collaborative exchange visits of Kyoto University and UQ have been postponed due to COVID-19. This has significantly affected the international travel, living cost and project planning. Nevertheless, we have carried out the planned research activities as highlighted below:

1. Successfully achieved low amplified spontaneous emission (ASE) thresholds and electroluminescence from a solution-processable organic laser dye C545T blended with TADF materials (ACRXTN). The low ASE threshold of  $4.7 \mu\text{J cm}^{-2}$  at the wavelength of 540 nm was obtained by constructively making use of triplet excitons from the TADF material (**Fig. 1**). Furthermore, we also achieved a high maximum external quantum efficiency (EQE)  $\sim 10\%$  from the solution processed ACRXTN:C545T based OLEDs. However, the EQE roll-off was significant. This was partly due to the slow reverse intersystem crossing rate (RISC) of ACRXTN.

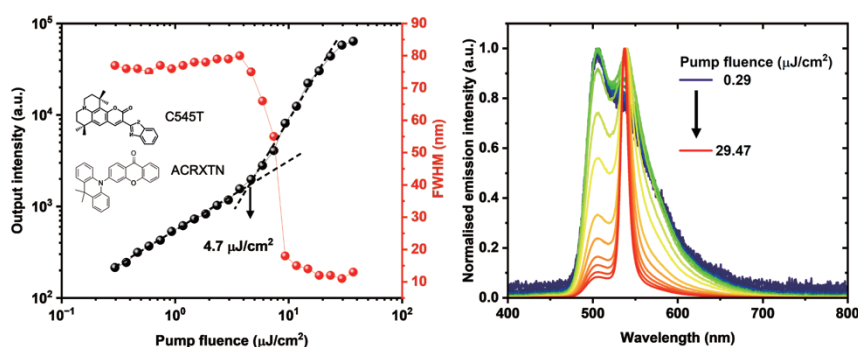


**Fig 1:** ASE study of the mCP:ACRXTN:C545T (89:10:1 wt%) blend films, spin coated from solution. Excitation wavelength at 337 nm (nitrogen laser).

2. The above results indicate that TADF materials with a high reverse intersystem crossing rate (RISC) is crucial to reduce the EQE roll-off at high current density and ASE threshold. Hence, Prof. Hironori Kaji and his team supplied two next generation of TADF materials (TpAT-tFFO and MCz-TXO) with ultra-high RISC rates to UQ. Unfortunately, progress on these materials has been slowed down due to laser breakdown and reduced staff at UQ. Hence, we would like to request the project extension by 1 year. At this stage we are recruiting a suitable research student to complete the pending work.

**Publication:** Part of the study was presented at “The 7th International TADF Workshop (on-line), Dec2022.



## **Intracellular delivery of biofunctional proteins using artificial protein nanocages**

Yusuke Azuma Jagiellonian University

Proteins that self-assemble into hollow, cage-like structures present an attractive platform to develop nanocarriers for intracellular delivery of intact cargo molecules in vivo. To achieve this, efficient methods for guest encapsulation and its release in recipient cells are needed. One of the applicants (Azuma) holds expertise in protein cage engineering, devising strategies for encapsulation of cargo molecules, such as other proteins, in the lumen as well as control of cage assembly-disassembly by an external stimulus. The Futaki laboratory (the host at ICR) is developing peptidyl tools for intracellular delivery of biofunctional proteins including antibodies. By combining the specialties of both groups, this project aimed to develop novel intracellular delivery systems for biofunctional proteins that are potentially applicable to clinical study. Expected outcomes of this project included: (i) obtaining insight into the effect of nanocage/peptide structures on their cellular uptake efficacy; (ii) establishing the approaches for design of protein nanocage capable of delivering biofunctional protein cargoes into cells; (iii) providing guidelines for designing effective delivery systems for nanomedicines; and (iv) strengthening research exchange between Jagiellonian University and ICR.

As the first step, we discussed the possible candidates of protein nanocages via e-mail and planned experiments for production of protein cages encapsulating model guest proteins. Meanwhile, we realized that improvement on delivery peptides is likely a priority objective to attain delivery of protein nanocages with satisfactory efficacy, the knowledge being obtained through a Futaki group's work on the development of a nanocage delivery system using a delivery peptide called HAad (*Angew. Chem. Int. Ed. Engl.* 59, 19990-19998 (2020)). Prior to this collaboration work, Azuma and Futaki have reported a cationic lytic peptide that markedly promotes the endosomal escape of biomacromolecules (*Angew. Chem. Int. Ed. Engl.* 57, 12771-12774 (2018)). However, metal ions employed in this preliminary study may prohibit the application in vivo. Based on this design concept, the Futaki group lately developed new delivery peptides without the need for metal ions. One of the designed peptides exhibited a marked activity, successfully delivering a large protein, antibody (150 kDa), into various types of cells without significant cytotoxicity. We anticipate that applying our latest peptide to protein cages will provide a versatile nanocarrier system for efficient intracellular cargo delivery.

## Real-Time Visualization of Cellular Phase-Separating Proteins

Kazuya Kikuchi   Osaka University

### Objectives

A growing number of proteins contain disordered regions of low-sequence complexity which induces protein condensation via liquid-liquid phase separation (LLPS). Although these protein condensates initially have liquid-like properties, they can also age into more solid-like states leading to many diseases. The goal of the present collaboration is to develop a new chemical technique that allows us to monitor the transition of liquid-liquid phase separation into the more solid or viscous state in live cells.

### Results

Together with the Uesugi group of ICR, we designed and experimentally tested a new chemical technique that detects the status of protein condensates. This fluorescence-based technique uses a unique protein labeling method (PYP method) that has been developed by our group in Osaka. The PYP method takes advantage of the relatively small size of PYP protein for visualizing proteins of interest fused with PYP. First, HEK293 and U2OS cells were transfected with each of 18 plasmids that encode a PYP protein fused to 18 different phase-separating proteins. The addition of a PYP ligand fluorescent probe into the culture medium permitted the detection of the 18 PYP fused phase-separating proteins in live cells under a confocal microscope. To monitor the formation of solid-like condensates, we performed pulse-chase analysis, in which PYP ligand probes with different colors were added at different time points (Orange probe first and Far-red probe later). We hypothesized that solidified protein condensates would only be labeled by Orange probe. Newly formed liquid protein condensates would only be marked by Far-red probe, and the remaining liquid protein condensates would be double-labeled with both Orange and Far-red probes. The results suggest that this is in fact the case, although the conclusion needs to be confirmed by other techniques in the future.

### Future plan

We plan to establish the proposed method to analyze solid aggregates and liquid condensates quantitatively. Sorting of the cells harboring those proteins by a FACS machine would facilitate ranking the 18 phase-separating proteins to identify the highly aggregating protein under different conditions. In addition, sorted cells will be subjected to RNA sequencing and proteomic analysis to identify genes and proteins involved in the condensate solidification process.

## 合成小分子化合物による細胞の遠隔操作

西川元也 東京理科大学

●**研究目的** 細胞の中には多くの自己集合体が存在する。これらの自己集合体はマテリアルと生命体を分ける境界をなす。細胞内で最もマテリアルに近い自己集合体はメラニンだろう。この黒色の集合体はメラニン産生細胞の細胞小器官であるメラノソーム内で生合成される。メラノソーム内のチロシナーゼが出発物質のチロシンを認識し、酸化重合を引き起こすことでメラニンが生成する。本研究では、合成小分子化合物による細胞内メラニンの化学的加工を試みる。究極的な目標は、非天然の機能性が付与された人工メラニンを利用した生細胞の遠隔操作である。

●**背景** 京都大学化学研究所の上杉グループでは、チロシン誘導体によりメラニンの生合成メカニズムをハイジャックし、細胞内メラニンを化学的に加工する手法を開発している。この手法の応用例として、常磁性チロシン誘導体による細胞内メラニンへの磁気応答性の付与と細胞の磁気制御が2022年の *Journal of the American Chemical Society* に報告されている<sup>1)</sup>。本論文は、メラニンの自己集合性を磁気応答性マテリアルの合成に応用した初めての報告例である。磁気応答性メラニンは、常磁性の鉄錯体が結合したチロシン誘導体を細胞内チロシナーゼで酸化重合することにより生合成される。磁気応答性メラニンを生合成した細胞に外部磁場を印加すると磁気配列させることが可能である。細胞内自己集合性分子と磁性学を融合した新たな生理活性化化合物の概念を提案した。

●**実験方法** 共同研究では、磁気応答性が付与されたメラノーマ細胞の磁気制御をマウス体内で検討した。メラノーマ細胞をマウスに静脈注射すると肺転移することが知られている。肺移行性を磁場で遠隔操作できるかを西川グループで調べた。初めに、上杉グループで確立した手法を元にB16F10メラノーマ細胞内で磁気応答性メラニンを生合成した。この磁性化メラノーマ細胞をDiRにより蛍光標識した後、尾静脈注射し、マウスの胸部にネオジム磁石を配置した。静注3時間後、肺を摘出し、DiR由来の蛍光強度を測定することで肺移行性を評価した。磁性化メラノーマ細胞は外部磁場に引き寄せられ、肺転移が増進すると予想した。

●**結果と考察** 磁性化メラノーマ細胞の肺移行性は外部磁場存在下で顕著な増進が見られなかった。マウス体内で磁気制御できるほどの磁性が人工メラニンに備わっていなかったことが原因として考えられる。磁気特性を増強する必要がある。磁性材料の磁気特性に大きな影響を与える要素は、その材料を構成する常磁性分子の集合様式である。磁気応答性メラニンは常磁性鉄錯体とチロシンを含むペプチドのハイブリッド化合物が重合し、高度に自己集合することで合成される。ペプチド部位のアミノ酸をチューニングすることで磁気応答性メラニンの集合性を調節し、磁気特性を改善できる余地がある。現在、上杉グループで新たな磁性チロシン誘導体の開発を進めている。

- 1) K. Nishio, K. Toh, A. Perron, M. Goto, M. Abo, Y. Shimakawa, M. Uesugi, Magnetic Control of Cells by Chemical Fabrication of Melanin, *J. Am. Chem. Soc.* 2022, *144*, 16720.

## 有機合成・単分子測定・計算化学の協同による 2次元ドナー・アクセプター分子系の構築

木村謙介 理化学研究所

ドナー・アクセプター(DA)分子界面における励起子の挙動は、電荷分離、熱活性化遅延蛍光、光化学反応といった分子が有する様々な光化学機能の根源である。このような励起子の挙動は、DA分子がナノメートルスケールで近接した際に起こる現象であることから、DA分子間の空間的な配置を決定したうえで光学測定を行うことが重要である。本研究では、共同研究者である梶教授らにより化学研究所のスーパーコンピュータシステムを用いた量子化学計算により表面上に2次元DA分子系を形成する最適な組み合わせを見出したのち、研究代表者らを中心に理化学研究所のKim研究室に設置されている走査トンネル顕微鏡(STM)をベースとした単分子発光測定手法を用いて、2次元平面上にモデルDA分子系を構築し、その光学特性の評価を行った。

計算化学を用いたスクリーニングにより、Mgフタロシアニン(MgPc)をD分子、HAT-CNをA分子として用いて近接させたときDA二量体からの電荷分離発光が期待されることを見出した(図1a)。そこで、これらの分子を自作した2源蒸着器を用いてNaCl超薄膜を成長させたAu(111)表面に吸着させ、STM探針を用いた分子移動技術を用いて近接させた。図1bはMgPc(左)とHAT-CN(右)を1.06 nmの距離まで近接させたときのSTM像であり、分子の最低空軌道(LUMO)が可視化されている。図1cは作成したDA二量体に対してSTM発光を測定した結果である。図1(b)中の赤点の位置にSTM探針を置いて電荷注入をしたとき、659.5 nmに発光ピークが観られ(図1c 赤線)、MgPcモノマーの発光波長は656.5 nmであることから、3 nmほど長波長化している。次に、青点にSTM探針を置いて発光測定を行うと発光ピークが分裂する現象を観測した。このように励起位置により発光スペクトルの形状が変化した現象は、4回対称のMgPcに対してHAT-CNが近接することで対称性が崩れたことに起因すると考えられる。現在、STMによって決定したDA分子の配置に基づいて二量体の励起状態計算を行うことにより、スペクトル変化の詳細な起源を調べている。

本研究に関しての具体的な成果報告は未だ行えていないが、次年度は学会発表および論文化を目指して、引き続き研究を進めていく。

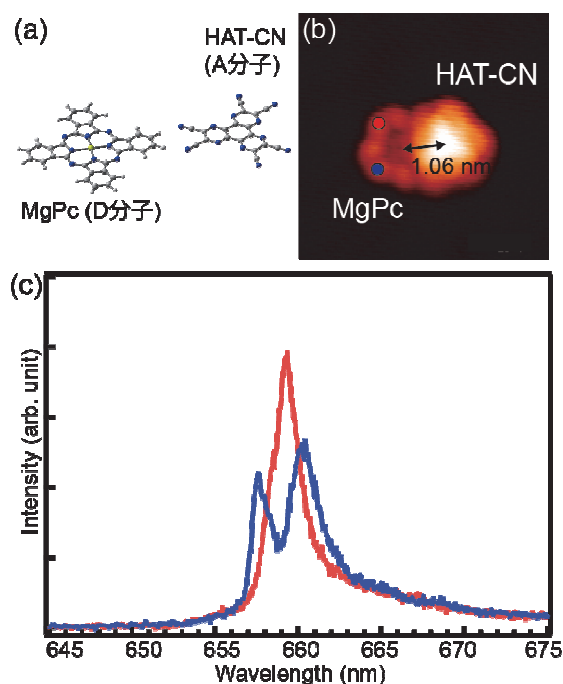


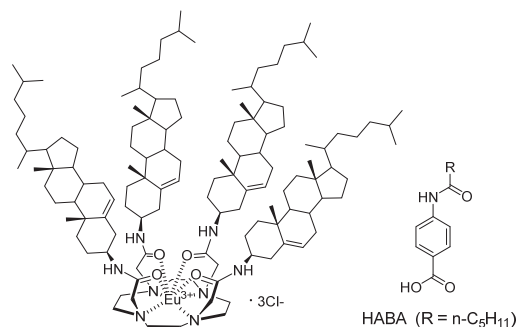
図1  
(a) 量子化学計算で見出したモデルDA分子系であるMgフタロシアニン(MgPc)とHAT-CNの分子構造。  
(b) MgPcとHAT-CNを近接二量体のSTM像( $V = 2.0$  V,  $I = 10$  pA,  $6 \times 6$  nm<sup>2</sup>)  
(c) DA二量体のSTM発光スペクトル( $V = 2.0$  V)。赤線と青線は、図1(b)中の対応する赤点と青点で取った発光スペクトルである。

## 両親媒性希土類錯体を利用した薄膜発光体の作製

三枝栄子 大阪公立大学

## 【背景・目的】

3 価のランタノイドイオンの発光は、長寿命でスペクトルの線幅が狭いことが特徴であり、この発光特性を利用してレーザーやバイオセンサーなどに応用されている。我々は、環状ポリアミンにコレステリル基を導入した両親媒性キレート配位子を開発し、様々なランタノイド錯体を報告している。この錯体は水溶液中で自己会合コロイドを形成し、疎水場の効果によりランタノイドイオンの長寿命発光を実現した。これまでの成果より、配位子 **L** およびユウロピウム錯体 **EuL** の単分子膜を LB 法により作製することに成功した。pMAIRS (偏光多角入射分解分光) 法を用いた赤外分光分析を行い、膜中の微細構造を明らかにした。**EuL** 積層膜の発光スペクトルから  $\text{Eu}^{3+}$  由来の微弱な発光を観測したが、膜厚と発光強度の定量評価には至らなかった。

Fig.1 Structures of **[EuL]·3Cl** and sensitizer (HABA).

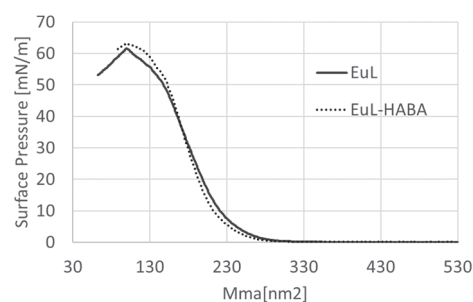
また先行研究において、**EuL** コロイドに増感剤を添加すると強い増感発光が得られ、溶液中のアニオン交換で消光することが見出されている<sup>1)</sup>。本研究では、これを薄膜に拡張し固体センサーとして利用できるか検証することを目的とし、**EuL** の積層膜作製および増感剤を添加した場合の膜構造変化と発光特性について検討した。

## 【実験方法】

LB 法により Si 基板上に **EuL** の積層膜と、増感剤 (HABA, Fig.1) を 1 当量添加した積層膜 (**EuL**-HABA) を作製し、pMAIRS 法を用いた赤外分光分析により膜構造解析を行った。それぞれの発光スペクトルを測定し、薄膜中の増感効果について評価した。

## 【結果・考察】

**EuL** および **EuL**-HABA の水面上単分子膜の $\pi$ -A 曲線を Fig.2 に示す。**EuL** の単分子膜は、これまでの結果をよく再現した。**EuL**-HABA の $\pi$ -A 曲線は、**EuL** 単独の膜に比べて極限面積はほとんど変わらないが表面圧の立ち上がりが大きくなった。HABA が錯体同士を引き付ける働きをする可能性が示唆された。この成膜条件で作製した **EuL** 積層膜の pMAIRS スペクトルから、 $1627\text{ cm}^{-1}$  に C=O 伸縮、 $1574\text{ cm}^{-1}$  に NH 変角の吸収が観測されたが、面内・面外の配向性は見られなかった。**EuL**-HABA 積層膜も同様に評価を行ったが、増感剤がどのように存在しているか詳細な解析に至らなかった。発光スペクトル測定から、**EuL**-HABA 積層膜は **EuL** 積層膜に比べて強い発光を示し、膜中の増感効果を確認することができた。

Fig.2  $\pi$ -A curve of **EuL** w/o HABA

【文献】 1) T. Sagami *et al.*, *Chem. Commun.*, **2017**, 53, 3967.



## フッ素系樹脂の摩擦界面における分子挙動の解明

粕谷素洋 公立小松大学

フッ素樹脂は優れた自己潤滑性を示すため、固体潤滑剤として自動車や船のエンジン内ピストン摺動部等に用いられている。一方で、フッ素樹脂は耐摩耗が課題となっており、フィラー等の添加による改善が行われてきたが、そもそも摩擦・摩耗中の高分子鎖挙動やフィラーの役割について、分子レベルでは分かっておらず、さらなる摩耗特性の改善にはその化学的過程の理解が必要な状況である。

申請者はこれまでシリコン系水潤滑材料やゴム-氷間における摩擦挙動を含む界面分子挙動を精密摩擦試験と分光手法を組み合わせることで、新規な分子レベルの摩擦・潤滑機構を解明してきた（例： J. Phys. Chem. 2013, Soft Matter 2019, 光化学 2021）。現在、同様の手法を医療用高分子材料やフッ素樹脂等、摩擦分野で重要な他の樹脂に展開すべく、研究を進めている。

これらの研究を通して、申請者は真に摩擦を分子レベルで理解するためには、① 分子数の少ない界面層を検出可能な感度の高さ、② 分子情報、特に配向を直接観測可能、という2点を兼ね備えた分光手法が必要、という着想を得て、本申請の共同研究者である京大化研長谷川教授の開発した多角入射分解赤外分光法(IR-MAIRS)を摩擦界面の評価法として展開することを着想した。

本研究では、IR-MAIRS 法によりフッ素樹脂の摩擦・摩耗に伴う分子構造変化を捉え、摩擦機構の分子レベルでの解明に利用可能であることを示すことを目的とした。実験としては、シリコンウェハにスピコート法により成膜したフッ素樹脂薄膜（ポリ（フルオロアルキルアクリレート））をもう一枚のシリコン基板と接触・せん断させ、前後での IR-MAIRS スペクトル変化を比較した結果を右図に示す。1300  $\text{cm}^{-1}$  周辺の  $\text{CF}_3$  伸縮振動に由来するピークには面内/面外の比率に変化がないのに対して、1200  $\text{cm}^{-1}$  周辺のフォノンバンドには大きな変化が観測された。これはパーフルオロアルキル鎖の配向は変化せず、集合構造は変化することを示している。

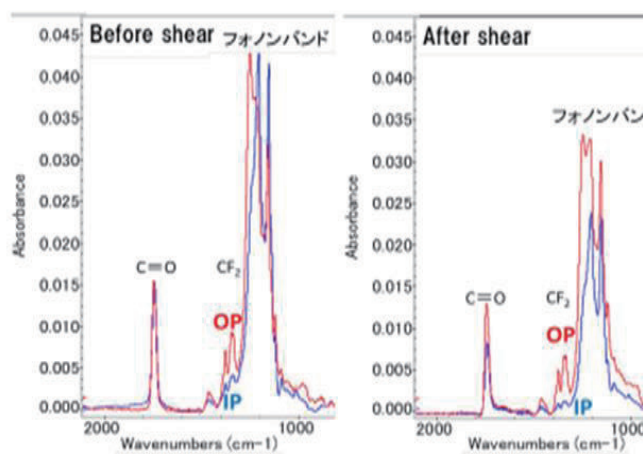


図 フッ素樹脂薄膜の摩擦に伴う面内および面外の赤外スペクトル変化

以上の結果より、IR-MAIRS 法が摩擦による分子構造変化の評価に適用可能であることを示すことができた。これらの成果の一部については、日本化学会第 103 春季年会(2023 年 3 月)、およびトライボロジー会議 2023 春 東京にて発表予定である。



## エクソソームの細胞内への送達設計

中瀬生彦 大阪公立大学

生体における殆ど全ての細胞は小胞を絶えず分泌しているが、例えば直径が約 30~200 nm のエクソソームは、分泌時に microRNA や酵素といった生理活性分子を内包し、それらの「メッセージ」を離れた細胞に送ることで細胞間情報伝達を行なっている。近年では、がんを含む疾患進展にエクソソームが影響を及ぼすことが明らかにされ、がんの転移を誘導するエクソソームや、エクソソームを化学的にブロックすることで転移を抑制する技術構築も進められている。一方でエクソソームは、薬学的な観点から (1) 免疫制御が可能、(2) 毒性が低い、(3) 遺伝子発現による膜タンパク質の人工化 (配向性制御)、(4) 活性分子カクテルの天然・人工内包、(5) 細胞間コミュニケーション経路の利用等の高い優位性より、次世代の薬物運搬体として大きく期待されており、国内は遅れているものの世界的に臨床研究も盛んに進められている。研究代表者は、これまでにエクソソームの細胞内移行におけるマクロピノサイトーシス経路の重要性を世界に先駆けて報告し、がん受容体 (EGFR や CXCR4) の活性化や K-Ras 変異体発現でのマクロピノサイトーシス誘導促進によるエクソソームを介した細胞間コミュニケーションの増強や、それを逆手にとるマクロピノサイトーシス誘導型エクソソームを基盤とした drug delivery system (DDS) の構築を展開してきた[1, 2]。本研究は、研究代表者がこれまでに開発してきたエクソソームを含む細胞外小胞の機能化において、特にがん細胞への高い標的性とサイトゾル送達性を兼ね添えたエクソソーム DDS の技術構築を目指すことを目的としている。これまで、研究代表者はポリアルギニンや、抗菌タンパク質由来新規細胞内送達ペプチド修飾によるエクソソームの細胞内取込促進を達成している[3,4]。本研究プロジェクトでは、さらに超音波を新たに用いることで、効率的な機能性ペプチド修飾技術を構築しつつある。これまでのペプチド修飾技術では、エクソソーム膜へ目的ペプチドを結合させるために 30 分以上反応させる必要があったが、見出した超音波を新たに用いる手法では数十秒といった短時間で、エクソソーム膜への十分なペプチドの結合性、及び、例えばマクロピノサイトーシスを誘導するペプチドを用いた場合では、がん細胞内への取り込み量の顕著な上昇が確認されている。現在、本手法で適用できる機能性ペプチドの種類や、化学結合様式、エクソソーム物性の評価を中心に、さらなる研究展開を続けており、生体から単離したエクソソームを如何に早く機能化できるかといった重要な課題の中で、本基盤技術・知見は DDS 技術構築に大きく貢献できることが強く考えられる。本研究課題を通して、医療応用を見据えたさらなる技術構築が達成できるように研究を一層進展させる。

## &lt;参考文献&gt;

[1] Nakase, I. *et al. Sci. Rep.* 5, 10300 (2015), [2] Nakase, I. *Processes* 9, 224 (2021), [3] Noguchi, K., Nakase, I. *et al. Mol. Pharm.* 18, 3290-3301 (2021), [4] Hirase, S., Nakase, I. *et al. Mol. Pharm.* 19, 1135-1145 (2022)

## 細胞外小胞の標的細胞への移行メカニズムの解明

江口暁子 三重大学

### 【目的】

研究代表者は、慢性肝疾患の病態進行過程において、障害肝細胞由来細胞外小胞(障害 HC-EV)と正常肝細胞由来細胞外小胞(正常 HC-EV)による標的細胞の活性化には、違いがあることを明らかにしている。しかし、障害 HC-EV と正常 HC-EV の標的細胞への取り込み量や取り込み経路の違いについては、全く解明できていない。そこで、障害 HC-EV が細胞間情報伝搬経路としてマクロピノサイトーシスを介して各種標的細胞へ取り込まれる機構を解明し、障害 HC-EV に特異的な取り込み経路を同定することを目的とする。この研究過程において、取り込み量の測定や取り込み経路の可視化等、様々な化学的な実験要素が必須となるため、化学研究所・二木史朗博士が開発した実験系を利用するために共同研究を実施する。研究代表者である江口は、共同研究者である二木史朗博士が開発した「細胞外小胞の細胞内動態検出系」を活用して、障害 HC-EV と正常 HC-EV の各種標的細胞への移行量を定量し、障害 HC-EV と正常 HC-EV 間の移行量の違いや標的細胞間における移行量の違いを明らかにする。

### 【実験方法】

共同研究者である二木史朗博士がこれまでの研究で培ったマクロピノサイトーシス等の細胞への取り込み経路の実験条件を利用して、各種阻害剤を用いて細胞内移行経路に関して検討することで、障害 HC-EV と正常 HC-EV の標的細胞への取り込み経路を明らかにする。なお、フローサイトメトリーや共焦点レーザー顕微鏡や標的細胞における遺伝子発現レベルを用いて、取り込み経路を評価する。

### 【実験結果】

様々な阻害剤を用いた検討から、障害 HC-EV と正常 HC-EV の標的細胞への取り込みは、マクロピノサイトーシスを始めとする様々な経路を介して行われていることや、標的細胞により取り込みの経路は異なることが明らかとなった。さらに2つの標的細胞を用いた比較実験から、障害 HC-EV や正常 HC-EV の取り込み経路の優位性は、標的細胞により異なる可能性があることが示唆された。現段階において、障害 HC-EV と正常 HC-EV の取り込み経路に大きな差異はないと思われるが、阻害剤を用いた検討で HC-EV の取り込み阻害が強くかからない標的細胞もあり、異なる取り込み経路の検討が必要である。

### 【考察】

標的細胞によって HC-EV の取り込み経路が異なることが明らかとなったが、阻害剤で取り込みが完全に抑制できない標的細胞もあることから、阻害剤以外の取り込み経路についても検討する必要がある。さらに、HC-EV が取り込まれる他の標的細胞についても検討をすすめる。

### 【成果報告】

特になし

## Role of PIP5K Genes in Pollen Tube Development

Li-Jia Qu Peking University

**Objectives:** Phosphatidylinositol (4,5)-bisphosphate [PtdIns(4,5) $P_2$ ], one of phosphoinositides serving as lipid signals on eukaryotic membranes, modulates various cellular processes including cytoskeletal organization, membrane trafficking, and signal transduction for gene expression. PtdIns(4,5) $P_2$  localizes mainly to the plasma membrane or its membrane subdomains, and physically interacts with various regulatory proteins. The spatiotemporal existence of PtdIns(4,5) $P_2$  is critical for its signaling function, and established basically via its metabolism. Although the metabolic pathways of phosphoinositides are elaborately linked to one another, phosphatidylinositol 4-phosphate 5-kinase (PIP5K), which produces PtdIns(4,5) $P_2$  by phosphorylating PtdIns(4) $P$ , is thought to be a key enzyme responsible for the spatiotemporal pattern of PtdIns(4,5) $P_2$  in higher plant cells, where some of the phosphoinositide metabolic pathways found in animal or fungal cells are missing. In plants, PtdIns(4,5) $P_2$  has been studied especially for its involvement in root hair and pollen tube growth mainly using the *Arabidopsis* system. We have identified a set of PIP5K genes the complete loss of functions of which caused male sterility. Pollens with the multiple mutations were found to be defective of pollen tube development. In this study, an essential role of PIP5K in pollen germination was investigated.

**Experimental Methods:** T-DNA or transposon tagging mutant lines of the *PIP5K4*, *PIP5K5*, and *PIP5K6* genes were obtained from public organizations for biological resources. Loss-of-function mutant lines for the genes were established, and crossed with one another to obtain multiple mutant lines. Single and multiple mutant lines of the *PIP5K4–6* genes were examined for their phenotypes in pollen development and germination by microscopic observation.

**Results and Discussion:** We investigate processes of the pollen development and germination by detailed microscopic observation. Using the double mutants *pip5k4pip5k5*, *pip5k4pip5k6*, and *pip5k5pip5k6*, we found that the *PIP5K4–6* genes redundantly function in pollen germination as well as pollen tube growth. The *pip5k4pip5k5pip5k6* triple mutant pollen grains, which were obtained from heterozygous triple mutants, were apparently normal in their morphology. However, they couldn't germinate under germination conditions while some of them swelled and ruptured their cell wall. Phylogenetic analysis of type-B PIP5Ks revealed that four clades, which contain PIP5K1–3, PIP5K4–6, PIP5K7–8, PIP5K9, respectively, are conserved in angiosperms, while gymnosperms have type-B PIP5Ks only in the parent clade containing the PIP5K7–8 and PIP5K9 clades. We hypothesize that a common ancestor of the *PIP5K4–6* genes evolutionally differentiated to function in the pollen germination, a critical process for the elaborate angiosperm pollen system.

## Construction of heterologous protein secretion system at low temperatures by using cold-adapted microorganisms

Xianzhu Dai   Southwest University

**[Background and Objectives]** *Shewanella vesiculosa* HM13, a psychrotrophic bacterium isolated by the group of the ICR partner researcher (Prof. Tatsuo Kurihara) from fish intestine, secretes a large number of spherical particles called extracellular membrane vesicles (EMVs) at low temperatures. These vesicles carry an S-layer protein-like protein, P49, as a single major cargo protein. P49 is translocated across the inner membrane from the cytoplasm to the periplasmic space by the Sec translocon and then translocated across the outer membrane to be secreted to the extracellular space by a type II secretion system (T2SS)-like apparatus. P49 is predicted to bind to capsular polysaccharide on the surface of the cells and EMVs. This cargo transportation mechanism is expected to be useful for vesiculation-mediated heterologous protein production. In the previous study, green fluorescent protein fused to P49 was detected in the cellular and EMV fractions, suggesting that P49 can transport its fusion partner to EMVs. However, the fusion of heterologous proteins was found to reduce the efficiency of transport of the fused P49 to EMVs. In this study, we evaluated the effects of the fusion of various peptide tags to N- and C-terminal regions of P49 on its transport to EMVs.

**[Results and Discussion]** When StrepII tag was inserted downstream of the P49 secretion signal for the Sec translocon, the tagged protein was not detected in both the cellular and extracellular fractions. This suggests that insertion of the tag to the immediate downstream region of the secretion signal affected the efficiency of translocation of P49 across the inner membrane by the Sec translocon and that the fusion protein was degraded in the cells. When StrepII, G11, and SpyT tags were introduced into the C-terminal region of P49, the tagged proteins were detected only in the cell fraction and not detected in the extracellular space. This suggests that the C-terminal tag insertion interfered with the interaction of P49 with the T2SS-like apparatus and inhibited the translocation of the fusion proteins across the outer membrane, resulting in their accumulation in the periplasmic space. Although the mechanism of the substrate recognition of this secretion apparatus is unknown, the C-terminal region of P49 might be involved in its interaction with this apparatus. For surface modification of EMVs by modification of P49, it is important to introduce a fusion partner without disturbing the translocation of P49 across both the inner and outer membranes. The type of tag sequence and insertion sites that do not interfere with the translocation of the fusion protein should be explored in future studies.

## Structural and functional analysis of the surface polysaccharides of outer membrane vesicles released by bacteria

Maria Michela Corsaro University of Naples Federico II

### Objectives:

The aim of this research has been the characterization of the capsular polysaccharides (CPS) isolated from the cells of the *nfnB* mutant of *Shewanella vesiculosa* HM13. Previous studies suggested that the affinity between CPS and P49 is reduced in the mutant that lacks *nfnB*, a gene in the close vicinity of the P49 gene. Therefore, we have been focused on the structural analysis of polysaccharides isolated from this mutant. The group of the ICR partner researcher (Prof. Tatsuo Kurihara) has furnished the samples, and the characterization has been performed by NMR spectroscopy.

### Experimental:

Dried cells (1.9 g) of *nfnB* mutant from *S. vesiculosa* HM13 were extracted with either phenol/chloroform/light petroleum (PCP) or hot phenol/water methods (Galanos et al 1969), and the crude lipooligosaccharide (LOS) was precipitated as already reported (Di Guida et al. 2020). The extracts were dialyzed against water (cut-off 3500 Da) and lyophilized. The samples were treated with 1% CH<sub>3</sub>COOH (100 °C, 3 h) and, after centrifugation, the supernatants were fractionated on a Bio-Gel P-10 column (Sigma, 90 × 0.75 cm, flow rate 12.0 mL/h, fraction volume 2.5 mL) eluted with water. Two fractions were obtained and analysed.

### Results:

The glycosyl GC-MS analysis, performed on the first fraction, disclosed the presence of rhamnose (Rha), glucose (Glc), and 2-amino-2-deoxy-glucose (GlcN), as already reported (Casillo et al., 2022). In addition, this fraction was analysed by <sup>1</sup>H NMR. The spectrum confirmed the presence of the same CPS already characterized from the wild-type cells. Furthermore, the <sup>1</sup>H NMR spectrum of the second fraction isolated from the water/phenol extract revealed the production of an additional CPS. The latter will be characterized by means of chemical analyses and 2D NMR experiments.

Casillo, A. et al. Marine Drugs (2019), 17, 34.

Di Guida et al. Marine Drugs (2020), 18, 231.

Casillo et al., Carbohydrate Polymers (2022), 297, 120036.

**Molecular mechanisms for the inactivation of a growth hormone in rice**

Zuhua He Chinese Academy of Sciences

**Objectives:** Gibberellins (GAs) are a group of tetracyclic diterpenoid carboxylic acids. They act as plant hormones that control diverse developmental processes. Bioactive GAs play critical roles in promoting growth, including internode (stem) elongation of rice. The *elongated uppermost internode 2 (eui2)* mutant of rice shows a tall phenotype due to its elongated uppermost internode. Because of this reason, this mutant has been utilized in hybrid rice breeding in order to eliminate panicle enclosure in male sterile parents. Previously, we have shown by map-based cloning that EUI2 is a functionally-uncharacterized protein that belongs to the  $\alpha,\beta$ -fold hydrolase superfamily. In collaboration with Shinjiro Yamaguchi's group, we have previously characterized the rice *eui* mutant and found that *EUI* encodes a cytochrome P450 enzyme that deactivates GAs via 16 $\alpha$ ,17-epoxidation. Based on these results, we speculated that EUI2 might act as an epoxy hydrolase and further deactivate epoxidated GAs in the uppermost internode of rice. In fact, our collaboration showed that EUI2 protein could hydrolyze epoxy GAs *in vitro*. In addition, we determined the levels of endogenous 16 $\alpha$ ,17-epoxy GAs in wild type and the *eui2* mutant by LC-MS/MS analysis.

**Experimental methods:** Various 16,17-modified GA derivatives were chemically synthesized, and their biological activities were determined using GA-deficient rice seedlings. Endogenous levels of epoxy GAs in another genetic background of WT and *eui2* mutant rice plants were determined by LC-MS/MS using deuterium labeled epoxy GAs as internal standards.

**Experimental results:** We chemically synthesized 16,17-modified GA<sub>4</sub> derivatives and found that many of them are weakly, but significantly active in promoting the second leaf sheaths of rice seedlings. In addition, our data also showed that the biological activity of the hydrolyzed product (16,17-dihydroxy GA<sub>4</sub>) was significantly weaker. This finding suggests that EUI2 plays a role in further deactivating epoxy GA<sub>4</sub>. Previous X-ray crystallographic analysis of the GA<sub>4</sub>-GID1 complex suggested that C-17 plays an important role in closing the lid of the GID1 receptor through hydrophobic interaction. Therefore, the introduction of a hydroxyl group at C-17 may inhibit this hydrophobic interaction. This would explain why 16,17-dihydroxy GA<sub>4</sub> (EUI2 product) is nearly inactive. To confirm the results obtained before, we analyzed endogenous epoxy GAs in another genetic background of WT and *eui2* mutant rice plants. Consistent with the previous data, the *eui2* mutant accumulated epoxy GAs at much higher levels than does WT.

**Publications:** In preparation.



## Analysis of novel transporters for strigolactones or their biosynthetic intermediates

Yunde Zhao   University of California San Diego

**Objectives:** Strigolactones (SLs) are carotenoid-derived plant hormones that regulate various processes of plant growth and development. They are also secreted from plant roots into the rhizosphere and function as allelochemicals for symbiosis with arbuscular mycorrhizal fungi and for stimulating seed germination of parasitic plants. Classical grafting studies have suggested that SL and/or its biosynthetic intermediate(s) can move from roots to shoots, but much has not been fully elucidated about SL transport. Previously, we likely have identified novel transporters for SLs or intermediates for SL biosynthesis in rice. The knockout mutants of the transporters increased tiller numbers, which are phenotypically very similar to those well-characterized SL biosynthesis mutants and signaling mutants. The physiological and biochemical roles of the identified transporters need to be experimentally demonstrated.

### Experimental methods:

#### Our group

- Phenotypic and genetic interaction studies of the mutants whose ability to transport SLs or SL biosynthetic intermediates have potentially been compromised.
- Generation of additional mutants using CRISPR/Cas9 gene-editing technology.

#### ICR partner researchers (Dr. Kiyoshi Mashiguchi, Prof. Shinjiro Yamaguchi)

- Analysis of the endogenous levels of SLs and SL biosynthetic intermediates by LC-MS/MS to find transporters' substrate(s).
- Elucidation of SLs and SL biosynthetic intermediates that can move from roots to shoots
- Evaluation of transporters' export/import activity toward the candidate compound(s).

**Experimental results:** This year, we further conducted genetic studies on the putative SL transporters. Moreover, ICR partner researchers discovered that two SL biosynthetic intermediates, carlactone and carlactonoic acid, can move from roots to shoots in Arabidopsis. Furthermore, they also showed that methyl carlactonoate, a bioactive SL in Arabidopsis, is not likely mobile. In addition, they found SL-related compounds in xylem sap in Arabidopsis and rice. We are going to analyze the endogenous amounts of SLs and their biosynthetic intermediates using the knockout mutants of the transporters.

**Publications:** No publications from the collaboration in FY2022.

## Phase separation in mixture of nematic liquid crystal and solvent

Ryoko Shimada Japan Women's University

Mixtures of liquid crystalline (LC) molecules and ordinary solvents have two order parameters, the concentration  $\phi$  and orientation  $Q$  of the LC molecules, that are fluctuating with time in a coupled way. This study focuses on such a mixture of dimethyl terephthalate (DMT) and 4-cyano-4'-pentylbiphenyl (5CB) to examine their phase diagram shown in Fig.1. (This diagram was obtained from FTIR analysis of aliquots taken from the phase-separated DMT/5CB mixture.)

The previous study<sup>1)</sup> combined the Flory-Huggins (FH) and Landau-de Gennes<sup>2)</sup> (LdG) theories to formulate a model describing the phase behavior in the absence of crystalline. This study extends the model to allow coexistence of the isotropic or nematic phase with the DMT crystalline phase. For example, the extended model expresses the free energies  $G$  of the nematic and crystalline phases as

$$\begin{aligned} \text{nematic phase: } \frac{G^{[\text{nem}]}}{RT} = & n_{\text{DMT}}^{[\text{nem}]} \ln \phi_{\text{DMT}}^{[\text{nem}]} + n_{5\text{CB}}^{\text{total}} \ln \phi_{5\text{CB}}^{[\text{nem}]} + \chi N n_{5\text{CB}}^{\text{total}} \phi_{\text{DMT}}^{[\text{nem}]} \\ & + n_{5\text{CB}}^{\text{total}} \left\{ A \left[ T - T^{**} \right] Q^2 + B Q^3 + C Q^4 \right\} + \frac{n_{\text{DMT}}^{[\text{nem}]}}{RT} \mu_{\text{DMT}}^{[\text{liq}]} \end{aligned} \quad (1)$$

$$\text{crystalline phase: } \frac{G^{[\text{cry}]}}{RT} = \frac{n_{\text{DMT}}^{\text{total}} - n_{\text{DMT}}^{[\text{nem}]}}{RT} \mu_{\text{DMT}}^{[\text{cry}]} \quad (2)$$

where  $RT$  is the thermal energy,  $n_i^{[\alpha]}$  and  $\phi_i^{[\alpha]}$  denote the mole number and volume fraction of the component  $i$  in the phase  $\alpha$ ,  $n_{5\text{CB}}^{\text{total}}$  is the total mole number of 5CB,  $N (\cong 2)$  is the molar volume ratio of 5CB to DMT, and  $\mu_{\text{DMT}}^{[\text{liq}]}$  and  $\mu_{\text{DMT}}^{[\text{cry}]}$  are the chemical potential of DMT in the dissolved liquid state and undissolved crystalline state, respectively.  $A$ ,  $B$ ,  $C$ , and  $T^{**}$  are the LdG parameters introduced previously<sup>1)</sup>. For adequately tuned LdG parameters, minimization of the total free energy  $G^{[\text{nem}]} + G^{[\text{cry}]}$  gives  $\phi_{\text{DMT}}^{[\text{nem}]}$ . The result is shown in Fig.1 with the blue curve. The green and red curves show  $\phi_{\text{DMT}}^{[\text{iso}]}$  in the isotropic phase coexisting with the nematic (DMT/5CB) and crystalline (DMT) phases. This  $\phi_{\text{DMT}}^{[\text{iso}]}$  is obtained from  $G^{[\text{nem}]}$  and/or  $G^{[\text{cry}]}$  combined with  $G^{[\text{iso}]}$  (expressed in a way similar to eq. (1) but with  $Q = 0$ ). These curves well describe the experimental phase boundaries (black circles), and suggest an apparent triple point (green circle) at a given pressure. It is of interest to compare the fluctuation of  $\phi$  and  $Q$  deduced from the model and that obtained in future experiments.

1) Shimada, Urakawa, Inoue, and Watanabe, *Soft Matter*, **17**, 6259-6272 (2021).

2) de Gennes and Prost, *The Physics of Liquid Crystals*, Clarendon Press, Oxford, 1993.

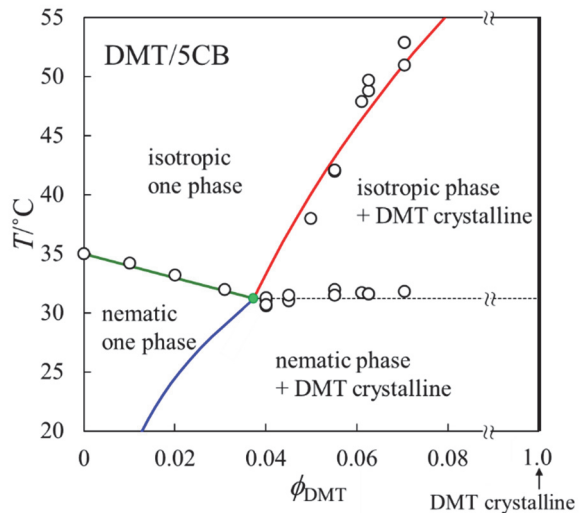


Fig. 1 Phase diagram of DMT/5CB mixture

## Chromatin, epigenetic and proteolytic regulation of RNA processing in plant morphogenesis

Vicente RUBIO National Center of Biotechnology

Objectives: We focus to understand molecular mechanisms bridging proteolysis to mRNA processing in environmental adaptation. Arabidopsis was used as a model to investigate CRLs, DCAFs, CSN and their binding factors, that are highly conserved among kingdoms. To date, plants have utilized these protein complexes in adaptation to light environmental changes. CFI (cleavage factor I) is a complex that binds CSN in mammals and plants, and is involved in processing 3' UTR ends of pre mRNAs. In my group at CNB-CSIC, taking advantage of “tandem affinity purification” and “protein detection” system, CFI-interacting proteins has been analyzed using different bait and environmental conditions. The results are being cross-examined against the DCAF list that we have. Preliminary results suggested promising overlaps in certain proteins categories of each list.

Experimental results: Through complementary collaboration with Dr. Tsuge's group at ICR, numerous proteins have been listed up as interacting partners for CRLs, DCAFs, CSN and their binding factors. However, it remains unclear which network is the key network linking proteolysis to mRNA processing regulation. We revealed that Arabidopsis CFI 25a subunit interacts with CFI 25a, CFI 59, and CFI 68, confirming that an intact CFI complex could be formed in plants. Six out of 8 subunits composing the CSN protein complex was also identified. The two smaller subunits might have not been identified due to the resolution of the experimental setup. We also observed an overrepresentation of proteins involved in proteolysis. This led us to believe that CSN-CFI interaction could be a key link between proteolysis and mRNA processing regulation.

Discussion: These unique results were outcome of taking advantage of the plant system as a model to comprehend a universal regulatory system. We favor our hypothesis that diverse yet temporal-regulated transcript usages are key to respond to specific environmental stimuli. Further collaboration will gain understanding of the key general platform for gene expression regulation *via* proteolysis and transcriptional regulation.

Publications: Zhang X, Nomoto M, Garcia-León M, Takahashi N, Kato M, Yura K, Umeda M, Rubio V, Tada Y, Furumoto T, Aoyama T, Tsuge T. (2022) CFI 25 Subunit of Cleavage Factor I is Important for Maintaining the Diversity of 3' UTR Lengths in *Arabidopsis thaliana* (L.) Heynh. ***Plant Cell Physiol.*** 63:369-383. doi: 10.1093/pcp/pcac002.

*In preparation*, " Plant Cleavage Factor I complex regulates cleavage and polyadenylation of its own subunit mRNAs"

## Site-Selective Protein Acetylation and Phosphorylation by Small Molecules

Lu Zhou Fudan University

Post-translational modifications (PTMs) play essential roles in regulating a myriad of cellular processes in mammalian cells, including signal transduction, metabolism, and gene transcription. Dysregulation of protein modifications causes metabolic diseases, immune diseases and cancers. Among protein modifications, acetylation and phosphorylation represents the most critical PTM. In FY2022, we collaborated with the Uesugi research group of ICR to develop small molecules that specifically acetylate cellular proteins to control human immune responses.

The presence of DNA in the cytoplasm is normally a sign of microbial infections and is quickly detected by cyclic GMP-AMP synthase (cGAS) to elicit anti-infection immune responses. It has been reported that Lys acetylation of cGAS inhibits its activation to impair cGAS-mediated immune responses. To discover a small molecule that selectively acetylates cGAS, we exploited the structure of RU521, a known cGAS inhibitor, as a starting point. The introduction of an acetyl ester group to the structure at varied positions led to a series of candidate cGAS-acetylation compounds. In FY2022, we found that one of these compounds, CCY-G2o8, acetylated cGAS in vitro and in cells. In line with its ability to acetylate cGAS, CCY-G2o8 reduced the protein expression level of IFN $\beta$ <sub>1</sub>, a representative cGAS-responsive interferon, in human THP-1 immune cells. Consistent with this, other biological assays conducted in our Fudan lab also showed that CCY-G2o8 inhibits phosphorylation of IFR<sub>3</sub>, a downstream event of cGAS, to decrease the promoter activity of the IFN $\beta$ <sub>1</sub> gene.

In a separate project, we collaborated with the Uesugi group of ICR to develop non-cysteine-targeting covalent inhibitors. Our collaboration was published in *ACS Chem. Biol.* in 2022.

### Publication

Jung Y, Noda N, Takaya J, Abo M, Toh K, Tajiri K, Cui C, Zhou L, Sato S, Uesugi M.  
Discovery of Non-Cysteine-Targeting Covalent Inhibitors by Activity-Based Proteomic Screening with a Cysteine-Reactive Probe.  
*ACS Chem. Biol.* 17, 340-347 (2022).

# Developments of highly efficient and high color purity organic electroluminescent devices based on thermally activated delayed fluorescent materials exhibiting ultrafast reverse intersystem crossing process

Lian Duan Tsinghua University

This project focused on the thermally activated delayed fluorescence (TADF) sensitized fluorescent (TSF) systems, which realize high efficiency and high color purity simultaneously on organic light-emitting diodes. The systems generally consist of a host, a TADF sensitizer, and a fluorescent terminal emitter (TE). Hosts can affect photophysical properties of TADF molecules, which may further influence the performance of TSF systems. However, most reported TSF systems focused on TADF sensitizers and TEs, and there have been rare investigations about the host effects on the TSF systems.

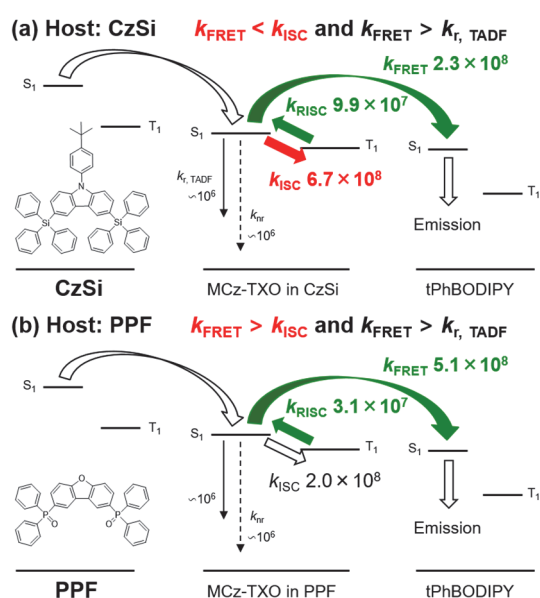


**Figure 1.** The excitons transfer processes in the solution-processed 0.5 wt% tPhBODIPY: 20 wt% MCz-TXO: (a) CzSi/ (b) PPF, respectively.

Experimentally, both TSF systems showed fast FRET from MCz-TXO to tPhBODIPY. However, the PPF-host TSF system is expected to show a much more effective FRET. At first, the rate constant of FRET,  $k_{\text{FRET}}$ , ( $5.1 \times 10^8 \text{ s}^{-1}$ ) in PPF is larger than the  $k_{\text{FRET}}$  ( $2.3 \times 10^8 \text{ s}^{-1}$ ) in CzSi; second, the  $k_{\text{FRET}}$  is larger than the rate constant of intersystem crossing ( $k_{\text{ISC}}$ ) in PPF while the  $k_{\text{FRET}}$  is smaller than the  $k_{\text{ISC}}$  in CzSi. Therefore, more excitons can be transferred to tPhBODIPY for narrow emission in the PPF-host TSF system than the CzSi-host one. Dexter energy transfer (DET) behaviors were also investigated. Experimentally, DET was successfully inhibited in the PPF-host system although it occurs in the CzSi-host system. These investigations experimentally demonstrated the profound impacts of hosts on the FRET and DET in the TSF systems and also provided a novel strategy for suppressing the undesired DET.

The manuscript highlighting this work will be submitted soon. In addition, another manuscript closely related to this joint work and also focusing on the host effects in the solution-processed TSF systems is in preparation.

[1] Y. X. Ren *et al.*, Appl. Phys. Express **14**, 071003 (2021). [2] X. Z. Song *et al.*, Adv. Opt. Mater., **8**, 2000483 (2020).

## Fabrication of nanotopographical polymer surfaces for bactericidal properties-IV

Maya Endoh Stony Brook University

**Objective.** The adhesion of unwanted pathogenic bacteria creates a great challenge and health risks when designing implantable medical devices. In response, significant efforts have been made to design effective antibacterial surface coatings. Antibacterial surfaces are typically based on liquid-repellent (superhydrophobic) or bactericidal properties. However, either single property alone has a disadvantage in practical applications: liquid-repellent surfaces cannot kill bacteria, while accumulations of dead bacteria and debris on the bactericidal surfaces may compromise long-term biocidal activity or trigger immune responses and inflammation. Here we develop synergistic surfaces combining bacteria-releasing and bactericidal properties against *Escherichia coli* (*E. coli*, a Gram-negative bacterium) using block copolymer (BCP) lithography.

**Experimental.** A cylinder-forming polystyrene-*block*-poly(methyl methacrylate) (PS-*block*-PMMA) diblock copolymer ( $M_{w,PS}=45,900$  g/mol,  $M_{w,PMMA}=138,000$  g/mol, polydispersity ( $M_w/M_n$ )=1.16) was purchased from Polymer Source Inc. Additionally, PS with  $M_w=30,000$  g/mol ( $M_w/M_n$ =1.06, Pressure Chemical Co.) was used to prepare a “non-preferential” surface coating (hereafter assigned as “PS nanocoating”) for the development of perpendicular oriented microdomains in block copolymer thin films deposited on silicon (Si) substrates<sup>1</sup>. The detail of the sample preparation process is explained in Ref. 1. Since PS is not biocompatible, we deposited a very thin titanium oxide (TiO<sub>2</sub>) layer (about 3 nm in thickness) on the PS nanopillars using atomic layer deposition.

**Results.** We found that the PS “nanopillars” (with height of about 10 nm, size of about 50 nm, and spacing of about 70 nm) exhibit highly effective bactericidal and bacteria releasing properties (“dual properties”) against *E. coli* for at least 36 h of immersion in an *E. coli* solution (Fig. 1). Interestingly, the PS nanopillars coated with a thin layer of TiO<sub>2</sub> (“TiO<sub>2</sub> nanopillars”) show much improved dual properties against *E. coli* compared to the PS nanopillars. To understand the mechanisms underlying the dual properties, implicit solvent coarse-grained molecular dynamics (MD) simulations of a lipid bilayer (as a simplified model for *E. coli*) in contact with a substrate containing cylindrical hydrophilic pillars were performed. The MD data revealed the critical role of a bacterium/substrate interaction in the adhesion of a bacterial cell wall on nanopatterned surfaces. Membrane rupture occurs when the nanopillars generate sufficient tension within the lipid bilayer clamped at the edges of the nanopillars, leading to the formation of pores between nanopillars. The adhesion-mediated rupture is more pronounced for Gram-positive bacteria since the adhesion area to the nanopillar surface is limited owing to the stiffer mechanical properties, causing higher stress concentrations within the bacterial cell wall at the edge of pillars. The results are summarized in the recent publication of *ACS Applied Materials & Interfaces*. (See Ref. 1.)

### Reference

1. Structure-Based Design of Dual Bactericidal and Bacteria-Releasing Nanosurfaces (D. Salatto, Z. Huang, P. T. Benziger, J.-M. Y. Carrillo, Y. Bajaj, A. Gauer, L. Tsapatsaris, B. G. Sumpter, R. Li, M. Takenaka, W. Yin, D. G. Thanassi, M. Endoh, T. Koga), *ACS Appl. Mater. Interfaces*, 2023, 15, 2, 3420-3432.

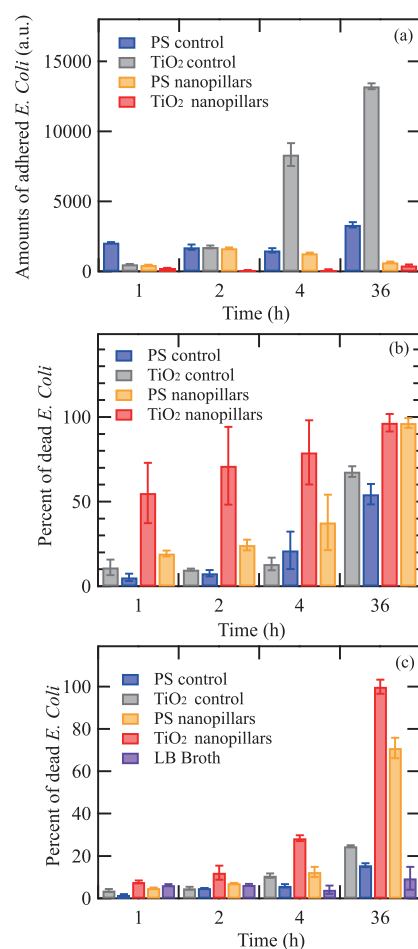


**Figure 1.** (a) Time dependence of the amount of adhered *E. coli* after incubating the samples, (b) the percentage of dead *E. coli* adhered onto the sample surfaces, (c) the percentage of dead *E. coli* extracted from the well solution (LB broth) for the planar PS thin film (15 nm thick), the planar TiO<sub>2</sub> thin film (3 nm thick), the PS nanopillars, and TiO<sub>2</sub> nanopillars. Data from Ref. 1.



## Verification and development of dynamic stiction theory

Ken Nakano   Yokohama National University

**Objectives** – Since the time of Charles-Augustin de Coulomb (1736–1806), we have believed that there exist two types of solid friction: static and kinetic. However, in 2020, Nakano and Popov published a different friction theory indicating that static friction might be an illusion made by the rotation of kinetic friction [Nakano & Popov, *Phys. Rev. E* **102**, 063001 (2020)]. This friction theory, termed the dynamic stiction (DS) theory, is described within a purely mechanical framework by introducing a geometrical misalignment, the impact of which had been overlooked over two hundred years. In this study, we aimed to verify and develop the DS theory for polymeric materials, including the unique polymeric swollen materials termed the concentrated polymer brushes (CPBs) developed by Professor Yoshinobu Tsujii, ICR, Kyoto University.

**Results and Discussion** – A physical model of sliding friction, termed the viscoelastic foundation (VEF) model [Nakano & Kono, *Front. Mech. Eng.* **6**, 38 (2020)], was extended to describe the relationship between the viscoelasticity of CPBs and the DS theory. A rigid indenter was assumed to slide on an array of single-degree-of-freedom viscoelastic elements. The standard linear solid model was used as the viscoelastic element. Analyzing numerical simulation results finds three types of dimensionless parameters determining the friction coefficient of the VEF model. The master curve of friction is branched by the ratio of the two types of time constants, the retardation time and relaxation time of the standard linear solid element. However, the master curve has three types of asymptotes for low-, middle, and high-speed regions, the same as the asymptotes for the Voigt-type VEF model (for low- and middle-speed regions) and the Maxwell-type VEF model (for middle- and high-speed regions). This means that when we describe the relationship between the viscoelasticity of materials and the DS theory, the Voigt-type VEF model is sufficient as the DS mode vanishes for the high-speed region.

**Outcome reports** – [1] K. Nakano, “Contact and Friction of Elastomers”, *TTRF-TAIHO International Symposium on Automotive Tribology 2022*, Online, 14 April 2022 (Invited). [2] T. Watanabe, S. Hatanaka, K. Nakano, “Description of hysteresis friction by the standard linear solid model”, JAST Tribology Conference, Fukui, 09 November 2022. [3] K. Nakano, “Virtual damping generated by friction vector rotation”, *AsiaBrake 2023 Conference and Exhibition*, Bangkok, Thailand, 28 March 2023 (Invited).

## Synthesis of Polyether Nanocomposite Solid Polymer Electrolytes for Lithium-Ion Batteries

Robert C. Ferrier, Jr. Michigan State University

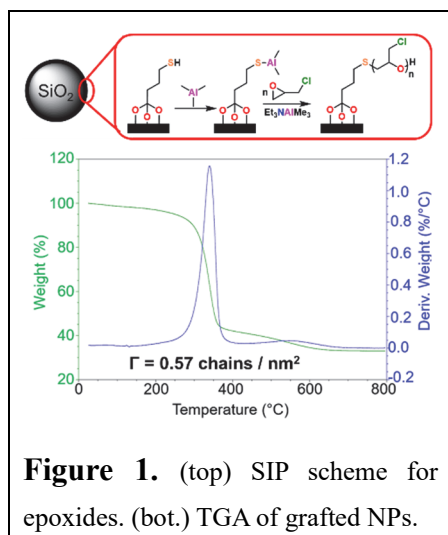


**Figure 1.** (top) SIP scheme for epoxides. (bot.) TGA of grafted NPs.

**Objective:** The objective of this work was to develop novel polyether nanocomposites by combining the epoxide polymerization techniques of the PI with the polymer brush synthetic expertise of Prof. TSUJII at Kyoto University. **Experimental Methods:** Initiators were characterized by <sup>1</sup>H NMR spectroscopy. Polymers were characterized by size-exclusion chromatography (SEC), <sup>1</sup>H and <sup>13</sup>C NMR spectroscopy, and differential scanning calorimetry (DSC). Silica nanoparticles (NPs) were characterized by scanning electron microscopy and thermogravimetric analysis (TGA). **Outcomes:**

Ionic conductivity results showed interesting behavior for high dielectric materials, such as polyepichlorohydrin (PECH) with a dielectric constant ( $\epsilon$ ) of *ca.* 17. We developed a surface-initiated polymerization (SIP) scheme by grafting thiolated silanes to NPs and reacting the thiol with trimethyl aluminum to form an initiator (*cf.*, Figure 1 top). SIP of ECH produced PECH brush grafted NPs. This is the first time, to our knowledge, SIP of epoxides has been demonstrated. We further synthesized single ion conductors through PECH modification, which we will apply to PECH brushes. New initiators were developed from NHS-ester thiols allowing us to graft polymers to aminated surfaces to tune membrane interfaces. **Analysis:** TGA was performed on the synthesized brush grafted NPs (*cf.*, Figure 1 bottom). The grafting density was calculated to be 0.57 chains / nm<sup>2</sup> based on the targeted molecular weight of 40 kg/mol. FTIR and NMR spectroscopy were consistent with the presence of grafted brushes. Furthermore, brush grafted NPs were soluble in organic solvents. **Publications:** (1) N. Safaie *et al.*, *Polymer Chemistry*, **2022**, 13 (19), pp 2803-2812. (2) Robert C. Ferrier, Jr. “Facile Epoxide Polymerizations with Sustainable Aluminum Catalysts.” Invited seminar. Kyoto University, January 2023. (3) Robert C. Ferrier, Jr. “Facile Epoxide Polymerizations with Sustainable Aluminum Catalysts.” Invited seminar. ACS Mid-Michigan, October 2022. (4) Robert C. Ferrier, Jr., Synthesis of (co)poly(thio)ethers using Earth abundant aluminum-based compounds. Seminar. ACS National Meeting, Chicago, IL, August 2022.

## Development and characterization of metal oxide nanocrystalline films for solar water splitting

Yasuhiro Tachibana RMIT University

### Introduction

Photocatalytic water splitting is an attractive technology to produce sustainable hydrogen gas from water using solar energy. To develop such photocatalytic materials, it is vital to initiate water reduction and oxidation reactions before photogenerated electrons and holes recombine. It is necessary to form nanocrystalline films to accelerate water splitting reaction and retard charge recombination reaction.

In this project we have developed oxygen deficient tungsten oxide nanorods using a simple method. Optical properties and photocatalytic performance were characterized by employing a series of spectroscopies. We have conducted this project with Professor Teranishi at the ICR.

### Experimental

Tungstic acid (1 mmol) was dispersed in 15 mL OLA and 6.5 g ODE. The solution was degassed to remove oxygen and water under vacuum at 125°C for 2 hrs. Subsequently, the solution was heated to 320 °C under nitrogen atmosphere. The solution was maintained at 320 °C for up to 12 hrs. The synthesized WO<sub>x</sub> nanorods were purified by adding excess ethanol to remove excess ligands, the unreacted precursors, i.e. tungstic acid, or by-products. Finally, the precipitated WO<sub>x</sub> nanorods were re-dispersed in OA/toluene.

### Results and Discussion

While the reaction temperature rises up to 320 °C, the solution colour was changed from yellow to green, and finally to navy blue. The final navy blue solution was purified and analysed using TEM, resulting in WO<sub>x</sub> nanorods with an average length of 13.5 nm and width of 9.4 nm. The synthesized WO<sub>x</sub> nanorods are highly emissive with the emission peak around 490 nm, a PL lifetime of around 4 ns and a PLQY of 2.3 %.

In addition to the synthesis and characterisation of WO<sub>x</sub> nanorods, we are also successful in synthesizing lead free metal halide perovskite nanocrystals.[1]

### Outcomes

[1] T. Teranishi, Y. Tachibana and co-workers, *J. Photopolym. Sci. Technol.*, **Accepted** (2022).

## Interdisciplinary Approach to Nanostructured Materials for Applications

Jean-Pierre Bucher   Université de Strasbourg

We summarize here the progress on two fronts of our interdisciplinary project for which Professor T. Teranishi is our ICR contact

**Structural changes of inorganic nanoparticles (Teranishi, Kyoto) can be characterized with much advantage by HR-TEM (Banhart, Strasbourg).**

In 2022, Teranishi's group has achieved the following results:

- 1) Synthesis of  $\sim 3$  nm Pd nanoparticles (NPs) capped with 1-dodecanethiol or triphenylphosphine ligand and confirmation of phase change from Pd to PdS<sub>x</sub> at around 250 °C by using synchrotron XRD.
- 2) Synthesis of wurtzite-CoS and spinel-Ni<sub>3</sub>Se<sub>4</sub> NPs larger than 15 nm.

**Self-organization of single molecule magnets (SMM's) by means of macrocycle networks and LT-STM characterization.**

The SMMs were synthesized in Strasbourg (Ruben's group). This compound has been sent to Nagoya where it will be incorporated in the synthesis of the 2D-crystal made of properly functionalized pi-conjugated macrocycles (Tanaka's group).

Simultaneously Tanaka's group has undertaken the synthesis of the proper ligand to grow the macrocycle. This optimization process is still ongoing. Next step will consist in characterizing the crystallized sample, by means of conventional techniques such as X-ray diffraction and optical techniques, before the drop cast 2D network is examined on Au(111).

Simultaneously M. Boero in Strasbourg, in collaboration with Bucher's group, undertook a molecular dynamics calculation to solve a long standing issue on the conformation of self-assembled TbPc<sub>2</sub> SMM in a 2D network. The results were compared with the STM data for the simple case of self-assembled TbPc<sub>2</sub> on Au(111). The calculated electron densities of the TbPc<sub>2</sub> molecules compare well with STM results and deepen our knowledge of these double-decker SMMs in interaction with their environment. In particular, it is found that it is not necessary to consider an azimuthal angle different from 45° between the two Pc ligands to account for the experimental result. A publication is in preparation.

## Search for four-wave-mixing in the vacuum – Unveiling dark components in the Universe –

Kensuke Homma Hiroshima University

### **Purpose and Method**

The purpose of this study is to search for Four-Wave-Mixing (FWM) phenomena in the vacuum in order to understand dark components in the Universe. So far, we have constructed and improved an ultra-high vacuum chamber in ICR toward the search. In this vacuum chamber, two-color laser pulses are collinearly combined and focused into the vacuum along the same optical axis. If photon-photon interactions occur in the vacuum environment, generation of intrinsic FMW photons via the stimulated interaction  $\omega + \omega \rightarrow (2-u)\omega + u\omega$  is enhanced, where  $\omega$  is the energy of the creation laser pulse and  $u\omega$  is the energy of the inducing laser pulse with  $0 < u < 1$ . The signal photon energy in this scattering process corresponds to  $(2-u)\omega$ .

### **Progress and Achievements**

We have extended the search by increasing laser intensity and developing a new method to handle backgrounds from atomic FWM processes, in particular, from the optical elements included in the searching system.

We summarize the published papers and a press release relevant to this subject during FY2022 as follows.

### **Published papers:**

- [1] Search for sub-eV axion-like particles in a stimulated resonant photon-photon collider with two laser beams based on a novel method to discriminate pressure-independent components, Yuri Kirita, Takumi Hasada, Masaki Hashida, Yusuke Hirahara, Kensuke Homma\*, Shunsuke Inoue, Fumiya Ishibashi, Yoshihide Nakamiya, Liviu Neagu, Akihide Nobuhiro, Takaya Ozaki, Madalin-Mihai Rosu, Shuji Sakabe & Ovidiu Tesileanu (The SAPPHIRES collaboration), Journal of High Energy Physics volume 2022, Article number: 176 (2022). (acknowledge the support by ICR)
  
- [2] Hunting dark energy with pressure-dependent photon-photon scattering, Taishi Katsuragawa, Shinya Matsuzaki, and Kensuke Homma, Phys. Rev. D 106, 044011 – Published 3 August 2022. (acknowledge the support by ICR)
  
- [3] Sensitivity to Axion-like Particles with a Three-Beam Stimulated Resonant Photon Collider around the eV Mass Range, Kensuke Homma \*, Fumiya Ishibashi, Yuri Kirita and Takumi Hasada, Universe 2023, 9(1), 20. (acknowledge the support by ICR)

### **Press release:**

- [1] <https://www.hiroshima-u.ac.jp/news/72499> (acknowledge the support by ICR)

## Tin-perovskite thin film crystallization on new hole-transporting materials

Antonio Abate    Helmholtz-Zentrum Berlin

Perovskites solar cells (PSCs) are bringing third-generation photovoltaic technologies to their golden age, with power conversion efficiencies (PCE) over 25% and 32% for single junction and tandem devices, respectively. Among their several advantages, their low cost of manufacturing is particularly remarkable, opening the door to their implementation in all kind of environments, including their integration in buildings and residences. However, the main component of the currently best performing devices, i.e. lead (Pb), is strongly hindering the potential of this technology for this application. The most promising candidate up to date to replace Pb is tin (Sn), with proven much lower toxicity and the potential to overcome the PCE of Pb-based solar cells owing to their lower bandgap. These compositions, while showing encouraging PCE values around 15%, face strong stability challenges due to their structural and chemical nature. With this work, we aimed to point out these problems from a critical perspective and propose the directions for the field to achieve efficient and long-term stable lead-free Sn-based perovskite solar cells for the future implementation in all kind of environments.

First, the composition of the Sn-based perovskite material is critical for its structural and thermal stability. Using several A-site cations or introducing 2D/3D mixtures can lead to big increases in long-term in-operando stabilities. Here, phenylethylammonium cations have shown a unique ability to lower the density of defects, improve interfaces and blocking water penetration into the materials. Second, we discussed the charge-selective layers with the strongest potential for Sn perovskites. We highlighted the wide applicability and opportunities of fullerenes as electron transporting materials and interface modifiers for p-i-n device architectures, as well as the possibility to optimize PEDOT-based hole selective layer for enhancing charge extraction and stability at the bottom interface. We pointed out the need for further investigations on the influence of inorganic charge selective layers on the stability of Sn perovskites. Moreover, Sn(II)-containing materials always face the oxidation-driven degradation. To address it, we proposed the use of DMSO-free solvents, as well as other additives such as SnX<sub>2</sub> ones or reductive organic materials. We also listed the typically less-discussed intrinsic factors affecting Sn perovskites stability. Finally, we emphasized encapsulation strategies as a critical step to develop towards the commercialization of lead-free Sn-based perovskite photovoltaics and optoelectronics.

- [1] E. Aktas, N. Rajamanickam, J. Pascual, S. Hu, M. H. Aldamasy, D. Di Girolamo, W. Li, G. Nasti, E. Martínez-Ferrero, A. Wakamiya, E Palomares, A. Abate, *Commun. Mater.* **2022**, 3, 104.



## Biochemical characterization of aldehyde dehydrogenases involved in the biosynthesis of plant volatile benzenoids

Takao Koeduka Yamaguchi University

【Research aims】 Aromatic compounds, especially volatile benzenoids, derived from natural resources, including rare plants, are known as functional components showing health-promoting activities and as signaling molecules for interactions among organisms in ecosystems. Therefore, human being, especially plant biochemists, are strongly interested in understanding their biosynthesis and regulatory mechanisms. In this study, we aim to understand the formation and control mechanisms of diverse aromatic compounds at the molecular level, and to analyze the function of dehydrogenases that convert benzaldehyde, an important intermediate for volatile benzenoids, to benzoic acid.

【Method and results】 We have succeeded in obtaining comprehensive gene expression data by transcriptome analysis of the petal limb, flower buds, and leaves of petunia (*Petunia hybrida*), which nocturnally emits volatile benzenoids as floral scent. We searched for candidate genes by tBLASTx analysis using aldehyde dehydrogenase (HcBD) from *Hypericum calycinum* as a query against the gene expression data of petunia. As a result, we found a gene (*contig\_15074*) that shows 73% identity at amino acid level with HcBD and was co-expressed with known biosynthetic genes for volatile benzenoid. Next, we extracted total RNA from petunia petals at different developmental stages of petunia flowers and at different times of the day and night, and performed qRT-PCR analysis to examine the expression pattern of *contig\_15074*. Then, we found that *contig\_15074* was highly expressed post-anthesis and specifically in the evening. Furthermore, we also expressed the recombinant proteins of *contig\_15074* in *E. coli* cells and purified them by Ni-affinity chromatography. The resulting purified enzymes showed the activity to produce benzoic acid from benzaldehyde in the presence of NAD<sup>+</sup> or NADP<sup>+</sup>. The high enzymatic activity was found at a wide pH range of pH 6.5-10.0 and the purified enzymes displayed apparent  $K_m$  value of  $92.7 \pm 6.0$   $\mu$ M for benzaldehyde. These results suggest that *contig\_15074* encodes a benzaldehyde dehydrogenase that produces benzoic acid (hereafter referred to as PhBALDH). The substrate specificity of PhBALDH is currently being analyzed.

【Summary】 In petunia that attracts nocturnal moths as pollinators, the production of floral scent increases after flowering at night. The expression pattern of *PhBALDH* was positively correlated with the production pattern of petunia floral scent, suggesting that it is responsible for the biosynthesis of floral scent in petals. This is the first report of benzaldehyde dehydrogenase in Solanaceous plants, and the ability to utilize both NAD<sup>+</sup> and NADP<sup>+</sup> as cofactors is the first enzymatic property of this enzyme family. To elucidate the contribution of PhBALDH in petunia petals, we are now trying to generate transgenic petunias overexpressing or deleting *PhBALDH* to examine the effect of benzaldehyde dehydrogenase on the production of floral scent.

## Regulatory Role of Phytohormone Cytokinin on Leaf Epidermal Cell Differentiation

Shiori Aki   Nara Institute of Science and Technology

**Objectives:** The leaf surface is composed of various types of cells including pavement, trichome, and stomatal cells, all of which differentiate from meristematic cells in the leaf epidermis concomitantly with leaf development. Although the differentiation of leaf epidermal cells proceeds basically according to the genetic program, it is greatly influenced by environmental conditions and plant growth statuses. Due to the accessibility of the leaf surface for many purposes, differentiation processes of leaf epidermal cells have been intensively investigated in genetic and physiological studies. As a result, regulatory factors and their networks have been clarified to a large extent for leaf epidermal cell differentiation, especially for differentiation of trichomes and stomata in *Arabidopsis thaliana*. However, regulatory mechanisms for the transition of leaf epidermal cells from the proliferation state to the differentiation state remain relatively unclear. In this study, we focus on cytokinin, a phytohormone involved in the transition from proliferation to differentiation, and genetically examined its involvement in leaf epidermal cells differentiation.

**Experimental Methods:** The *Arabidopsis* transposon-tagging mutants SM\_3\_33583 and SM\_3\_38189 for the cytokinin oxidase/dehydrogenase genes *CKX4* (AT4G29740) and *CKX5* (AT1G75450), respectively, were obtained from Arabidopsis Biological Resource Center (ABRC). Their homozygous mutant lines were established and crossed with each other to obtain their double mutant. Single and double mutant lines of the genes were examined for their morphological phenotypes in the leaf surface and total plant development.

**Results and Discussion:** To investigate effects of cytokinin on the cell differentiation of leaf epidermal cells genetically, we utilized *Arabidopsis* mutants defective in cytokinin oxidase/dehydrogenase (CKX), a cytokinin-metabolizing enzyme that irreversibly inactivates the endogenous cytokinin *trans*-zeatin. Among seven *Arabidopsis* CKX genes, we selected *CKX4* and *CKX5*, which are expressed at relatively high levels in the shoot apex including the leaf epidermal meristem, and obtained their transposon-tagging mutant lines, SM\_3\_33583 and SM\_3\_38189 (designated as *ckx4* and *ckx5*, respectively) from ABRC. We determined that both *ckx4* and *ckx5* contain the transposon insertion in the first coding exons of their relevant CKX genes, indicating that they are loss-of-function mutants. We crossed them and obtained the *ckx4ckx5* double mutant in the F2 generation. Neither the single nor double mutants exhibited obvious phenotypes in the leaf surface. Because environmental stresses greatly enhanced the expression of those CKX genes, their phenotypes are assumed to appear only conditionally. Phenotypic analyses under stressed conditions, e.g., treating with exogenous cytokinin, will be effective for further investigation.

## Electronic and spintronic properties of multilayer system including $\text{NiCo}_2\text{O}_4$ and $\text{Fe}_3\text{O}_4$

Taro Nagahama    Hokkaido University

**Introduction:** Oxide magnetic materials are a promising new class of spintronic materials, characterized by advantageous features such as a high transition temperature and large spin polarization. Furthermore, its various electrical conductivity makes it a crucial component in the semiconductor spintronics, currently facing material issues. In this investigation, the epitaxial heterojunction of  $\text{Fe}_3\text{O}_4$  and  $\text{NiCo}_2\text{O}_4$  were evaluated with an aim towards realizing p-n junctions in the future.  $\text{Fe}_3\text{O}_4$ , a conventional Fe oxide, has been reported to exhibit n-type semiconductor behavior, while  $\text{NiCo}_2\text{O}_4$ , a newly-observed oxide magnet attracting much attention, has reported to have p-type conductivity. Since both are spinel structures, it is expected that epitaxial growth can be achieved. In this study,  $\text{Fe}_3\text{O}_4/\text{NiCo}_2\text{O}_4$  bilayer films were prepared by reactive molecular beam epitaxy and their properties were investigated.

**Experiment:** Multilayers were prepared on  $\text{MgO}(100)$  substrates by reactive molecular beam epitaxy method in the oxygen atmosphere. The layer structure of the MTJs was  $\text{MgO}(100)$  substrate/ $\text{MgO}$  buffer (20 nm)/ $\text{NiCo}_2\text{O}_4$  (24 nm)/ $\text{MgO}$  (0 or 1 nm)/ $\text{Fe}_3\text{O}_4$  (30 nm) / $\text{AlO}_x$  (5 nm). Epitaxial growth and crystal structure were investigated by RHEED and XRD.

**Results and discussions:** In the sample preparations, the order of deposition was an important point. In the order of the subst./ $\text{Fe}_3\text{O}_4/\text{NiCo}_2\text{O}_4$ , the annealing in high oxygen partial pressure of 300 Pa was necessary to grow epitaxial  $\text{NiCo}_2\text{O}_4$  layer, which would bring about excessive oxidation of bottom  $\text{Fe}_3\text{O}_4$  layer. On the other hands, for the opposite order, subst./ $\text{NiCo}_2\text{O}_4/\text{Fe}_3\text{O}_4$ , the multilayers were exposed to heat treatment at a high temperature of 873K, which would result in the phase separation of  $\text{NiCo}_2\text{O}_4$  layer. Adding to that, bottom interface of  $\text{Fe}_3\text{O}_4$  tend to show dense anti-phase boundary. Figure 1 showed RHEED patterns and XRD profiles of  $\text{NiCo}_2\text{O}_4/\text{Fe}_3\text{O}_4$  films. The epitaxial growth of each layer was confirmed in the Fig.1. We investigated the magnetic coupling of bilayer by insertion of  $\text{MgO}$  layer of 1 nm. Obvious direct magnetic coupling was observed in the bilayer without  $\text{MgO}$  layer.

**Publication and Conference:** 1, Hara et al., "Inverse Tunnel Magnetoresistance of Magnetic Tunnel Junctions with a  $\text{NiCo}_2\text{O}_4$  Electrode" *AIP Advances* accepted. 2, Nagahama et al., " Observation of the negative spin polarization of  $\text{NiCo}_2\text{O}_4$  by tunnel magnetoresistance" ICMSF2022 Okinawa, July 2022.

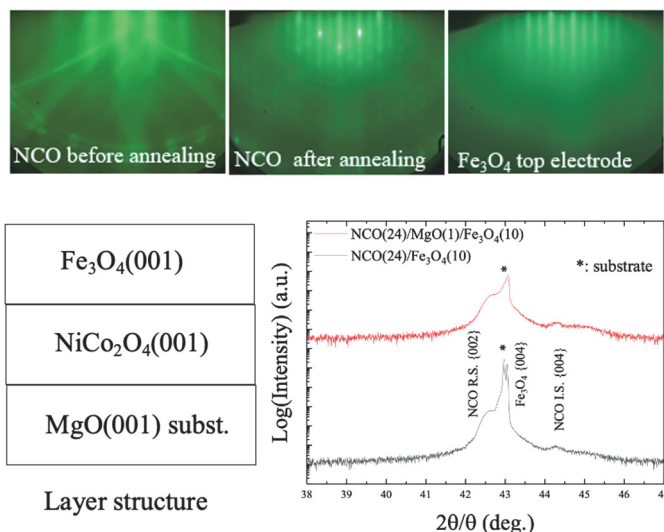


Fig.1 RHEED patterns and XRD profiles for  $\text{NiCo}_2\text{O}_4/\text{Fe}_3\text{O}_4$ .

## アルツハイマー病治療に向けたアミロイド光酸素化触媒の構造最適化

金井求 東京大学

アルツハイマー病は進行性の神経変性疾患であり、認知機能の低下を引き起こすため、社会的に大きな問題となっている。アミロイド性タンパク質であるアミロイドベータ(A $\beta$ )はアルツハイマー病の原因物質と考えられており、A $\beta$ の凝集抑制・分解ができればアルツハイマー病の予防・治療につながると期待される。我々は、スイッチ機能を有する光触媒が促進するアミロイド選択的酸素化反応を利用することで、A $\beta$ の凝集性低減・毒性低下・モデルマウス個体内からの除去が実現できることを見出している。現在、大型動物およびヒトでの治験の応用に向けた触媒活性の向上のため、BBB透過性を持つ分子サイズを保ったまま、長波長光照射における触媒の項間交差効率を上昇させる分子設計を目指している。一方で化学研究所の梶らは、計算化学による項間交差速度の予測に成功している。梶研究室との共同研究により、理論化学と実験化学との融合研究から、アルツハイマー病治療研究のステージを進めるアミロイド光酸素化触媒の創出をおこなうことを本研究の目的とした。

検討の結果、以前までに見出しているアゾベンゼンボロン錯体母骨格では大幅な活性向上は困難であることが明らかになった。一方で我々はトリアリールメタン系色素がスイッチ機能を持つ有望な光酸素化触媒になりうることを見出した。本色素は芳香環に共役したC=N二重結合を有しており、励起状態において項間交差に有利なn- $\pi^*$ 性の増大・反応性の向上が期待される。また、本色素は比較的コンパクトな構造を有するため、BBB透過性の向上が期待できる上に、置換基を変更することによりその吸収波長を長波長化することができる。種々の検討の結果、最適な触媒としてEV(Ethyl Violet)を得た。595 nmの光にて凝集A $\beta$ の酸素化反応を検討したところ、反応はA $\beta$ 選択的に進行し、従来型触媒の約100倍の活性を示すことが明らかになった。現在、梶らと共同し、EVの項間交差速度の予測からそのスイッチ機構発現のメカニズムと酸素化効率の向上のメカニズムについて解析を行っている段階である。

さらに我々はEVの高細胞毒性、低BBB透過性という問題点を解決するためにプロドラッグ化戦略をとることとした。すなわち、中央のカルボカチオンにヒドリドイオンを結合させ中性種としたロイコ体LEV(Leuco Ethyl Violet)をプロドラッグとし、酸化刺激によって系中で活性種であるカチオン種を遊離させることを目指した。その結果、LEVの細胞毒性は光照射の有無に関わらず大きく低下し、BBB透過性も約4倍向上した。そこでこの触媒を用い、生体マウスでの反応を検討した。アルツハイマー病モデルマウスに触媒投与と頭部への光照射を2か月間継続し、マウス脳由来サンプルをウエスタンブロッティング法にて評価した。その結果、EV,LEVを投与したマウスではA $\beta$ 量の減少が確認された。また、LEVで処置したマウスは頭部の外傷が認められなかった。これはBBB透過性、標的選択性の向上により、頭皮組織での活性酸素生成が抑制されたためであると考えている。

# 動的効果を考慮した熱活性化型遅延蛍光速度論の確立

浦谷浩輝 早稲田大学

有機発光ダイオード (OLED) の発光効率を高める手段として熱活性化型遅延蛍光 (TADF) の利用が注目されている。TADF 速度論の理論予測にあたっては、蛍光、無輻射失活、系間交差、逆系間交差のそれぞれに関する速度定数の理論計算が必要となる。従来、これらの計算は単一の分子構造を仮定して行われてきた[1]。しかし現実の OLED においては、発光分子は周辺分子との相互作用を受けて様々な配座をとっており、動的な構造ゆらぎも存在する。本研究は、これらの効果を取り込んだ新たな TADF 速度論の構築を目的とする。

ターゲットとして、ホスト分子に CBP、発光分子に DACT-II を用いた非晶質有機薄膜を選択した。ホスト分子との相互作用による発光分子の配座及び環境のばらつきを再現するため、古典分子動力学計算により凝集構造を作成した。得られた構造から、発光分子と周囲のホスト分子を含むクラスターモデルを複数抽出した (Fig. 1)。各モデルに対し、無輻射失活速度定数を支配する因子である振電相互作用強度 ( $|V_m|$ ) を計算した。クラスターモデルは 20 分子程度からなる大規模な系であるため、半経験的量子化学計算手法である密度汎関数強束縛 (DFTB) 法を用いた。本研究では、DFTB 法に基づく  $|V_m|$  の近似式を導き、計算ルーチンを DCDFTBMD プログラム[2]に実装した。

16 種類のクラスターモデルに対して  $|V_m|$  のスペクトル分布を計算した結果を Fig. 2 に示す。比較のため、気相における安定構造の DACT-II に対する計算結果も示す。クラスターモデルにおけるスペクトル分布は、気相中のものと異なるピーク強度を持ち、かつ、ばらつきを持つことがわかる。このことから、非晶質有機薄膜における個々の発光分子の TADF 速度論は、周辺分子との相互作用の影響を強く受けており、気相中分子を仮定して得られる速度論とは異なっていることが示唆される。

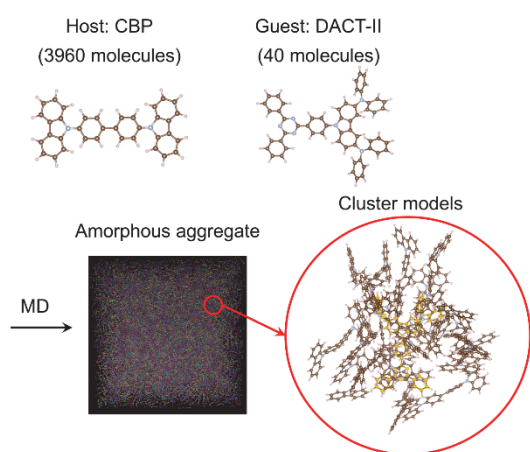


Fig. 1. Model construction.

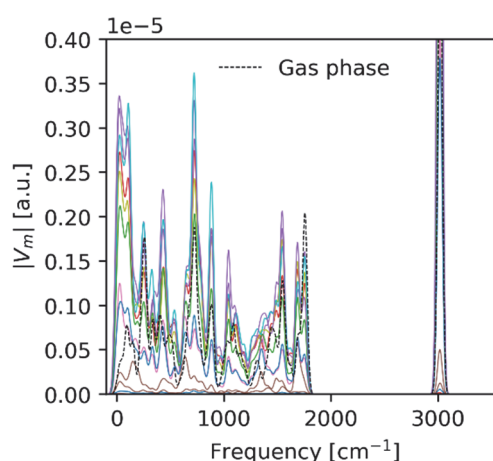


Fig. 2. Spectral distribution of  $|V_m|$ .

[1] K. Shizu and H. Kaji, *J. Phys. Chem. A* **125**, 9000 (2021).

[2] Y. Nishimura and H. Nakai, *J. Comput. Chem.* **40**, 1538 (2019).



## Analysis of the physiological functions of extracellular vesicles produced by intestinal bacteria and their application

Atsushi Kurata Kindai University

### Introduction:

The animal gastrointestinal tract is inhabited by a complex community of bacteria. Gut bacteria contribute to the maintenance of host physiological functions through the production of bacterial metabolites. Membrane vesicles (MVs) produced by intestinal bacteria are attracting the attention as novel bioactive substances. Within this context, the first objective of this study is to elucidate the physiological effects of enterobacterial MVs on host organisms and the production mechanisms of MVs from intestinal bacteria. The second objective is to develop the novel expression systems for heterologous proteins using MVs-producing bacteria.

### Results:

#### 1. Properties of MVs produced by intestinal bacteria.

We detected a large amount of MVs in the rat gastrointestinal tract. *Lactiplantibacillus plantarum* produces MVs that activate innate and acquired immune responses. *L. plantarum* induces an immunostimulation through the Toll-like receptor 2 recognition of the *N*-acylated amino acid moiety of lipoprotein in the MVs. *Bifidobacterium longum* subsp. *infantis* produces MVs. Extracellular solute-binding protein in *B. infantis* MVs is involved in the production of IgA by acquired immune cells via the production of IL-6 by innate immune cells. These bacterial strains produce useful MVs. We plan to develop novel strains that produce large amounts of MVs using the bacterial strains.

On the other hand, abnormal immune responses in the gut causes inflammatory bowel disease. MVs derived from *L. plantarum* NBRC 15891 inhibited the lipopolysaccharide-induced inflammation in HT-29 cells. Additionally, MVs were orally administered to mice with dextran sodium sulfate-induced colitis, which tended to decrease neutrophil infiltration in the colonic lamina propria and reduced the symptoms of colitis.

#### 2. Function of the major cargo protein of MVs from *Shewanella vesiculosa* HM13.

*S. vesiculosa* HM13 isolated from intestinal contents of horse mackerel (*Trachurus japonicus*) abundantly produces MVs, which carry a major cargo protein named P49 on their surface. By nanoparticle tracking analysis of MVs from a P49-less mutant and its parent strain, we found that MVs from the mutant were prone to aggregation. We also found that the addition of purified P49 to the P49-free MVs improved their dispersibility. Thus, P49 on the surface of MVs probably suppresses aggregation of MVs. This function may be beneficial for increasing the surface area of MVs and for their long-distance delivery.



## Analysis of membrane lipid-dependent fermentation stress response in acetic acid bacteria

Yosuke Toyotake   Ritsumeikan University

**[Introduction]** Acetic acid shows potent antimicrobial activity and inhibits the growth of most microorganisms even at low concentrations. However, acetic acid bacteria (AAB) such as *Acetobacter* spp. can produce acetic acid from ethanol and possess extraordinary resistance to acetic acid. Many researchers have analyzed the mechanism of acetic acid resistance in AAB, but the full extent of this mechanism has not yet been elucidated. In particular, the contribution of membrane lipids of AAB to acetic acid tolerance has not been fully understood.

AAB produce phosphatidylcholine (PC) as a membrane phospholipid (PL), constituting the cell membrane. Although previous studies have suggested that PC is involved in acetic acid tolerance, the physiological functions of PC in detail remain unknown. To elucidate PC functions in AAB, we previously constructed the PC-deficient mutant of *A. pasteurianus* SKU1108. In this study, we showed that the loss of PC reduces various stress tolerance in *A. pasteurianus* SKU1108.

**[Results and Discussion]** AAB synthesize PC from phosphatidylethanolamine (PE) using PE *N*-methyltransferase (PmtA). Thus, we constructed a markerless *pmtA*-deletion mutant ( $\Delta pmtA$ ) from the parental strain of *A. pasteurianus* SKU1108 by homologous recombination. We confirmed that PC was not produced, but PE was accumulated in  $\Delta pmtA$  by analyzing the membrane PLs using thin-layer chromatography. In addition, the introduction of the *pmtA*-complementation plasmid, under the control of its native promoter, into  $\Delta pmtA$  restored the synthesis of PC.

The colony-forming ability of  $\Delta pmtA$  on agar medium supplemented with acetic acid was compared with that of the parental strain, and  $\Delta pmtA$  showed higher sensitivity to acetic acid than the parental strain. In addition,  $\Delta pmtA$  did not grow well on agar medium acidified with hydrochloric acid to pH 3.5 compared with the parental strain. These results indicated that PC is important for the growth of this strain both in the presence of acetic acid and in low pH environments. In addition, we demonstrated that  $\Delta pmtA$  did not grow well at higher temperatures or under oxidative stress caused by hydrogen peroxide, suggesting that PC also contributes to the thermotolerance and oxidative tolerance of *A. pasteurianus* SKU1108.

### [Conference]

1. **Toyotake Y**, Yamamoto S, Hara Y, Tsuji A, Kawamata Y, Matsui D, Wakayama M “Analysis of phosphatidylcholine-regulated membrane functions of acetic acid bacteria.” Japanese Society for Extremophiles 2022
2. Yamakawa W, **Toyotake Y**, Tsuji A, Matsui D, Wakayama M “Physiological function analysis of squalene cyclase homologs from acetic acid bacteria” Japanese Society for Extremophiles 2022

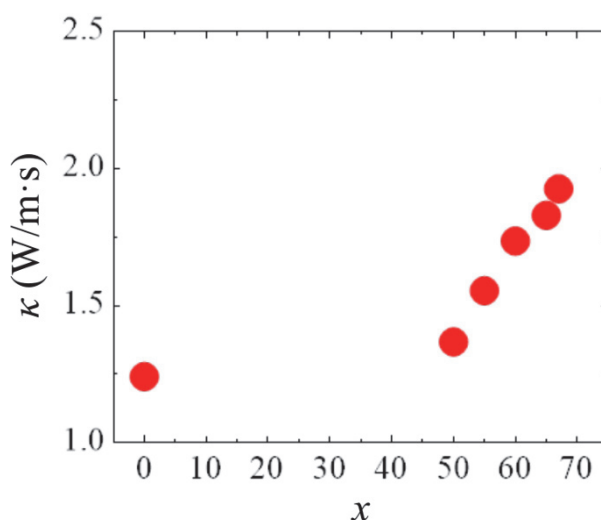
## 擬秩序ガラスの熱伝導

増野敦信 弘前大学

目的：酸化物ガラスは一般に、 $\text{SiO}_2$  などの網目形成酸化物の四面体ユニットが頂点共有して 3 次元ランダムネットワークを形成しているが、 $\text{MgO}$  などの修飾酸化物を添加すると、ネットワークが切断され非架橋酸素が生成する。 $\text{SiO}_2$  が少ない組成ではネットワーク形成が困難になりガラス化できないが、この限界は無容器法を用いることで克服できる。例えば  $\text{MgO-SiO}_2$  二元系は無容器法によって  $\text{MgO}$  が多い組成までガラス化範囲を広げられる。これまでの構造解析の研究から、ネットワークの切断が進むほど原子充填密度が増加し、原子配列において結晶のような秩序性があらわれることがわかってきた。このようなネットワーク連結様式の変化、あるいは秩序性の増加は、ガラス中の熱伝導に影響を及ぼすと考えられる。そこで本研究では、 $\text{MgO-SiO}_2$  二元系において幅広い組成範囲でガラスを合成し、その熱輸送特性の組成依存性を調べた。

実験と結果：ガス浮遊炉を用いて  $x\text{MgO}-(100-x)\text{SiO}_2$  二元系ガラス ( $0 \leq x \leq 67$ ) を合成した。Raman 散乱スペクトルから、 $x$  が 50 を超えるとネットワークの切断が著しく進行し、 $x = 67$  では、孤立した  $\text{SiO}_4$  や二量体  $\text{Si}_2\text{O}_7$  などが多く存在していることがわかった。ピクノメータによってガラスの密度を計測したところ、 $\text{MgO}$  含有量の増加とともに密度と充填密度は増加していた。示差走査熱量測定 (DSC) によりガラスの比熱を、そして温度波法によって熱拡散率を測定した。得られた密度、比熱、熱拡散率から、熱伝導率を算出した。

Figure 1 に、 $x\text{MgO}-(100-x)\text{SiO}_2$  二元系ガラスの熱伝導率を示す。 $\text{MgO}$  含有量の増加に伴い熱伝導率は大きくなり、 $67\text{MgO}-33\text{SiO}_2$  ガラスでは、 $1.9 \text{ W/m}\cdot\text{s}$  を超える値を示した。 $\text{Si-O-Si}$  のネットワークが切断されることで熱伝導率は低下する、とした当初の予想とは逆の結果であった。このメカニズムは現時点では不明であるが、 $\text{Mg-O-Mg}$  の新たなネットワークが形成されたか、あるいは原子配列の秩序性の増大によるものと考えている。

Figure 1.  $x\text{MgO}-(100-x)\text{SiO}_2$  ガラスの熱伝導率.

成果報告：阿保健太，増野敦信，「 $\text{MgO-SiO}_2$  系ガラスの熱伝導特性」，令和 4 年度日本セラミックス協会東北北海道支部研究発表，2022.11.10.

## 電気化学的プロトン脱挿入を利用した金属酸化物の新奇物性探索

土屋敬志 物質・材料研究機構

機能性材料である遷移金属酸化物の構造・物性は遷移金属の価数と密接に関連している。電界を利用して遷移金属の価数を制御することは、酸化物の新奇機能を開発やデバイス応用にも有用である。特に電界で制御できる電気化学的な酸化還元反応を利用した場合には、可逆的に価数を変調できるだけでなく、酸化物中へプロトンなどの余分なイオンを挿入することも可能であり、新しい物質相の発見も期待できる。これまでに我々は、ゲート絶縁体としてプロトン伝導性電解質であるナフィオンを用いたトランジスタ構造デバイスが遷移金属酸化物の電気化学的制御、さらにはプロトン注入による新物質開発に有用であることを明らかにしてきた[1]。本課題では、エピタキシャル成長技術によって安定化された準安定酸化物に着目し、ナフィオンを利用した電気化学的な物性制御やプロトン注入を行うことで、新物質相や新奇物性の開発を目指した。

以下に例として  $\text{TiO}_{2-\delta}$  薄膜に関する実験結果を示す。パルスレーザー堆積法により、(100)LSAT 基板上に蒸着することで準安定構造であるアナターゼ型の結晶構造を有する  $\text{TiO}_{2-\delta}$  エピタキシャル薄膜を製膜した。作製した薄膜をチャネルとしてプロトン伝導性電解質であるナフィオンをゲート絶縁体としたトランジスタ構造（図1）を作製し、3 V のゲート電圧  $V_{\text{GS}}$  を印加することで電気化学的に水素を薄膜チャネルに注入した。水素注入前後において  $\text{TiO}_{2-\delta}$  薄膜チャネルの電気抵抗には変化が見られなかった。また薄膜チャネルに対して弾性反跳原子検出法（ERDA）を行った。図2に得られた反跳水素のエネルギースペクトルを示す。水素注入を行った薄膜試料では、900 keV 付近における反跳水素に由来するピーク強度がわずかに増加していた。これらの結果は、 $\text{TiO}_{2-\delta}$  薄膜へ注入した水素の大部分は、薄膜内部には導入されず、蓄積されていくとしても薄膜表面近傍であることを示すものである。このことは薄膜チャネルの抵抗が水素注入前後でほとんど変化しなかった実験結果とも整合する。

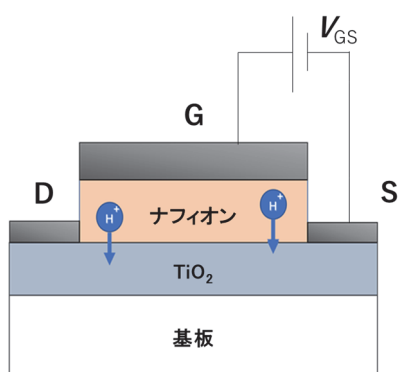


図1. トランジスタ構造の模式図

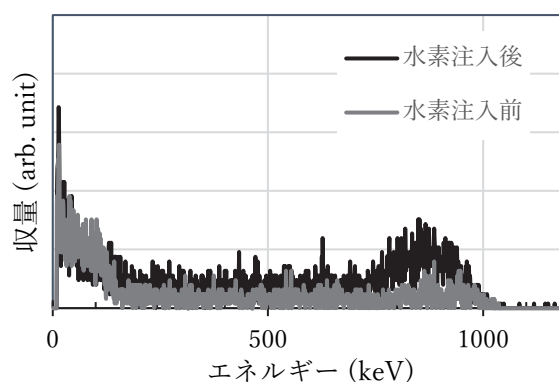


図2. アナターゼ  $\text{TiO}_{2-\delta}$  薄膜の ERDA スペクトル

[1] Y. Isoda, et al., Appl. Phys. Lett. 120, 091601 (2022).

## 高圧合成による新規フッ化物イオン伝導体の探索

齊藤高志 高エネルギー加速器研究機構

遷移金属イオン (M) が酸素イオン (O) に加え他のアニオン (X) とも結合した複合アニオン化合物は、結晶構造内において M-O 結合及び M-X 結合からなるネットワークが形成されることで酸化物とは異なる機能・物性を持つことが期待される。本研究では X アニオンとしてフッ化物イオンに着目し、ペロブスカイト構造酸化フッ化物の合成を試みた。フッ化物イオン F は酸素イオン  $O^{2-}$  とイオンサイズが近いため、酸化フッ化物を高温での焼成による通常の固相反応で作製した場合、一般的には F/ $O^{2-}$  が無秩序に入り混じった結晶構造となる。そこで本研究では、ペロブスカイト型  $SrFeO_{3-\delta}$  を還元して得られる  $SrFeO_2$  の酸素欠損サイトへ F をカチオンのフレームワークを保ったまま低温でトポタクティックに挿入することにより、F と  $O^{2-}$  が秩序列した酸化フッ化物  $SrFeO_2F$  の合成を試みた。

まず  $SrCO_3$  と  $Fe_2O_3$  の固相反応から得られた  $SrFeO_{3-\delta}$  を  $CaH_2$  で還元することで Fe イオンが酸素平面 4 配位構造となる  $SrFeO_2$  を作製した。続いて、得られた無限層構造酸化物  $SrFeO_2$  を化学研究所が有する高圧合成装置を用いて圧力下において比較的低温で  $XeF_2$  と反応させることにより  $SrFeO_2F$  を合成した。図 1 に示す X 線回折の結果から、生成物がペロブスカイト型構造を持つことが明らかになった。またメスバウアー分光測定から Fe イオンの価数は 3+ であったが、Fe サイトは 1 種類しかなく、F/ $O^{2-}$  が無秩序配列していることが示唆された。メスバウアー分光測定から Fe イオンの価数は 3+ であり、フッ素の挿入による  $Fe^{2+}$  の酸化が起こったと考えられる。

合成した  $SrFeO_2F$  のイオン伝導特性に関しては、交流インピーダンス測定法などにより今後詳細に検討を進めていく予定である。

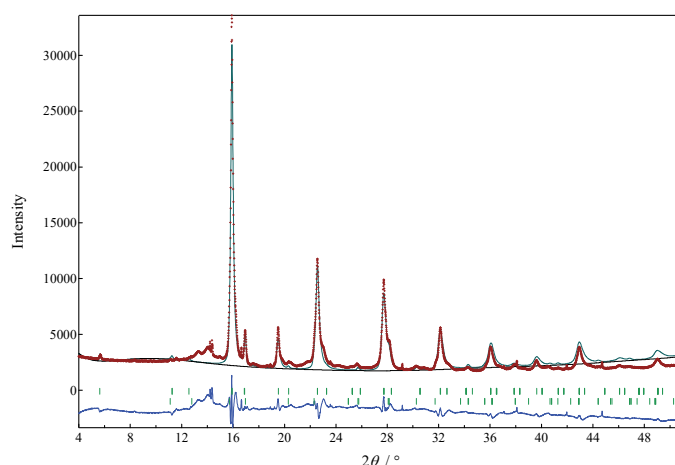


図 1.  $SrFeO_2F$  の X 線回折パターン

## 界面活性剤を利用した溶媒含浸樹脂による金属分離

倉橋健介 大阪公立大学工業高等専門学校

### 1. 目的

固相抽出法による金属の分離は、溶媒抽出法に比べ、人体や環境に有害な揮発性有機溶媒の利用が少ないことから、資源の偏在などによって資源枯渇のリスクを抱える希土類金属元素のリサイクルなどで注目されている。我々の研究グループでは、多孔性樹脂に界面活性剤を含浸させた溶媒含浸樹脂(SIR)を調製することで、他の抽出剤の助けなしに希土類金属元素を樹脂相へ吸着できることを見出した。溶媒含浸樹脂は簡便な手法で調製が可能であることに加え、抽出剤として用いる界面活性剤も入手が容易であることから、界面活性剤を用いた溶媒含浸樹脂は安価かつ環境に配慮した吸着剤としての用途が期待される。本研究では、この界面活性剤のみを用いた溶媒含浸樹脂による分離法を確立するため、吸着した金属イオンの回収法についての検討を行った。

### 2. 実験方法

エタノールで洗浄後、乾燥した多孔性樹脂 Amberlite XAD-7HP 1.0 g に対し、界面活性剤として Sodium Dodecylsulfate (SDS) を 0.2 mmol 含むエタノール溶液 20 mL を加え、1 日含浸させた。溶媒を減圧留去し、50°C で 1 日真空乾燥させ、目的の SIR を調製した。1 ppm の La と緩衝液として 0.1 M クロロ酢酸ナトリウムを含む水溶液 2.5 mL を HCl と NaOH で pH 2.0 に調整し、SIR を 0.1 g 加え、15 分振とうした。振とう後、3000 rpm で 5 分間遠心分離し、水相のみを 2.0 mL 採取した。残った樹脂に、任意の濃度の HCl を加え、15 分振とうした後、遠心分離後の水相を分取することで逆抽出操作とした。得られた水相は Ni を内標準として、誘導結合プラズマ発光分光分析装置(ICP-OES)を用いて金属濃度を測定した。

### 3. 結果と考察

pH 2.0 で La を抽出した樹脂に対し、濃度を 0.1~1.0 M とした HCl を投与し、樹脂からの La の回収を試みた。結果を図 1 に示す。HCl 濃度の上昇に伴って La 回収率は向上し、0.5 M HCl を用いることで、SIR に吸着した La を完全に回収することができた。SDS を用いた SIR では pH が低いほど減少することから、樹脂に吸着した La が、水相の水素イオンと交換されることで、溶液に放出されたと考えられる。また、逆抽出を行った後の SIR によって、再度 La の抽出を試みたところ、純水により SIR を洗浄することで、1 回目と同様の La 抽出率を得ることができ、最低 1 回の再利用が可能であることがわかった。

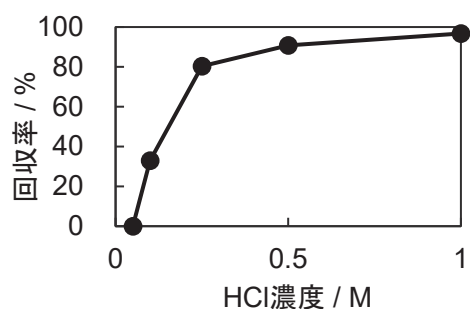


図1 SDS を含浸させた SIR からの HCl を用いた La の逆抽出

### 4. 成果報告

- 1) 大石智也ら, 第 25 回化学工学会学生発表会, オンライン開催, 2023. 3.
- 2) 大石智也, 第 25 回工業高等専門学校生 化学研究発表会, 大阪, 2023. 3.



## 全反射近赤外分光法による高分子ブラシ層内の水の構造解析

源明誠 富山大学

**[目的]** 固体高分子は高分子鎖が絡み合った状態で、特異な官能基を付与することで生体適合性や電気伝導性などの機能材料として、構造物やフィルムなどに使われている。近年開発された原子移動ラジカル重合法による固体表面に高分子鎖を緻密に生長させた高分子ブラシは、次元規制された高分子鎖によって、防汚性や生体適合性などの機能を付与するとされる。この機能発現には水が関与しているとされるが、これまでにブラシ内部のみの評価はなされていない。本研究では、内部全反射近・中赤外吸収 (ATR near/mid-IR) スペクトルから Poly(polyethylene glycol monomethoxy ether methacrylate) (P(PEGMA)) ブラシ内部のみの水構造を評価した。

**[実験]** 自作の高多重反射 ATR セルを使用し、種々濃度の P(PEGMA) 水溶液中の水、および ATR 結晶 (シリコン) 上に、高圧下における表面原子移動ラジカル重合法により調整した、種々膜厚 (70, 218, 1130 nm) の P(PEGMA) ブラシ中の水の ATR near/mid-IR スペクトルを得た。

**[結果および考察]** 図 1 に、OH 伸縮振動結合音 ( $\nu_{\text{syn}} + \nu_{\text{asyn}}$ ) および稜動振動 ( $\nu_L$ ), HOH 変角振動 ( $\delta$ ),  $\nu_{\text{syn}}$  の結合音 ( $\nu_{\text{syn}} + \delta + \nu_L$ ) 含む、近赤外領域の純水の吸収スペクトルを示す。最高波数の成分は、 $\nu_L$  を含んでおり、水分子のダイナミクスに関する情報を与える。

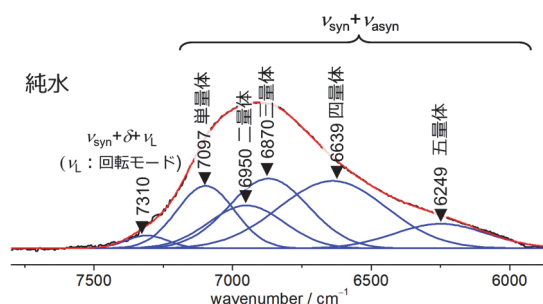


図 1. 純水の ATR-NIR スペクトルおよび成分分離

種々の膜厚の P(PEGMA) ブラシ中の水の ATR-NIR スペクトルの評価から、膜内部のみのスペクトルを与えることのできるのは、乾燥時膜厚 1130 nm のブラシのみであった。一般にエバネッセント波の潜り込み深さ  $d_p$  (分析深さ) は Harrick's 式で示され、本系においては 200 nm 程度と見積もられるが、それ以上の膜厚が必要であった。これは、Harrick's 式においては  $d_p$  を表面の電場強度が  $1/e$  になる深さと定義していることによるものである。

種々濃度 (含水率 0–60 wt%) の P(PEGMA) 水溶液および液体水に接触した P(PEGMA) ブラシ中の水の吸収強度の比較から、膨潤 P(PEGMA) ブラシの含水率を  $\sim 30$  wt% と見積もられた。P(PEGMA) 水溶液と P(PEGMA) ブラシ

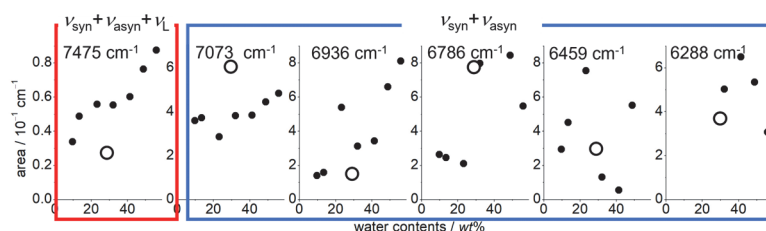


図 2. P(PEGMA) 水溶液および膨潤 P(PEGMA) ブラシ中の水の近赤外吸収スペクトルの成分分離結果

中の水の NIR 領域のスペクトル成分の分離結果を図 2 に示す。水分子の回転運動を反映する  $nL$  成分の結合音である  $\nu_{\text{syn}} + \delta + \nu_L$  バンドの吸収強度は、同含水率の P(PEGMA) 水溶液の強度の半分程度であり、P(PEGMA) 水溶液  $\sim 10$  wt% と同程度であった。これは、高分子ブラシの一端の固定化に起因する高分子鎖の運動性低下に伴い、水和水の運動性も低下していることを示している。この高分子ブラシ中の水分子の運動性の低下は、ブラシ内における水の凍結挙動、あるいは膨潤ブラシの弾性特性に大きく影響を及ぼすと考えられる。



## 3D プリンタを用いたモノリスの3次元構造制御

村瀬浩貴 共立女子大学

多孔材料は、各種の分離フィルタ、各種電池セパレータ、透湿防水布としての快適性衣料、海水淡水化膜や水浄化膜などの環境関連材料、血液透析膜や細胞培養基材などの医療材料など幅広い分野で利用されている。これまで、様々な多孔材料が実用化されてきたが、モノリス(Monolith)は3次元ネットワーク状の骨格構造を持ち、ネットワークの骨格サイズと、その空隙である連続空孔のサイズを独立に制御できる次世代多孔材料として注目されている。京都大学化学研究所の辻井敬亘教授と榊原圭太氏(元化学研究所助教、現産業技術総合研究所)は、界面化学的手法を駆使して、重合誘起スピノーダル分解を経由するエポキシ系ポリマーモノリスで新規な多孔材料を創生してきた。一方、報告者はこれまで、Additive Manufacturing (AM, 3D Printing と呼ばれる) の技術を応用して、新規な構造を有する複合繊維や繊維-樹脂複合型布帛の開発、セルロースナノファイバーの3次元造形に取り組んできた。本研究ではAMの技術と、辻井教授らの界面制御技術・高性能モノリス合成技術を融合し、3次元構造を制御した新規ポリマーモノリスを創生することを目的とする。

辻井教授らの技術では、ポリビニルアルコール(PVA)の基材の上にエポキシ系モノリスを形成することで、孔の閉塞したスキン層の発生を防ぐことに特徴がある。PVA製の鋳型をAMによって作製することにより、任意の3次元形状のモノリス膜を作製することができる。本年度は、モノリスを成形する際の鋳型を複雑化する検討を行った。今回、その構造モデルとして3次元ボロノイ構造を選択した。ボロノイ図(Voronoi Diagram)とは、ある空間に任意の位置に配置された複数の点(母点)に対して、それぞれの母点間の2等分線によって区切られた領域によって構成される平面である(ただし2次元ユークリッド平面の場合)。これを3次元ユークリッド空間に拡張したものが3次元ボロノイ図である。任意の形状の3次元ボロノイ構造をモデル化するための3D-CADとして、Rhinceros (AppliCraft社)とグラフィカルアルゴリズムエディターGrasshopperを用いた。Grasshopperを用いると、3次元空間に発現させる母点の数や、支柱の太さをパラメトリックに制御できる。Figure 1は、母点の数を3水準変更した3次元ボロノイ構造の例と、AMで造形した3次元ボロノイ構造である。今後は、本構造の鋳型をPVAで作製する技術を開発する。

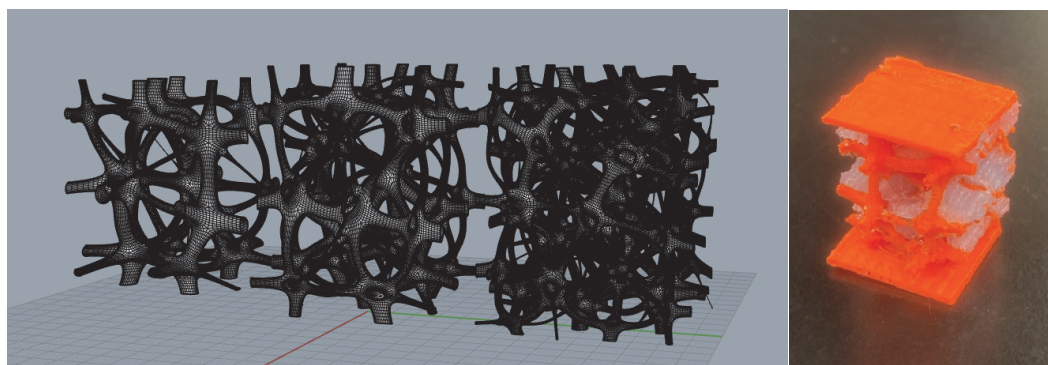


Figure 1. Models created with Rhinoceros with Grasshopper (left) and a 3D Voronoi structure modelled with additive manufacturing (right).

# 単電子トランジスタにおける巨大磁気抵抗効果の検討

真島豊 東京工業大学

本研究では、磁性ナノギャップ電極間に1つのナノ粒子を化学吸着したデバイス構造において、磁場印加時にスピンの依存する単電子トンネル磁気抵抗効果を観察し、巨大磁気抵抗効果を実現することを目的とした。

線幅 30 nm のコバルトと白金の交互積層ナノワイヤのアニール（加熱）処理のみで、10 kOe 以上の高保磁力を有する  $L1_0$  規則化強磁性単結晶ナノワイヤを Si/SiO<sub>2</sub> 基板上に直接作製する「ナノ構造誘起法」を開発した<sup>(1)</sup>。

電子線リソグラフィにより Si/SiO<sub>2</sub> 基板上に、強磁性ナノワイヤ材料としての Co/Pt 交互積層ナノワイヤを直接形成し、アニール処理をした（図1左）。ナノ構造誘起法では、アニール処理のみで 10 kOe を超える保磁力を有する強磁性ナノワイヤが形成されている（図1右）。

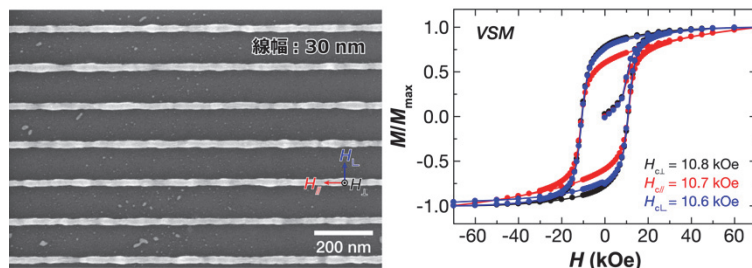


図1 ナノ構造誘起法により作製した  $L1_0$  規則化 CoPt 単結晶ナノワイヤの SEM 像（左）と、M-H カーブ（右）

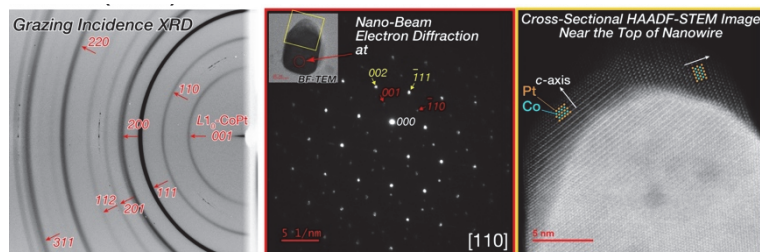


図2 強磁性ナノワイヤの2次元微小角入射X線回折（GI-XRD）パターン（左）。どんぐり型のナノワイヤの断面 BF-TEM 像（中央左上）、赤丸で撮影したナノビーム電子回折（NED）パターン、超格子回折スポット（赤矢印）と、基本スポット（黄矢印）（中央）。高角度環状暗視野走査透過電子顕微鏡（HAADF-STEM）像（右）。

2次元微小角入射X線回折（GI-XRD）パターンと、ナノビーム電子回折（NED）パターンにおいて（図2左・中央）、強磁性ナノワイヤが  $L1_0$  型規則相を形成していることを確認した。ナノワイヤ断面は、ナノスケールにおいて表面エネルギーが最小になるどんぐり型の形状になっていた（図2中央左上）。さらに、高角度環状暗視野走査透過電子顕微鏡（HAADF-STEM）像で断面を拡大し、ナノワイヤが双晶を含む単結晶になっていることを確認した（図2右）。

8 nm のギャップ長を有する規則化強磁性ナノギャップ電極をナノ構造誘起法により作製し、共同研究者の寺西教授が合成するナノ粒子を、自己組織化プロセスによりナノギャップ電極間に1つ化学吸着させた。磁性ソース電極／ナノ粒子／磁性ドレイン電極からなる単電子トランジスタにおいて、明瞭なクーロンダイヤモンド特性を測定した。さらに、磁化の向きに起因したスピン依存単電子トンネル磁気抵抗効果を、電流の磁場掃引依存性により確認した。

1. R. Toyama, S. Kawachi, J. Yamaura, T. Fujita, Y. Murakami, H. Hosono, Y. Majima, *Nanoscale Advances*, **4**, 5270-5280 (2022).

## 担持金属表面に金属酸化物クラスターを修飾した二元機能触媒の創製

山添誠司 東京都立大学

担持金属ナノ粒子触媒を用いた  $H_2$  を還元剤とする水素化反応では、 $H_2$  の活性化サイトである金属ナノ粒子表面や金属-金属酸化物界面の設計が極めて重要である。本研究では、酸化還元能をもつ担持金属触媒の金属粒子表面に、塩基触媒作用を持つニオブやタンタルの金属酸化物クラスター (POM) を修飾させる新しい合成手法の開発と、開発した触媒を用いた二元機能触媒作用の解明を水素化反応で検証した。

1. 担持金粒子-金属酸化物クラスター二元機能触媒の開発とニトロ基の水素化反応への応用<sup>1)</sup>

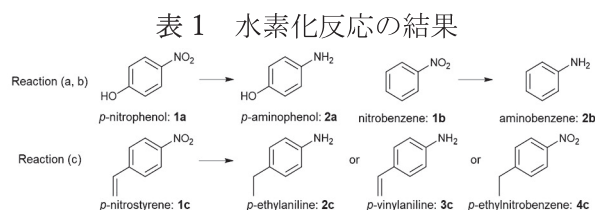
$Al_2O_3$  表面に金ナノ粒子を担持した触媒 ( $Au/Al_2O_3$ ) を塩析出法と水素化還元法により作製した。 $Au/Al_2O_3$  の  $Au$  に対し過剰量の POM の水溶液 ( $K_8Nb_6O_{19}$ ,  $K_8Ta_6O_{19}$ ) に  $Au/Al_2O_3$  を混合した。攪拌後、洗浄・回収し、333 K で真空乾燥させて POM を修飾した  $Au/Al_2O_3$  ( $Nb_6$ -,  $Ta_6$ - $Au/Al_2O_3$ ) を得た。STEM、EDX、XAFS、XPS より、 $Au$  粒子表面にクラスターが選択的に吸着し、クラスターから  $Au$  粒子への電子供与が起こっていることを明らかにした。 $p$ -ニトロフェノール ( $p$ -NP) の水素化反応では、 $Au/Al_2O_3$  への POM 修飾により転化率の向上が確認された。 $Al_2O_3$  に  $Nb_6$  を含浸担持した試料

では転化率が低く、塩基として  $K_2CO_3$  を加えると  $Au/Al_2O_3$  で反応が進行したことから、 $Au$  ナノ粒子と塩基の共存が重要であると考えられる。また、 $Nb_6$  による修飾によりニトロベンゼン (NB) 及び  $p$ -ニトロスチレン ( $p$ -NS) の水素化反応の転化率が向上した。以上から、 $Au$  NPs と POM の界面にて  $H_2$  の活性化が効率よく進行し、水素化活性が向上したと結論した。

2.  $Pt(Nb_6O_{19})_2$  触媒を用いた二酸化炭素によるピペリジンの N-ホルミル化反応への応用<sup>2)</sup>

合成した  $Cs_2K_{10}Pt(Nb_6O_{19})_2 \cdot 18H_2O$  を触媒として二酸化炭素によるピペリジンの N-ホルミル化反応を行った。1.0 MPa の  $CO_2$ 、2.0 MPa の  $H_2$  条件下、130℃で反応を行ったところ、ピペリジンから 1-ホルミルピペリジンが選択的に生成した。反応後の触媒を TEM、XAFS、FT-IR で調べたところ、 $Nb_6O_{19}$  の一部が分解してできた  $Nb_2O_5$  表面に  $Pt$  ナノ粒子が生成し、一部の  $Nb_6O_{19}$  が  $Pt$  ナノ粒子表面に吸着した触媒が形成しており、この触媒が N-ホルミル化反応に活性を示したと結論した。本触媒はピペリジンだけではなく、他のアミンのホルミル化にも活性を示すことを見出した。

- 1) "Dual functional catalysis of  $[Nb_6O_{19}]^{8-}$ -modified  $Au/Al_2O_3$ ", S. Kikkawa, S. Fukuda, J. Hirayama, N. Shirai, R. Takahata, K. Suzuki, K. Yamaguchi, T. Teranishi, S. Yamazoe, *Chem. Commun.*, 58, 9018-9021 (2022).
- 2) "Bifunctional platinum-incorporated polyoxoniobate derived catalyst for N-formylation of piperidine using  $CO_2$ ", V. Chudatemiya, S. Kikkawa, J. Hirayama, R. Takahata, T. Teranishi, M. Tamura, S. Yamazoe, *Asian J. Org. Chem.*, 2022, e202200521 (2022). カバーアートに選出



Substrate	Catalyst	Conversion (%)	Selectivity (%) (2c:3c:4c)
$p$ -NP	$Nb_6/Al_2O_3$	6.3	-
	$Au/Al_2O_3$	40	-
	$Nb_6$ - $Au$	84	-
	$Ta_6$ - $Au$	66	-
	$Au+K_2CO_3$	65	-
NB	$Au/Al_2O_3$	24	-
	$Nb_6$ - $Au$	43	-
$p$ -NS	$Au/Al_2O_3$	21	3:97:>1
	$Nb_6$ - $Au$	96	92:4:4



# 電子顕微鏡内での単一三次元量子ドット超格子の電子輸送特性と構造相転移挙動の同時観測

浅香透 名古屋工業大学

化学的なボトムアップアプローチで作られるナノサイズの半導体（量子ドット）は、省スペース・省電力な電子回路の構成要素として期待されている。化学研究所の猿山（共同研究者）らにより独自に開発された  $\text{Cu}_{2-x}\text{S}$  量子ドット超格子ロッドは、迅速な一段階の液相法で得られる自立可能な三次元量子ドット集合体である。 $\text{Cu}_{2-x}\text{S}$  量子ドットは  $\text{Cu}^+$  欠陥量 ( $x$ ) によってホール密度やバンドギャップを制御でき、かつ電圧印加や電子線照射により結晶構造が変化して異なる電子的特性を示すなど、電子材料として特異な挙動を示し、ミクロな半導体素子としての可能性を有する。そこで、我々は観察試料に STM のプローブを用いて電圧印加が可能な機構をもつ透過型電子顕微鏡を（TEM）用いて  $\text{Cu}_{2-x}\text{S}$  量子ドット超格子ロッドへ電圧印加その場観察と電気的測定の同時計測を行い、構造と電気的特性に関する基礎物性を評価した。

$\text{Cu}_{2-x}\text{S}$  量子ドット超格子ロッドは液相法により合成されたものを共同研究者の猿山氏より譲り受け TEM 観察に使用した。超格子ロッド 1 本を集束イオンビーム加工装置（FIB）によりピックアップ、特殊形状 TEM グリッドにタングステンで接着し、TEM 観察試料とした（図 1）。電気測定およびその場 TEM 観察のために、片方の電極をグリッド、もう片方の電極を STM プローブとし、超格子ロッドのみの電場応答を計測できるようにした（図 2）。

TEM 内で STM プローブを操作し、超格子ロッドの一端に接触させることで、電圧印加その場 TEM 観察を行い、同時に電流電圧特性の測定（IV 測定）を行うことに成功した。電圧印加時、TEM 像の分解能は大きく損なわれることはなく、通常の格子像の観察が可能であった。電圧は 0.8 V 程度まで印加することが可能であった。IV 曲線は非オーミックな特性を示し、整流効果と考えられる挙動を示した（図 3）。TEM グリッドとの界面と STM プローブは共にタングステンであり、試料は半導体である。本実験では金属-半導体接合界面が形成されており、ショットキー接合による整流効果が表れた可能性がある。また、電圧を上昇させ、電流が多く流れるようになった時、超格子ロッドの構造に変化が見られたが、この変化が純粋な電圧誘起あるいは電流誘起の現象なのか、電流増加時のジュール加熱によるものか、現時点では判断が難しい。今後、高分解能 TEM 観察や組成分析による詳細な評価が必要である。

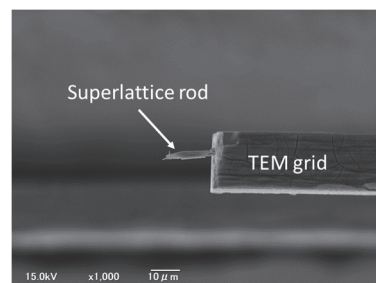


図 1 TEM グリッドに設置した試料

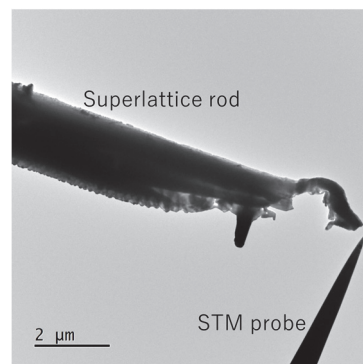


図 2 試料と電極の STM プローブ

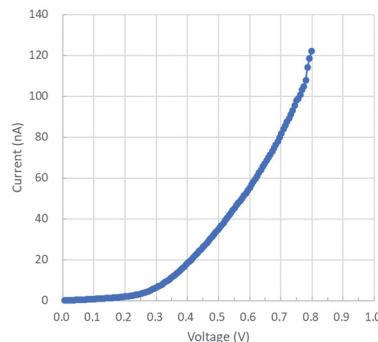


図 3 単一超格子ロッドの IV 曲線

## 再生可能資源・木質バイオマスの先端化学材料への効率的変換法の開発

秦野修 奈良県立医科大学

### 目的:

本研究は再生可能資源である木質バイオマスから、主成分であるセルロースやリグニン等を、先端化学材料を含む有用化学物質への効率的変換/利用法の開発を目的とする。研究協力者の化学研究所・中村研究室では、過酸化水素水と、有機酸触媒や金属錯体触媒を用いて、木材の効率的分解/合成/利用法の開発を行っている。この際、有機酸触媒等を木質ペレットに直接作用させ、軽量で高剛性な先端化学材料として注目されるセルロースナノファイバー (CNF) 様の構造物が直接、生成されることを見出している。申請者は、スギ木幹部の薄い切片を作成して、形態学的側面から、これら触媒反応による組織構造の前後変化を可視化する系を構築した。この際、光学顕微鏡と SEM を併用して、リグニン、セルロース等の存在部位を可視化し (光学顕微鏡)、SEM を用いて電顕レベルの形態学的変化を追跡する系を構築した (CLEM 法: 光学・電子顕微鏡相関法)。本研究は、過酸化水素水と触媒等による木材分解過程を、主に組織形態学的変化の解析に重点を置き、木材から先端化学材料等の有用化学物質への効率的分解/合成/利用法の開発・解析を行うことを目的とする。

### 実験方法、実験結果、考察:

本年度 (2022 年) は、光学顕微鏡用の薄いスギ切片 (9  $\mu\text{m}$  厚) を用いて、簡便な木材分解実験系を構築した。スギ木幹・心材部の木口面切片 (約 4 mm x 5 mm x 0.009 mm) を作成して、35%、30 %、25 %、20 %、0 %  $\text{H}_2\text{O}_2$  液中に浸して、静置化で 60  $^{\circ}\text{C}$  保温を行ない、切片の形がくずれる時間を調べたところ、30 %  $\text{H}_2\text{O}_2$  液中では約 1.5 日後、20 %  $\text{H}_2\text{O}_2$  液中では約 2.5 日後に目視で切片の形状が崩れ、ごく薄い切片を用いることにより、 $\text{H}_2\text{O}_2$  の添加のみで (触媒の添加なしで) 効率的に仮道管細胞壁の分解が起こることが明らかになった。反応液の量は 0.04~0.3 ml と変化させたが、ほぼ同様の結果であった。又、0 %  $\text{H}_2\text{O}_2$  中では、切片の形状は 4 週間経過後も保たれていた。又、60  $^{\circ}\text{C}$  以外の温度 (50  $^{\circ}\text{C}$ 、65  $^{\circ}\text{C}$ 、70  $^{\circ}\text{C}$ 、80  $^{\circ}\text{C}$ ) でも同様の実験を行ったところ、温度が高いほど、又、 $\text{H}_2\text{O}_2$  濃度が高いほど、早く切片の形状が崩れた。この実験系は、薄い切片を 60  $^{\circ}\text{C}$  等の加温した  $\text{H}_2\text{O}_2$  液中に静置するだけの簡便さで、ごく微量の木材量 (約 4 x 5 x 0.009 mm = 0.18 mm<sup>3</sup>) と、ごく少量の過酸化水素水 (0.04 ml 可能) を用いて、効率的にスギ木幹部の化学分解過程を追跡可能である。本実験系は微量の反応液で可能なため、96 穴プレート等を用いて、より効率的な化学分解を達成する触媒のスクリーニングにも応用可能と考えられる。

今後は、この反応過程における木質分解産物の同定を質量分析法等で行っていくと共に、分解過程の組織形態変化を Lignin, Cellulose, Hemicellulose 量等の変化に着目して行っていきたい。

## Functional analysis of non-canonical strigolactones as plant hormones and root-derived signals

Yoshiya Seto Meiji University

【The aim of this study】 Strigolactones (SLs) are plant hormones that regulate shoot branching, and also function as root-derived chemical signals. SLs are biosynthesized from carotenoids via a key intermediate molecule called carlactone (CL). In a model plant, *Arabidopsis*, CL is further converted into carlactonoic acid (CLA) by a cytochrome P450 monooxygenase, MORE AXILLARY GROWTH1 (CYP711A). We previously identified methyl esterified derivative of CLA, methylcarlactonoate (MeCLA) in *Arabidopsis*, and found that MeCLA can interact with the *Arabidopsis* SL receptor protein, AtD14. On the other hand, CL and CLA were not able to interact with AtD14, suggesting that the methyl esterification step is

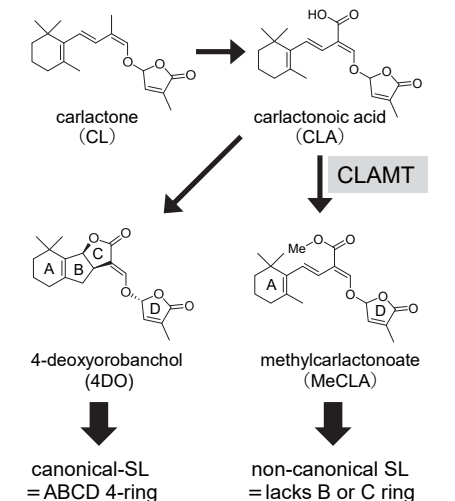


Fig. 1. The outline of the biosynthetic pathway for canonical and non-canonical SLs.

critical to converting a biologically inactive precursor to a bioactive hormone molecule. Conventional SL molecules have the tricyclic lactone ring part (ABC-ring) that is connected to another butanolide lactone part (D-ring) via an enol ether bridge. However, CL derivatives lack BC ring system and possess only the A and D rings. After the discovery of CL derivatives, structurally similar molecules have been isolated from various plant species. Currently, these new types of SL molecules are classified to be 'non-canonical' SLs, whereas the conventional SLs are called 'canonical' SL (Fig. 1). Although, these new types of SL molecules have been identified, the functional difference between canonical and non-canonical SLs are not fully understood. In this collaborative project with Prof. Shinjiro Yamaguchi in ICR, Kyoto University, we planned to clarify the biological role of non-canonical SL by focusing on carlactonoic acid methyltransferase (CLAMT), which is the key enzyme to produce non-canonical SLs (Fig. 1).

【Results】 To understand the functional difference between canonical and non-canonical SLs, we chose tomato as a plant material in which both of these two types of SLs are biosynthesized from a common intermediate, CLA. We found a *CLAMT* candidate gene in the tomato genome (*SlCLAMT*) and attempted to obtain the *clamt* knockout mutant using CRISPR-CAS9 method. We have successfully obtained several mutant lines in all of which some nucleotides are inserted or deleted in the coding region of the *SlCLAMT* gene. We grew these *slclamt* mutants and found that the growth of the axillary buds in *slclamt* mutant is activated compared with that in the WT plant. We compared the phenotype of the *slclamt* mutant with another SL biosynthetic mutant, *slccd8*. As a result, the branching phenotype of *slccd8* was much more severe compared with that of *slclamt*. These results strongly suggest that the CLAMT pathway products have an important role in shoot branching inhibition in tomato.



# Preparation of multi-stimuli-responsive polymer via controlled radical polymerization

Shinichi Yusa University of Hyogo

**Introduction:** A lower critical solution temperature (LCST) type polymer can dissolve in water below the LCST, however it cannot dissolve in water above the LCST. In this study, diblock copolymers ( $E_{95}N_n$ ) composed of poly(di(ethylene glycol) ethyl ether acrylate) (PeDEGA, E) and poly(*N*-isopropylacrylamide) (PNIPAM, N) were prepared via organotellurium-mediated radical polymerization (TERP).  $E_{95}N_n$  composed of PeDEGA ( $LCST_A$ ) and PNIPAM ( $LCST_B$ ) shows a two-stage LCST ( $LCST_A < LCST_B$ ). It is expected that  $E_{95}N_n$  can be applied for drug delivery (DDS) (Fig 1). Hydrophobic drugs can be encapsulated in the PeDEGA core of polymer micelles which are formed at  $LCST_A < T < LCST_B$ , and have good retention in blood. When drug-encapsulated micelles are introduced into blood, the micelles accumulate in the tumor due to the EPR effect. Furthermore, when the temperature of the affected area is locally heated above the  $LCST_B$ , the PNIPAM shells become hydrophobic to aggregate at the heated area. Furthermore, it is expected that endocytosis of the polymer micelles is accelerated due to the hydrophobic interactions. After the micelles are taken into the cells, cooling the affected area below the  $LCST_A$  causes the micelles to dissociate inside the cells, achieving controlled release of the drug.

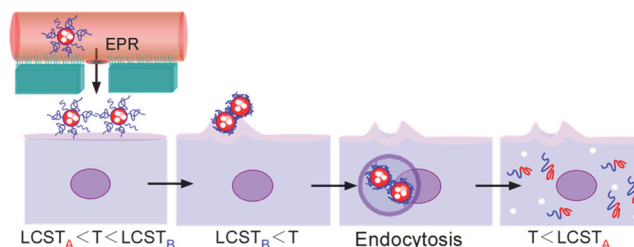
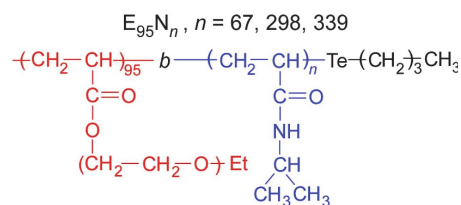


**Fig. 1** Conceptual diagram of dual temperature-responsive diblock copolymers in DDS.



**Scheme 1** Chemical structures of  $E_{95}N_n$ .

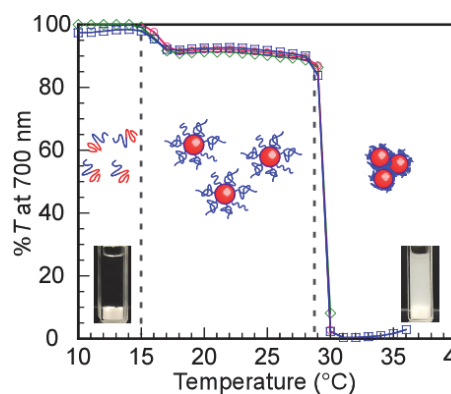


**Fig. 2** %T of  $E_{95}N_{67}$  ( $\diamond$ ),  $E_{95}N_{298}$  ( $\circ$ ), and  $E_{95}N_{339}$  ( $\square$ ) aqueous solutions as a function of temperature. Inserts are TEM observations for  $E_{95}N_{67}$  at 25 and 50 °C.

**Results and discussion:** The %T values of  $E_{95}N_n$  PBS solutions were measured as a function of the temperature (Fig. 2). All polymers were dissolved below 15 °C with unimer state. Core-shell polymeric micelles with the PeDEGA block core and the PNIPAM shells were formed at 15–29 °C. Above 32 °C the hydrophobic PNIPAM shell chains aggregated between the polymer micelles and the %T was further decreased. Unimer state with hydrodynamic radius ( $R_h$ ) of 4.08 nm can be observed at 10 °C with DLS. At 25 °C polymer micelles with  $R_h$  of 38.6 nm were observed. SAXS and TEM showed that the micelles formed at 25 °C.

**Conclusions:**  $E_{95}N_n$  were prepared via TERP.  $E_{95}N_n$  were unimer state below  $LCST_A$ , formed spherical micelles at  $LCST_A \leq T \leq LCST_B$ , and aggregated micelles above  $LCST_B$ . Fluorescence experiments showed that hydrophobic domains were formed above  $LCST_A$  in PBS.

## 積層 CNT ターゲットへの高強度レーザー照射による 高圧ガス生成に関する実験研究

松井隆太郎 京都大学

**研究背景と目的：**集光強度が  $10^{18-19} \text{ W/cm}^2$  のフェムト秒高強度レーザーを物質に照射することで生成する高エネルギー密度プラズマは、小型の粒子線癌治療装置の開発をはじめとした医療・産業・学術への幅広い応用が期待されている。レーザーの標的には通常、炭素化合物等の固体薄膜が用いられているが、その場合に生成するプラズマはパルス幅と集光径で決まる時空間領域に局在する非定常状態になる。一方、我々は先行シミュレーション研究により、波長程度(サブ $\mu\text{m}$ )の微細構造を付与した物質(ロッド)を標的とすることで、プラズマ中に準定常状態が導入可能であること、プラズマ温度が制御可能であることを見いだしている[1]。これに対して、nm オーダのミクロな構造物の集合体であり、ロッド径を極限まで下げた媒質と位置付けられる炭素ナノチューブ(CNTの質量密度は黒鉛の20%)は、レーザー照射により、ミクロな構造に起因する指向性を持つ相対論電子が生成されることから、癌治療への利用可能性が指摘されてる[2]。本研究では、医療応用をはじめとするプラズマの新機能の創出を目指して、CNTに高強度レーザーを照射する実験を行い、レーザーとの相互作用特性と発生する高エネルギー電子の空間分布を調べた。

**実験方法：**我々は、本学エネルギー理工学研究所(松田一成教授)から提供された積層CNTターゲット(図1(a)参照)を用いて、これに京大化研のT<sup>6</sup>レーザーを照射する実験を実施した。具体的には、厚さ500 $\mu\text{m}$ のシリコン基板上に作製された高さ300 $\mu\text{m}$ の積層CNTに対して、パルス幅および集光径が

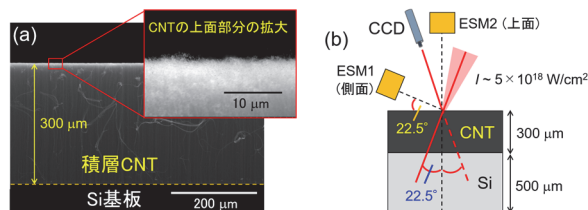


図1 (a)レーザー照射実験で使用した積層CNTターゲット(SEM画像)。(b)レーザー照射配位。上面・側面の2方向にESMを設置。

40 fs と 10  $\mu\text{m}$  (FWHM) で集光強度が  $5 \times 10^{18} \text{ W/cm}^2$  の高強度レーザーをCNTの高さ方向に対して22.5°で照射した。プラズマの電子温度を計測するため、CNTの側面(22.5°)と上面(90°)に、同一の性能を有する電子スペクトルメータを設置した(図1(b)参照)。

**結果と考察：**CNTの側面方向で得られた電子温度は、使用したレーザー集光強度から見積もられる理論値(242 keV)よりも高い値が得られた。また、正面方向と比較して、側面方向の電子温度は1.5倍程度大きくなった。同一のレーザー照射条件において、表面が均一の平坦構造であるシリコン基板を用いた場合、電子温度は側面・正面方向でほぼ等しかったことから、CNTへの高強度レーザー照射で生成するプラズマの電子温度は、(正面方向からのレーザー照射にもかかわらず)異方性を持つことが明らかとなった。また、CNTの側面方向の電子エネルギースペクトルには、500 keV付近の領域に特徴的な平坦構造が現出することを見いだした。今後、CNT中での航跡場の励起など、この異方性の起源とともに、それを促進して方向性を持った高エネルギーの電子ビームとして取り出すなどの可能性を追求する。

**成果報告：**松井隆太郎, 林 直仁, 石原聖也, 升野振一郎, 井上峻介, 橋田昌樹, 時田茂樹, 阪部周二, 岸本泰明, レーザー学会学術講演会第43回年次大会, 2023年1月20日, 名古屋。

**参考文献：**[1] R. Matsui, Y. Kishimoto *et al.*, International Conference on High Energy Density Sciences 2022, April 21st, 2022, Yokohama. [2] Dante Roa *et al.*, *Photonics* **9**, 403 (2022).

# 高強度レーザーと構造的媒質の相互作用による高エネルギー密度プラズマの生成・保持に関する実験研究

岸本泰明 京都大学

【計画全体の目的】集光強度が  $1\sim 10^{18-20}$  W/cm<sup>2</sup> の高強度レーザーをサブ  $\mu$ m オーダの微細構造を有する物質(構造的ターゲット)に照射することにより高エネルギー密度状態のプラズマが生成するとともに、その過程において現出するプラズマの自己組織化機能や構造形成機能を制御することにより、kT オーダの準定常強磁場の生成やそれによる生成プラズマの慣性時間を越えた保持(閉じ込め)を実現できる可能性が提案者等のシミュレーション研究により示されている[1]。本研究は、自然界にないナノメートルレベルの人工的な物質と光との相互作用を巧みに制御することにより新機能を創出するメタマテリアル概念に、レーザー照射によって生成されるプラズマの要素を取り入れた非線形領域のメタマテリアル科学と位置付けられる。これが実現すれば、中性子を出さない究極の核融合である陽子・ホウ素(P-B)反応など、これまでにない新たな応用が期待される。本研究では、この仮説を検証することを目的に、ナノ工学と材料工学を用いて構造的ターゲットを作製するとともに、これに京大化研 T<sup>6</sup> レーザーを照射する実験を行うことにより本仮説を検証する。

【2022 年度の成果】2022 年度は、2021 年度の成果を基礎に、1)高強度磁場生成用の構造的ターゲット作製、および、2)T<sup>6</sup> レーザー照射・計測系の構築を進めるとともに、3)作製した構造的ターゲットに照射強度が最大  $2\times 10^{19}$  W/cm<sup>2</sup> レベルのレーザー照射実験を行う環境を構築した。以下に詳細を記述する。

1) サブ  $\mu$ m サイズの構造的ターゲットの作製：電子線リソグラフィーとプラズマエッチングを含む半導体技術を併用することにより、レーザー照射時に目的に沿った多様な機能を有するサブ  $\mu$ m オーダの微細構造を有する構造的ターゲット作製を可能にする技術の向上・獲得を図った。図1は、照射レーザーを100 $\mu$ m オーダのリング構造に捕獲・電流路を形成することにより高強度の準定常磁場を生成するメタマテリアル様のターゲットの一例を示す。周辺には、レーザーの集光と強度調整用の多様なマーキングを配置している。リング中心には、レーザー照射時に特定な密度のプラズマを発生するロッド集合体を配置している。

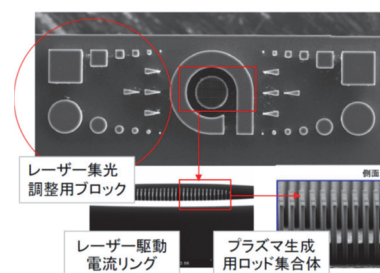


図 1. 2022 年度に開発に成功した高強度磁場生成用の構造的ターゲットの例。

2) T<sup>6</sup> レーザー照射・計測系の構築：多様な構造を有するターゲットに集光強度が  $10^{17-20}$  W/cm<sup>2</sup> レベルの高強度レーザーを複数の方向(上面・側面方向など)から照射可能な自由度の高い実験系を構築した。図2は、生成された高エネルギー密度プラズマのエネルギー分布を2方向から同時計測するための電子エネルギースペクトルメータ(ESM)を設置した様子を示す。今後、密度計測および磁場計測系の構築を目指す。

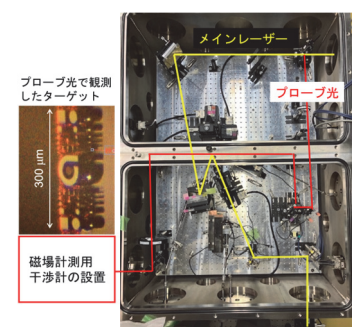


図 2. 2022 年度に設置した 2 台 ESM を有する構造的ターゲットとレーザーの相互作用実験の配位。左は図1で示したレーザーを閉じ込める円形リングを付与したロッド集合体を示す。

3) レーザー照射実験の実施：1)および 2)で作製・構築したシステムを用いたレーザー照射実験を開始した。実験では、平面ターゲットと異なった空間充填率を有するロッド集合体の照射実験を実施、充填率の違いによる電子エネルギー分布の相違など、微細構造に起因する特性の違いなどを示す結果を取得し、関連学会等で報告を行った。

参考文献：[1]Y. Kishimoto, et al., 10<sup>th</sup> IFSA 2017, St Malo, France September 11-15 (2017)

[2] 岸本泰明, 松井隆太郎:「高強度レーザーと構造的媒質との相互作用による高エネルギー密度プラズマの生成と保持:背景理論と実験検証に向けた取り組み」レーザー学会第 43 回年次大会, 2023 年 1 月 20 日

## Determine the three-dimensional structure of $^{13}\text{C}$ labeled $\alpha$ -synuclein(61-95) in the Langmuir-Blodgett film and supported phospholipid bilayer by MAIRS2

Chengshan Wang Middle Tennessee State University

### A. Objectives:

1.  $^{13}\text{C}$  labeled  $\alpha$ -syn(61-95) containing residues 61-95 of  $\alpha$ -synuclein will be synthesized and purified.
2. Screen the conformation and orientation of specific amino acid residue of  $\alpha$ -syn(61-95) in Langmuir-Blodgett film.
3. Screen the conformation and orientation of specific amino acid residue of  $\alpha$ -syn(61-95) in supported phospholipids bilayers.

### B. Experimental methods:

Peptide of  $^{13}\text{C}$  labeled  $\alpha$ -syn(61–95) at position 93G was synthesized via solid phase (Fmoc) chemistry and purified by semipreparative reversed-phase high-performance liquid chromatography (RP-HPLC) on Waters Breeze 2 separation system equipped with 1525 EF binary pump. The success of the synthesis and the purity of the peptide were confirmed by a Waters SYNAPT q-TOF tandem mass spectrometer. The surface pressure-area ( $\pi$ -A) isotherm of  $\alpha$ -syn(61–95) were conducted in a A Kibron  $\mu$ trough. The Langmuir-Blodgett (LB) films of  $\alpha$ -syn(61–95) were made by transferring the  $\alpha$ -syn(61–95) Langmuir monolayers to quartz slides and silicon (Si) slides under the surface pressure 10 mN/m. The circular dichroism (CD) spectra of the LB films of the  $^{13}\text{C}$  labeled  $\alpha$ -syn(61–95) were measured by a JASCO J-810 spectropolarimeter. p-Polarized Multiple-Angle Incidence Resolution Spectroscopy (pMAIRS) measurements were performed on the Nicolet IS50 FT-IR spectrometer (Thermo Scientific, Waltham, MA) equipped with a pMAIRS accessory. The LB film monolayer of the  $^{13}\text{C}$  labeled  $\alpha$ -syn(61–95) at position 93G on Si substrate was put in the pMAIRS accessory and the IR beam transmitted through the sample.

### C. Experimental results:

The  $^{13}\text{C}$  labeled  $\alpha$ -syn(61–95) was synthesized and purified. Figure 1A shows the  $\pi$ -A isotherm of the  $^{13}\text{C}$  labeled  $\alpha$ -syn(61–95) and the isotherm is very similar to that of the unlabeled  $\alpha$ -syn(61–95). This is not a surprise because replacement of a  $^{12}\text{C}$  by  $^{13}\text{C}$  in the backbone carbonyl (i.e.,  $\text{C}=\text{O}$ ) should not change the overall biophysical behavior of the peptide, which contains hundreds of carbon atoms in it. Thus, the CD spectrum of the  $^{13}\text{C}$  labeled  $\alpha$ -syn(61–95) is also similar to that of unlabeled peptide as shown in Figure 1B. For the LB films of the  $^{13}\text{C}$  labeled  $\alpha$ -syn(61–95), two negative peaks at 222 and 208 nm in addition to one positive peak at 192 nm are detected. Therefore, the  $^{13}\text{C}$  labeled  $\alpha$ -syn(61–95) also transforms to  $\alpha$ -helix at the



interface. On the other hand, pMAIRS was used to determine the tilted angle of the axis of  $\alpha$ -syn(61–95) at 93G and is very different to that of the unlabeled peptide. As shown in Figure 1C, The In-plane Spectrum ( $S_{IP}$ ) result of the  $^{13}\text{C}$  labeled  $\alpha$ -syn(61–95) was shown as the top curve in Figure 1C. Both regular amide I and II bands were detected at 1655 and 1535  $\text{cm}^{-1}$ , respectively. A very strong  $^{13}\text{C}$  amide I band was also detected at 1625  $\text{cm}^{-1}$  in the  $S_{IP}$ . The position at 1625  $\text{cm}^{-1}$  shows that the 93G is in  $\alpha$ -helical conformation in the LB film. In addition, the  $^{13}\text{C}$  amide I band in the  $S_{IP}$  result is even more intensive than the regular amide I band which is the absorption sum of all the other thirty-four residues in the sequence of  $\alpha$ -syn(61–95). Such an intensive  $^{13}\text{C}$  amide I band suggests a very small tilt angle (i.e., parallel orientation) of the  $^{13}\text{C}$  amide I transition moment. The out-of-plan Spectrum ( $S_{OP}$ ) shown in the bottom curve of Figure 1C also detects the amide I band at 1659 and 1645  $\text{cm}^{-1}$ . More importantly, the  $^{13}\text{C}$  amide I band at 1625  $\text{cm}^{-1}$  was not detected in the  $S_{OP}$  result, even though the  $^{13}\text{C}$  label does exist at position 93G. According to the selection rule of pMAIRS, the tilt angle of the  $^{13}\text{C}$  amide I transition moment at 93G is  $\sim 0^\circ$ . Because the tilt angle of the axis of  $\alpha$ -helix is equal to that of the  $^{13}\text{C}$  amide I transition moment, the tilt angle of the axis of  $\alpha$ -helix at 93G is also  $\sim 0^\circ$ .

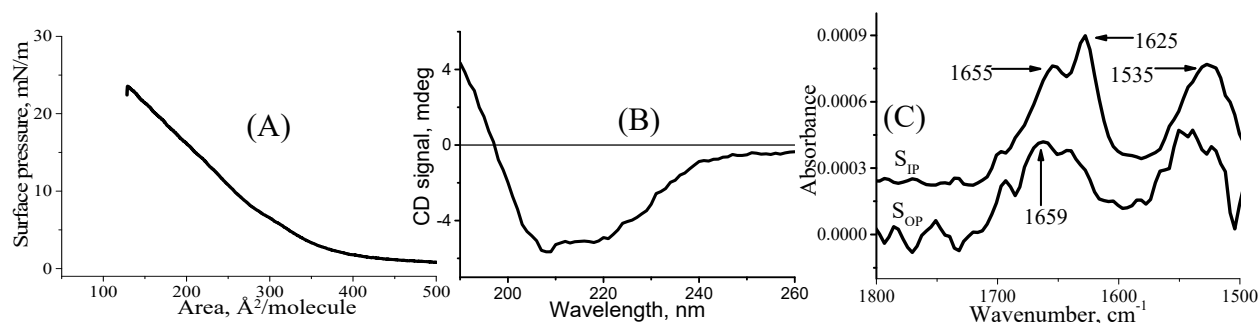


Figure 1. (A) Surface pressure-area isotherm of the  $^{13}\text{C}$  labeled  $\alpha$ -syn(61–95) on pure water, (B) CD spectra of the LB films of the  $^{13}\text{C}$  labeled  $\alpha$ -syn(61–95) on quartz slides. (C) p-MAIRS results of the LB monolayer of the  $^{13}\text{C}$  labeled  $\alpha$ -syn(61–95) transferred under 10 mN/m.

#### D. Discussion

X-ray crystallography and NMR are two major methods to determine protein's structure. However, neither of them can elucidate the high resolution structure of membrane proteins, which weighs  $\sim 30$ -35% of the total proteins, in monolayer structure. Dr. Wang and Dr. Hasegawa are developing a novel method for membrane proteins even in monolayer structure with high resolution by pMAIRS, which will be a supplement to X-ray crystallography and NMR.

#### E. Publication.

One paper about Figure 1 was published by Wang C., Zhou Y., Ewuola C., Akinleye T., Hasegawa T., Leblanc R. M. in *Analytical Sciences*, **2022**, *38*, 935-940.

## The 16th International Workshop for East Asian Young Rheologists

Tadashi Inoue Osaka University

【Purpose of project】 The ICR budget was used to organize the 16th International Workshop on Young Rheologists in East Asia (IWEAYR-16). The purpose of this workshop is to promote international exchange among young faculty and graduate students in cooperation with researchers from various countries in East Asia in several research fields, such as polymer science and materials science. IWEAYR allows participants to present their research results and discuss and exchange research ideas in a friendly atmosphere. The workshop will deepen our research activity and form the basis for future cooperation. This year, IWEAYR-16 was held in Udon Thani, Thailand. Because registration took place before November 2022, there were no participants from China, where travel was prohibited due to Covid-19, but there were still more than 100 participants. Many undergraduate and graduate students participated, and the mission of strengthening future collaboration was not compromised in the slightest despite three years break. The budget was effectively utilized to support the participation of as many Japanese researchers as possible.

【Place and schedule of workshop】 IWEAYR - 16 was held from February 18 - 21, 2023, at Centra Hotel & Convention Centre Udon Thani and Montatip Hall Expo & Convention Centre, Udon Thani, chaired by Doctor Adisak Takhulee of Udon Thani Rajabhat University, Thailand..

【Purpose of the workshop】 From the beginning, the purpose of this workshop is to promote international exchange and collaboration among young faculties and graduate students who will be the leading researchers in the field of rheology and material science in the near future and, therefore, to provide a place for research presentation and discussion, and to revitalize related fields. At the same time, in order to further develop joint research activities among several research groups, it is to provide a place for people exchange.

【Background of workshop】 This workshop has been held annually since the first IWEAYR in Seoul (February 2006). After that, it was organized in Kyoto (January 2007), Shanghai (January 2008), Nakhon Ratchasima (January 2009), Busan (January 2010), Yamagata (January 2011), Beijing (February 2012), Phuket (January-February 2013), Seoul (February 2014), Fukuoka (February 2015), Shenzhen (January 2016), Pattaya (February 2017), Jeju Island (January 2018), Nagoya (January 2019), and Changchun (January 2020) (in a circulating order of Korea, Japan, China, and Thailand). There have been some changes in the organization of the workshop due to various circumstances in the hosting countries; every IWEAYR has served as a place for faculties and graduate students to engage in international exchange and collaboration.

【Participants】 Doctor Takhulee, the organizer, was an alumnus of IWEAYR. He understands the purpose of IWEAYR very well, and therefore the conference was conducted with meticulous attention to detail. The number of participants in this IWEAYR-16 was 26(31) professors and 84 (91) students, which was the average level in recent years, although China could not attend. (Numbers in () are the numbers of participants IWEAYR-15). The breakdown by country was Japan 35 (10+25), Korea 71(12+59), China 0, and Thailand (4+9). The main participants were:

Kyung Hyun Ahn, Professor,	Seoul National University,	Korea,
Jaewook Nam, Professor,	Seoul National University,	Korea,
Kyu Hyun, Professor,	Pusan National University,	Korea,



Youngdon Kwon, Professor,	Sungkyunkwan University,	Korea,
Visit Vao-soongnern, Asso. Prof.	Udon Thani Rajabhat University	Thailand
Exkarach Deenang, Asso. Prof.	Udon Thani Rajabhat University	Thailand
Hiroshi Watanabe, Professor,	Kyoto University	Japan
Takashi Taniguchi, Asso. Prof.,	Kyoto University	Japan
Hiroshi Suzuki Professor,	Kobe University	Japan
Ruri Hidema, Associate Prof.,	Kobe University	Japan



Opening Seremony



Photo of Banquet

【Overview of IWEAYR-16】 Total number of submitted papers was 29(Oral) + 53(Poster). On the first day, the session started with one invited talk. After that, long oral presentations (12) were given by mostly Ph.D. students. After lunch, the short oral presentations (53) by master course students were presented before the poster presentations. On the second day, long oral presentations (14) were given by Ph.D. students. Then, a group excursion was organized. The four best presentation awards of Ph.D. students were chosen by the participant's vote.

At this conference, there were many studies on battery slurry for manufacturing Li-ion batteries, particularly by Korean groups whose major is chemical engineering. The studies on new materials such as nano cellulose as well. In addition, there was basic research on the analysis of various rheological properties and hierarchical structures of polymers. Some issues, such as theory, simulation, and flow control of soft matter, were also presented.

The author has attended IWEAYR in Thailand four times. The host city, Udon, locates near the border with Laos. He wondered what kind of place, but the venue, Centra Hotel & Convention Centre Udon Thani, was a very nice and modern hotel with a large shopping mall next to it. The workshop was sponsored by Thai universities and Thai companies, and the author felt the great development of the Thai economy and, at the same time, the deterioration of Japan due to the weak yen. The immigration procedures were also simplified at the time of the event, and the author felt that things were gradually returning to the way they were before the COVID-19 pandemic.

【Summary】 All students enjoyed the workshop, and the author believes that this experience will help maintain a network of young rheologists in East Asia. Also, Covid-19 feels us of the importance of continuing such a workshop to keep the international relationship. In conclusion, IWEAYR-16 successfully achieved its purpose. Finally, the author should note that the next IWEAYR-17 will be held in Pusan, Korea, in the wintertime.

## Tackling the Electronic Instability of Charge-Density Waves by Electron Energy-Loss Spectroscopy

Ming-Wen Chu National Taiwan University

This project (2022-126) aims at resolving the electron-phonon coupling in the charge-density-wave (CDW) state of CuTe by electron energy-loss spectroscopy (EELS), in collaboration with Prof. Hiroki Kurata at ICR. CuTe stands for a prototypical CDW, with the quasi-one-dimensional crystal structure and iconic Fermi surface nesting both characteristic of the Peierls-transition classics of CDWs. Due to the COVID-19 pandemic, it has, however, been unlikely for my group to conduct the desired high-resolution EELS study in Prof. Kurata's laboratory. Nonetheless, we were still committed to the EELS investigation of CuTe using in-house EELS with a momentum resolution of  $\sim 0.09 \text{ \AA}^{-1}$  and energy resolution of  $\sim 0.54 \text{ eV}$ , which are sufficient for tackling the plasmon excitations in CuTe though insufficient for the desired electron-phonon coupling with a typical energy scale below  $100 \text{ meV}$ . As a result, we turned our interest to the subject of plasmon dispersions in CDWs, whereby the impact of the static electronic order of CDWs on the dynamical charge oscillation of plasmons remains a largely unsettled problem. Here below, we show a plasmon dispersion map acquired in my laboratory in National Taiwan University using the EELS with a compromised capability. This map serves as the important first step toward our in-depth experiments to come in ICR in 2023 and has manifested the quadratic dispersion as a function of momentum transfer ( $q$ ) in agreement with the free-electron gas behavior. The intriguing correlation with the CDW order of CuTe is to be resolved shortly together with Profs. Kurata and Haruta in ICR.

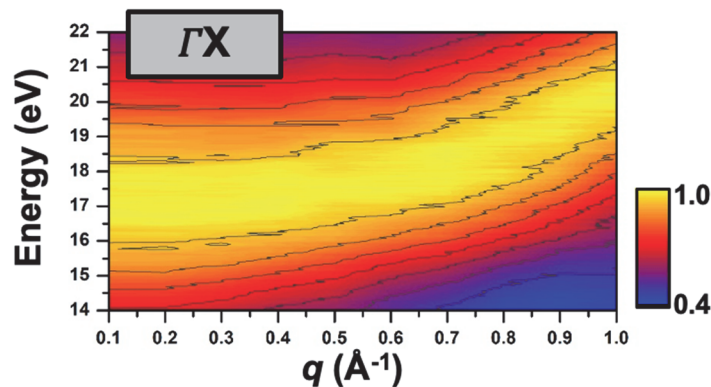


Figure. The plasmon dispersion of CuTe along the CDW-order direction of  $\Gamma X$ .

# Micro- and Nano-structural Characterization by Advanced Transmission Electron Microscopy of Novel Functional Materials

Torranin Chairuangsrri Chiang Mai University

Our research group from Thailand visited ICR onsite in collaboration with Prof. Hiroki KURATA, Assoc. Prof. Mitsutaka HARUTA, Dr. Atsushi YAMAGUCHI and Mr. Tsutomu KIYOMURA, for characterizing nano-structure of novel functional materials by advanced transmission electron microscopy. The results can be summarized as follows.

## I. Novel $\text{SiO}_2/\text{rGO}/\text{Polymer}$ and $\text{FeO}_x/\text{C}$ composites from biomass as Anode in LIBs

Polyaniline-coated nano-silica@reduced graphene oxide ( $\text{PANI-SiO}_2/\text{rGO}$ ) composites were fabricated. STEM revealed that  $\text{SiO}_2$  nanoparticles were homogeneously loaded on graphene sheets and the PANI fibrous network uniformly covers the  $\text{SiO}_2/\text{rGO}$  composites. STEM also showed structural stability of the composites after cycling without aggregation of the  $\text{SiO}_2$  nanoparticles. However, some  $\text{SiO}_2$  nanoparticles transformed to be Si nanoparticles after cycling. For  $\text{FeO}_x/\text{C}$  composites from biomass, HRTEM depicts the presence of graphitic domains scattered in amorphous structure. EELS from carbon revealed two peaks at 287 eV and 290-300 eV, suggesting an amorphous carbon structure.

## II. Annealed 28wt.%Cr-1wt.%(Mo/W) Cast Irons

Carbides in annealed 28 wt.% Cr-2.6 wt.% C high chromium cast irons with the addition of Mo or W have been characterized by STEM and EELS was also used to identify  $\text{M}_7\text{C}_3$  and  $\text{M}_{23}\text{C}_6$  carbides in these irons. Fine structures in C K-edge spectra were found to be useful for distinguishing between  $\text{M}_7\text{C}_3$  and  $\text{M}_{23}\text{C}_6$  carbides. The C K-edge of  $\text{M}_{23}\text{C}_6$  incorporates a shoulder-like feature at approximately 287 eV, the second peak from  $\text{M}_7\text{C}_3$  in the Mo1 and W1 irons has lower intensity than that in the R iron, and the peak height ratio of the first and second peaks from  $\text{M}_{23}\text{C}_6$  in the Mo1 and W1 irons is lower than that in the R iron.

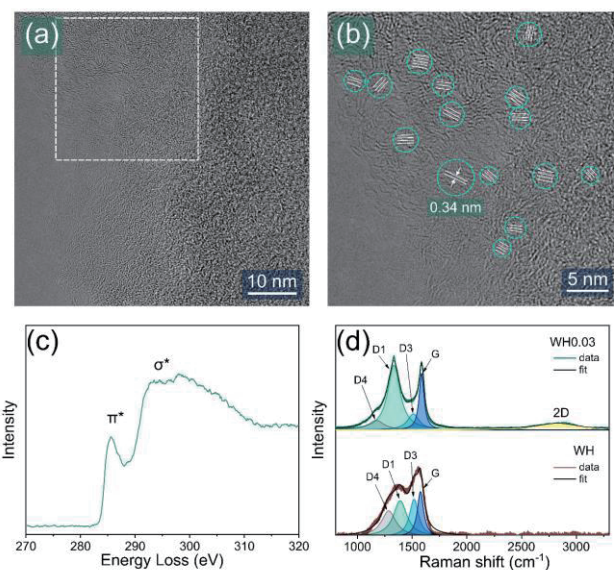


Fig. 1 (a) TEM image of the carbon matrix in  $\text{FeO}_x/\text{C}$  composites, (b) The examples of graphitic domains within carbon region, (c) EELS spectrum of the carbon matrix, and (d) Raman spectra from  $\text{FeO}_x/\text{C}$  composites as compared to those from raw materials.

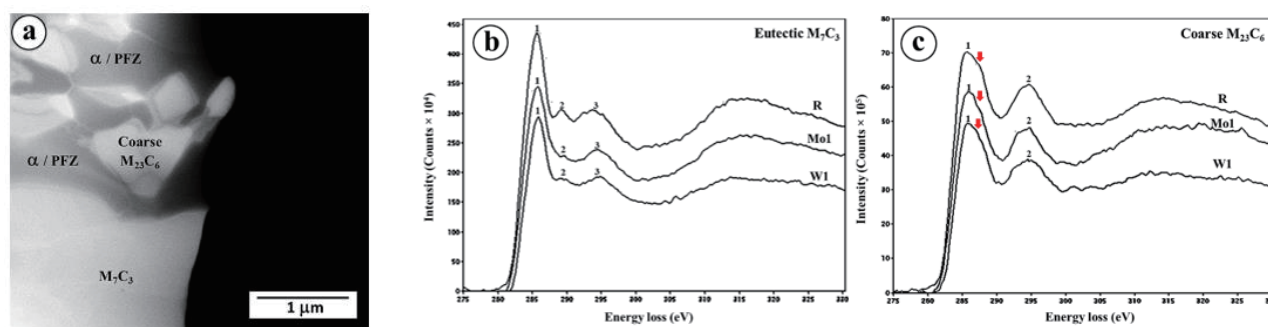


Fig. 2 STEM-ADF image shows the microstructure of the R iron after annealing (a) and C K-edge spectra from (b) eutectic  $\text{M}_7\text{C}_3$  and (c) coarse  $\text{M}_{23}\text{C}_6$  in the irons.

## Publications:

1. Rice husks-derived nano- $\text{SiO}_2$  assembled on reduced graphene oxide distributed on conductive flexible polyaniline frameworks towards high-performance lithium-ion batteries (RSC Advances, 12(23) (2022), 14621-14630).
2. Recycling water hyacinth stem waste for cost-effective production of carbon/ $\text{FeO}_x$  nanocomposite anodes for sustainable fast-charging lithium-ion batteries (submitted to Journal of Material Science: Materials in Electronics).
3. Electron microscopy of carbides in annealed 28wt.%Cr-1wt.%(Mo/W) cast irons (submitted to Materials Characterization).

## High-pressure synthesis of transition metal oxides with novel physical properties

Kunlang Ji University of Edinburgh

**Objectives:** High pressure-high temperature (HPHT) synthesis is used to stabilize unusual oxidation states and coordination environments in transition metal oxides, resulting in interesting physical properties. In collaboration with Professor Shimakawa in ICR at Kyoto University, a unique high-pressure multianvil apparatus which reaches up to 20 GPa and 2273 K is available to use. This equipment provides a good opportunity for synthesizing the double corundum/perovskite with small tolerance factor and develop their potential multiferroics.

**Experimental methods:** Due to the Covid-19 special circumstance, we developed our collaboration by communicating e-mails. We focus on finishing the paper of the new double corundum  $\text{Co}_2\text{InSbO}_6$  synthesized at Kyoto University during early 2020, while Professor Shimakawa providing very useful scientific guidance for the paper through emails. The paper has been finally published on *Angewandte Chemie International Edition* in 2022.

**Experimental results:**  $\text{Co}_2\text{InSbO}_6$  recovered from high pressure has a new, ordered-*R*32  $\text{A}_2\text{BCO}_6$  variant of the corundum structure.  $\text{Co}_2\text{InSbO}_6$  is also remarkable for showing an unprecedented sequence of two cation redistributions, to  $(\text{Co}_{0.5}\text{In}_{0.5})_2\text{CoSbO}_6$  and then  $\text{Co}_2\text{InSbO}_6$  variants of the ordered- $\text{LiNbO}_3$   $\text{A}_2\text{BCO}_6$  structure on heating. The cation distributions change magnetic properties as the final ordered- $\text{LiNbO}_3$  product has a sharp ferrimagnetic transition at 65 K whereas the initial ordered-*R*32 material has a broader feature indicative of short range spin ordering.

**Discussion:** The selective site exchange only between  $\text{Co}^{2+}$  and  $\text{In}^{3+}$  at different temperatures results from the small size and charge mismatch between  $\text{Co}^{2+}$  ( $r^{\text{VI}} = 0.745 \text{ \AA}$ ) and  $\text{In}^{3+}$  ( $r^{\text{VI}} = 0.8 \text{ \AA}$ ), compare to that between  $\text{Co}^{2+}$  and  $\text{Sb}^{5+}$  ( $r^{\text{VI}} = 0.6 \text{ \AA}$ ).

**Publication:** K. Ji, E. Solana-Madruga, M. A. Patino, Y. Shimakawa\* and J. P. Attfield\*, *Angew. Chem. Int. Ed.*, 61, e202203062 (2022)

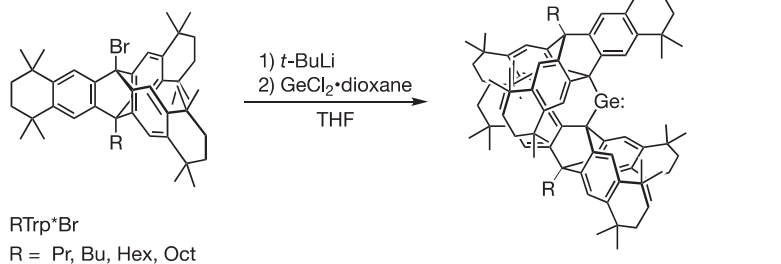
## Synthesis and Characterization of Novel Group 16 Element Compounds

Mao Minoura Rikkyo University

In general, germanium-chalcogen double bond compounds are known to be highly reactive and the double bond compounds dimerize easily. By utilizing bulky protecting groups, germanium-chalcogen double bond compounds can be synthesized and isolated; Tokitoh *et al.* reported the synthesis of germanium-chalcogen double bond compounds with large aromatic Tbt groups. However, no stable germanium-chalcogen double bond compounds have been reported for alkyl substituted compounds due to the difficulty of ligand design.

Recently, our group has designed and synthesized Trp\*, *i.e.*, a novel triptycene (Trp)-based aliphatic bulky group that bears bulky fused ring-type substituents at the periphery of the Trp framework. In our experiences, compounds with bulky substituents, such as Trp\*, have low solubility and poor crystallinity. In fact, the synthetic studies of Trp\*-substituted germanium compounds initially yielded only crystals that were too small to be analyzed structurally by X-ray diffraction. To improve the solubility and crystallinity of Trp\* compounds, alkyl chains were installed at the bridgehead position. In this paper, we report the synthesis of Trp\* groups having alkyl chains (R= Pr, Bu, Hex, Oct), RTrp\*, and applied them to the synthesis of dialkylgermylenes (RTrp\*<sub>2</sub>Ge:) in the expectation of improving those crystallinities by intermolecular interactions with the packing forces in the solid states. The isolated RTrp\*<sub>2</sub>Ge: showed better solubility and crystallinity than the corresponding Trp\*<sub>2</sub>Ge:. Especially, HexTrp\*<sub>2</sub>Ge: and HexTrp\*<sub>2</sub>Ge=S showed characteristic change in the packing structure to form suitable single crystals for X-ray analysis.

We thank Professors Norihiro Tokitoh, Yoshiyuki Mizuhata, and Mariko Yukimoto for their kind discussions.





## Analyzing chemical properties and origins of dissolved organic matter in lakes and soils by FT-ICR-MS

Morimaru Kida Kobe University

**Objectives:** Dissolved organic matter (DOM) represents one of the largest actively cycled carbon pools on earth. The molecular composition of DOM plays a major role in its long-term persistence in aquatic systems, yet the extreme complexity and heterogeneity of DOM have so far hindered its full characterization at the molecular level. The high resolution and mass accuracy of FT-ICR MS allow the assignment of molecular formulae to tens of thousands of compounds in DOM. We first aimed to establish the very first platform to enable a high-quality FT-ICR-MS analysis of DOM. Then, we aimed to elucidate the factors that influence the molecular composition of various DOM in lakes and soils.

**Materials and methods:** We first optimized the conditions for FT-ICR-MS measurement of DOM using an international reference DOM sample and electrospray ionization (ESI). Because FT-ICR MS at ICR was unfortunately out of order during the duration of this project, FT-ICR MS at RISH was used instead. After the optimal condition was established, DOM samples collected from lakes and diverse soils were analyzed. Molecular formulae of detected masses were determined using an online mass spectra processing pipeline, ICBM-OCEAN. Multivariate analysis was conducted to identify environmental and edaphological factors that determine the molecular composition.

**Results and discussion:** A significant portion of the project duration was dedicated to the optimization of the measurement conditions. This was further complicated by the difference in machine conditions between ICR and RISH FT-ICR-MS. We could eventually, however, start analyzing samples under the optimized conditions, and the analysis is still ongoing.

**Outcome reports:** No reports yet published.



## Preparation of high-efficiency spin-injection materials using optimization of magnetism and crystal structure

Masaaki Tanaka Nagoya Institute of Technology

The spin-filtering effect, where the spin-polarized current is generated using electron tunneling through a ferromagnetic insulator, is one of the candidates for the spin injection method. Independently, it is known that magnetic insulator cobalt ferrite (CFO) films grown epitaxially on MgO (001) substrates have large perpendicular magnetic anisotropy (PMA) which is induced by the in-plane tensile strain. In this study, the spin-filtering effect of insulative Fe-rich CFO (I-CFO) films with PMA grown on conductive Fe-rich CFO (C-CFO) films was investigated.

The multilayered films of C-CFO(20 nm)/I-CFO(3.0 nm)/MgO(1.0 nm)/Co(1.0nm)/{Tb(0.45 nm)/Co(0.56 nm)}<sub>15</sub>/Co(2.0 nm) were prepared on MgO (001) substrates with I-CFO (20 nm) buffer layers using the pulsed laser deposition (PLD) and electron beam deposition technique. The systematic change between the I-CFO and C-CFO films was performed by the change of the source materials and gas conditions during the PLD. The magnetization measurements clarified that the C-CFO/I-CFO layers have PMA. The magnetic tunnel junctions (MTJs) with a junction diameter of several micrometers were fabricated using photolithography and dry etching by an ion-milling method. This microfabrication was carried out at ICR, Kyoto University. The magnetoresistance measurements of the MTJs were performed using a four-probe method at various temperatures.

The current-voltage measurements indicated that the CFO/MgO layer shows good tunneling properties. The resistance increased dramatically with decreasing temperature, which indicates that the conductivity of the junction is governed by the tunneling current. The tunnel magnetoresistance (TMR) ratio of  $-20\%$  was obtained at 100 K at the bias voltage of 100 mV. The estimated spin injection efficiency was  $-28\%$ . It is found that the bias-voltage dependence of the TMR ratio can be interpreted by the Fowler-Nordheim tunneling mechanism, which means that the spin-polarized current is generated by the spin-filtering effect of the ferromagnetic insulator I-CFO layers. The I-CFO spin-filtering layer is, therefore, applicable as a spin injection source for spintronics devices when perpendicularly spin-polarized electronic currents are required.

### 成果報告

M. Tanaka, M. Furuta, T. Ichikawa, M. Morishita, Y.-M. Hung, S. Honda, T. Ono, and K. Mibu, “Generation of spin-polarized electronic currents using perpendicularly magnetized cobalt-ferrite spin-filtering barriers grown on spinel-type-conductive layers”, *Applied Physics Letters*, **122**, 042401 (2023).

## Development of a highly efficient CsPbBr<sub>3</sub> scintillator

Hikaru Saito Kyushu University

It has been reported that CsPbBr<sub>3</sub> nanoparticles embedded in Cs<sub>4</sub>PbBr<sub>6</sub> matrix (CsPbBr<sub>3</sub>/Cs<sub>4</sub>PbBr<sub>6</sub> nanocomposite) exhibit high photoluminescence (PL) quantum yield [1]. The size distribution and the density of CsPbBr<sub>3</sub> nanoparticles in Cs<sub>4</sub>PbBr<sub>6</sub> matrix have not been analyzed by electron microscopy probably because this nanocomposite is very sensitive to electron beams. Recently we have found sub-nanosecond cathodoluminescence (CL) decay from CsPbBr<sub>3</sub>/Cs<sub>4</sub>PbBr<sub>6</sub> nanocomposite by using Hanbury Brown-Twiss interferometry [2], which is applicable to high performance scintillator for fast electron beams. To elucidate the CL mechanism, we have attempted 4D-STEM and electron energy-loss spectroscopy (EELS) to analyze the nanostructure of CsPbBr<sub>3</sub>/Cs<sub>4</sub>PbBr<sub>6</sub> nanocomposite.

Fig. 1 shows 4D-STEM obtained from CsPbBr<sub>3</sub>/Cs<sub>4</sub>PbBr<sub>6</sub> nanocomposite at a probe current of 2.3 pA and an acceleration voltage of 300 kV, indicating that cubic CsPbBr<sub>3</sub> crystals with a size of about 10 nm were contained in the Cs<sub>4</sub>PbBr<sub>6</sub> matrix. 4D-STEM can only detect CsPbBr<sub>3</sub> nanoparticles satisfying diffraction conditions, meaning that it is not appropriate for particle density measurements. Therefore, we applied STEM-EELS for a CsPbBr<sub>3</sub>/Cs<sub>4</sub>PbBr<sub>6</sub> nanocomposite thin film. Fig. 2 shows the results obtained at a probe current of 1.6 pA and an energy resolution of 50 meV and an acceleration voltage of 60 kV. EELS spectrum at each measurement point was decomposed into two component spectra corresponding to CsPbBr<sub>3</sub> (Fig. 2b) and Cs<sub>4</sub>PbBr<sub>6</sub> (Fig. 2c), which clearly indicates that high density CsPbBr<sub>3</sub> nanoparticles with sizes of about 10-20 nm are embedded in the Cs<sub>4</sub>PbBr<sub>6</sub> matrix. This information would be crucial to derive a model for the found sub-nanosecond CL, leading to development of high performance optical nanomaterials including fast scintillators.

[1] Ya-Meng Chen, et al., *ACS Appl. Mater. Interfaces*, **10**, 15905 (2018).

[2] Sotatsu Yanagimoto, et al., *Phys. Rev. B*, **103**, 205418 (2021).

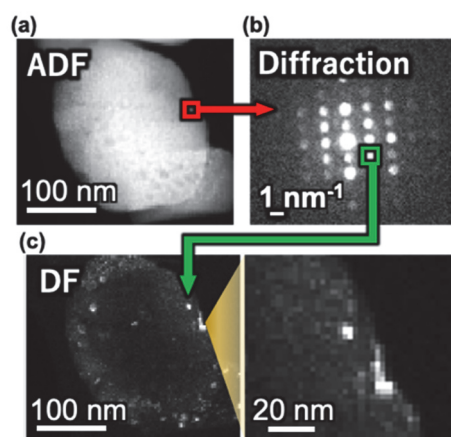


Fig. 1 (a) ADF-STEM image of CsPbBr<sub>3</sub>/Cs<sub>4</sub>PbBr<sub>6</sub> nanocomposite and (b) diffraction pattern from the rectangular area in (a). (c) Virtual DF image by using intensity of the diffraction spot indicated by the rectangular area shown in (c).

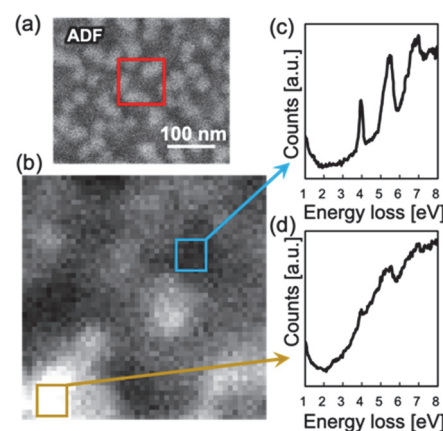


Fig. 2 (a) ADF-STEM image of a CsPbBr<sub>3</sub>/Cs<sub>4</sub>PbBr<sub>6</sub> nanocomposite thin film and (b) CsPbBr<sub>3</sub> map derived by EELS mapping. (c,d) EELS spectra corresponding to Cs<sub>4</sub>PbBr<sub>6</sub> and CsPbBr<sub>3</sub> extracted from the areas indicated in (b).

## 核融合プラズマ対向材料中の水素・ヘリウム挙動の高精度測定

宮本光貴 島根大学

タングステンは将来の核融合炉ダイバータ材料としての利用が予定されている。本研究では、タングステン中のヘリウムバブルが水素保持に及ぼす影響について、モノクロメータ搭載低加速原子分解能分析電子顕微鏡(STEM-EELS, 京都大学)を用いて直接捉えることを目的とした。

島根大学のイオン銃直結型透過型電子顕微鏡を用いて薄膜化したタングステン試料に比較的大きなヘリウムバブル( $d \sim 10$  nm)を導入するために、室温で 3 keV-He<sup>+</sup>を照射後、1473 K でアニールした。その後、室温で 3 keV-D<sub>2</sub><sup>+</sup>を  $1 \times 10^{21}$  /m<sup>2</sup> まで照射した試料を STEM-EELS により、室温から 100 K 刻みの等時焼鈍を行い、各温度における重水素、およびヘリウムの存在位置を高い空間分解能で定量的に評価した。

図 にヘリウム予照射後、重水素照射したタングステンを昇温した際の各温度における(a)高角度散乱円環暗視野像(HAADF 像), および(b)重水素, (c)ヘリウムの濃度分布像を示す。HAADF 像中の黒いコントラストはヘリウム予照射に起因したヘリウムバブルを示す。重水素マッピングからバブル内に明瞭に高濃度の重水素が存在することが明らかとなり、重水素保持量の増加に寄与したと考えられた。バブル内の重水素濃度は温度の上昇に伴い低下し、473K 程度で放出されることが分かった。一方、バブル内のヘリウム濃度は温度の上昇に伴い上昇した。これはバブル外に多くのヘリウムが捕獲されており、高温下では、より安定な捕捉サイトとなるバブル内に蓄積していくことを示している。以上の結果より、重水素のほとんどはバブル内に、ヘリウムはバブル外にも捕捉され、イオン種によって捕捉挙動が異なることが示された。

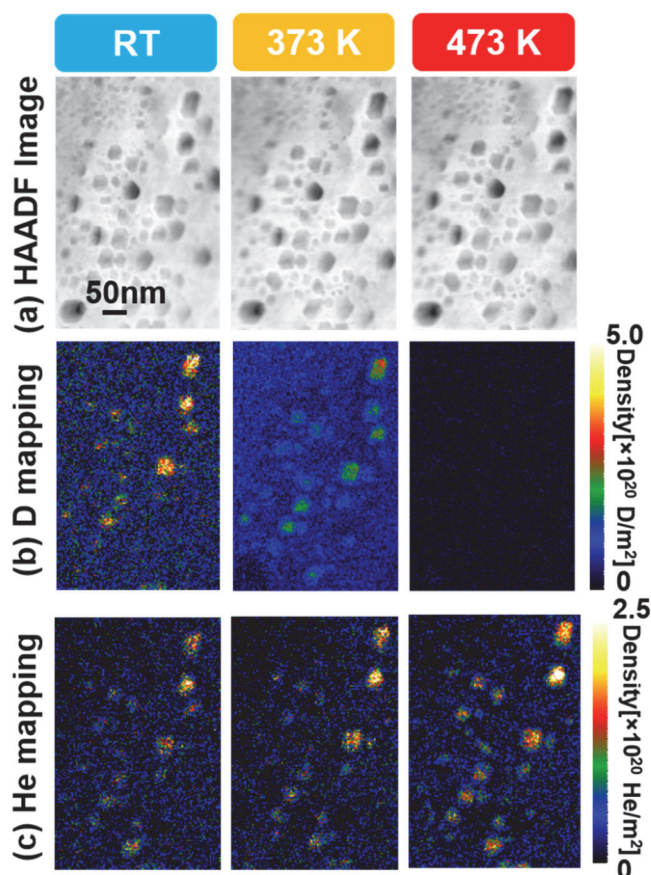


図 ヘリウム予照射後、重水素照射したタングステンの昇温下における (a)高角度散乱円環暗視野像と(b)重水素および(c)ヘリウムの濃度分布像。

なお、本研究は倉田博基教授、治田充貴准教授（京都大学化研）、佐野航平、澤江伴弥（島根大学）らとの共同研究として実施されたものである。また、本成果については、2023 年 5 月に開催の国際会議 PFMC-19 にて報告予定である。

## Synthesis and Structural Characterization of Lewis Base Adducts of Tetrylenes

Tsukasa Matsuo Kindai University

In this collaborative research, we examined the synthesis and structures of Lewis base adducts of tetrylenes incorporating the fused-ring bulky Rind groups (Rind = 1,1,3,3,5,5,7,7-octa-R-substituted *s*-hydrindacen-4-yl).

The bulky Eind-based dibromodigermene, (Eind)BrGe=GeBr(Eind) (**1**), was prepared by the reaction of (Eind)Li with GeCl<sub>2</sub>·dioxane (Scheme 1). The digermene **1** exists as the monomeric germylene, (Eind)BrGe:, in solution. The following reaction with *N*-heterocyclic carbene (NHC = 1,3,4,5-tetramethylimidazol-2-yliden) produced the bis-NHC adduct of the formal germyliumylidene cation, [(Eind)(NHC)<sub>2</sub>Ge:][Br] (**2**). The structure of **2** was confirmed by X-ray crystallography (Figure 1).

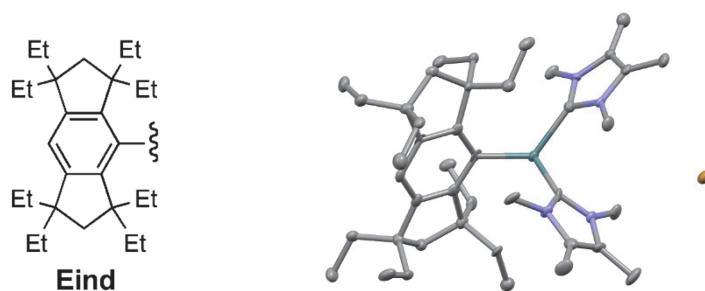
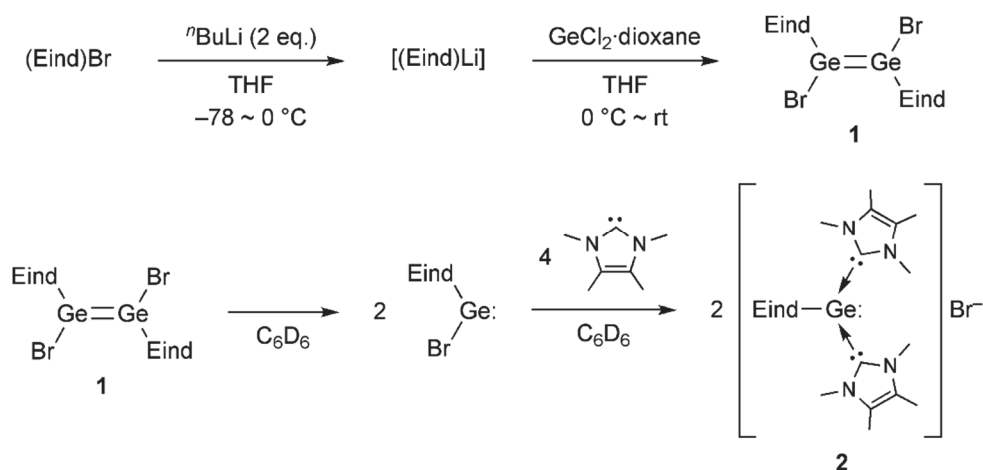


**Figure 1.** Eind group and molecular structure of **2**.



**Scheme 1.** Synthesis of **1** and **2**.

# Synthesis and structures of cationic aromatics bearing chalconenopyrylium units

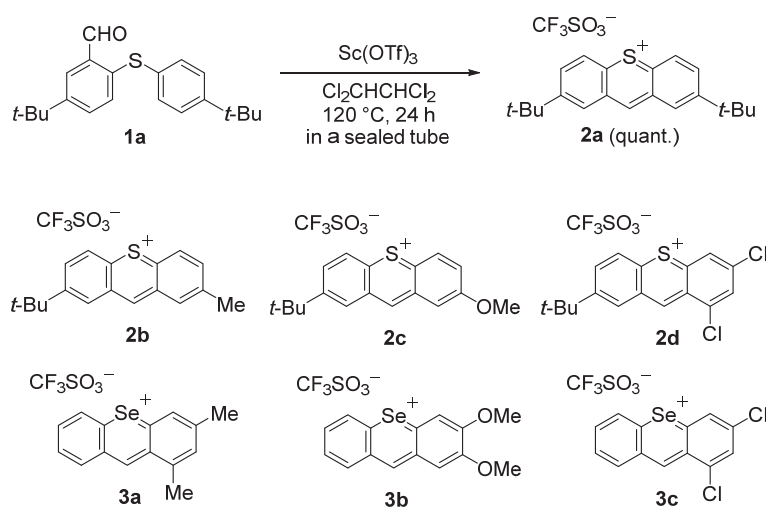
Noriyoshi Nagahora Fukuoka University

## Introduction

Thio- and selenopyrylium salts exhibit a unique electronic structure, which renders these compounds interesting potential building blocks for sulfur-/selenium-containing aromatic molecules. Recently, thiopyrylium-containing molecules have received substantial attention due to their fascinating structures, optoelectronic and physicochemical properties. In this work, we present studies on the synthesis of linearly fused thio- or selenopyrylium compounds via Lewis- or Brønsted-acid-promoted intramolecular cyclization of thio- or selenoethers.

## Results and Discussion

In order to optimize the reaction conditions, we initially investigated the Lewis/Brønsted-acid-induced cyclization of diarylthioether **1a**. When the Lewis acid  $\text{Sc}(\text{OTf})_3$  was used, the cyclization of **1a** proceeded at high temperature to quantitatively afford thiopyrylium trifluoromethanesulfonate **2a**. We also discovered that TfOH is the most effective Brønsted acid for the promotion of the cyclization, which affords **2a** in quantitative yield at room temperature within 1 h. The reactions still proceeded when several substituted diarylthioethers **1b-d** were treated with TfOH at room temperature for 2 h. Next, we focused formation of selenopyrylium salts promoted by a Brønsted acid. Even the corresponding selenoethers reacted with TfOH affording selenopyrylium trifluoromethanesulfonates **3a-c** in acceptable yields. This versatile cyclization thus not only extends the scope of the synthetic methods of pyrylium-fused cationic framework but also that of material chemistry using thio- or selenopyrylium molecules.



## Publications

1. (a) Nagahora, N.; Tanaka, R.; Tada, T.; Yasuda, A.; Yamada, Y.; Shioji, K.; Okuma, K. *Org. Lett.* **2020**, 22, 6192–6196. (b) Nagahora, N.; Kitahara, K.; Mizuhata, Y.; Tokitoh, N.; Shioji, K.; Okuma, K. *J. Org. Chem.* **2020**, 85, 7748–7756. (c) Hirano, K.; Yasuda, A.; Sasamori, T.; Shioji, K.; Okuma, K.; Nagahora, N. *Heterocycles* **2021**, 102, 451–464.



# Theoretical design of low-dimensional silicon material embedded in a flat two-dimensional sheet and exploration for operating principles

Masae Takahashi Tohoku University

**【Objectives】** Two-dimensional (2D) Dirac materials represent a special class of quantum matter hosting linearly dispersing Dirac cones. The Dirac cone categorized into type-I shows tilted anisotropic linear dispersions in all  $k$  directions, together with a point-like Fermi surface. We report here designing a silicon-based type-I Dirac material with planar configuration, based on the first-principles calculations. The flat structure obtained in this study is essential for the air stability of silicon  $\pi$ -electron conjugated systems.

**【Computational Details】** We performed structural and electronic calculations in the density functional theory framework, as implemented in CASTEP code (ver. 2018 and 2019). The geometries were fully optimized for both the cell parameters and atomic coordinates under the constraints of group symmetry of  $D_{2h}$ . The calculation of phonon dispersion was performed using the linear response theory. The phonon dispersions throughout the Brillouin zone confirmed that obtained structure is dynamically stable because of the absence of any imaginary frequencies.

**【Results and Discussion】** The band structure calculation has revealed that the obtained 2D material with planar configuration is a type-I Dirac semimetal with linear dispersion in the vicinity of the Fermi energy and is regarded as a qualitatively new class of 2D material that hosts anisotropic Dirac fermions (Fig. 1). The Fermi

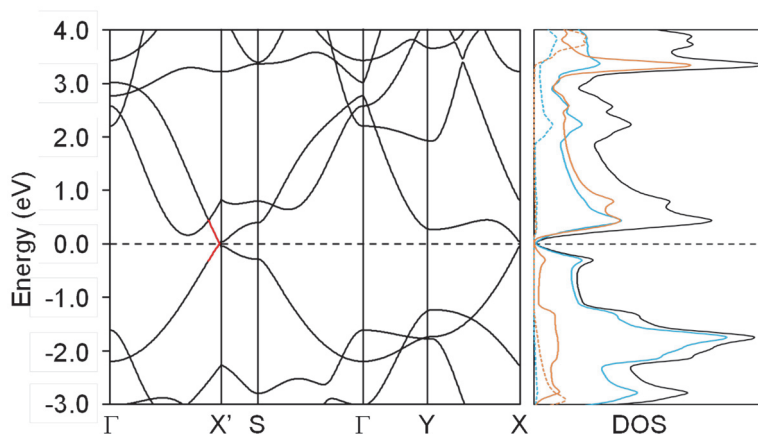


Fig. 1. Electronic band structure and the projected DOS.

velocity in the  $\Gamma$ - $X'$  direction is estimated to be  $0.5 \times 10^6$  and  $0.7 \times 10^6 \text{ m s}^{-1}$ , which is 2 and 1.5 times smaller than that of graphene. The Fermi velocity in the direction perpendicular to the  $\Gamma$ - $X'$  line is much smaller ( $0.3 \times 10^6 \text{ m s}^{-1}$ ). The most remarkable difference in the band structure from graphene is that the van Hove singularity is located much closer to the Fermi energy than in graphene: the energy interval is 0.3 eV, while that in graphene is 2 eV. This is due to the smaller energy gap at the  $\Gamma$  point than that in graphene. It was recently reported that the Fermi-level shift by 0.5 eV in graphene is achieved by chemical doping, suggesting that the Fermi-level shift by 0.3 eV by chemical doping is quite possible. The obtained 2D material is a silicon-based air-stable Dirac material with an anisotropic Dirac cone inducing the anisotropic carrier mobility, which has a high potential for application to various novel silicon-based electronic devices.

**【Publications】** [1] [M. Takahashi](#), S. Chen, H. Matsui, N. Morimoto, Y. Ikemoto, *Sci. Rep.* **2022**, 12, 20393.  
[2] [M. Takahashi](#), WIRMS2022, October 6-9, **2022**, Hiroshima and Hybrid Format, Japan (Invited talk).



## 2. 国際会議、シンポジウム・研究会報告



## 24th International Colloquium on Magnetic Films and Surfaces (ICMFS2022) 実施報告書

主 催：ICMFS2022 実行委員会

共 催：京都大学化学研究所 国際共同利用・共同研究拠点、京都大学化学研究所 スピントロニクス学術連携研究教育センター、東北大学 スピントロニクス学術連携研究教育センター、大阪大学基礎工学研究科 スピントロニクス学術連携研究教育センター、慶応義塾大学グローバルリサーチインスティテュート、公益財団法人 市村清新技術財団、公益財団法人 新世代研究所、一般財団法人 沖縄観光コンベンションビューロー、International Union of Pure and Applied Physics、IEEE Magnetics Society

日 時：2022 年 7 月 10 日（日）～7 月 15 日（金）

場 所：沖縄科学技術大学院大学

2022 年 7 月 10 日（日）～7 月 15 日（金）の 6 日間にわたり、24th International Colloquium on Magnetic Films and Surfaces (ICMFS2022)（学会ホームページ <https://icmfs2022.jp/index.html>）を開催した。International Colloquium on Magnetic Films and Surfaces (ICMFS) は、磁性薄膜と表面に関する研究発表、知識の交換、情報の提供等を行う国際会議であり、1964 年から数年おきに世界各地で開催されている歴史ある会議である。参加者は世界 20 カ国以上から 150～300 人程度である。本会議は 2021 年 7 月 11 日～2021 年 7 月 16 日に沖縄で開催する予定であったが、新型コロナウイルス感染症拡大防止の観点から開催を 2022 年に延期した。

第 24 回目となる今回は、京都大学化学研究所 国際共同利用・共同研究拠点、京都大学化学研究所 スピントロニクス学術連携研究教育センター、東北大学 スピントロニクス学術連携研究教育センター、大阪大学基礎工学研究科 スピントロニクス学術連携研究教育センター、慶応義塾大学グローバルリサーチインスティテュート、公益財団法人 市村清新技術財団、公益財団法人 新世代研究所、一般財団法人 沖縄観光コンベンションビューロー、International Union of Pure and Applied Physics、IEEE Magnetics Society の支援を受けた。

コロナ渦でのハイブリッド会議となったが、総勢 289 名の参加者のうち 215 名が現地参加であった。また海外からの参加者 116 名のうち現地参加者は 66 名に上った。この参加者数からも、研究者が対面の会議や議論を熱望している現状がうかがわれる。学生の参加も 118 名（国内 76 名、海外 42 名）と学生参加費を 25000 円と格安とした効果があった。これも京都大学化学研究所国際共同利用・共同研究拠点をはじめとする各所の援助によるものである。若手育成は本会議の大きな目的の一つであり、十分な成果があったといえる。

本会議は従来 International Conference on Magnetism(ICM)のサテライト会議として開催されてきた。今回も上海開催が予定されていた ICM のサテライト会議となるはずであっ

たが、コロナ渦により ICM 上海が中止され単独開催となった。従来 ICM で行われていた IUPAP Magnetism Award と IUPAP Young Scientist Prize の表彰式を ICMFS で行い、受賞者による Plenary 講演と招待講演が行われた。

最後に、本コロキウムを開催するにあたりご支援をいただいた京都大学化学研究所国際共同利用・共同研究拠点に厚く御礼を申し上げる。

文責：小野 輝男

## 化学研究所国際共共拠点・分子材料化学セミナー 実施報告書

1. 日程

2022 年 8 月 5 日

2. 会議名

化学研究所国際共共拠点・分子材料化学セミナー

3. 主催機関

京都大学化学研究所

4. その他 共催・協賛機関など (掲載が必要な場合のみ)

5. 世話人 (化学研究所を代表する報告者、役職名も変更可<例：プログラム委員長>)

梶 弘典 (京都大学化学研究所)

6. 参加者数

20 名

7. 開催場所

京都大学宇治キャンパス 共同研究棟大セミナー室

8. 報告文

新型コロナウイルスに関する国内外の往来が今年度から可能となったため、今回、テネシー大学の Bin Hu 教授と名古屋大学の阿波賀邦夫教授をお招きし、京都大学化学研究所で講演を行って頂く機会を得た。Bin Hu 教授からは、Spin-orbital Coupling Effects in Organic Molecules and 2D-superlattice Perovskites と題した講演をお願いし、最近特に注目を集めている、熱活性化遅延蛍光(TADF)、また、二次元超格子ペロブスカイトに関し、スピン軌道相互作用という観点からご講演をいただいた。阿波賀邦夫教授からは、Interdisciplinary Research on Solid-State Science and Electrochemistry of Molecular Materials と題した講演をして頂いた。分子クラスター電池や金属有機構造体(MOF)電池に始まり、大型の研究費の取り方に至るまで、分野外の研究者にも極めてわかりやすい講演が行われ、会は成功裏に終了した。





## 化学研究所国際共同拠点・ 分子材料化学セミナーのご案内



### Spin-orbital Coupling Effects in Organic Molecules and 2D-superlattice Perovskites

*Professor Bin Hu*  
*Department of Materials Science and Engineering,*  
*University of Tennessee,*  
*Knoxville, Tennessee 37996, USA*

日時：2022年8月5日（金）13:50－14:50

場所：化学研究所 共同研究棟 大セミナー室 (CL-110)

**Abstract:**

Spin-orbital coupling (SOC) is known as the key parameter that determines spin-dependent optoelectronic properties at different length and time scales. In organic molecules where the inversion symmetry breaking is lacking, the traditional method of generating SOC is mainly from the utilization of heavy elements. Recently, we found that charge-transfer states intrinsically possess an electric-magnetic coupling phenomenon, functioning as un-conventional SOC. Especially, this un-conventional SOC generated by charge-transfer states provides a vital mechanism to enable an endothermic upward electronic transition from triplets to singlets, activating so-called TADF (thermally activated delayed fluorescence), rather than creating an exothermic downward electronic transition from triplets to ground state to generate a phosphorescence in organic molecules. In 2D-superlattice perovskites where inversion symmetry breaking is existing, SOC generates spin-up and spin-down Rashba band structures with circularly polarized orbital momentums. This leads to a unique mechanism to mutually tune spin and orbital orders in 2D-superlattice perovskites. This presentation will discuss the SOC effects in both organic molecules and 2D-superlattice perovskites.

連絡先：化学研究所・分子材料化学研究領域 梶弘典（内線3149）



## 化学研究所国際共同拠点・ 分子材料化学セミナーのご案内



### Interdisciplinary Research on Solid-State Science and Electrochemistry of Molecular Materials

*Professor Kunio Awaga*  
*Department of Chemistry and IRCCS*  
*Nagoya University*

日時：2022年8月5日（金）15:00－16:00

場所：化学研究所 共同研究棟 大セミナー室 (CL-110)

**Abstract:**

Solid state electrochemistry is a traditional discipline, but has recently gained attention in the development of energy devices such as rechargeable batteries and capacitors. Solid-state electrochemistry is also recognized as providing an excellent methodology for controlling band filling in solid-state physics and materials science. In this presentation, we would like to explain our study on the following topics.

- (i) Molecular rechargeable batteries such as molecular cluster batteries and MOF batteries, in which molecular species are employed as cathode active materials for the Li negative electrode.
- (ii) Organic field-effect transistors and photoelectron conversion aided by an electric double layer that can achieve effective carrier injection and charge separation.
- (iii) Construction of molecular-based structures with "strong isotropy" and redox control by solid-state electrochemical methods.

連絡先：化学研究所・分子材料化学研究領域 梶弘典（内線3149）



## 第6回 MAIRS ワークショップ

主 催：(公社) 日本分光学会・赤外ラマン研究部会

共 催：京都大学化学研究所共同利用・共同研究拠点

協 賛：日本化学会，応用物理学会，日本分析化学会，分子科学会

日 時：2022 年 11 月 18 日（金） 13:00～17:00

場 所：京都大学化学研究所・共同研究棟 大セミナー室，および Zoom 配信によるハイブリッド形式

2016 年からシリーズ化して開催している，赤外分科会企画の部会イベントである“MAIRS ワークショップ”の第 6 回を，昨年に引き続いて対面とオンラインのハイブリッド方式で実施した．一件当たりの講演にゆとりを持たせるため，今年は講演件数を少なめに設定したが，例年以上に話題の分野に広がりを持たせることができた．参加者は，対面に 19 名，オンラインで 41 名で合計 60 名であった．学生の参加者が 18 名と，若手の参加者も多かった．

今年も日本化学会，日本分析化学会，分子科学会，応用物理学会の 4 学協会の協賛を得て実施し，これら協賛学会からの参加者は分光学会員と同額の参加費とした．また，コロナ禍での出費の厳しさも勘案して低価格に設定し，とくに学生は例年通り無料とした．

ハイブリッド開催をスムーズに実現するため，専門業者にマイクなどの設定を任せ，最終的に 60,247 円の黒字で終了した．

6 回目の今回は“第 6 回 MAIRS ワークショップ | 薄膜概念の拡張”として開催した．対面式の会場は京大化研で，プログラムは次のとおりである．

1. 基調講演：ATR-遠紫外分光法で表面を診る（尾崎幸洋・関西学院大）
2. In situ MAIRS-蒸着複合装置を用いた有機-無機ハイブリッド材料の薄膜反応過程の観察（丸山伸伍・東北大）
3. フッ素系撥油剤の評価（山崎秀樹・日東分析センター）
4. pMAIRS 法で解析するシリコン表面ナ

ノ溝配列における赤外吸収の増強（島田透・弘前大）

5. 金属酸化物上の脂肪族分子の pMAIRS 測定を用いた吸着挙動追跡（細見拓郎・東大）



基調講演の尾崎先生は，尾崎研で開拓された遠紫外（FUV）分光法による表面分析についてご講演いただいた．紫外領域を極端紫外・深紫外と FUV に分けて初心者にもわかりやすく丁寧に説明していただき，吸収が強すぎるがゆえに利用が難しかった FUV に挑戦し， $\sigma$  結合の化学という位置付けて進めてこられたことや，装置開発の経緯を詳しくご説明いただいた．その上で，ATR 法を組み合わせ実現した ATR-FUV 分光法が，結果的に界面から数十 nm という領域を解析できることの実証なども示された．今後，この領域で MAIRS の実施が待たれる．

東北大の丸山先生は，真空蒸着法を利用した複合膜の成膜過程を追うため，MAIRS2 を導入する理由をわかりやすくご説明された．また，MAIRS で配向を議論するというよりは，MAIRS 固有の機能である「無配向状態のスペクトル Aiso が得られる」ことを前面

に打ち出し、成膜の仮定での成分の増減を Aiso とケモメトリックスを組み合わせで実現されていた。また、その結果から薄膜成長過程のアレーニウスプロットも初めて実現し、MAIRS によって物理化学としての深みが増すことを述べられて、非常に印象的だった。

日東分析センターの山崎さんは、PTFE を薄くした網目状の化合物である日東電工の Temish という製品に関する構造－物性相関の研究を紹介された。すべてお一人で実験・解析されたデータが多数紹介された。たとえば、静的接触角測定で違いが出ないものでも、滑落角にすると大きな違いが出る例など、印象的な写真やデータを多数見ることができた。また、MAIRS で現れるフォノンバンドからモルフォロジーの変化を議論するポイントも紹介され、MAIRS の新たな使い方として聴衆に強い印象を残した。

弘前大の島田先生は、表面増強赤外分光 (SEIRAS) の増強機構についての研究であった。過去に提唱されたホットスポット説とプラズモンの誘電率変化説の二つの機構は、いずれも完全ではなく、それぞれが説明できないポイントを持つことを説明され、研究の動機が明確であった。ここで新たに提案された機構は、不連続な微粒子上でしか SEIRAS が起こらないことに注目したもので、微粒子のサイズと間隔を系統的に制御した実験を丁寧に行った。その結果、サイズと間隔の比をパラメータにすると、ばらばらに見えていた実験値がすべてひとつの曲線に載ることがわかり、理論的にも説明がつくことが判明した。これを非金属のシリコンでも検討し、プラズモンでなくてもこのような誘電率の効果が、SEIRAS の根幹に関わっていることを示し、強いインパクトを与えた。質疑でも、この点を高く評価するコメントがあり、この説が今後大いに重要視されることを印象付けた。

最後のトリは東大の細見先生によって、

柳田研で行われているナノワイヤ上での呼気分子の吸着と反応に関する詳細な検討結果が大迫力で報告された。ZnO ナノワイヤは、基板に垂直に伸びたナノサイズの太さを持つ針がたくさん生えた基板で、このワイヤに吸着する呼気分子は、基板に直接吸着する場合に比べて配向が 90 度ずれる。MD 計算や実験と組み合わせた予想を pMAIRS で実証する実験に成功しており、とくにメチル基の非対称伸縮振動の分裂をうまく利用した解析は、分光学会での議論にふさわしく、MAIRS をフル活用しているという意味でも、素晴らしい取り組みだった。

このように、今年の講演会は、MAIRS がユーザーの手によってこれまで以上に自由に羽ばたき、想像以上の広がりを示し始めていることを実感できる充実の内容となった。

会のスムーズな運営を可能にしてくれた、国際共共拠点にこの場をお借りして、厚く御礼を申し上げる。

長谷川健 (分子環境解析化学研究領域)

### 3. 成果発表論文

紙数の都合により、目次に記載した論文の一部についてのみ、別刷りを次頁以降に掲載する。



## Article


# Nitrogen reduction by the Fe sites of synthetic $[\text{Mo}_3\text{S}_4\text{Fe}]$ cubes

<https://doi.org/10.1038/s41586-022-04848-1>

Received: 29 April 2021

Accepted: 9 May 2022

Published online: 6 July 2022

 Check for updates

 Yasuhiro Ohki<sup>1✉</sup>, Kenichiro Munakata<sup>2</sup>, Yuto Matsuoka<sup>1</sup>, Ryota Hara<sup>2</sup>, Mami Kachi<sup>2</sup>, Keisuke Uchida<sup>2</sup>, Mizuki Tada<sup>2</sup>, Roger E. Cramer<sup>3</sup>, W. M. C. Sameera<sup>4,5</sup>, Tsutomu Takayama<sup>6</sup>, Yoichi Sakai<sup>6</sup>, Shogo Kuriyama<sup>7</sup>, Yoshiaki Nishibayashi<sup>7</sup> & Kazuki Tanifuji<sup>1</sup>

Nitrogen ( $\text{N}_2$ ) fixation by nature, which is a crucial process for the supply of bio-available forms of nitrogen, is performed by nitrogenase. This enzyme uses a unique transition-metal–sulfur–carbon cluster as its active-site co-factor ( $[(R\text{-homocitrate})\text{MoFe}_7\text{S}_9\text{C}]$ , FeMoco)<sup>1,2</sup>, and the sulfur-surrounded iron (Fe) atoms have been postulated to capture and reduce  $\text{N}_2$  (refs. <sup>3–6</sup>). Although there are a few examples of synthetic counterparts of the FeMoco, metal–sulfur cluster, which have shown binding of  $\text{N}_2$  (refs. <sup>7–9</sup>), the reduction of  $\text{N}_2$  by any synthetic metal–sulfur cluster or by the extracted form of FeMoco<sup>10</sup> has remained elusive, despite nearly 50 years of research. Here we show that the Fe atoms in our synthetic  $[\text{Mo}_3\text{S}_4\text{Fe}]$  cubes<sup>11,12</sup> can capture a  $\text{N}_2$  molecule and catalyse  $\text{N}_2$  silylation to form  $\text{N}(\text{SiMe}_3)_3$  under treatment with excess sodium and trimethylsilyl chloride. These results exemplify the catalytic silylation of  $\text{N}_2$  by a synthetic metal–sulfur cluster and demonstrate the  $\text{N}_2$ -reduction capability of Fe atoms in a sulfur-rich environment, which is reminiscent of the ability of FeMoco to bind and activate  $\text{N}_2$ .

Nitrogen ( $\text{N}_2$ ) is an essential element to maintain every known form of life on Earth. Although the element is inexhaustible in the atmosphere as  $\text{N}_2$ , only diazotrophs or lightning in thunderstorms can transform this stable molecule into bio-available forms (for example, ammonia ( $\text{NH}_3$ ) and nitrogen oxides) in the natural world. Other organisms consequently rely on the products of the fixation processes and limited pre-existing sources to afford the necessary nitrogen. In this sense,  $\text{N}_2$  fixation is one of the most crucial bottlenecks in Earth's ecosystem. Key players of  $\text{N}_2$  fixation are nitrogenase enzymes that reduce  $\text{N}_2$  to  $\text{NH}_3$ . The most studied of these, molybdenum (Mo)-nitrogenase, has a unique metal–sulfur–carbon co-factor described as  $[(R\text{-homocitrate})\text{MoFe}_7\text{S}_9\text{C}]$  (FeMoco; Fig. 1)<sup>1,2</sup> and performs the catalytic reduction at ambient temperature and pressure. As FeMoco is found only in nitrogenase, its chemical and physical properties have attracted significant interest regarding its desirable  $\text{N}_2$ -reduction activity. How FeMoco reduces  $\text{N}_2$  has long been studied by biochemical analyses of the enzyme<sup>3,13</sup> and by structural and functional modelling of FeMoco with small-molecule complexes<sup>14,15</sup> and metal–sulfur (M–S) clusters<sup>16,17</sup>.

Although the detailed  $\text{N}_2$ -reduction mechanism of FeMoco remains elusive, a growing number of studies suggest that FeMoco eliminates one of the  $\mu_2$ -bridging sulfur (S) atoms and captures substrates at the produced vacant coordination sites on the iron (Fe) atoms<sup>4–6</sup>. Analogously, a common approach to generating small-molecule  $\text{N}_2$  complexes has been removal of a metal-bound ligand under reducing conditions. However, applying this method to the available synthetic counterparts of FeMoco, namely, M–S clusters, has been challenging. As these clusters contain coordinative S atoms in their inorganic cores, a vacant metal site often attracts core S atoms of M–S clusters rather than

$\text{N}_2$ , which leads to aggregation<sup>17</sup>. Limiting the number of vacant metal atoms in the core is thus a plausible approach and led to the isolation of  $\text{N}_2$ -bound clusters in several previous and recent examples, including ours<sup>7–9</sup>. Nevertheless, catalytic reduction of  $\text{N}_2$  by these clusters remains unknown despite its relevance to the natural system.

Our framework to overcome these hurdles implements a triangular  $[\text{Mo}_3\text{S}_4]$  fragment bearing robust Mo–Cp<sup>R</sup> bonds (Cp<sup>R</sup> =  $\text{C}_5\text{Me}_5$  (Cp<sup>\*</sup>),  $\text{C}_5\text{Me}_4\text{SiMe}_3$  (Cp<sup>L</sup>) and  $\text{C}_5\text{Me}_4\text{SiEt}_3$  (Cp<sup>XL</sup>), where Si is silicon, Me is methyl and Et is ethyl)<sup>11,12</sup> as a platform to structurally encumber and protect a fourth metal incorporated into the vertex (Fig. 1). A titanium (Ti) derivative  $[\text{Cp}^*\text{Mo}_3\text{S}_4\text{Ti}]$  captures and activates  $\text{N}_2$  in the presence of potassium graphite ( $\text{KC}_8$ ), indicating that the  $[\text{Mo}_3\text{S}_4\text{Ti}]$  cube is robust under reducing conditions and avoids undesirable aggregation<sup>8</sup>. In contrast, catalytic reduction of the bound  $\text{N}_2$  was not observed, probably owing to the strong Ti–N bond that inhibits product release. We then hypothesized that a softer Fe atom as found in the biological systems might function more successfully to carry out  $\text{N}_2$  reduction instead of the harder Ti atom. The results below demonstrate the capture and catalytic silylation of  $\text{N}_2$  by the vertex Fe atoms of  $[\text{Mo}_3\text{S}_4\text{Fe}]$  cubes. Although it is likely that there are mechanistic differences between the silylation of  $\text{N}_2$  and  $\text{NH}_3$  production by nitrogenase, our results demonstrate that an Fe centre built into a M–S core and in a S-rich coordination environment can activate inert  $\text{N}_2$  sufficiently for chemical conversion.

The treatment of our reported  $[\text{Mo}_3\text{S}_4\text{Fe}]$  clusters,  $[\text{Cp}^*\text{Mo}_3\text{S}_4\text{FeCl}]$  (Cp<sup>R</sup> = Cp<sup>\*</sup> (**1a**), Cp<sup>R</sup> = Cp<sup>L</sup> (**1b**) and Cp<sup>R</sup> = Cp<sup>XL</sup> (**1c**))<sup>11,12</sup> with strong reductants ( $\text{KC}_8$  for **1a** and sodium naphthalenide  $\text{Na}(\text{C}_{10}\text{H}_8)$  for **1b** and **1c**) under  $\text{N}_2$  in tetrahydrofuran (THF) led to the formation of the corresponding  $\text{N}_2$  clusters (Fig. 2a). The  $\text{N}_2$  coordination mode varies

<sup>1</sup>Institute for Chemical Research, Kyoto University, Uji, Japan. <sup>2</sup>Department of Chemistry, Graduate School of Science, and Research Center for Materials Science, Nagoya University, Nagoya, Japan. <sup>3</sup>Department of Chemistry, University of Hawaii, Honolulu, HI, USA. <sup>4</sup>Instituted of Low Temperature Science, Hokkaido University, Sapporo, Japan. <sup>5</sup>Department of Chemistry, University of Colombo, Colombo, Sri Lanka. <sup>6</sup>Department of Chemistry, Daido University, Nagoya, Japan. <sup>7</sup>Department of Applied Chemistry, School of Engineering, The University of Tokyo, Tokyo, Japan. ✉e-mail: ohki@scl.kyoto-u.ac.jp

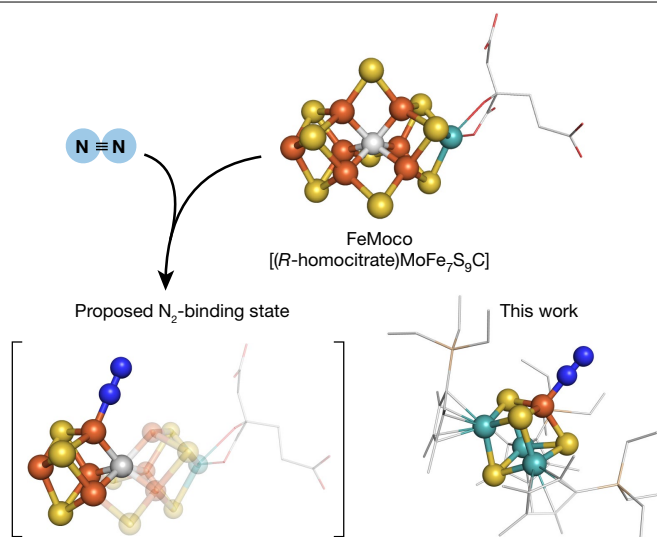


**Fig. 1 | A proposed  $N_2$ -binding state for FeMoco and a  $N_2$ -bound Mo-Fe-S cluster in this work.** Orange, iron; teal, molybdenum; yellow, sulfur; grey, carbon; blue, nitrogen.

depending on the bulkiness of the  $Cp^R$  ligands, so that a  $[Mo_3S_4Fe]$  dimer bridged by  $N_2$ ,  $[Cp^R_3Mo_3S_4Fe]_2(\mu-N_2)]^{2-}$  (**2a**), and monomers each bearing a terminal  $N_2$  ligand,  $[Cp^R_3Mo_3S_4Fe(N_2)]^-$  ( $Cp^R = Cp^L$  (**2b**) and  $Cp^R = Cp^{XL}$  (**2c**)), were obtained. The  $N_2$  binding modes of **2a–2c** were assigned primarily from the  $^{15}N$  NMR spectra of  $^{15}N_2$ -labelled clusters (Supplementary Figs. 1–3). Cluster **2a** exhibited a single signal at a chemical shift  $\delta = -40.9$  ppm as expected from the equivalent N atoms of the bridging  $^{15}N_2$ . Conversely, **2b** and **2c** gave two signals at  $\delta = 22.0$  ppm and  $\delta = -5.3$  ppm for **2b** and  $\delta = 22.6$  ppm and  $\delta = -5.7$  ppm for **2c**, corresponding to the inequivalent proximal and distal N atoms in these molecules. Terminal  $N_2$  binding in **2b** and **2c** was further confirmed by infrared-active N–N stretches observed at  $1,896\text{ cm}^{-1}$  and  $1,902\text{ cm}^{-1}$ , respectively, both of which exhibited a bathochromic shift upon  $^{15}N_2$  labelling (Supplementary Figs. 7 and 8). Despite our efforts, no meaningful N–N stretch for **2a** was detectable via resonance-Raman or infrared measurements (Supplementary Fig. 6), perhaps owing to slightly broken symmetry of the  $N_2$  binding mode. X-ray crystallographic analyses revealed the molecular structures of **2a** and **2c** (Fig. 2b,c, Supplementary Figs. 11 and 12, and Supplementary Table 5). The structure of **2a** is an  $N_2$ -bridged  $[Mo_3S_4Fe]$  dimer with an inversion centre at the middle of the two N atoms, whereas **2c** is a monomeric cluster bearing a terminally bound  $N_2$ . The N–N distances ( $1.151(4)\text{ \AA}$  for **2a** and  $1.136(5)\text{ \AA}$  for **2c**) are in between those of free  $N_2$  ( $1.098(1)\text{ \AA}$ ) and  $N_2H_2$  ( $1.252\text{ \AA}$ ), suggesting a weakened N–N bond. Likewise, the N–N stretching frequencies of **2b** and **2c** are close to the lower end of those reported for  $N_2$  complexes of  $Fe^{II}$  or  $Fe^I$  (ref. 18), and the activation levels are even comparable to an  $Fe^0-N_2$  complex supported by S- and carbon (C)-based ligands<sup>19</sup>.

Successful activation of  $N_2$  at the Fe atoms of **2a–2c** prompted us to pursue the catalytic reduction of  $N_2$  using the  $[Mo_3S_4Fe]$  cubes. Reduction to  $NH_3$  was observed but was not catalytic, giving at most  $1.6 \pm 0.1$  equiv.  $NH_3$  (per **2c**) under typical conditions<sup>14,15,20</sup> (Supplementary Table 4). Protonation of S atoms possibly occurs in this reaction, which weakens the Fe–S bonds and releases a vertex Fe atom from  $[Mo_3S_4Fe]$ , in a relevant manner to degradation of the cubes under electrochemical oxidation<sup>11,12</sup>. Nonetheless, more importantly, we found that the chloride (Cl) clusters **1a–1c** and  $N_2$  clusters **2b** and **2c** all catalytically reduce  $N_2$  to  $N(SiMe_3)_3$  in the presence of excess sodium (Na) and trimethylsilyl chloride ( $ClSiMe_3$ ). A minimum of  $122.9 \pm 3.0$  equiv. (per **1c**) and up to  $248.0 \pm 15.6$  equiv. (per **1b**) of  $N(SiMe_3)_3$  were generated after

100 h under a  $N_2$  (1 atm) atmosphere at room temperature (Table 1 and Supplementary Tables 1 and 2). Although the cause of the differences in the activity of these complexes has not been conclusively identified at this point, we assume that the steric, not electronic, effects of the  $Cp^R$  ligands play a major role (vide infra) because the  $Cp^R$  substituents did not notably affect the redox behaviours of **1a–1c** (half-wave potential  $E_{1/2}([Mo_3S_4Fe]^{5+/4+}) = -0.17\text{ V}$  (**1a**),  $-0.19\text{ V}$  (**1b**) and  $-0.24\text{ V}$  (**1c**) versus  $Ag/Ag^+$ )<sup>12</sup> or the redox features of **2b** and **2c** observed in cyclic voltammetry (Supplementary Fig. 14).

The  $N(SiMe_3)_3$  yields, on a per-active-metal basis produced by **1b** and **2c**, are about three-times higher than those of other Fe catalysts reported so far (Supplementary Table 3)<sup>21–25</sup>, and are comparable to the highest yields by Mo (ref. 26) and Co (refs. 27,28) catalysts. Similar to known systems, the catalytic reactions in THF concurrently formed  $Me_3SiSiMe_3$ ,  $Me_3SiOC_4H_9$  and  $Me_3SiOC_4H_8SiMe_3$  as by-products (Supplementary Figs. 15–17). These by-products should originate from reactions of the trimethylsilyl radical  $\cdot SiMe_3$  with itself or the THF solvent<sup>28</sup>, as treatment of  $ClSiMe_3$  with alkaline metals has been accepted to generate  $\cdot SiMe_3$  (ref. 26). Although the THF solvent is much more abundant than the  $N_2$  reactant, the selectivity for  $N(SiMe_3)_3$  was high in the case of **1b** and reached 37.2% (Table 1, entry 2). It is striking that any of the corresponding  $[Mo_3S_4]$  platforms,  $[Cp^R_3Mo_3S_4]$  ( $Cp^R = Cp^*$  (**4a**),  $Cp^R = Cp^L$  (**4b**) and  $Cp^R = Cp^{XL}$  (**4c**)), several relevant FeS clusters or  $FeCl_2$  (ref. 20) did not provide  $N(SiMe_3)_3$  at significant levels under the same conditions (Table 1 and Supplementary Table 3). After a catalytic run using **1a**, a mass spectrum of the reaction mixture revealed  $[Mo_3S_4Fe]$  cubes binding ring-opening products of THF (Supplementary Fig. 19), indicating sufficient stability of the cubic core during catalysis. Moreover, a carbon monoxide (CO)-trapping experiment revealed the formation of a low yield (11%) of  $[Cp^{XL}_3Mo_3S_4Fe(CO)]$  (**5**) from a catalytic reaction mixture with **1c**, Na and  $ClSiMe_3$  (200 equiv. each) under  $N_2$  (Supplementary Figs. 24–27), implying the generation of  $[Mo_3S_4Fe]$  species with labile ligands (for example, THF or  $N_2$ ) on Fe. These results suggest that the Fe centre of each  $[Mo_3S_4Fe]$  cube is the actual  $N_2$ -reduction site.

Considering previous proposals for analogous reactions<sup>26,28</sup>, we propose a mechanism for  $N_2$  silylation by our  $[Mo_3S_4Fe]$  cubes (Supplementary Fig. 18). In this pathway, we suppose that the Cl atom

**Table 1 | Catalytic reduction of  $N_2$  into  $N(SiMe_3)_3$  promoted by  $[Mo_3S_4Fe]$  clusters**

$N_2 + 6\text{ Na} + 6\text{ Me}_3\text{SiCl} \xrightarrow[\text{THF, r.t., 100 h}]{\text{Precatalyst}} 2N(SiMe_3)_3$ <p>(1 atm)</p>		
Entry	Precatalyst	$N(SiMe_3)_3$ yield (equiv. per catalyst) <sup>a</sup>
1	<b>1a</b>	$127.0 \pm 34.6$
2	<b>1b</b>	$248.0 \pm 15.6$
3	<b>1c</b>	$122.9 \pm 3.0$
4	<b>2b</b>	$142.5 \pm 16.0$
5	<b>2c</b>	$227.1 \pm 40.8$
6	<b>3</b>	$258.3 \pm 6.1$
7	$Cp^*_3Mo_3S_4$ ( <b>4a</b> )	$6.5 \pm 1.5$
8	$Cp^L_3Mo_3S_4$ ( <b>4b</b> )	$9.6 \pm 2.7$
9	$Cp^{XL}_3Mo_3S_4$ ( <b>4c</b> )	$12.9 \pm 8.7$

Na and  $ClSiMe_3$  (2,000 equiv. of each) were added to the catalyst in THF at room temperature and stirred for 100 h under 1 atm  $N_2$ . Reactions by **2a** were not examined owing to the low isolated yield and the lower performance of the  $Cp^*$  ( $C_6Me_6$ ) system. Yields represent the average of three runs. <sup>a</sup>Yields were obtained from three independent experiments ( $n=3$ ) and are shown as mean  $\pm$  s.d.



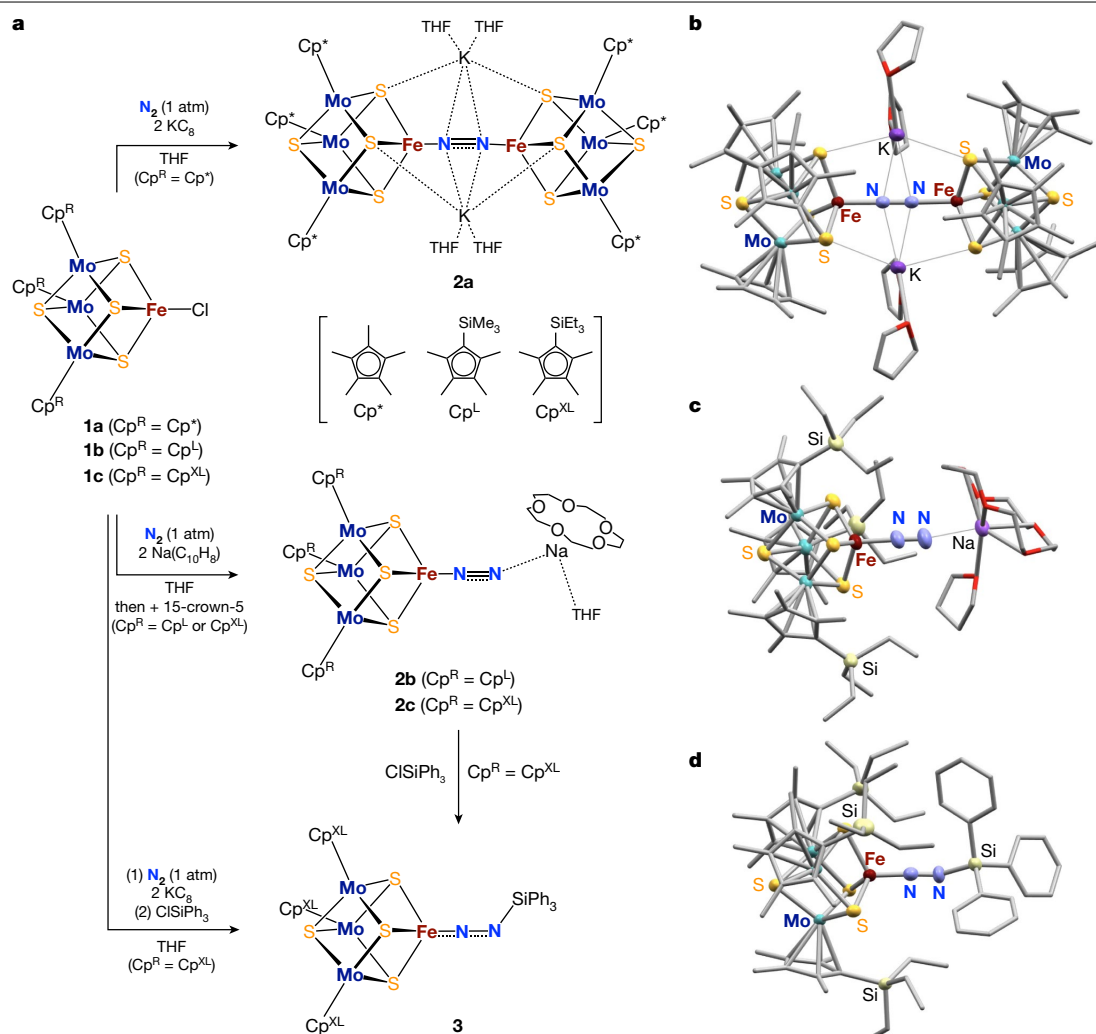


**Fig. 2 | Synthesis and chemical modification of  $N_2$ -bound  $[Mo_3S_4Fe]$  clusters. a**, Synthetic schemes for the  $N_2$ -bound  $[Mo_3S_4Fe]$  clusters **2a–2c** and subsequent silylation of the bound  $N_2$  to give **3**. **b–d**, The structure of

**2a (b)**, **2c (c)** and **3 (d)**. The equivalence of **2a** (1/2 equiv.) is omitted for readability. Carbon and oxygen atoms are drawn as capped sticks for clarity.

on Fe is removed by  $\cdot SiMe_3$  to generate a vacant Fe site that binds  $N_2$ . In the resultant  $Fe-N_2$  species, the more exposed distal N atom probably undergoes the first silylation to generate the  $Fe-NNSiMe_3$  species. Further silylation and reduction would dissociate a hydrazido anion  $[Me_3SiN-N(SiMe_3)_2]^-$ , as theoretically proposed for Mo- and Co-catalysed reactions<sup>26,28</sup>. Dissociation of the hydrazido anion can regenerate a vacant Fe site for the next catalytic cycle. It is noted that we cannot exclude the possibility that the catalysis is mediated by unidentified species generated in the solution. However, the isolation of the  $N_2$ -bound clusters establishes the substrate binding by the  $[Mo_3S_4Fe]$  clusters. Below, we additionally describe stoichiometric experiments that indicate the feasibility of the initial silylation of  $N_2$ .

The initial silylation of the  $N_2$  ligand is arguably the most vital step in  $N_2$  reduction. To validate it, the in situ-generated **2c** (from **1c** and 2.3 equiv.  $KClO_4$ ) was treated with 1.1 equiv.  $ClSiPh_3$  (where Ph is phenyl) to furnish a monosilylated  $N_2$  species ( $[Cp^{XL}_3Mo_3S_4Fe(N_2SiPh_3)]$ , **3**) in 20% yield (Fig. 2a,d and Supplementary Figs. 4, 9 and 13). The same cluster **3** was alternatively generated from **2c** and  $ClSiPh_3$  in  $C_6D_6$  (Supplementary Fig. 5). The X-ray structure of **3** shows an elongated N–N distance (1.193(7) Å) from that found in the  $N_2$ -bound **2c** (1.136(5) Å), in accordance with a weakened N–N bond (stretching frequency  $\nu_{N-N} = 1,706\text{ cm}^{-1}$ ). These values are close to those previously

reported for Fe complexes bearing  $[N_2SiR_3]$  ligands (Supplementary Table 6)<sup>22,29,30</sup>. Although the phenyl substituents on the Si atom of **3** differ from the methyl groups employed in the catalytic process, the isolation of **3** supports the possible generation of an  $Fe-NNSiMe_3$  analogue of **2c** in the catalytic cycle. This assumption was further reinforced when **3** was used as the precursor for the successful catalytic silylation of  $N_2$ , yielding  $258.3 \pm 6.1$  equiv. of  $N(SiMe_3)_3$  (Table 1, entry 6).

The irreversible chemical modification of the bound  $N_2$  molecule highlights a reactivity difference between our system and a  $N_2$ -bridged  $[MoFe_3S_4]$  dimer reported recently<sup>9</sup>. Treatment of  $[Cp^*MoFe_3S_4(IPr)_2(\mu-N_2)]$  ( $IPr = 1,3\text{-bis}(2,6\text{-diisopropylphenyl})\text{-imidazol-2-ylidene}$ ) with  $[Cp^L_2Ti]$  has been reported to give an equilibrium mixture of the  $[MoFe_3S_4]_2(\mu-N_2)$  dimer and a heterometallic  $N_2$ -bridged complex  $[Cp^*MoFe_3S_4(IPr)_2(\mu-N_2)(Cp^L_2Ti)]$ , but no further chemical conversions or catalytic reduction of the bound  $N_2$  was reported. The difference in reactivity between this  $N_2$  bridging system and the terminally bound  $N_2$  system reported herein points to the importance of a terminal  $Fe-N_2$  moiety for the successful reduction of  $N_2$ . In addition, the isolation of a stable intermediate analogue by our  $[Mo_3S_4Fe]$  platform indicates its potential utility as a synthetic toolkit to investigate catalytic as well as stoichiometric activation of other small molecules.

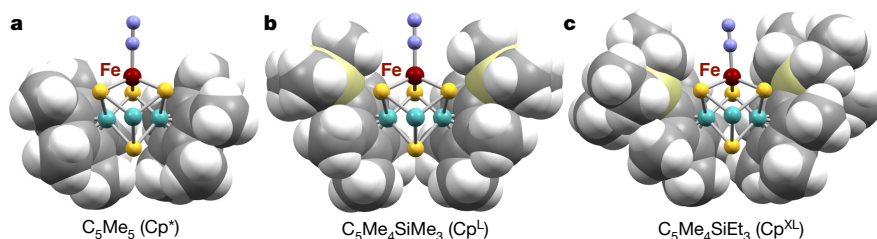


**Fig. 3 | Structural models of  $N_2$ -bound  $[Mo_3S_4Fe]$  clusters.** A space-filling model is applied to two  $Cp^R$  ligands, whereas the other  $Cp^R$  is omitted to show the  $[Mo_3S_4Fe]-N_2$  moiety. **a**,  $C_5Me_5$  ( $Cp^*$ ). **b**,  $C_5Me_4SiMe_3$  ( $Cp^L$ ). **c**,  $C_5Me_4SiEt_3$  ( $Cp^{XL}$ ).

Panels **a** and **c** were prepared from the crystal structures of **2a** and **2c**; panel **b** was prepared via software using the Cl-bound cluster **1b**.

Structural models of the  $N_2$ -bound clusters reveal that the  $Cp^R$  ligands surround the  $N_2$  ligand and the  $[Mo_3S_4Fe]$  cores (Fig. 3). The  $-SiMe_3$  and  $-SiEt_3$  groups of the  $Cp^R$  ligands are forced into the space around the Fe sites of the  $[Mo_3S_4Fe]$  cubes (Fig. 3b,c) to minimize steric repulsion between the  $Cp^R$  ligands. Thus, the  $-SiR_3$  groups efficiently offer steric protection of the  $[Fe-N_2]$  moiety and prevent dimerization of cubes through either an  $Fe-N_2-Fe$  bridge or an inter-cube  $Fe-S$  interaction. In contrast, the less bulky  $Cp^*$  ligands lead to a more exposed Fe site (Fig. 3a) and allow the approach of the Fe site of another  $[Mo_3S_4Fe]$  cube to give an  $Fe-N_2-Fe$  dimer. The bulkiness of the  $Cp^R$  ligands should affect the catalytic activities as well, as we suggest that the first  $N-Si$  bond formation occurs at the distal N atom. In an  $Fe-N_2-Fe$  dimer, both N atoms are protected until one of the  $Fe-N$  interactions breaks to generate monomers. In the catalytic reactions using  $Fe-Cl$  cubes, chloride abstraction (initiation) is expected to be slower with the bulkier  $Cp^R$  ligands.

To better understand the properties of **2a–2c** and **3**, zero-field  $^{57}Fe$  Mössbauer spectra were measured at 78 K using powdered crystals (Supplementary Fig. 10). The spectra were fitted as single quadrupole doublets with the following values of the isomer shift ( $\delta$ ) and the quadrupole splitting ( $|\Delta E_Q|$ ):  $\delta = 0.479(4) \text{ mm s}^{-1}$  (**2a**),  $\delta = 0.410(2) \text{ mm s}^{-1}$  (**2b**),  $\delta = 0.401(3) \text{ mm s}^{-1}$  (**2c**) and  $\delta = 0.263(3) \text{ mm s}^{-1}$  (**3**), respectively;  $|\Delta E_Q| = 1.258(8) \text{ mm s}^{-1}$  (**2a**),  $|\Delta E_Q| = 1.422(5) \text{ mm s}^{-1}$  (**2b**),  $|\Delta E_Q| = 1.466(5) \text{ mm s}^{-1}$  (**2c**) and  $|\Delta E_Q| = 0.906(5) \text{ mm s}^{-1}$  (**3**), respectively. The  $\delta$  values of **2a–2c** are lower than those of the precursors **1a–1c** featuring  $Fe^{II}$  centres ( $\delta = 0.555(2)–0.563(3) \text{ mm s}^{-1}$ ), even though **2a–2c** are supposedly more reduced. A reduced Fe centre typically shows a higher  $\delta$  than an oxidized Fe in similar coordination environments, owing to shielding of electrons in  $s$  orbitals by the increased  $3d$  electron densities. This has also been verified for  $[Fe_4S_4]$  and  $[Fe_3S_4]$  clusters bearing thiolate ligands<sup>31</sup>. The opposite trend observed here could be ascribed to  $\pi$  back-donation from Fe to the  $N_2$  ligand. As suggested from theoretical calculations, such increased covalency of the  $Fe$ -ligand bond leads to high electron density at the Fe nucleus and, consequently, a low  $\delta$  value<sup>32</sup>. Thus, although determination of the Fe oxidation state is not straightforward, we tentatively assign the Fe centres in **2a–2c** as close to  $Fe^{II}$  but only slightly reduced. Kohn–Sham frontier orbitals of optimized **2a** and **2c** reveal major contributions of Mo atoms in the occupied orbitals to store reducing equivalents (Supplementary Figs. 21–23). The density-functional-theory-calculated  $\delta$  values of **2a**, **2c** and **3** based on the crystal and optimized structures are qualitatively in agreement with the experimental data (Supplementary Tables 7–10), supporting the utility of orbital analysis.

The covalent nature of  $Fe-N$  interaction can also rationalize the  $\delta$  value of **3**. As illustrated by the  $N-N$  bond distance and  $N-N$  stretching frequency of the cluster, silylation of the  $N_2$  ligand has led to stronger back-donation from Fe and a shorter  $Fe-N$  distance ( $1.687(5) \text{ \AA}$ ) than those of **2a** and **2c**. This is consistent with a highly covalent  $Fe-N$  interaction and does not contradict the decrease of the  $\delta$  value in **3** compared with **2a–2c**, implying a major contribution of a resonance structure of  $Fe=N=N-SiPh_3$ . A notably bent  $N-N-Si$  angle of **3** ( $133.4(5)^\circ$ ), a linear

$Fe-N-N$  alignment ( $171.6(6)^\circ$ ) and computed Mayer bond orders ( $Fe-N$ ,  $1.49$  (**3**) versus  $0.89$  (**2a**) and  $1.12$  (**2c**);  $N-N$ ,  $1.68$  (**3**) versus  $2.00$  (**2a**) and  $2.31$  (**2c**); Supplementary Tables 11–13) are in good agreement with a diazenido assignment. The effect of the  $Fe-N$  interaction on the  $\delta$  variation of a series of clusters can be illustrated by a plot of their  $Fe-N$  bond distances versus  $\delta$  values. The plot using data points of **2a**, **2c** and **3** exhibits a pseudo-linear relationship as shown in Supplementary Fig. 20. Interestingly, similar relationships were also seen in  $[(SiP^{i-Pr}_3)_3Fe(N_2)]^{0/-}$  and  $[(SiP^{i-Pr}_3)_3Fe(N_2SiMe_3)]$  ( $SiP^{i-Pr}_3 = Si(o-C_6H_4P^{i-Pr}_2)_3$ )<sup>30</sup>, and  $[LSnFe(N_2)]^{0/-}$  and  $[LSnFe(N_2SiMe_3)]$  ( $L = [N(o-(NCH_2P^{i-Pr}_2)(C_6H_4)_3)]^{3-}$ )<sup>33</sup>, and regression lines from each series have nearly the same slope.

Overall, the above results represent the first catalytic silylation of  $N_2$  by a synthetic  $M-S$  cluster and suggest some key features for successful  $N_2$  reduction. Sufficient stability of the  $M-S$  core under reducing conditions can make an Fe centre sufficiently electron-rich to activate  $N_2$ . These results imply that suppression of intermolecular aggregation of  $M-S$  cores is a key to stabilizing a terminal  $N_2$ -bound species and maintaining the reactivity at the distal N atom of the bound  $N_2$  molecule. In this sense, the steric protection given by the  $Cp^R$  ligands loosely mirrors the role of a protein matrix isolating metal centres to control reactivity and avoid undesirable decomposition. Although  $N_2$  reduction to  $NH_3$  or to  $N(SiMe_3)_3$  should have substantial mechanistic differences, our results provide compelling clues that the  $N_2$  molecule can become susceptible to reduction by Fe centres in S-rich environments, as is the case with  $FeMoco$ .

## Online content

Any methods, additional references, Nature Research reporting summaries, source data, extended data, supplementary information, acknowledgements, peer review information; details of author contributions and competing interests; and statements of data and code availability are available at <https://doi.org/10.1038/s41586-022-04848-1>.

1. Spatzal, T. et al. Evidence for interstitial carbon in nitrogenase FeMo cofactor. *Science* **334**, 940–940 (2011).
2. Lancaster, K. M. et al. X-ray emission spectroscopy evidences a central carbon in the nitrogenase iron-molybdenum cofactor. *Science* **334**, 974–977 (2011).
3. Seefeldt, L. C. et al. Reduction of substrates by nitrogenases. *Chem. Rev.* **120**, 5082–5106 (2020).
4. Spatzal, T., Perez, K. A., Einsle, O., Howard, J. B. & Rees, D. C. Ligand binding to the FeMo-cofactor: structures of CO-bound and reactivated nitrogenase. *Science* **345**, 1620–1623 (2014).
5. Sippel, D. et al. A bound reaction intermediate sheds light on the mechanism of nitrogenase. *Science* **359**, 1484–1489 (2018).
6. Kang, W., Lee, C. C., Jasniowski, A. J., Ribbe, M. W. & Hu, Y. Structural evidence for a dynamic metalocofactor during  $N_2$  reduction by Mo-nitrogenase. *Science* **368**, 1381–1385 (2020).
7. Mori, H., Seino, H., Hidai, M. & Mizobe, Y. Isolation of a cubane-type metal sulfido cluster with a molecular nitrogen ligand. *Angew. Chem. Int. Ed.* **46**, 5431–5434 (2007).
8. Ohki, Y. et al.  $N_2$  activation on a molybdenum–titanium–sulfur cluster. *Nat. Commun.* **9**, 3200 (2018).
9. McSkimming, A. & Suess, D. L. M. Dinitrogen binding and activation at a molybdenum–iron–sulfur cluster. *Nat. Chem.* **13**, 666–670 (2021).
10. Smith, B. E. et al. Exploring the reactivity of the isolated iron-molybdenum cofactor of nitrogenase. *Coord. Chem. Rev.* **185–186**, 669–687 (1999).

11. Ohki, Y. et al. Cubane-type  $[\text{Mo}_3\text{S}_4\text{M}]$  clusters with first-row groups 4–10 transition-metal halides supported by  $\text{C}_5\text{Me}_5$  ligands on molybdenum. *Chem. Eur. J.* **24**, 17138–17147 (2018).
12. Ohki, Y. et al. Synthesis of  $[\text{Mo}_3\text{S}_4]$  clusters from half-sandwich molybdenum(V) chlorides and their application as platforms for  $[\text{Mo}_3\text{S}_4\text{Fe}]$  cubes. *Inorg. Chem.* **58**, 5230–5240 (2019).
13. Jasniowski, A. J., Lee, C. C., Ribbe, M. W. & Hu, Y. Reactivity, mechanism, and assembly of the alternative nitrogenases. *Chem. Rev.* **120**, 5107–5157 (2020).
14. Chalkley, M. J., Drover, M. W. & Peters, J. C. Catalytic  $\text{N}_2$ -to- $\text{NH}_3$  (or  $-\text{N}_2\text{H}_4$ ) conversion by well-defined molecular coordination complexes. *Chem. Rev.* **120**, 5582–5636 (2020).
15. Tanabe, Y. & Nishibayashi, Y. Comprehensive insights into synthetic nitrogen fixation assisted by molecular catalysts under ambient or mild con. *Chem. Soc. Rev.* **50**, 5201–5242 (2021).
16. Lee, S. C. & Holm, R. H. The clusters of nitrogenase: synthetic methodology in the construction of weak-field clusters. *Chem. Rev.* **104**, 1135–1157 (2004).
17. Tanifuji, K. & Ohki, Y. Metal–sulfur compounds in  $\text{N}_2$  reduction and nitrogenase-related chemistry. *Chem. Rev.* **120**, 5194–5251 (2020).
18. Hazari, N. Homogeneous iron complexes for the conversion of dinitrogen into ammonia and hydrazine. *Chem. Soc. Rev.* **39**, 4044–4056 (2010).
19. Čorić, I., Mercado, B. Q., Bill, E., Vinyard, D. J. & Holland, P. L. Binding of dinitrogen to an iron–sulfur–carbon site. *Nature* **526**, 96–99 (2015).
20. Anderson, J. S., Rittle, J. & Peters, J. C. Catalytic conversion of nitrogen to ammonia by an iron model complex. *Nature* **501**, 84–87 (2013).
21. Yuki, M. et al. Iron-catalysed transformation of molecular dinitrogen into silylamine under ambient conditions. *Nat. Commun.* **3**, 1254 (2012).
22. Ung, G. & Peters, J. C. Low-temperature  $\text{N}_2$  binding to two-coordinate  $\text{L}_2\text{Fe}^0$  enables reductive trapping of  $\text{L}_2\text{FeN}_2^-$  and  $\text{NH}_3$  generation. *Angew. Chem. Int. Ed.* **54**, 532–535 (2015).
23. Araake, R., Sakadani, K., Tada, M., Sakai, Y. & Ohki, Y.  $[\text{Fe}_2]$  and  $[\text{Fe}_3]$  hydride clusters supported by phosphines: synthesis, characterization, and application in  $\text{N}_2$  reduction. *J. Am. Chem. Soc.* **139**, 5596–5606 (2017).
24. Piascik, A. D., Li, R., Wilkinson, H. J., Green, J. C. & Ashley, A. E. Fe-catalyzed conversion of  $\text{N}_2$  to  $\text{N}(\text{SiMe}_3)_3$  via an Fe-hydrazido resting state. *J. Am. Chem. Soc.* **140**, 10691–10694 (2018).
25. Liang, Q. et al.  $[\text{2Fe–2S}]$  cluster supported by redox-active o-phenylenediamide ligands and its application toward dinitrogen reduction. *Inorg. Chem.* **60**, 13811–13820 (2021).
26. Tanaka, H. et al. Molybdenum-catalyzed transformation of molecular dinitrogen into silylamine: experimental and DFT study on the remarkable role of ferrocenyldiphosphine ligands. *J. Am. Chem. Soc.* **133**, 3498–3506 (2011).
27. Li, M., Gupta, S. K., Dechert, S., Demeshko, S. & Meyer, F. Merging pincer motifs and potential metal-metal cooperativity in cobalt dinitrogen chemistry: efficient catalytic silylation of  $\text{N}_2$  to  $\text{N}(\text{SiMe}_3)_3$ . *Angew. Chem. Int. Ed.* **60**, 14480–14487 (2021).
28. Siedschlag, R. B. et al. Catalytic silylation of dinitrogen with a dicobalt complex. *J. Am. Chem. Soc.* **137**, 4638–4641 (2015).
29. Piascik, A. D. et al. Cationic silyldiazenido complexes of the  $\text{Fe}(\text{diphosphine})_2(\text{N}_2)$  platform: structural and electronic models for an elusive first intermediate in  $\text{N}_2$  fixation. *Chem. Commun.* **53**, 7657–7660 (2017).
30. Lee, Y., Mankad, N. P. & Peters, J. C. Triggering  $\text{N}_2$  uptake via redox-induced expulsion of coordinated  $\text{NH}_3$  and  $\text{N}_2$  silylation at trigonal bipyramidal iron. *Nat. Chem.* **2**, 558–565 (2010).
31. Rao, P. V. & Holm, R. H. Synthetic analogues of the active sites of iron–sulfur proteins. *Chem. Rev.* **104**, 527–560 (2004).
32. Neese, F. Prediction and interpretation of the  $^{57}\text{Fe}$  isomer shift in Mössbauer spectra by density functional theory. *Inorg. Chim. Acta* **337**, 181–192 (2002).
33. Dorantes, M. J., Moore, J. T., Bill, E., Mienert, B. & Lu, C. C. Bimetallic iron–tin catalyst for  $\text{N}_2$  to  $\text{NH}_3$  and a silyldiazenido model intermediate. *Chem. Commun.* **56**, 11030–11033 (2020).

**Publisher's note** Springer Nature remains neutral with regard to jurisdictional claims in published maps and institutional affiliations.

© The Author(s), under exclusive licence to Springer Nature Limited 2022

## Data availability

X-ray data are available free of charge from the Cambridge Crystallographic Data Centre under reference numbers CCDC 2079174–2079176 and 2141451. All other experimental, spectroscopic, crystallographic and computational data are included in the Supplementary Information.

**Acknowledgements** We thank T. Ohta (Sanyo-Onoda City University) for attempted resonance-Raman measurements of **2a** and <sup>15</sup>N-labelled **2a**. We acknowledge supercomputing resources at the Research Center for Computational Science at Okazaki and the Institute for Chemical Research at Kyoto University (Japan). This work was financially supported by Grant-in-Aids for Scientific Research (19H02733, 20K21207, 21H00021 for Y.O., 20H05671 and 20K21203 for Y.N., 20K15295 for S.K. and 21K20557 for K.T.) from the Japanese Ministry of Education, Culture, Sports, Science and Technology (MEXT), CREST grant (JPMJCR21B1 for Y.O. and JPMJCR1541 for Y.N.) from JST, the Takeda Science Foundation, the Tatematsu Foundation, and the Yazaki Memorial Foundation (for Y.O.), International Collaborative Research Program of

ICR, Kyoto University (for Y.O. and W.M.C.S.), and The Kyoto University Research Fund for Young Scientist (Start-Up) (for K.T.).

**Author contributions** Y.O. designed the study. K.M., Y.M., R.H., M.K., K.U. and K.T. conducted the experiments. M.T. participated in the discussion. Y.O. and K.T. interpreted the data. R.E.C. analysed the single-crystal XRD data. W.M.C.S. collected and analysed the computational data. T.T. and Y.S. collected and analysed the Mössbauer spectra. S.K. and Y.N. conducted experiments for ammonia synthesis. Y.O. and K.T. wrote the manuscript with input from all authors.

**Competing interests** The authors declare no competing interests.

### Additional information

**Supplementary information** The online version contains supplementary material available at <https://doi.org/10.1038/s41586-022-04848-1>.

**Correspondence and requests for materials** should be addressed to Yasuhiro Ohki.

**Peer review information** *Nature* thanks Daniël Broere, Thomas Rauchfuss and the other, anonymous, reviewer(s) for their contribution to the peer review of this work.

**Reprints and permissions information** is available at <http://www.nature.com/reprints>.



# Field-free superconducting diode effect in noncentrosymmetric superconductor/ferromagnet multilayers

Hideki Narita<sup>1</sup>✉, Jun Ishizuka<sup>2</sup>, Ryo Kawarazaki<sup>1</sup>, Daisuke Kan<sup>1,3</sup>, Yoichi Shiota<sup>1,3</sup>, Takahiro Moriyama<sup>1,3</sup>, Yuichi Shimakawa<sup>1,3</sup>, Alexey V. Ognev<sup>4</sup>, Alexander S. Samardak<sup>4</sup>, Youichi Yanase<sup>5,6</sup> and Teruo Ono<sup>1,3,4,7</sup>✉

**The diode effect is fundamental to electronic devices and is widely used in rectifiers and a.c.–d.c. converters. At low temperatures, however, conventional semiconductor diodes possess a high resistivity, which yields energy loss and heating during operation. The superconducting diode effect (SDE)<sup>1–8</sup>, which relies on broken inversion symmetry in a superconductor, may mitigate this obstacle: in one direction, a zero-resistance supercurrent can flow through the diode, but for the opposite direction of current flow, the device enters the normal state with ohmic resistance. The application of a magnetic field can induce SDE in Nb/V/Ta superlattices with a polar structure<sup>1,2</sup>, in superconducting devices with asymmetric patterning of pinning centres<sup>9</sup> or in superconductor/ferromagnet hybrid devices with induced vortices<sup>10,11</sup>. The need for an external magnetic field limits their practical application. Recently, a field-free SDE was observed in a NbSe<sub>2</sub>/Nb<sub>3</sub>Br<sub>8</sub>/NbSe<sub>2</sub> junction; it originates from asymmetric Josephson tunnelling that is induced by the Nb<sub>3</sub>Br<sub>8</sub> barrier and the associated NbSe<sub>2</sub>/Nb<sub>3</sub>Br<sub>8</sub> interfaces<sup>12</sup>. Here, we present another implementation of zero-field SDE using noncentrosymmetric [Nb/V/Co/V/Ta]<sub>20</sub> multilayers. The magnetic layers provide the necessary symmetry breaking, and we can tune the SDE by adjusting the structural parameters, such as the constituent elements, film thickness, stacking order and number of repetitions. We control the polarity of the SDE through the magnetization direction of the ferromagnetic layers. Artificially stacked structures<sup>13–18</sup>, such as the one used in this work, are of particular interest as they are compatible with microfabrication techniques and can be integrated with devices such as Josephson junctions<sup>19–22</sup>. Energy-loss-free SDEs as presented in this work may therefore enable novel non-volatile memories and logic circuits with ultralow power consumption.**

We fabricated noncentrosymmetric ferromagnet/superconductor multilayers [Nb (4.5 nm)/V (4.5 nm)/Co (1.7 nm)/V (4.5 nm)/Ta (4.5 nm)]<sub>20</sub> by replacing the V layers in Nb/V/Ta superlattices<sup>1,2,23,24</sup> with symmetric V/Co/V units to control the Rashba superconductor<sup>25</sup> by magnetization. The crystalline structure of the multilayers was characterized by low-angle and high-angle X-ray diffraction profiles (Methods and Supplementary Fig. 1). Figure 1a shows a

schematic of the measurement configuration, wherein the magnetic field, electrical current and polar axis are perpendicular to each other. Figure 1b shows a photomicrograph of the device with the polar axis along the *z* direction. Electric current and magnetic field were applied along the *y* and *x* directions, respectively.

Figure 1c shows the temperature dependence of the resistivity of the device at an electrical current density of 0.455 kA cm<sup>−2</sup> under various magnetic fields ranging from 0 to 0.5 T.

The superconducting transition temperature, *T<sub>c</sub>* (the temperature at which the resistivity drops to half of that above the transition), of the device was determined to be 2.6 K in the absence of a magnetic field. The *T<sub>c</sub>* of the present device is lower than that of the previously studied [Nb (1 nm)/V (1 nm)/Ta (1 nm)]<sub>40</sub> device<sup>1</sup>. This is possibly due to the pair-breaking effect of the Co layers<sup>16</sup> and/or the difference in the repetition number (Supplementary Fig. 2).

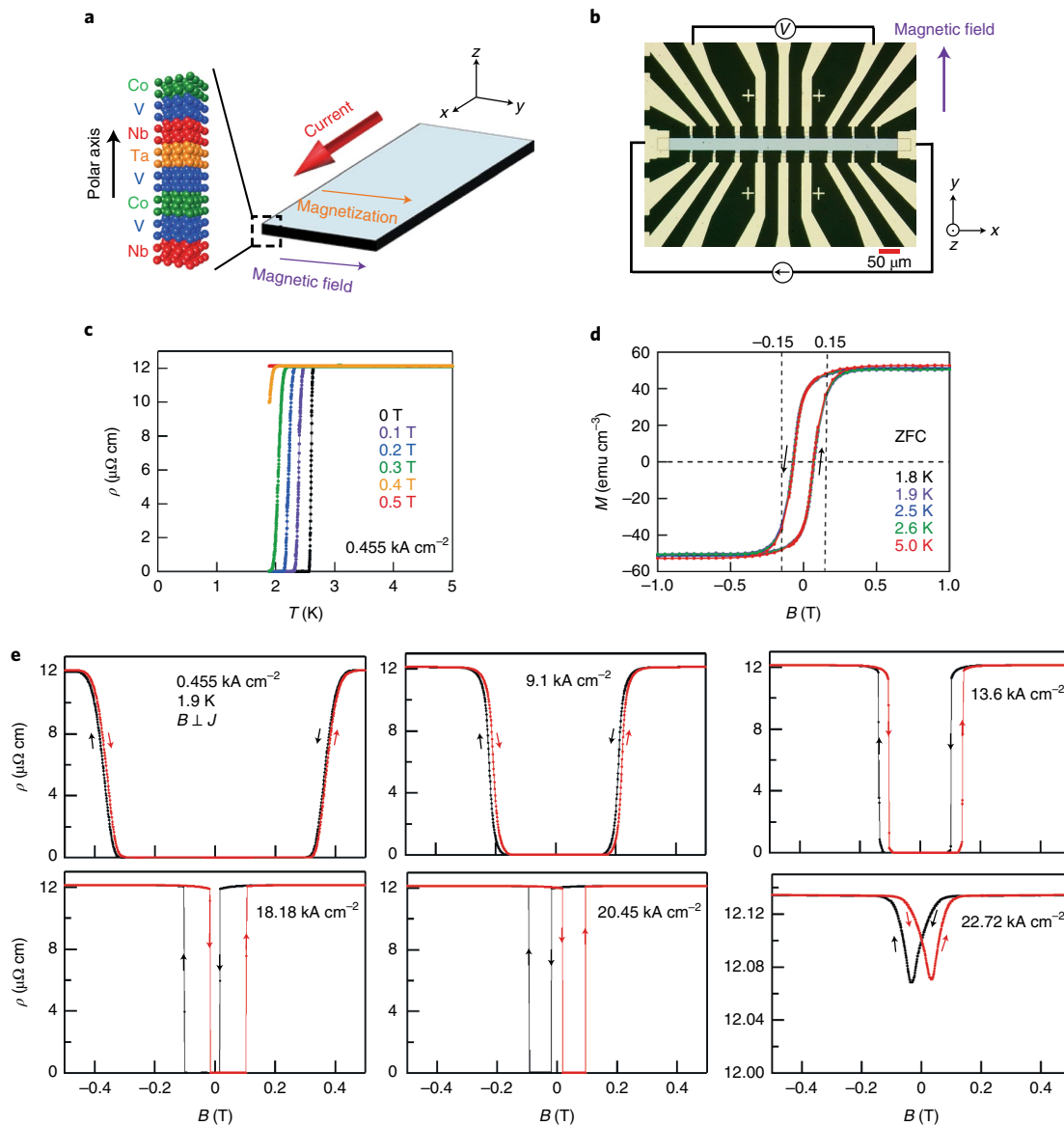
Furthermore, vortices were observed to start breaking the superconducting phase with increasing magnetic field, and the superconducting phase completely disappeared above 0.5 T at the lowest measurement temperature of 1.9 K. The superconducting coherence length  $\xi(0)$  at 0 K was estimated to be 24 nm (Supplementary Fig. 3). The magnetization curves of the multilayers at different temperatures in Fig. 1d show the characteristic ferromagnetic responses with a coercive field of 0.065 T in the multilayers above and below the *T<sub>c</sub>*.

Figure 1e presents the magnetic field dependences of the resistivity at several electrical current densities evaluated at 1.9 K. We observed switching between normal and superconducting states, similar to that observed in previous studies<sup>13,14</sup>. This is caused by the interplay between superconductivity and ferromagnetism. Previous reports have suggested that the switching between the normal and superconducting states is due to the internal exchange field at the superconductor–ferromagnet interface<sup>13,14</sup>. In our experiments, the switching between the normal and superconducting states was observed in the current density range of 0.455–20.45 kA cm<sup>−2</sup>. Because of the suppression of superconductivity by the external magnetic fields, the electrical resistivity increases monotonically with the magnetic fields at a low current density of 0.455 kA cm<sup>−2</sup>.

As the current density increases, the hysteresis of magnetoresistance becomes more pronounced, and the conventional magnetoresistance of Co is observed above 22.72 kA cm<sup>−2</sup>, where the

<sup>1</sup>Institute for Chemical Research, Kyoto University, Gokasho, Uji, Kyoto, Japan. <sup>2</sup>Institute for Theoretical Physics, ETH Zurich, Zurich, Switzerland. <sup>3</sup>Center for Spintronics Research Network, Institute for Chemical Research, Kyoto University, Uji, Japan. <sup>4</sup>Laboratory of Spin-Orbitronics, Institute of High Technologies and Advanced Materials, Far Eastern Federal University, Vladivostok, Russia. <sup>5</sup>Department of Physics, Graduate School of Science, Kyoto University, Kyoto, Japan. <sup>6</sup>Institute for Molecular Science, Okazaki, Japan. <sup>7</sup>Center for Spintronics Research Network, Graduate School of Engineering Science, Osaka University, Toyonaka, Japan. ✉e-mail: [narita.hideki.3x@kyoto-u.ac.jp](mailto:narita.hideki.3x@kyoto-u.ac.jp); [ono@scl.kyoto-u.ac.jp](mailto:ono@scl.kyoto-u.ac.jp)





**Fig. 1 | Device structure, transport, magnetic properties and SDE. a**, Schematic of the SDE and measurement configuration. The magnetic field is applied perpendicular to both the polar axis and the electrical current. **b**, Photomicrograph of the device. The wires of the [Nb/V/Co/V/Ta]<sub>20</sub> multilayers were electrically connected to the Au (100 nm)/Ti (5.0 nm) metal electrodes. V, voltage. The red scale bar corresponds to 50 μm. **c**, Temperature (T) dependence of the device resistivity (ρ) at an electrical current density (0.455 kA cm<sup>-2</sup>) in the multilayers under a magnetic field in the range of 0 to 0.5 T. **d**, Magnetization loops at several temperatures for the multilayers above and below T<sub>c</sub>. **e**, Magnetic field dependence of the resistivity in the multilayers for several electrical current densities at 1.9 K. The direction of the magnetic field was perpendicular to the polar axis and the electrical current.

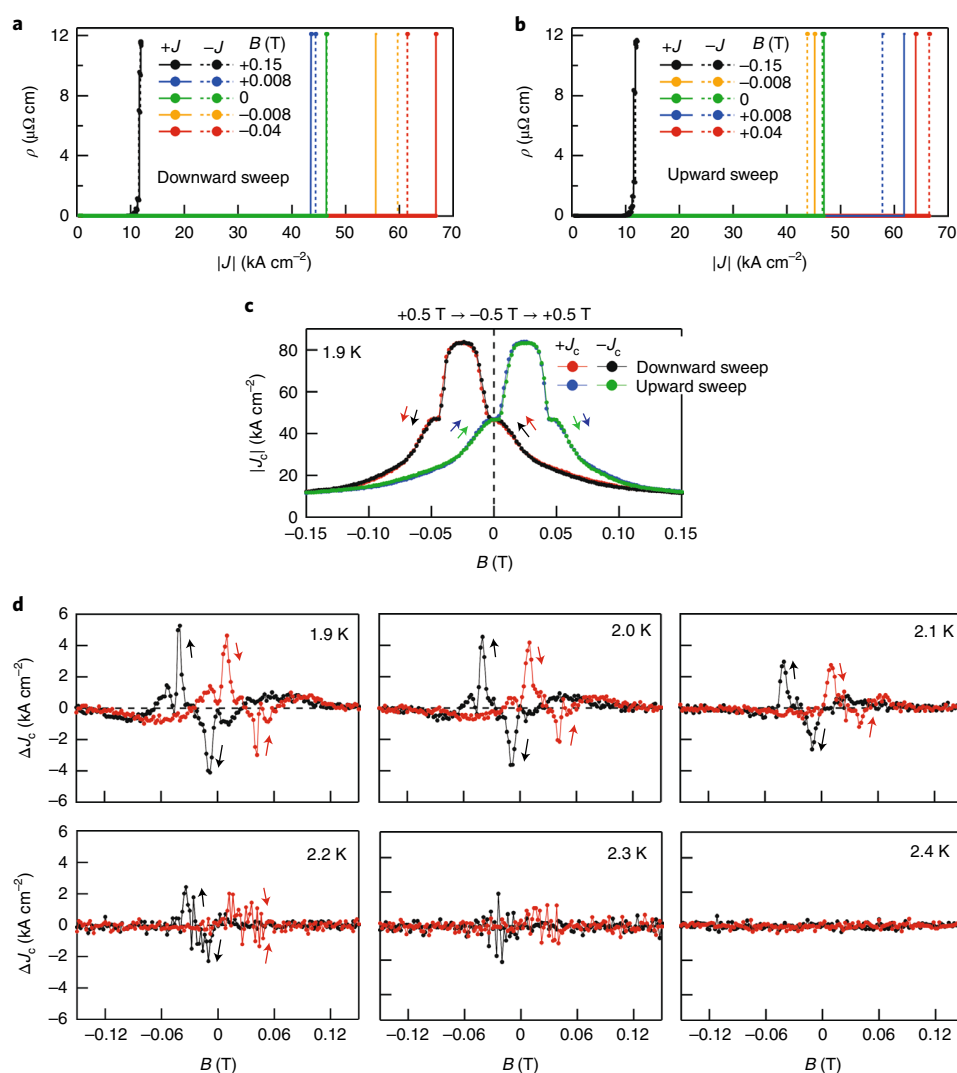
superconductivity is completely destroyed. The observation of the conventional magnetoresistance of Co also indicates that the device fabrication process does not alter the ferromagnetic properties of the multilayers.

Figure 2a,b shows the resistivity as a function of the current density,  $J$ , under various magnetic fields for positive and negative currents at 1.9 K. We observed the SDE in our noncentrosymmetric superconductor/ferromagnet multilayers; the critical current density  $J_c$  (the current density at which the resistivity increases to half of that above the transition) depends on the polarity of the current. Note that  $J_c$  is determined by the transition from the superconducting state to the normal conductive state. Therefore, there is no influence from the Joule heating. The variation in  $J_c$  with the magnetic field at 1.9 K is shown in Fig. 2c. In these

$J_c$  measurements, the magnetic field was initially set to +0.5 T, which is sufficiently large to saturate the magnetization, determined from the results in Fig. 1c. Subsequently,  $J_c$  was measured by sweeping the magnetic field in the order of +0.5, 0, -0.5, 0, +0.5 T.  $J_c$  also exhibits hysteresis, reflecting the magnetic hysteresis of the Co layer.  $J_c$  shows a symmetric behaviour with respect to zero field (dashed line) for the sweep of the magnetic field in the order of -0.5, 0, +0.5, 0 T. The pronounced peak around the coercive field can be attributed to enhanced vortex pinning on the network of proliferating domain walls<sup>26</sup>.

Figure 2d shows the magnetic field dependences of the non-reciprocal components of the critical current densities,  $\Delta J_c = |J_c| - |-J_c|$ , at different temperatures ( $+J_c$  and  $-J_c$  are the critical current densities corresponding to positive and negative





**Fig. 2 | Magnetic field and temperature dependences of SDE. a**, Current density ( $J$ ) dependence of the resistivity under various magnetic fields for positive and negative currents at 1.9 K. The magnetic field was swept from +0.5 T to −0.5 T (downward sweep). **b**, Dependence of the resistivity on  $J$  under various magnetic fields for positive and negative currents at 1.9 K. The magnetic field was swept from −0.5 T to +0.5 T (upward sweep). **c**,  $J_c$  as a function of the magnetic field at 1.9 K. First, the magnetic hysteresis of  $J_c$  was measured from +0.5 to −0.5 T (downward sweep) for positive (red) and negative (black) currents. Subsequently, the sweep direction was reversed, and the magnetic field was swept from −0.5 to +0.5 T (upward sweep) for positive (blue) and negative (green) currents. The arrows indicate the sweep directions. **d**, Non-reciprocal component of the critical current density,  $\Delta J_c$ , as a function of the magnetic field at various temperatures. The magnetic hysteresis of  $\Delta J_c$  was measured from +0.5 to −0.5 T (downward sweep, black). Subsequently, the sweep direction was reversed, and the magnetic field was swept from −0.5 to +0.5 T (upward sweep, red). The arrows indicate the sweep direction.

currents, respectively). Here, the magnetic field was initially set to +0.5 T. Then,  $\Delta J_c$  was measured by sweeping the magnetic field in the order of +0.5, 0, −0.5, 0, +0.5 T. In the downward sweep from the magnetic field of +0.5 T at 1.9 K (black dots), a negative peak of  $\Delta J_c$  appears at approximately +0.008 T, and  $\Delta J_c$  approaches zero at 0 T. As the magnetic field decreases further, large negative and positive peaks of  $\Delta J_c$  appear at approximately −0.008 and −0.04 T, respectively. The  $\Delta J_c$  value then gradually decreases to zero at around −0.5 T. After saturating the magnetization at −0.5 T,  $\Delta J_c$  was measured again by sweeping the magnetic field in the order of −0.5, 0, +0.5 T. Moreover, the magnetic field dependence of  $\Delta J_c$  in the upward sweep shows a trend (red dots) opposite to that of the downward sweep (black dots). The microscopic origin of the observed peaks and dip structures in the magnetic field dependence of  $\Delta J_c$  is not clear. However, it is possibly related to the evolution of complex magnetic domains. We also checked the reproducibilities

of  $J_c$  and  $\Delta J_c$  in two additional devices (Supplementary Fig. 4), and we observed that there was no clear hysteresis of  $\Delta J_c$  in the configurations of  $B \parallel x$  and  $B \parallel z$  (Supplementary Fig. 5). This hysteresis behaviour of  $\Delta J_c$  for  $B \parallel y$  is in clear contrast with the SDE observed in Nb/V/Ta superlattices<sup>1</sup>, wherein no hysteresis is observed. Note that the symmetric [Nb/V/Co/V/Nb]<sub>20</sub> multilayers without a polar structure do not exhibit the clear non-reciprocal components of the critical current densities even though they exhibit hysteresis in the magnetization curves (Supplementary Fig. 6). Therefore, the polar structure is essential to realize the magnetization-mediated SDE.

The polarity control of SDE in a zero field is essential to develop non-volatile devices based on SDEs. We demonstrate it using the minor hysteresis loops of the magnetization. Figure 3a shows the magnetic field dependences of  $J_c$  for positive and negative currents in minor hysteresis loops. For this, the magnetic field was swept in the order of +0.5, 0, −0.15 T (downward sweep) and then −0.15, 0,

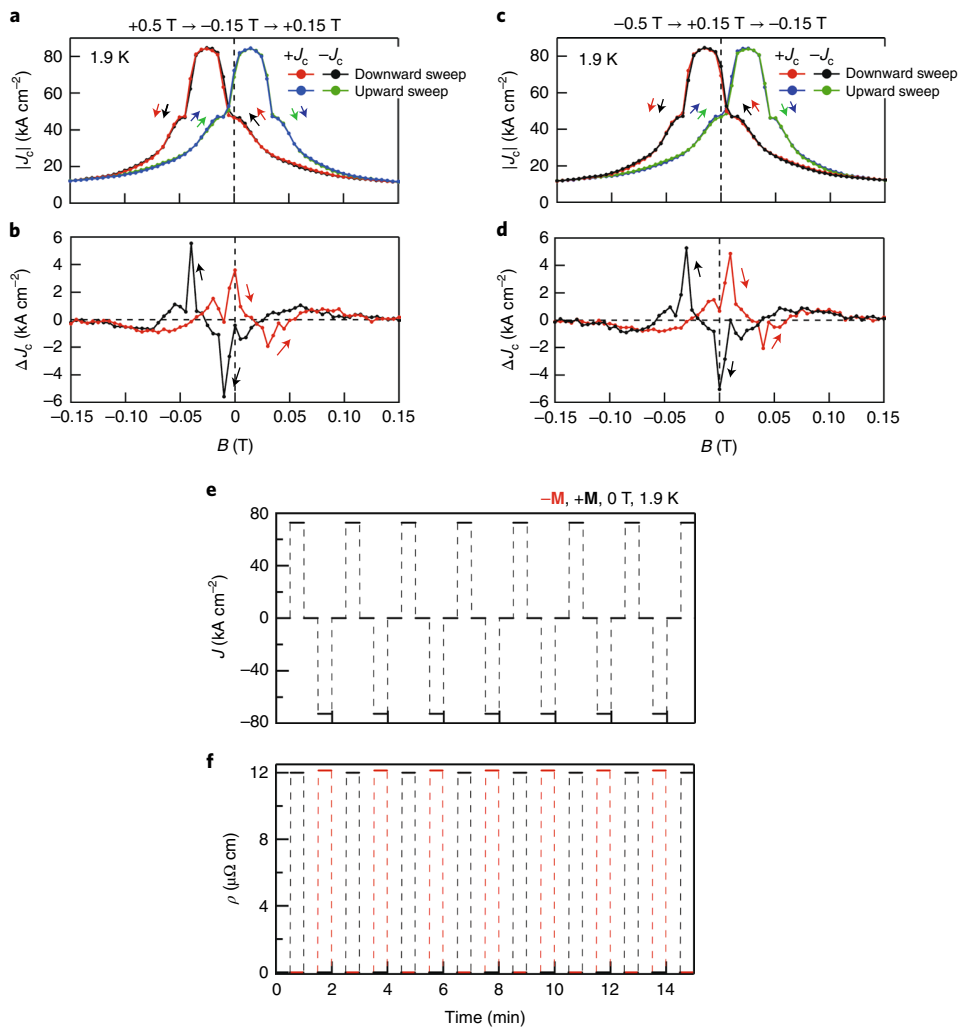


**Fig. 3 | Field-free SDE controlled by magnetization.** **a**, Magnetic field dependences of  $J_c$  for positive and negative currents in minor hysteresis loops at 1.9 K. Magnetic field was swept in the order of +0.5, 0, −0.15 T (downward sweep) and then −0.15, 0, +0.15 T (upward sweep). **b**, Magnetic field dependence of  $\Delta J_c$  in the minor hysteresis loops obtained by Fig. 3a. **c**, Magnetic field dependences of  $J_c$  for positive and negative currents in minor hysteresis loops at 1.9 K. Magnetic field was swept in the order of −0.5, 0, +0.15 T (upward sweep), and then +0.15, 0, −0.15 T (downward sweep). **d**, Magnetic field dependence of  $\Delta J_c$  in the minor hysteresis loops obtained by Fig. 3c. **e**, Repeated application of current densities  $J = 72.7 \text{ kA cm}^{-2}$  and  $J = -72.7 \text{ kA cm}^{-2}$  at 1.9 K without a magnetic field. **f**, Non-volatile SDE at 1.9 K. Red and black dots represent the results for negative magnetization (−**M**) and positive magnetization (+**M**), respectively. The device shows a superconducting state or normal conducting state depending on the polarity of the current. Note that the polarity of the SDE depends on the direction of magnetization. The −**M** or +**M** state is achieved after sweeping the magnetic field in the order of +0.5, 0, −0.15, 0 T or −0.5, 0, +0.15, 0 T, respectively.

+0.15 T (upward sweep). The limiting field of the minor loops is 0.15 T, as shown by the dashed line in Fig. 1d. Owing to the asymmetrical magnetic field sweeping,  $J_c$  shows asymmetry with respect to the zero field (dashed line). Consequently, we observe the positive  $\Delta J_c$  in the zero field after sweeping the magnetic field in the order of +0.5, 0, −0.15, 0 T, as shown in Fig. 3b. Moreover,  $J_c$  also shows asymmetry with respect to zero field after sweeping the magnetic field in the order of −0.5, 0, +0.15, 0 T, resulting in a negative  $\Delta J_c$  under the zero-field condition, as shown in Fig. 3c,d. Therefore, we could control the polarity of the SDE by magnetization.

Here, we demonstrate the non-volatile SDE. With repeated application of current densities in Fig. 3e, the red and black dots in Fig. 3f represent the resistivities measured with  $J = 72.7 \text{ kA cm}^{-2}$  at 1.9 K for negative (−**M**) and positive (+**M**) magnetizations, respectively. The −**M** (+**M**) is the state after sweeping the magnetic field in the order of +0.5, 0, −0.15, 0 T (−0.5, 0, +0.15, 0 T). The device exhibits a

superconducting state or a normal conducting state depending on the polarity of the current, and the polarity of the SDE depends on the direction of magnetization.

Finally, we discuss theoretical viewpoints in detail. We performed a first-principles band structure calculation in the non-magnetic electronic state for a Nb/V/Co/V/Ta supercell, where two atomic layers of body-centred cubic Nb, V, Co, V and Ta were repeatedly stacked, as shown in Fig. 4a,b. The Rashba splitting of bands at the Fermi energy  $E_F$  was observed as  $E_R = 1\text{--}10 \text{ meV}$ , which is close to the value of a Nb/V/Ta superlattice. Although the Rashba splitting of Co bands was minor ( $\sim 1 \text{ meV}$ ), the density of states due to the Co bands near  $E_F$  was predominantly larger than that due to the Nb, V and Ta bands, as shown in Fig. 4b. To gain more insight, we also performed a spin-polarized band structure calculation with the magnetization direction [010] and obtained a ferromagnetic ground state, where the total energy was lower than that of the non-magnetic

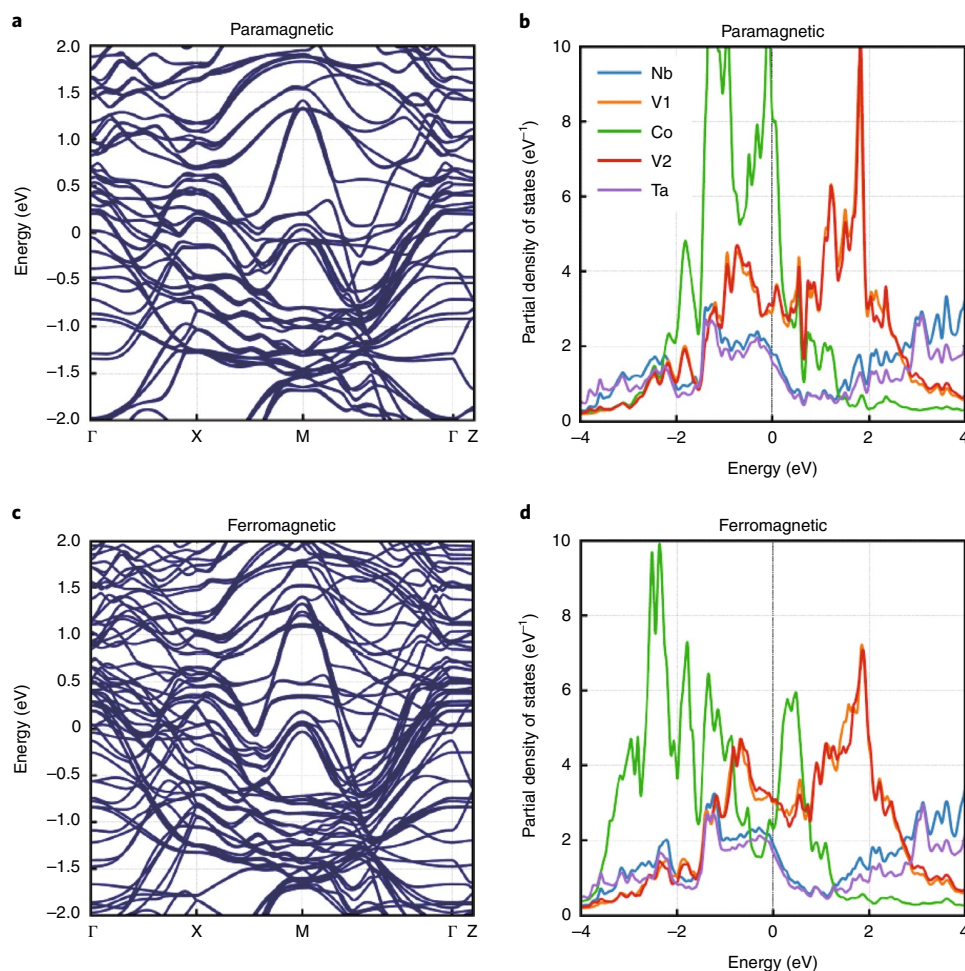


**Fig. 4 | Band structure of a bulk Nb/V/Co/V/Ta superlattice. a**, Band structure obtained from first-principles calculation for paramagnetic state. **b**, Partial density of states for paramagnetic state. **c**, Band structure for ferromagnetic state. **d**, Partial density of states for ferromagnetic state. The V layer between Nb and Co is labeled with V1 and that between Co and Ta is labeled with V2.

state, as shown in Fig. 4c,d. The magnitude of the magnetic moment  $|M|$  at Co atoms was calculated as  $|M| = 1.93\mu_B$  where  $\mu_B$  is the Bohr magneton. The V atoms adjacent to Co atoms had a considerable magnetization  $|M| = 0.5\mu_B - 1\mu_B$ , while others had only  $|M| = 0.01\mu_B - 0.05\mu_B$ . Thus, the atoms that are not adjacent to Co atoms can stabilize the superconductivity against the Pauli depairing effect due to the ferromagnetic spin polarization. We indeed noticed that the partial densities of states are almost unchanged for Nb, V and Ta atoms, and all atoms contribute at  $E_F$  in the ferromagnetic state, as shown in Fig. 4d. In other words, the superconducting transition temperature of this system may be determined from the total density of states consisting of three types of atoms.

Pairing states that exhibit the diode effect would correspond to helical superconductivity, which has been investigated in non-centrosymmetric superconductors such as CePt<sub>3</sub>Si (refs. 27,28), the surface/interface of SrTiO<sub>3</sub>/LaAlO<sub>3</sub> (ref. 29) and heavy-fermion superlattices<sup>30</sup>. The asymmetric band dispersion is essential for the helical superconductivity, and it appears in the noncentrosymmetric ferromagnet. Our spin-polarized band structure calculation indeed shows asymmetric behaviours (Supplementary Fig. 7). The SDE has been analysed by the Ginzburg–Landau theory and microscopic Hamiltonian<sup>3,6–8</sup>. Higher-order gradient terms in the Ginzburg–Landau expansion exhibit the non-reciprocity of critical current, and the microscopic calculation predicts an anomalous ‘sign-reversal effect’ in the helical superconducting state<sup>6</sup>. Thus,

it will be intriguing to clarify the asymmetric and sign-reversing behaviour observed in Fig. 2d in future works.

The experiments revealed that noncentrosymmetric superconductor/ferromagnet multilayers exhibited magnetization-mediated non-reciprocal critical currents, that is, a magnetization-mediated SDE. The field-free SDE demonstrated here enables rectification without an external magnetic field. However, significant issues still need to be overcome for practical application. The rectification still requires precise control of the applied current and temperature, which are major limitations for practical device operation. Therefore, it is essential to explore materials with a larger  $\Delta J_c$  and higher  $T_c$  to realize a wide temperature range of operation. The proposed method of symmetry breaking using artificial stacked structures is versatile and controllable. Furthermore, the electronic band structure can be controlled by modulating the thickness and period of each constituent layer, which offers a promising route for exploring new materials for practical application. Our findings pave the way for obtaining rewritable superconducting diode logic circuits using the non-volatility of magnetic materials.

#### Online content

Any methods, additional references, Nature Research reporting summaries, source data, extended data, supplementary information, acknowledgements, peer review information; details of author contributions and competing interests; and statements of

data and code availability are available at <https://doi.org/10.1038/s41565-022-01159-4>.

Received: 20 November 2021; Accepted: 23 May 2022;  
Published online: 30 June 2022

## References

- Ando, F. et al. Observation of superconducting diode effect. *Nature* **584**, 373–376 (2020).
- Miyasaka, Y. et al. Observation of nonreciprocal superconducting critical field. *Appl. Phys. Express* **14**, 073003 (2021).
- Wakatsuki, R. et al. Nonreciprocal charge transport in noncentrosymmetric superconductors. *Sci. Adv.* **3**, e1602390 (2017).
- Yasuda, K. et al. Nonreciprocal charge transport at topological insulator/superconductor interface. *Nat. Commun.* **10**, 2734 (2019).
- Itahashi, Y. M. et al. Nonreciprocal transport in gate-induced polar superconductor SrTiO<sub>3</sub>. *Sci. Adv.* **6**, eaay9120 (2020).
- Daido, A., Ikeda, Y. & Yanase, Y. Intrinsic superconducting diode effect. *Phys. Rev. Lett.* **128**, 037001 (2022).
- Yuan, N. F. Q. & Fu, L. Supercurrent diode effect and finite momentum superconductors. *Proc. Natl Acad. Sci. USA* **119**, e2119548119 (2022).
- He, J. J., Tanaka, Y. & Nagaosa, N. A phenomenological theory of superconductor diodes. *New J. Phys.* **24**, 053014 (2022).
- Lyu, Y.-Y. et al. Superconducting diode effect via conformal-mapped nanoholes. *Nat. Commun.* **12**, 2703 (2021).
- Aladyshkin, A. Yu., Fritzsche, J. & Moshchalkov, V. V. Planar superconductor/ferromagnet hybrids: anisotropy of resistivity induced by magnetic templates. *Appl. Phys. Lett.* **94**, 222503 (2009).
- Aladyshkin, A. Yu. et al. Reverse-domain superconductivity in superconductor-ferromagnet hybrids: effect of a vortex-free channel on the symmetry of *I*-*V* characteristics. *Appl. Phys. Lett.* **97**, 052501 (2010).
- Wu, H. et al. The field-free Josephson diode in a van der Waals heterostructure. *Nature* **604**, 653–656 (2022).
- Zhu, Y., Pal, A., Blamire, M. G. & Barber, Z. H. Superconducting exchange coupling between ferromagnets. *Nat. Mater.* **16**, 195–199 (2017).
- Li, B. et al. Superconducting spin switch with infinite magnetoresistance induced by an internal exchange field. *Phys. Rev. Lett.* **110**, 097001 (2013).
- Baek, B., Rippard, W. H., Benz, S. P., Russek, S. E. & Dresselhaus, P. D. Hybrid superconducting-magnetic memory device using competing order parameters. *Nat. Commun.* **5**, 3888 (2014).
- Obi, Y., Ikebe, M., Wakou, H. & Fujimori, H. Superconducting transition temperature and dimensional crossover in Nb/Co and V/Co multilayers. *J. Phys. Soc. Jpn* **68**, 2750–2754 (1991).
- Monton, C., de la Cruz, F. & Guimpel, J. Magnetic behavior of superconductor/ferromagnet superlattices. *Phys. Rev. B* **75**, 064508 (2007).
- Banerjee, N. et al. Controlling the superconducting transition by spin-orbit coupling. *Phys. Rev. B* **97**, 184521 (2018).
- Misaki, K. & Nagaosa, N. Theory of the nonreciprocal Josephson effect. *Phys. Rev. B* **103**, 245302 (2021).
- Baumgartner, C. et al. A Josephson junction supercurrent diode. *Nat. Nanotechnol.* **17**, 39–44 (2022).
- Davydova, M., Prembabu, S. & Fu, L. Universal Josephson diode effect. *Sci. Adv.* **8**, eabo0309 (2022).
- Bauriedl, L. et al. Supercurrent diode effect and magnetochiral anisotropy in few-layer NbSe<sub>2</sub>. Preprint at *arXiv* <https://doi.org/10.48550/arXiv.2110.15752> (2022).
- Ando, F. et al. Fabrication of noncentrosymmetric Nb/V/Ta superlattice and its superconductivity. *J. Magn. Soc. Jpn* **43**, 17–20 (2019).
- Ando, F. et al. Investigation of the upper critical field in artificially engineered Nb/V/Ta superlattices. *Jpn. J. Appl. Phys.* **60**, 060902 (2021).
- Wakatsuki, R. & Nagaosa, N. Nonreciprocal current in noncentrosymmetric Rashba superconductors. *Phys. Rev. Lett.* **121**, 026601 (2018).
- Curran, P. J. et al. Continuously tunable critical current in superconductor-ferromagnet multilayers. *Appl. Phys. Lett.* **110**, 262601 (2017).
- Baur, E. et al. Heavy fermion superconductivity and magnetic order in noncentrosymmetric CePt<sub>3</sub>Si. *Phys. Rev. Lett.* **92**, 027003 (2004).
- Kaur, R. P., Agterberg, D. F. & Sigrist, M. Helical vortex phase in the noncentrosymmetric CePt<sub>3</sub>Si. *Phys. Rev. Lett.* **94**, 137002 (2005).
- Reyren, N. et al. Superconducting interfaces between insulating oxides. *Science* **317**, 1196–1199 (2007).
- Naritsuka, M. et al. Extremely strong-coupling superconductivity in artificial two-dimensional Kondo lattices. *Phys. Rev. B* **96**, 174512 (2017).

**Publisher's note** Springer Nature remains neutral with regard to jurisdictional claims in published maps and institutional affiliations.

© The Author(s), under exclusive licence to Springer Nature Limited 2022

## Methods

**Device fabrication.** The [Nb/V/Co/V/Ta]<sub>20</sub> multilayers were grown on MgO(100) substrates by direct current (d.c.) magnetron sputtering in a high-vacuum system with a base pressure of approximately  $5 \times 10^{-6}$  Pa. Before the film growth, the MgO(100) substrate was heated at 600 °C for 30 min in a sputtering chamber to remove impurities. Subsequently, the MgO substrate was heated to 300 °C during the deposition. All the films were deposited under an Ar pressure of approximately 0.1 Pa. The Nb, V, Co, V and Ta layers were repeatedly sputtered on the MgO substrate in the same sequence for 20 cycles. The deposition rates were maintained constant at 0.36, 0.22, 0.45 and 0.18 Å s<sup>-1</sup> for Nb, V, Ta and Co, respectively. The total deposition time was approximately 5 h. After deposition, the films were cooled from 300 to 30 °C. X-ray diffraction was performed using a conventional four-circle diffractometer (PANalytical, X'pert MRD) with Cu K $\alpha$  radiation (wavelength,  $\lambda = 0.154$  nm). Supplementary Fig. 1a,b shows the low-angle and high-angle X-ray diffraction profiles of the multilayers, respectively. In this study, the thickness of the ferromagnetic layer was adjusted to realize ferromagnetic properties, and it was set to be sufficiently small to avoid the Bloch domain wall effect.

The deposited films were then patterned into a wire (dimensions, 50  $\mu\text{m} \times 1,000 \mu\text{m} \times 0.44 \mu\text{m}$ ) using conventional photolithography and Ar-ion milling. Finally, Au (100 nm)/Ti (5.0 nm) metal electrodes were electrically connected to the wire. The surface layer was removed through weak Ar-ion milling before the electrode deposition to create ohmic contacts.

**Transport and magnetization measurements.** During the transport measurements, the temperature and magnetic field were controlled using a commercial refrigerator (Quantum Design, Physical Property Measurement System) with d.c. applied using a current source (Yokogawa 7651). The voltage was measured using a four-terminal configuration with a nanovoltmeter (Keithley 2182A).

The magnetization of the sample was studied under a magnetic field parallel to the film surface, using a superconducting quantum interference device magnetometer (Quantum Design MPMS3). Before starting the measurements, the magnetic field was reduced from 1.0 to 0 T using an oscillating field sequence to remove any trapped flux in the superconducting magnet. Subsequently, the magnetic hysteresis loops of the zero-field-cooled (ZFC) magnetization were measured in the 'd.c. and no overshoot' mode using film samples with dimensions of 7 mm  $\times$  2 mm. ZFC means that the sample was cooled from 10 K without the magnetic field before magnetization measurements. The magnetization of the MgO substrate was subtracted to determine the intrinsic magnetic properties of the multilayers with the field parallel to the surface.

**Details of band structure calculation.** We conducted first-principles calculations for non-magnetic and ferromagnetic states on a bulk Nb/V/Co/V/Ta superlattice. We adopted the full-potential linearized augmented plane wave plus local orbitals method within the generalized gradient approximation in the WIEN2k package<sup>31,32</sup>. A supercell was constructed with ten atoms consisting of two layers of Nb, V, Co, V and Ta atoms. We used the muffin-tin radius  $R_{\text{MT}}$  of 2.50 a.u.; the maximum reciprocal lattice vector  $K_{\text{max}}$  as  $R_{\text{MT}}K_{\text{max}} = 8.0$ ; and  $21 \times 21 \times 4$   $k$ -point sampling for self-consistent calculation. Supplementary Fig. 7 shows the band structures and the partial densities of states in non-magnetic and ferromagnetic states. If we neglect the Co bands, the band structure is similar to that in the Nb/V/Ta superlattice.

The partial densities of the states of Co show an exchange splitting, while they are almost unchanged for Nb, V and Ta. Thus, Nb, V and Ta layers form spin-splitting bands with weak magnetization. Therefore, it is verified that Nb/V/Co/V/Ta is a noncentrosymmetric superconductor that exhibits a SDE without a magnetic field.

## Data availability

The data that support the findings of this study are available from the corresponding authors upon reasonable request.

## References

- Blaha, P. et al. WIEN2k: an Augmented Plane Wave Plus Local Orbitals Program for Calculating Crystal Properties (Techn. Universität, 2018).
- Blaha, P. et al. WIEN2k: an APW+lo program for calculating the properties of solids. *J. Chem. Phys.* **152**, 074101 (2020).

## Acknowledgements

This work was partly supported by Japan Society for the Promotion of Science KAKENHI (grant nos 15H05702, 15H05884, 15H05745, 18H04225, 18H01178, 18H05227, 19H05823, 20H05665, 21K13883 and 21K18145); the Cooperative Research Project Program of the Research Institute of Electrical Communication, Tohoku University; and the Collaborative Research Program of the Institute for Chemical Research, Kyoto University. This study was also supported by the Futaba Foundation's Futaba Research Grant Program, and Iketani Science and Technology Foundation. A.V.O., A.S.S. and T.O. acknowledge the Russian Ministry of Science and Higher Education for state support of scientific research conducted under the supervision of leading scientists in Russian institutions of higher education, scientific foundations and state research centres (project no. 075-15-2021-607).

## Author contributions

H.N. and T.O. conceived the project. H.N. deposited the multilayers and fabricated the devices. H.N. performed the measurements and data analysis. H.N. and T.O. wrote the manuscript with the assistance of the other authors. J.I. and Y.Y. calculated the band structure and assisted with the analysis of the experimental results. All authors contributed jointly to the interpretation of the results.

## Competing interests

The authors declare no competing interests.

## Additional information

**Supplementary information** The online version contains supplementary material available at <https://doi.org/10.1038/s41565-022-01159-4>.

**Correspondence and requests for materials** should be addressed to Hideki Narita or Teruo Ono.

**Peer review information** *Nature Nanotechnology* thanks the anonymous reviewers for their contribution to the peer review of this work.

**Reprints and permissions information** is available at [www.nature.com/reprints](http://www.nature.com/reprints).





## 4. 參考資料



京都大学化学研究所  
化学関連分野の深化・連携を基軸とする先端・学際グローバル研究拠点  
令和4年度国際共同利用・共同研究公募要領

京都大学化学研究所は、「化学に関する特殊事項の学理及び応用の研究を掌る」ために、化学を中心とする分野で基礎研究に重点を置いた先端研究に邁進してまいりました。平成30年化学研究所は、国立大学共同利用・共同研究拠点活動におけるグローバル共同利用・共同研究が評価され、文部科学大臣から国際共同利用・共同研究拠点として認定されました。これを受けて、平成31年度からの国際共同利用・共同研究拠点活動においては、多様でグローバルな化学分野の共同研究を一層強力に推進すべく、さらなる事業展開を図って参りました。この国際共同利用・共同研究拠点活動が評価され、令和3年10月文部科学大臣から国際共同利用・共同研究拠点として再認定されました。

つきましては、化学に関わる分野でご活躍の皆様のご意見・ご要望を尊重しつつ、世界の化学の基礎・応用研究を皆様とともに一層推進することを念頭に置き、下記の要領で令和4年度の拠点共同利用・共同研究の課題公募をさせていただきます。

この公募に当たりましては、分野選択型（計画研究型）、課題提案型、連携・融合促進型および施設・機器利用型の四つに分けて研究課題を募集いたします。今回から、分野選択型には従来の【基幹分野】の他に、化学研究所が重要分野と考える【特定分野】を設けました。これらの課題の実施に際しては当研究所の専任教員または客員教員との共同研究を基調といたしますが、いずれの課題でも後述の共通設備・機器・資料等のご利用が可能です。なお、各課題とも、海外研究者を研究代表者あるいは研究協力者とする国際共同研究（この場合、英語フォームで申請下さい）と、国内研究者を研究代表者とする国内共同研究を実施致します。これらの点も勘案いただき、本公募要領の詳細について十分ご確認の上、期日までにご申請下さいますようお願いいたします。

京都大学化学研究所長 辻井敬亘  
共同研究ステーション長 寺西利治

## 1. 研究期間

1年間（令和4年4月1日から令和5年3月31日まで）。

## 2. 研究課題分類

下記のような分類（型）ごとに研究課題を募集いたします。いずれの課題についても、分類ないし分野の担当者もしくは当研究所で対応する共同研究者にご一報の上、ご申請下さい。

### 2-1. 分野選択型（計画研究型）研究課題

分野選択型（計画研究型）研究課題は、あらかじめ設定された分野に関して化学研究所内の研究者と共同で遂行する課題です。令和4年度は下記の基幹5分野および特定1分野について課題を公募いたします。6分野を合わせて、萌芽的な課題と発展的な課題をそれぞれ25件程度、採択の予定です。

#### 2-1-1. 分野選択型【基幹分野】研究課題

ビーム科学分野（担当者：若杉 昌徳；wakasugi.masanori.8z@kyoto-u.ac.jp）

基本テーマ：先進量子ビームの開発と新奇診断分析手法の創出

趣旨：レーザー、X線、電子線、イオンビームなどの量子ビームの高度化とその先端的診断分析法への応用を進めます。また、これらの量子ビームを複合的に用いて、極微細領域での超高速化学・物理現象の解明を目指します。

元素科学分野（担当者：大木 靖弘；ohki@scl.kyoto-u.ac.jp）

基本テーマ：元素科学に基づく物質創製・機能創出

趣旨：元素の新たな特性を引き出し、この特性をもとに優れた機能を有する新物質を創製します。元素と社

会との関わりを俯瞰した元素戦略研究も推進します。物質の機能は、構成元素の特性を相乗的に反映して発現します。この発現機構を明らかとし、望みの機能を意のままに創出することを目指します。

バイオ情報学分野（担当者：阿久津 達也; takutsu@kuicr.kyoto-u.ac.jp）

基本テーマ：バイオ情報を含む複合情報の融合解析

趣旨：ゲノムやメタゲノムに代表される最新バイオ情報に立脚して、バイオ情報がいかに生体内や自然環境における化学現象と関わっているかを明らかにし、生命システムについての化学的理解の深化を図ります。さらに、その成果を応用して、ゲノム創薬やパーソナライズド医療などへの展開も目指します。

物質合成分野（担当者：村田 靖次郎; yasujiro@scl.kyoto-u.ac.jp）

基本テーマ：複合機能材料の戦略的創製

趣旨：異種材料のハイブリッド化・複合化ならびにナノサイズ化に重点を置き、新規な機能をもつ新世代材料や分子システムの創製を目指すとともに、生体の認識、応答、反応などの諸機能を担う例えば生体膜等も複合機能材料と捉え、機能物質と生命現象の化学的相関の解明も目指します。

現象解析分野（担当者：長谷川 健; htakeshi@scl.kyoto-u.ac.jp）

基本テーマ：複合測定に基づく物質解析

趣旨：化学を基盤とする多種の分光学的手法・解析的手法を複合的に駆使して、天然および人工物質の構造・性質を分子レベルから巨視的レベルまで階層的に理解・記述することを目指し、一方、その結果を還元することによって新たな物質科学の枠組みを構築する取組みも目指します。

## 2-1-2. 分野選択型【特定分野】研究課題

量子情報・スピントロニクス分野（担当者：小野 輝男; ono@scl.kyoto-u.ac.jp）

基本テーマ：量子情報・スピントロニクス分野

趣旨：物理学、応用物理学、電子工学、磁気工学、材料科学、化学、情報科学および境界領域の新しい科学技術の創造により、古典情報と量子情報技術を融合・発展させ、Society 5.0 とポストコロナ社会で必要とされる将来情報技術の基盤構築を目指します。

## 2-2. 課題提案型研究課題（担当者：寺西 利治; teranisi@scl.kyoto-u.ac.jp）

課題提案型研究課題は、前項 1 で設定した一つの分野に留まらない分野、あるいはそれ以外の分野について、化学関連分野の研究者から自由にご提案いただく課題です。萌芽的な課題と発展的な課題を、それぞれ 20 件程度、採択の予定です。新分野の開拓につながるような課題を特に歓迎いたします。なお、緊急性・重要性が極めて高いと判断した課題については、前記の応募期日にかかわらず、直ちに採択することもあります。

## 2-3. 連携・融合促進型研究課題（担当者：栗原 達夫; kurihara@scl.kyoto-u.ac.jp）

連携・融合促進型研究課題は、化学関連分野における国内外の研究連携の強化を主目的とする共同研究課題です。国外も念頭に置く場合は、化学研究所の部局間国際学術交流締結先 ([http://www.kuicr.kyoto-u.ac.jp/sites/international\\_exchange/agreement/](http://www.kuicr.kyoto-u.ac.jp/sites/international_exchange/agreement/) 参照)との共同研究を開始する場を求めていることも可能です。また、この目的に沿った研究集会の開催も本課題として応募いただけます。5 件程度を採択する予定です。

## 2-4. 施設・機器利用型研究課題（担当者：二木 史朗; futaki@scl.kyoto-u.ac.jp）

施設・機器利用型研究課題は、拠点ホームページに記載の共通設備・機器・資料等 (<https://www.icr-ijurc.jp/equipment/>) の利用を主とする共同研究課題です。15 件程度を採択する予定です。

令和4年度国際共同利用・共同研究経費概算値

	経費上限／件 <sup>*</sup> （千円）	
	国際共同研究	国内共同研究
分野選択型萌芽的研究	1,000	800
分野選択型発展的研究	2,000	1,500
課題提案型萌芽的研究	1,000	800
課題提案型発展的研究	2,000	1,500
連携・融合促進型研究	1,000	800
施設・機器利用型研究	1,000	800

<sup>\*</sup>表中の金額は目安です。予算の状況に応じた減額もありえますことをご了解下さい。  
経費内での備品費、消耗品費、旅費の配分は、申請者と化学研究所の共同研究者が協議して決定下さい。特に、旅費については、地域性を勘案してご決定下さい。

### 3. 共同研究応募方法

#### 3-1. 申請資格

国公立大学、国公立研究機関、独立行政法人等の専任研究者、または、これに準ずる者。

#### 3-2. 申請書記入要領

申請に当たっては、該当する募集分類・分野の担当者もしくは当研究所で対応する共同研究者と、事前に研究課題、研究内容、研究経費に関して、必ずご協議下さい。対応する共同研究者は、当研究所の専任教員または令和4年度客員教員からお選び下さい。なお、教員のリストは下記の化学研究所ホームページをご参照下さい。

教員リスト [http://www.kuicr.kyoto-u.ac.jp/sites/research\\_activities/chemist/](http://www.kuicr.kyoto-u.ac.jp/sites/research_activities/chemist/)

また、対応する共同研究者をお決めになれない場合は、各分類・分野の担当者に、まず、ご相談ください。  
上記の表の経費上限は目安です。特に、経費内での備品費、消耗品費、旅費の配分については、当研究所で対応する共同研究者と十分にご協議の上で申請下さい。特に、旅費については、地域性を勘案してご申請下さい。

課題申請は、本要領に添付の分野選択型共同利用・共同研究申請書（様式1）、課題提案型共同利用・共同研究申請書（様式2）、連携・融合促進型共同利用・共同研究申請書（様式3）、施設・機器利用型共同利用・共同研究申請書（様式4）に必要事項を記入し、下記の要領で、化学研究所共同研究推進室にご提出下さい。

なお、各課題とも、海外研究者を研究代表者あるいは研究協力者とする国際共同研究も実施可能です。この場合、英語フォーム（Forms 1~4）の左肩の欄にチェックを入れて、当研究所の共同研究者に提出をご依頼下さい。

#### <記入上の注意事項>

1. ※を付した事項は当研究所で記入します。
2. 当研究所で対応する共同研究者は必ずご記入下さい。
3. 申請者（研究代表者）と共同研究者の役割分担を明記して下さい。事前に共同研究者の承諾を得ていただくことが必要です。
4. 申請書は3頁以内にまとめて下さい。

#### 3-3. 提出期限および提出先

応募に当たっては、前記の申請書にご記入の上、令和4年1月21（金）までに、下記宛に電子メール添付書類（Word 書類）としてお送り下さい。

問い合わせ先

京都大学化学研究所 共同研究推進室

E-mail: [icr-hub@scl.kyoto-u.ac.jp](mailto:icr-hub@scl.kyoto-u.ac.jp), 電話: (0774)38-3121

#### 4. 課題選考と採択通知

応募課題の採否は、当研究所の共同研究委員会で審査し、運営評議会の承認を経て決定されます。審査に際しては、共同研究の申請内容だけでなく、予算枠や、共通設備・機器・資料の使用時間等も考慮いたします。採否の結果（内定）については、令和4年3月に当研究所の所長から研究代表者に通知いたします。

#### 5. 研究の実施および研究成果報告

##### 5-1. 研究経費等

研究代表者と当研究所で対応する共同研究者には、予算の範囲内で、研究経費（備品費および消耗品費）と旅費が支給されます。また、研究協力者（学生も含めることが可能です\*）にも予算の範囲内で旅費が支給されます。共同研究の実施に当たっては、まず対応する共同研究者にご連絡下さい。なお、当研究所には、共同研究者のための宿泊施設はありません。

\* 研究協力者について、学生の場合は原則として大学院生といたします。なお、傷害保険等に参加していることが必要です。

##### 5-2. 研究成果報告

採択された研究課題については、研究成果報告書を次に記す作成要領に従って記載・提出していただきます。その報告書は、まとめて当研究所の国際共同利用・共同研究報告書集として公開させていただく予定です。また、その内容を研究成果報告会でご報告いただくことがあります。なお、報告会についての詳細は、採択課題の研究代表者に後日お知らせいたします。

##### 5-3. 研究成果報告書の作成要領

分野選択型研究、課題提案型研究、施設・機器利用型研究については1頁、連携・融合促進型研究については2頁の報告書を（様式5）を用いて作成下さい。A4版の用紙には1頁あたり1,200字程度が記載できます。図表などカラーを用いても構いませんが、報告書集刊行の際はモノクロ印刷になることもありますので、その点をお含み置き下さい。

1頁の1行目の中央に研究課題名、3行目に右詰めで研究代表者の氏名と所属、5行目から本文を記載して下さい。なお、当研究所で対応した共同研究者は報告書の共著者とはせず、必要に応じて本文中に明記して下さい。また、国際共同研究の場合、報告書は英文でご作成ください。

##### 5-4. 報告書の内容

形式は自由ですが、例えば、実験的研究では、目的、実験方法、実験結果、考察、成果報告（論文、学会発表等）をお書き下さい。なお、連携・融合促進型研究で研究集会を開催した場合には、研究集会のプログラム、参加者名簿（所属機関・部局・職名を明記）、および、作成された場合は要旨集またはプロシーディングスを添付して下さい。

##### 5-5. 報告書の提出

提出締切日は、令和5年2月末日とします。電子ファイル（WordファイルとPDFファイル）を、下記宛にお送り下さい。なお、ファイル名は「課題番号＋代表者名（姓）」として下さい（例：2022-1 田中.doc、2022-1 田中.pdf）。

問い合わせ先

京都大学化学研究所 共同研究推進室

E-mail: icr-hub@scl.kyoto-u.ac.jp, 電話: (0774)38-3121

##### 5-6. 研究成果の公開

学術論文などによる研究成果の公開に際しては、京都大学化学研究所の国際共同利用・共同研究として行われたことを明記して下さい。英文での謝辞例を次に示します。

謝辞例: This work was supported by the International Collaborative Research Program of Institute for Chemical Research, Kyoto University (grant # XXXX).

日本語での謝辞は、この英文表記に準ずるものとして下さい。



化学研究所 国際共拠点 R4年度採択課題 (応募195件, 採択 136件, 採択率 69.7 %, 国際共同研究割合46.3%)

課題番号	研究代表者	研究代表者所属	化研内 研究協力者	型	選択 分野	実施 状況	国際	課題名 (和文・英文)
2022-1	中川 充	地方独立行政法人大阪産業技術研究所	倉田 博基	分野選択型	1	萌芽的		分岐構造を有するらせん状金ナノワイヤーの合成および光学特性評価 Synthesis and optical characterization of helical gold nanowires with branches
2022-2	老川 典夫	関西大学・化学生命工学部	藤井 知実	分野選択型	1	発展的		根粒菌由来GraE タンパク質の結晶構造解析 Crystal Structure Analysis of GraE from Root-Nodule-Forming Bacterium
2022-3	大西 哲哉	理化学研究所・仁科加速器科学研究所センター	若杉 昌徳	分野選択型	1	萌芽的		ナノ構造を持つ ISOL 用標的の開発 Development of new nano-structure target for ISOL
2022-4	花山 良平	光産業創成大学院大学・光産業創成研究所	若杉 昌徳	分野選択型	1	発展的		ブリュリス付与による高変換TNSA イオン加速機構実証 Enhanced production of fast ions by TNSA with Pre-pulse Laser
2022-5	小平 聡	国立研究開発法人量子科学技術研究開発機構	小河原 亮	分野選択型	1	萌芽的		電子線をを用いた超高線量放射線がん治療 (FLASH) の作用機序の解明の試み Verification of radiochemical reaction mechanism for FLASH radiotherapy with electron beams
2022-6	Wei-Tin Chen	National Taiwan University, Center for Condensed Matter Sciences	島川 祐一	分野選択型	2	発展的	国際	Design and Tailoring Advanced Functional Materials: Symmetry Operation and High Pressure Synthesis
2022-7	ALAKANANDA HAJRA	DEPARTMENT OF CHEMISTRY, VISVA-BHARATI UNIVERSITY, SANTINIKETAN-731235, INDIA	中村 正治	分野選択型	2	発展的	国際	Carboboation and Carbosilylation by Merging Iron and Visible-Light Photocatalysis
2022-8	W. M. C. Sameera	University of Colombo, Department of Chemistry	大木 靖弘	分野選択型	2	萌芽的	国際	コバルトを反応点とするニトロゲナーゼのモデル反応の理論解析 Computational mechanistic study on the Co-catalyzed nitrogenase model reactions.
2022-9	Todd B. Marder	Julius-Maximilians-Universität Würzburg, Institut für Anorganische Chemie	梶 弘典	分野選択型	2	発展的	国際	剛直なフッ素化三配位ホウ素骨格をアクセプターとする新規発光材料の開発とデバイス評価 Development and device evaluation of new D- $\pi$ -A emitters based on rigidified triarylborone acceptors
2022-10	Zhenhong Tan	Institute of High Energy Physics (IHEP) of the Chinese Academy of Sciences, China Spallation Neutron Source (CSNS)	島川 祐一	分野選択型	2	発展的	国際	異常高原子価 Fe イオンを含む新規六方晶ペロブスカイト酸化物の高圧合成および磁気特性の研究 High pressure synthesis of novel hexagonal perovskite oxides containing unusually high-valence Fe ions and investigation of their magnetic properties
2022-11	Midori Etefani AMANO PATINO	Institut Charles Gerhardt Montpellier (ICGM, CNRS), D4: Chemistry of Materials, Nanostructures, Materials for Energy	島川 祐一	分野選択型	2	発展的	国際	高圧合成技術を用いた新規磁気四重極ペロブスカイトの作製とその特性評価 Preparation and Characterization of Novel Magnetic Quadruple Perovskites by High Pressure
2022-12	KOEDTRUAD Anucha	Chinese Academy of Science (CAS), Institute of High Energy Physics (IHEP), Chinese Spallation Neutron Source (CSNS)	島川 祐一	分野選択型	2	萌芽的	国際	ハイドライドおよび陰イオンクラスターを含んだ新規Na-アンチペロブスカイト型固体電解質材料の高圧合成とイオン伝導の研究 High-pressure synthesis and ionic conducting study of novel Na-antiperovskites containing hydride and cluster anions as solid electrolytes in batteries
2022-13	Rainer Streubel	Institute for Inorganic Chemistry, University of Bonn	水畑 吉行 時任 雪博	分野選択型	2	発展的	国際	新規なアニオン性FLPを用いた小分子活性化 Small molecule activation using anionic crypto-FLPs
2022-14	Takeaki Iwanoto	Tohoku University, Department of Chemistry	水畑 吉行	分野選択型	2	発展的	国際	非対称型高周期典型元素 $\pi$ 電子系の開拓と物性解明 Development of Unsymmetrical $\pi$ -Electron Systems of Heavier Main Group Elements and Elucidation of Their Property
2022-15	LAKSHMIKANTA ADAK	Department of Chemistry, Indian Institute of Engineering Science and Technology, Shibpur	中村 正治	分野選択型	2	発展的	国際	Development of 1,4-Addition Reactions via Iron Catalysis
2022-16	Apurba K. Das	Department of Chemistry, Indian Institute of Technology Indore	中村 正治	分野選択型	2	発展的	国際	Peptide Bolaamphiphile Anchored Nickel-based Metallohydrogel as Electrocatalyst for Hydrogen Production

2022-17	小笠原 正道	徳島大学・大学院社会産業理工学研究部	大木 靖弘	分野選択型	2	萌芽的	鉄含有リン系配位子の合成と金属クラスター錯体の合成への利用 Synthesis of Fe-containing phosphorus ligands and their application in the preparation of metal-cluster molecules
2022-18	若林 成知	新薬医療科学大学・保健衛生学部医療栄養学科	大木 靖弘	分野選択型	2	萌芽的	自己集合性含ホウ素化合物の合成、集合過程解明ならびに機能開拓 Synthesis of Self-Assembled Organoboron Compounds, Elucidation of Self-Assembly Process, and Creation of New Functions
2022-19	小田 晋	関西学院大学・理学部	堀 弘典	分野選択型	2	発展的	MR-TADF 発光材料を用いた高効率発光型有機EL 素子の開発 Highly Efficient Solution-Processed Organic Light-Emitting Diodes Employing Multiple Resonance-Induced Thermally Activated Delayed Fluorescence Emitter
2022-20	山口 佳隆	横浜国立大学・大学院工学研究院	中村 正治	分野選択型	2	発展的	3. 座ピンサー型NPN 配位子を利用した核殻錯体の合成とその触媒作用 Synthesis and its catalysis of dinuclear complexes utilizing a pincer-type NNP ligand
2022-21	橋本 徹	山陽小野田市立山口東京理科大学・工学部応用化学科	中村 正治	分野選択型	2	萌芽的	有機ケイ素化合物を触媒としたアルコールの脱水型エーテル合成 Synthesis of Alkyl Ethers Using Two Different Alcohols Catalyzed by Organosilane Compound
2022-22	光藤 耕一	岡山大学・大学院自然科学学域	若宮 淳志	分野選択型	2	萌芽的	優れた光物性・電気化学的特性を併せ持つ新奇ヘテロアセン分子の開発 Development of heteroarenes with excellent photophysical and electrochemical properties
2022-23	笹森 貴裕	筑波大学・数理物質系化学域	若宮 淳志	分野選択型	2	発展的	高性能ペロブスカイト太陽電池作製に有効な高活性酸化スカルベンジャーの開発 Creation of Effective Oxidation Scavenger for Efficient Perovskite-based Solar Cells
2022-24	Jiangning Song	Monash University, Biomedicine Discovery Institute	阿久津 達也	分野選択型	3	発展的	タンパク質のミセス突然変異による安定性の変化予測のための機械学習方式の開発 Developing machine learning approaches for prediction of protein stability changes upon missense mutations
2022-25	Jinn-Moon Yang	National Yang Ming Chiao Tung University, Department of Biological Science and Technology/Institute of Bioinformatics & Systems Biology	阿久津 達也	分野選択型	3	発展的	深層学習を用いたオミクスデータとモジュールに基づくネットワークデータの統合解析による腫瘍細胞分類 Integrating omics data and module-based network with deep learning to develop cancer type predictive models
2022-26	Morgan Gaia	CEA/Genoscope, UMR8030	緒方 博之	分野選択型	3	発展的	巨大ウイルスの進化と生命の起源との関係 Evolution of giant viruses and relationships with the origin of Life
2022-27	Samuel Chaffron	LS2N, CNRS UMR6004	遠藤 寿	分野選択型	3	発展的	群集インタクトーム解析による海洋微生物・ウイルス間相互作用の解明 Revealing marine microbial-viral interactions through community interactome analyses
2022-28	Masayuki Karasuyama	Nagoya Institute of Technology, Department of Computer Science	熊見塚 拓	分野選択型	3	萌芽的	統計的機械学習による効率的なグラフ構造データ解析法の開発 A Study on Statistical Machine Learning for Efficient Graph Structured Data Analysis
2022-29	岸本 利彦	東邦大学・理学部生物分子科学科	田村 武幸	分野選択型	3	萌芽的	オミクスデータと流挙動解析に基づく高温適応進化の機序解明 Revealing evolution mechanism of adaptation to high temperature based on omics data and flux balance analysis.
2022-30	ホセ ナチエル	東邦大学・理学部情報科学科	阿久津 達也	分野選択型	3	萌芽的	確率的最小支配集合による複雑ネットワークの制御と解析 Control and Analysis of Complex Networks via Probabilistic Minimum Dominating Sets
2022-31	渡辺 登喜子	大阪大学・微生物病研究所	緒方 博之	分野選択型	3	発展的	野生動物の保有するコロナウイルスの包括的検出法の開発研究 Development of a comprehensive detection method for coronaviruses originated in wildlife
2022-32	吉田 天士	京都大学・大学院農学研究科応用生物科学専攻	緒方 博之	分野選択型	3	萌芽的	無光圏における微生物生態 Microbial ecology in the dark sea
2022-33	茅野 光範	帯広畜産大学・グローバルヘルスメディシン研究センター	馬見塚 拓	分野選択型	3	発展的	効果的な分子ネットワーク解析方法の発展と医学・農学への応用 Effective molecular network analysis and application to medical and agricultural research
2022-34	Markus W. Ribbe	Department of Molecular Biology and Biochemistry, Department of Chemistry, University of California, Irvine	谷藤 一樹	分野選択型	4	萌芽的	<sup>57</sup> Fe ラベリングを用いた窒素還元酵素Fe タンパクの触媒的・生化学的動態解析 Investigations into Catalytic and Biochemical Behaviors of Nitrogenase Fe protein using <sup>57</sup> Fe labeling

2022-35	Atsushi GOTO	School of Physical & Mathematical Sciences, Division of Chemistry & Biological Chemistry, Nanyang Technological University	黄瀬 雄司	分野選択型	4	発展的	国際	おたまじやし状やス型セルロースナノクリスタルの精密合成と高次構制御 Precise synthesis and controlling higher order structure of tadpole-like Janus cellulose nanocrystal
2022-36	Akinori Saeki	Department of Applied Chemistry, Graduate School of Engineering, Osaka University	若宮 淳志	分野選択型	4	発展的	国際	ペロブスカイト太陽電池の組成探索: 素子性能と基礎物性の相関 Exploration of perovskite solar cell composition: correlating device performance and fundamental property
2022-37	Atsushi Takano	Nagoya University, Department of Molecular and Macromolecular Chemistry	松宮 由実	分野選択型	4	萌芽的	国際	高純度、高分子量環状高分子の精密合成と粘弾性 Precise synthesis and viscoelastic properties of ring polymers with high purity and high molecular weight.
2022-38	MARGETIC, Davor	Rudjer Boskovic Institute, Division of organic chemistry and biochemistry, Laboratory for physical organic chemistry	村田 靖次郎	分野選択型	4	発展的	国際	グアニジン修飾イサチンの付加環化反応に関する研究 Exploration of Cycloaddition Properties of Guanidine Functionalized Isatins
2022-39	CHAOLUMEN	Inner Mongolia University (IMU), College of Chemistry and Chemical Engineering	橋川 祥史	分野選択型	4	発展的	国際	ダブルヘリクス構造の導入による異なる開口方向をもつ新規ナノチューブ分子の合成 Synthesis of Novel Nanotube Molecules with Different Hole Directions by Introducing a Double Helix Structure
2022-40	太田 雄大	山口東京理科大学・工学部応用化学科	大木 靖弘	分野選択型	4	萌芽的		金属酵素化学モデルの創製と材料・医学への応用 Developing bioinspired molecular catalysts for materials science and medicinal chemistry.
2022-41	亀尾 肇	大阪府立大学・大学院理学系研究科	大木 靖弘	分野選択型	4	萌芽的		ニッケル-Z型 ( $\sigma$ 電子受容性) 配位子相互作用を鍵要素とする錯体固定 Dinitrogen Fixation based on nickel-Z-type ( $\sigma$ -Electron Acceptor) Ligand Interaction
2022-42	平井 智康	大阪工業大学・工学部応用化学科	竹中 幹人	分野選択型	4	萌芽的		キラリシカルの構造と分子認識との相関解明 Evaluation an Effect of Structure in Chiral Silica on Molecular Recognition
2022-43	永木 要一郎	北海道大学・大学院理学研究科	山子 茂	分野選択型	4	発展的		フロー合成法を用いた官能性ビニルテルリド合成法 Synthesis of functional vinyltelurides using flow reactors
2022-44	小林 健二	静岡大学・グリーン科学技術研究所(および理学部)	茅原 栄一	分野選択型	4	発展的		環状ヘキサ-2,7-アノントリエンエチレン誘導体と環状パラフェニレンとのホスト-ゲスト化学に基づく複合化 Host-Guest Complexation of Cyclohexa-2,7-anthylene Ethynylene Derivatives with [n]CPP
2022-45	高橋 裕	東北大学・未来科学技術共同研究センター	登阪 雅聡	分野選択型	4	発展的		超分子構造高分子の滑潤作用の解明と最適化 Elucidation of the lubrication properties of hyperbranched polymers and their optimization
2022-46	土戸 良高	東京理科大学・理学部第一部化学科	茅原 栄一	分野選択型	4	発展的		金(I)及び白金(II)多核錯体を媒した高歪み環状共役化合物の合成 Synthesis of Highly Strained Macrocyclic $\pi$ -Conjugated Molecules via a Multinuclear Au(I)-Pt(II) complex
2022-47	黒飛 敬	久留米工業高等専門学校・一般科目(理科学系)	村田 靖次郎	分野選択型	4	発展的		有機電子材料を指向したアザアズレン3量体の合成と応用 Synthesis and Applications of Novel Azazulene Trimer toward Electronic materials
2022-48	村田 理尚	大阪工業大学・工学部応用化学科	村田 靖次郎	分野選択型	4	萌芽的		高導電性n型有機金属材料の開発 Development of Organometallic n-Type Materials with High Electrical Conductivity
2022-49	上野 裕	東北大学・学際科学フロンティア研究所(FRS)	村田 靖次郎	分野選択型	4	発展的		未踏超不安定構造の単離および物性解明による新概念材料設計指針の創出 Isolation of ultra-unstable chemical species toward unprecedented element strategy
2022-50	Giovanni Ianniruberto	Dipartimento di Ingegneria Chimica, dei Materiali e della Produzione Industriale, Università degli Studi di Napoli "Federico II"	佐藤 健	分野選択型	5	萌芽的	国際	非からみあい高分子の非線形粘弾性 Non-linear viscoelasticity of untangled polymers
2022-51	Shilong Wu	Changchun Institute of Applied Chemistry, Chinese Academy of Sciences (CAS)	松宮 由実	分野選択型	5	萌芽的	国際	一定の絡み合い数とKuhn セグメント数を持つポリ(n-アルキルメタクリレート)メルトの非線形伸長レオロジー Nonlinear Extensional Rheology of Entangled Poly(n-alkyl methacrylate) Melts with Fixed Number of Entanglements and Kuhn Segments per Chain
2022-52	HO, Tung-Yuan	Academia Sinica, Research Center for Environmental Changes	奈林 由樹	分野選択型	5	発展的	国際	北太平洋における微量金属の元素・同位体組成・起源と内部循環 (3) Trace metal elemental and isotopic composition in the North Pacific Ocean: sources and internal cycling (3)

2022-53	Tadanori Koga	Stony Brook University, Department of Material Science and Chemical Engineering	竹中 幹人	分野選択型	5	発展的	国際	高分子ナノコンポジットの補強メカニズムの解明-II Resolving the structure-dynamics-property relationship in polymer nanocomposites under uniaxial stretching-II
2022-54	Sathish K. Sukumaran	Graduate School of Organic Materials Science, Yamagata University	佐藤 健	分野選択型	5	発展的	国際	高分子液体の高周波応答: レオロジーおよび誘電緩和 High Frequency Response of Polymeric Liquids: Rheology and Dielectric Relaxation
2022-55	Osamu Urakawa	Osaka University, Graduate School of Science, Department of Macromolecular Science	松宮 由実	分野選択型	5	萌芽的	国際	水素結合相互作用によるポリマーブレンド材料の力学特性の制御 Control of Mechanical Properties in Polymer Blend Materials by Hydrogen Bonding Interaction
2022-56	五月女 光	大阪大学・大学院基礎工学研究科物質創成専攻	梶 弘典	分野選択型	5	発展的		超低波数ラマン分光による熱活性化遅延蛍光材料の構造揺らぎ解析 Analyzing Structural Fluctuation in Thermally Activated Delayed Fluorescence Materials with Ultra-low-Frequency Raman Spectroscopy
2022-57	中口 謙	近畿大学・理工学部	宗林 由樹	分野選択型	5	萌芽的		海水中の微量重金属の分布に及ぼすマイクロプラスチックの影響(2) Effect of microplastics on distribution of trace heavy metals in sea water
2022-58	向井 浩	京都教育大学・教育学部理学科	宗林 由樹	分野選択型	5	萌芽的		イオンの電場応答を利用したイオン液体含有高分子膜による金属イオンの液膜輸送の開発 Exploration of liquid membrane transportation of metal ions with a polymer membrane containing ionic liquid by use of electric field response of ions
2022-59	藤原 明比古	関西学院大学・工学部	竹中 幹人	分野選択型	5	発展的		硫黄ポリマー材料におけるナノ構造不均一評価 Nano-scale structure characterization of organosulfur polymer
2022-60	大坂 昇	岡山理科大学・理学部化学科	竹中 幹人	分野選択型	5	萌芽的		食品油脂中の高分子鎖のコンフォメーション解析 Conformation analysis on polymer in food-grade oil
2022-61	飯田 健二	北海道大学・触媒科学研究所	寺西 利治	分野選択型	5	発展的		プラズマニック合金ナノ粒子を設計するための理論的指針の構築 Construction of Theoretical Guidelines for Designing Plasmonic Nanoalloys
2022-62	園山 正史	群馬大学・大学院理工学府	長谷川 健	分野選択型	5	萌芽的		新規ハイブリッド型部分アッ素化リン脂質二分子膜の構造・物性の解析 Physicochemical characterization of novel hybrid partially fluorinated phospholipid bilayers
2022-63	河内 孝之	京都大学・生命科学研究所	山口 信次郎	分野選択型	5	萌芽的		基幹陸上植物苔類ゼニゴケにおける活性型シペリンの単離と同定 Identification of active gibberellins in the basal land plant <i>Marchantia polymorpha</i>
2022-64	Kab-Jin Kim	Korea Advanced Institute of Science and Technology, Department of Physics	小野 輝男	分野選択型	特定	発展的	国際	磁性絶縁体での量子マグノン研究 Characteristics of quantum magnon in magnetic insulators
2022-65	Sanghoon Kim	University of Ulsan, Department of Physics	小野 輝男	分野選択型	特定	発展的	国際	Orbital Hall effect in transition metal dichalcogenides.
2022-66	Alexey Ognev	Far Eastern Federal University, Institute of High Technologies and Advanced Materials, Department of General and Experimental Physics	小野 輝男	分野選択型	特定	萌芽的	国際	磁気異方性とジャロソンスキー-守谷相互作用によるゴウ効率スピン軌道トルクの開拓 Investigation on high efficient spin-orbit torque effect in multilayers with combine anisotropy and DMI
2022-67	Takuya F. Sagawa	Laboratory for Physical Chemistry, ETH Zürich	水落 憲和	分野選択型	特定	発展的	国際	ナノダイヤモンド中のNV 中心作製効率化研究 Research on the efficiency enhancement of the NV centers creation in nanodiamond
2022-68	Gopalakrishnan Balasubramanian	Heimholtz-Zentrum Dresden-Rossendorf, Germany	水落 憲和	分野選択型	特定	発展的	国際	表面近傍NV 中心の安定化とスピンドメインミックスの研究 Research toward stable NV centers at shallow region and spin dynamics in diamond
2022-69	諸田 美砂子	産業技術総合研究所・デバイス技術研究部門	小野 輝男	分野選択型	特定	萌芽的		カルコゲナイド系超格子のトポロジカル相制御の実証 Demonstration of topological phase control in chalcogenide superlattices
2022-70	石橋 未央	東京大学・理学系研究科物理学専攻	小野 輝男	分野選択型	特定	萌芽的		人工反強磁性体のマグノンを利用した量子情報演算素子の基礎技術開発 Research and development of magnon quantum logic gate devices using synthetic antiferromagnets

2022-71	徳田 規夫	金沢大学・ナノマテリアル研究所	水落 憲和	分野選択型	特定	発展的	ダイヤモンド量子情報素子のための表面状態研究 Research of surface state for diamond quantum information device
2022-72	秋野 俊晴	産業技術総合研究所・先進パワーエレクトロニクス研究センター	水落 憲和	分野選択型	特定	発展的	量子センサの高感度化に向けたリンドーブダイヤモンド合成と量子科学技術研究 Research of quantum technology and diamond synthesis for higher sensitivity of NV quantum sensor
2022-73	Yan-Mei Li	Tsinghua University, Department of Chemistry	上杉 志成	課題提案型		発展的	がん免疫療法のための自己集合性アジュバント含有ワクチン Self-Assembling Adjuvant-Built-In Vaccines for Cancer Immune Therapy
2022-74	Pinghe Gai	Xiamen University, Department of Marine Chemistry and Geochemistry	宗林 由樹	課題提案型		発展的	Evaluation of CaCO <sub>3</sub> dissolution rates in deep-sea sediments by a novel tracer method
2022-75	Thomas Wirth	Cardiff University, School of Chemistry, Professor	中村 正治	課題提案型		発展的	Advanced Oxygen – mediated Flow Chemistry
2022-76	Silvia PUJALS	Institute for Advanced Chemistry of Catalonia	二木 史朗	課題提案型		発展的	ナノ医薬の新規細胞内効率的送達法 Novel strategy for intracellular delivery of nanomedicines
2022-77	Anne S. Ulrich	Karlsruhe Institute of Technology (KIT), Institute of Organic Chemistry (IOC) and Institute of Biological Interfaces (IBG-2), Chair of Biochemistry at IOC	二木 史朗	課題提案型		発展的	由差誘導ペプチドの構造活性相関と応用 Structural and functional analysis of curvature-inducing peptides and application
2022-78	Ebinazar B. Namdas	The University of Queensland, School of Mathematics and Physics, Centre for Organic Photonics & Electronics	権 弘典	課題提案型		発展的	熱活性化遅延蛍光を基盤とする高効率有機EL デバイスにおける効率低下の詳細解析 In-depth analysis of efficiency roll-off in highly efficient TADF-based organic electroluminescence devices
2022-79	Yusuke Azuma	Matopolska Center of Biotechnology, Jagiellonian University	二木 史朗	課題提案型		萌芽的	人工タンパク質ナノケージを用いた細胞内への機能性タンパク質の送達 Intracellular delivery of biofunctional proteins using artificial protein nanocages
2022-80	菊地 和也	大阪大学・大学院工学研究科	上杉 志成	課題提案型		萌芽的	細胞内相分離タンパク質のリアルタイム可視化 Real-Time Visualization of Cellular Phase-Separating Proteins
2022-81	西川 元也	東京理科大学・薬学部	上杉 志成	課題提案型		萌芽的	合成小分子化合物による細胞の遠隔操作 Remote Control of Cells by Synthetic Small Molecules
2022-82	木村 謙介	理化学研究所・開拓研究本部	権 弘典	課題提案型		発展的	有機合成・単分子測定・計算化学の協同による2次元ドナー・アクセプター分子系の構築 Construction of two-dimensional donor-acceptor systems by the collaboration of organic synthesis, single-molecule measurement, and computational chemistry.
2022-83	三枝 栄子	大阪公立大学・大学院理学研究科物質分子系専攻	長谷川 健	課題提案型		萌芽的	両親媒性希土類錯体を利用した薄膜発光体の作製 Fabrication of luminescent thin films using amphiphilic lanthanide complexes
2022-84	稲谷 素洋	公立小松大学・生産システム科学部生産システム科学科	長谷川 健	課題提案型		萌芽的	フッ素系樹脂の摩擦界面における分子運動の解明 Molecular characterization of fluoropolymer at frictional interface
2022-85	中瀬 生彦	大阪公立大学・大学院理学系研究科生物科学専攻	二木 史朗	課題提案型		発展的	エクソソームの細胞内への送達設計 Design of intracellular delivery systems for extracellular vesicles
2022-86	江口 咲子	三重大学・大学院医学系研究科消化器内科学	二木 史朗	課題提案型		発展的	細胞外小泡の標的細胞への移行メカニズムの解明 Investigation of cellular uptake mechanism using extracellular vesicles
2022-87	QU, Li-Jia	Peking University, School of Life Sciences	青山 卓史	課題提案型		発展的	花粉管形成におけるPIP5K 遺伝子の役割 Role of PIP5K Genes in Pollen Tube Development
2022-88	Xianzhu Dai	College of Resources and Environment, Southwest University	栗原 達夫	課題提案型		萌芽的	低温適応微生物を用いた低温異種タンパク質分泌生産系の構築 Construction of heterologous protein secretion system at low temperatures by using cold-adapted microorganisms

2022-89	Maria Michela Corsaro	University of Naples Federico II, Department of Chemical Sciences	栗原 達夫	課題提案型		発展的	国際	細菌が放出する外膜小胞の表面多糖の構造機能解析 Structural and functional analysis of the surface polysaccharides of outer membrane vesicles released by bacteria
2022-90	Zuhua He	Chinese Academy of Sciences, CAS Center for Excellence in Molecular Plant Sciences, Institute of Plant Physiology and Ecology	山口 信次郎	課題提案型		発展的	国際	イネの成長ホルモンの不活性化機構の解析 Molecular mechanisms for the inactivation of a growth hormone in rice
2022-91	Yunde Zhao	University of California San Diego, Division of Biological Sciences, Department of Cell and Developmental Biology	増口 潔	課題提案型		萌芽的	国際	新規ストリゴラクトン輸送タンパク質の解析 Analysis of novel transporters for strigolactones or their biosynthetic intermediates
2022-92	Ryoko Shimada	Department of Mathematical and Physical Sciences, Japan Women's University	佐藤 健	課題提案型		発展的	国際	ネマチック液晶/溶液混合系における相分離 Phase separation in mixture of nematic liquid crystal and solvent
2022-93	RUBIO, Vicente	National Center of Biotechnology (ONB-CSIC), Plant Molecular Genetics Dept.	柘植 知彦	課題提案型		発展的	国際	植物形態形成におけるRNA プロセッシングを制御する遺伝子発現制御ネットワーク Chromatin, epigenetic and proteolytic regulation of RNA processing in plant morphogenesis
2022-94	Lu Zhou	Fudan University, School of Pharmacy	上杉 志成	課題提案型		発展的	国際	小分子化合物による位置選択的タンパク質アセチル化リン酸化 Site-Selective Protein Acetylation and Phosphorylation by Small Molecules
2022-95	Lian Duan	Tsinghua University, Department of Chemistry	権 弘典	課題提案型		発展的	国際	迅速な逆間交差を示す熱活性化遅延蛍光材料を用いた高効率・高色純度有機EL素子の作製 Developments of highly efficient and high color purity organic electroluminescent devices based on thermally activated delayed fluorescent materials exhibiting ultrafast reverse intersystem crossing process
2022-96	Maya Endoh	Stony Brook University, Department of Material Science and Chemical Engineering	竹中 幹人	課題提案型		発展的	国際	高分子ナノ表面構造による殺菌効果-IV Fabrication of nanotopographical polymer surfaces for bactericidal properties-IV
2022-97	Ken Nakano	Yokohama National University, Faculty of Environment and Information Sciences	辻井 敬亘	課題提案型		萌芽的	国際	動的固着理論の検証と展開 Verification and Development of Dynamic Stiction Theory
2022-98	Robert C. Farrier, Jr.	Michigan State University, Chemical Engineering and Materials Science	辻井 敬亘	課題提案型		発展的	国際	リチウムイオン電池用ポリエーテル系ナノコンポジット固体電解質の合成 Synthesis of Polyether Nanocomposite Solid Polymer Electrolytes for Lithium Ion Batteries
2022-99	Yasuhiro Tachibana	RMIT University, School of Engineering	寺西 利治	課題提案型		発展的	国際	太陽光分解のための金属酸化物ナノ結晶膜の作製と物性評価 Development and characterization of metal oxide nanocrystalline films for solar water splitting
2022-100	Jean-Pierre Bucher	Université de Strasbourg, Institut de Physique et Chimie des Matériaux (IPCMS)	寺西 利治	課題提案型		発展的	国際	応用に向けたナノ構造材料への学際的アプローチ Interdisciplinary Approach to Nanostructured Materials for Applications
2022-101	Kensuke Homma	Hiroshima University, Physics	若杉 昌徳	課題提案型		発展的	国際	宇宙暗黒成分解明へ向けた真空室内四光波混合の探索 Search for four-wave-mixing in the vacuum - Unveiling dark components in the Universe -
2022-102	Antonio Abate	Novel Materials and interfaces for photovoltaic solar cells, Helmholtz-Zentrum Berlin, Germany	若宮 淳志	課題提案型		発展的	国際	新規正孔輸送層上でのSn ペロブスカイト半導体薄膜の結晶化 Tin-perovskite thin film crystallization on new hole-transporting materials
2022-103	肥塚 崇男	山口大学大学院創成科学研究科	柘植 知彦	課題提案型		発展的		植物誘導性ベンゼノイド生合成におけるアルデヒド脱水素酵素の機能解析 Biochemical characterization of aldehyde dehydrogenases involved in the biosynthesis of plant volatile benzenoids
2022-104	安喜 史織	奈良先端科学技術大学院大学・先端科学技術研究科	青山 卓史	課題提案型		萌芽的		葉表皮細胞の分化制御における植物ホルモン・サイトカイニンの役割 Regulatory Role of Phytohormone Cytokinin on Leaf Epidermal Cell Differentiation
2022-105	長浜 太郎	北海道大学・工学研究院応用化学部門	小野 輝男	課題提案型		発展的		Fe <sub>3</sub> O <sub>4</sub> /NiCo <sub>2</sub> O <sub>4</sub> 多層膜の電子およびスピン物性の解明 Electronic and spintronic properties of multilayer system including NiCo <sub>2</sub> O <sub>4</sub> and Fe <sub>3</sub> O <sub>4</sub>
2022-106	金井 求	東京大学大学院薬学系研究科	権 弘典	課題提案型		発展的		アルツハイマー病治療に向けたアミロイド光酸素化触媒の構造最適化 Structural optimization of amyloid photooxygenation catalysts for the treatment of Alzheimer's disease



2022-107	清谷 浩輝	早稲田大学・先進理工学部	梶 弘典	課題提案型		萌芽的	動的効果を考慮した熱活性化型遅延蛍光速度論の確立 Establishment of the thermally activated delayed fluorescence kinetics incorporating the dynamical effects
2022-108	倉田 淳志	近畿大学・農学部応用生命化学科	栗原 達夫	課題提案型		発展的	腸内細菌が生産する細胞外膜小胞の生理機能解析と応用 Analysis of the physiological functions of extracellular vesicles produced by intestinal bacteria and their application
2022-109	豊竹 洋佑	立命館大学・生命科学部生物工学科	栗原 達夫	課題提案型		萌芽的	酢酸菌における膜脂質依存的な発酵ストレス応答の解析 Analysis of membrane lipid-dependent fermentation stress response in acetic acid bacteria
2022-110	増野 敦信	弘前大学・大学院理工学研究科	島川 祐一	課題提案型		萌芽的	撥秩序ガラスの熱伝導 Thermal conduction of pseudo-ordered oxide glasses
2022-111	土屋 敬志	物質・材料研究機構・国際ナノアーキテクニクス研究拠点	菅 大介	課題提案型		萌芽的	電気化学的プロトン挿入を利用した金属酸化物の新奇物性探索 Novel functional properties of metal oxides explored by electrochemical proton insertion
2022-112	齊藤 高志	高エネルギー加速器研究機構・物質構造科学研究所	島川 祐一	課題提案型		萌芽的	高圧合成による新規フッ化物イオン伝導体の探索 Syntheses of novel fluoride-ion conductors using high pressures
2022-113	倉橋 健介	大阪公立大学工業高等専門学校・環境物質化学コース	宗林 由樹	課題提案型		萌芽的	界面活性剤を利用した溶媒含浸樹脂による金属分離 Metal separation by solvent impregnated resin using surfactant
2022-114	源明 誠	富山大学・学術研究部工学科	辻井 敬亘 大野 工司	課題提案型		発展的	全反射近赤外光法による高分子ブラン層内の水の構造解析 Structural Analysis of Water in Polymer Brush Layer Using Attenuated Total Reflection Near-Infrared Spectroscopy
2022-115	村瀬 浩貴	共立女子大学・家政学部家政学科	辻井 敬亘	課題提案型		発展的	3D プリンタを用いたモノリスの3次元構造制御 Manipulation of Three Dimensional Structure of Polymer Monoliths by 3D Printer
2022-116	真島 豊	東京工業大学・フロンティア材料研究所	寺西 利治	課題提案型		発展的	単電子トランジスタにおける巨大磁気抵抗効果の検討 Giant magnetic resistance on Single-Electron Transistor
2022-117	山添 誠司	東京都立大学・大学院理学研究科化学専攻	寺西 利治	課題提案型		萌芽的	担持金属表面に金属酸化物クラスターを修飾した二元機能軸線の創製 Development of bi-functional catalysts by modification of supported metal surface with metal oxide clusters
2022-118	浅香 透	名古屋工業大学・大学院工学研究科	猿山 雅亮	課題提案型		萌芽的	電子顕微鏡内での単一三次元量子ドット超格子の電子輸送特性と構造相転移移動の同時観測 Simultaneous observation of electron transport property and phase transition of a single 3D quantum dot superlattice in an electron microscope
2022-119	桑野 修	奈良県立医科大学・医学部	中村 正治	課題提案型		萌芽的	再生可能資源・木質バイオマスの先端化学材料への効率的変換法の開発 Development of efficient conversion method of woody biomass, renewable biological resources, to advanced chemical materials
2022-120	瀬戸 義哉	明治大学・農学部	山口 信次郎	課題提案型		発展的	「非典型的」ストロゴラクトン類の植物ホルモンおよび環状シグナルとしての機能解析 Functional analysis of non-canonical strigolactones as plant hormones and root-derived signals
2022-121	遊佐 真一	兵庫県立大学・大学院工学研究科	山子 茂	課題提案型		発展的	制御ラジカル重合による多重刺激応答性高分子の合成 Preparation of multi-stimulus-responsive polymer via controlled radical polymerization
2022-122	松井 隆太郎	京都大学・大学院エネルギー科学研究科	若杉 昌徳	課題提案型		萌芽的	積層CNTターゲットへの高強度レーザー照射による高圧ガス生成に関する実験研究 Study and experiment of the high-pressure gas generation by the high-power laser irradiation to the stacked CNT target
2022-123	岸本 泰明	京都大学・大学院エネルギー科学研究科	若杉 昌徳	課題提案型		発展的	高強度レーザーと構造性媒質の相互作用による高エネルギー密度プラズマの生成・保持に関する実験研究 Study of the generation and sustainment of high energy density plasmas due to the interaction between high power laser and structured medium
2022-124	Chengshan Wang	Middle Tennessee State University, Chemistry	長谷川 健	連携・融合促進型			Determine the three-dimensional structure of 13C labeled $\alpha$ -synuclein(61-95) in the Langmuir-Bodgett film and supported phospholipid bilayer by MAIRS2 国際

2022-125	Tadashi Inoue	Osaka University, Department of Macromolecular Science	松宮 由実	連携・融合促進型				国際	東アジア圏の若手レオロジストのための第16回ワークショップ The 16th International Workshop for East Asian Young Rheologists
2022-126	Ming-Wen Chu	National Taiwan University, Center for Condensed Matter Sciences	倉田 博基	施設・機器利用型				国際	Tackling the Electronic Instability of Charge-Density Waves by Electron Energy-Loss Spectroscopy
2022-127	Torranin CHAIRUANGSRI	Chiang Mai University, Industrial Chemistry	倉田 博基	施設・機器利用型				国際	Micro- and Nano-structural Characterization by Advanced Transmission Electron Microscopy of Novel Functional Materials
2022-128	Kunlang Ji	Centre for Science at Extreme Conditions and School of Chemistry, University of Edinburgh	島川 祐一	施設・機器利用型				国際	High-pressure synthesis of transition metal oxides with novel physical properties
2022-129	Mao Minoura	Rikkyo University, College of Science, Department of Chemistry	水畑 吉行	施設・機器利用型				国際	新規有機10族元素化合物の合成と性質解明 Synthesis and Characterization of Novel Group 16 Element Compounds
2022-130	Morimaru Kida	GSAS, Kobe University	中村 正治	施設・機器利用型				国際	FT-ICR-MSを用いた湖沼及び土壌環境中溶解有機物の化学特性および起源解析 Analyzing chemical properties and origins of dissolved organic matter in lakes and soils by FT-ICR-MS
2022-131	田中 雅章	名古屋工業大学・大学院工学研究科	小野 輝男	施設・機器利用型					磁位及び結晶構造の最適化による高効率のスピン注入材料の作製 Preparation of high-efficiency spin-injection materials using optimization of magnetism and crystal structure
2022-132	斉藤 光	九州大学・先端物質化学研究所	倉田 博基	施設・機器利用型					高効率CsPbBr <sub>3</sub> シンチレータの開発 Development of a highly efficient CsPbBr <sub>3</sub> scintillator
2022-133	宮本 光貴	島根大学・総合理工学部	倉田 博基	施設・機器利用型					核融合プラズマ対向材料中の水素・ヘリウム挙動の高精度測定 High accuracy measurement of hydrogen and helium behavior in plasma facing materials for nuclear fusion devices
2022-134	松尾 司	近畿大学・理工学部	水畑 吉行	施設・機器利用型					テトラレン・ルイス塩基付加体の合成と分子構造の解明 Synthesis and Structural Characterization of Lewis Base Adducts of Tetrylenes
2022-135	長岡 記嘉	福岡大学・理学部	水畑 吉行	施設・機器利用型					カルコゲノシリリウム骨格をもつカチオン性芳香族化合物の合成と構造解析 Synthesis and structures of cationic aromatics bearing chalconopyrylium units
2022-136	高橋 まさえ	東北大学・大学院農学研究科	水畑 吉行	施設・機器利用型					平面二次元シートに埋め込まれた低次元ケイ素材料の理論設計と動作原理の探索 Theoretical design of low-dimensional silicon material embedded in a flat two-dimensional sheet and exploration for operating principles

